Sede Amministrativa: Università degli Studi di Padova

Dipartimento di Scienze Chimiche

SCUOLA DI DOTTORATO DI RICERCA IN : Scienze Molecolari
INDIRIZZO: Scienze Chimiche
CICLO XXVI

SYNTHESIS AND CHEMICO-PHYSICAL AND STRUCTURAL CHARACTERIZATION OF NANOCRYSTALLINE INORGANIC MATERIALS OBTAINED VIA MINIEMULSIONS

Direttore della Scuola : Chiar.mo Prof. Antonino Polimeno
Coordinatore d’indirizzo: Chiar.mo Prof. Antonino Polimeno
Supervisore: Chiar.mo Prof. Maurizio Casarin

Dottorando : Paolo Dolcet

to the ones I love

The most exciting phrase to hear
in science, the one that heralds
new discoveries, is not “Eureka!”
but “That’s funny...”

I. Asimov

Contents

List of Figures 1

List of Schemes 3

List of Tables 5

List of Acronyms 7

Abstract 13

1. Introduction 15

2. Miniemulsions 19

- 2.1. Wet and colloidal chemistry routes for inorganic materials 19
- 2.2. Colloids and emulsion stability 20
- 2.3. Main features and applications of miniemulsions 25
- 2.4. Miniemulsion for inorganic chemistry 29

3. Pure and doped inorganic nanostructures for bioimaging 33

- 3.1. Basic principles of bioimaging 33
- 3.2. Inorganic systems for bioimaging: state of the art 35
- 3.3. Miniemulsions as chemical nanoreactors for the room temperature synthesis of inorganic crystalline nanostructures: ZnO colloids 39
- 3.4. Inorganic chemistry in a nanoreactor: Doped ZnO nanostructures by miniemulsion 47
- 3.5. Simple, common but functional: Biocompatible and luminescent Rare-Earth doped Magnesium and Calcium hydroxides from miniemulsion 57
- 3.6. Zinc sulfide 69
  - 3.6.1. Introduction 69
  - 3.6.2. Results and discussion 69
  - 3.6.3. Conclusions 81
- 3.7. Copper sulfide 83
  - 3.7.1. Introduction 83
  - 3.7.2. Results and discussion 84
  - 3.7.3. Conclusions 93
- 3.8. Calcium fluoride 95
  - 3.8.1. Introduction 95

3.8.2. Results and discussion . . . 95
3.8.3. Conclusions . . . 103

4. Inorganic nanostructures for catalysis 105
4.1. Introduction and general approaches . . . 105
4.2. Tin(IV) Oxide Coatings from Hybrid Organotin/Polymer Nanoparticles 107
4.3. Sol-gel processes at the droplet interface: hydrous zirconia and hafnia nanocapsules by interfacial inorganic polycondensation . . . 115
4.4. Inorganic chemistry in a nanoreactor: Au/TiO_2 nanocomposites by photolysis of a single-source precursor in miniemulsion . . . 123

5. Experimental details 131
5.1. Synthesis . . . 131
5.1.1. *Chemicals* . . . 131
5.1.2. *Synthesis of ZnS nanostructures* . . . 133
5.1.3. *Synthesis of CuS nanostructures* . . . 133
5.1.4. *Synthesis of CaF_2 nanostructures* . . . 133
5.2. Characterization . . . 134
5.2.1. *Dynamic Light Scattering* . . . 134
5.2.2. *UV-Vis and Reflectance Spectroscopy* . . . 134
5.2.3. *Transmission Electron Microscopy* . . . 134
5.2.4. *Scanning Electron Microscopy* . . . 134
5.2.5. *X-ray Diffraction* . . . 135
5.2.6. *X-ray Photoelectron Spectroscopy* . . . 135
5.2.7. *X-ray Absorption Spectroscopy* . . . 135
5.2.8. *Inductively Coupled Plasma – Mass Spectrometry* . . . 136
5.2.9. *Micro-Raman Spectroscopy* . . . 137
5.2.10. *FT-IR and Attenuated Total Reflectance-Infrared Spectroscopy* 137
5.2.11. *Thermogravimetric analysis – Differential Scanning Calorimetry* . . . 137
5.2.12. *Photoluminescence* . . . 138
5.2.13. *Viability and cytotoxicity tests* . . . 138

6. Conclusions and perspectives 141

A. Characterization Methods 145
A.1. Dynamic Light Scattering . . . 145
A.2. UV-Vis and Reflectance Spectroscopies . . . 146
A.3. Transmission Electron Microscopy . . . 146
A.4. Scanning Electron Microscopy . . . 147
A.5. X-ray Diffraction . . . 147
A.6. X-ray Absorption Fine Structure Spectroscopy . . . 149
A.7. X-ray Photoelectron Spectroscopy . . . 156
A.8. Inductively Coupled Plasma - Mass Spectrometry . . . 158

A.9. MicroRaman and Fourier Transformed Infrared Spectroscopies 158
A.10. Thermogravimetric Analysis and Differential Scanning Calorimetry . 159
A.11. Photoluminescence Spectroscopy 159
A.12. Lactate Dehydrogenase Cytotoxicity Assay 160
A.13. Resazurin Cell Viability Assay 160

Bibliography **161**

Acknowledgments **175**

List of Figures

2.1. Effect of molecular geometry and systems conditions on the packing parameter *p* and HLB values . . . 25
2.2. Ternary phase diagram for a water/hydrocarbon/surfactant system . 26
2.3. Homogenization of a miniemulsion . . . 27
2.4. Example of inverse miniemulsion stability . . . 28
2.5. Processes leading to the formation of inorganic nanoparticles in miniemulsion systems . . . 30

3.1. Bioconjugation basic principles . . . 37
3.2. UV-Vis of pure ZnS suspension . . . 70
3.3. TEM and SAED of ZnS nanostructures . . . 71
3.4. SEM micrograph of pure ZnS nanostructures . . . 71
3.5. XRD diffractograms of pure and doped ZnS NPs . . . 72
3.6. Diffuse Reflectance UV-Vis spectra of the obtained powders . . . 73
3.7. Excitation (thin) and emission (thick) spectra . . . 73
3.8. XANES spectra of ZnS samples . . . 77
3.9. Raman spectra of different ZnS samples . . . 80
3.10. TGA and DSC of ZnS NPs . . . 81
3.11. Covellite crystal structure . . . 83
3.12. DLS curves for pure CuS and CuS:Eu . . . 86
3.13. XRD diffractograms for samples obtained from Na_2S and different copper sources . . . 87
3.14. TEM, SAED and SEM of CuS nanostructures . . . 89
3.15. XRD diffractograms of pure and doped CuS nanostructures . . . 90
3.16. S 2p signal for pure CuS sample . . . 91
3.17. XANES and EXAFS spectra at Cu K-edge . . . 92
3.18. XANES spectra at S K-edge and EXAFS at dopants L_3-edges . . . 92
3.19. PL and PLE spectra for CuS nanostructures . . . 93
3.20. TGA-DSC curve of undoped CuS . . . 94
3.21. XRD diffractograms for pure and doped CaF_2 nanostructures . . . 96
3.22. Average crystallite size vs sonication time . . . 98
3.23. TEM and SAED for CaF_2 nanostructures . . . 99
3.24. SEM micrograph of CaF_2 nanoparticles obtained by miniemulsion . . 99
3.25. Emission spectrum and decay for CaF_2:Tb . . . 101
3.26. Emission spectrum and decay for CaF_2:Sm . . . 102
3.27. Dopant L_3-edge XANES spectra . . . 102

3.28. Raman spectra for pure and doped nanoparticles 103

5.1. Molecular structures for Brij® 52 and Igepal® CO-630 131

A.1. Schematic representation of Bragg's law 148
A.2. Normalized $\mu(E)$ for ZnS at Zn K-edge 150
A.3. Data reduction steps: a) raw data; b) identification of pre-edge (red line) and post-edge (blue) backgrounds; c) identification of $\mu_0(E)$ (red line); d) normalized data 155
A.4. XPS phenomena 157

List of Schemes

3.1. Emission processes for ZnS nanoparticles 74
3.2. Different reaction pathways tested 85

List of Tables

2.1. Classification of surfactant according to HLB values 24

3.1. Different optical imaging techniques 34
3.2. Bioconjugation chemistry for nanoparticles 38
3.3. ICP-MS measurements 74
3.4. XPS semi-quantitative analysis results 75
3.5. EXAFS analysis at Zn K-edge 78
3.6. EXAFS analyses at dopant edges 79
3.7. Significant Raman phonons in ZnS nanoparticles 79
3.8. Experiments with different copper and sulfur sources 85
3.9. Experiments with different Cu:S precursors molar ratios 88
3.10. Atomic percentages for CuS and CuS:Eu 90
3.11. ICP-MS measurement on doped CuS samples 91
3.12. Crystallite size, lattice constants and cations ionic radii for CaF_2 nanostructures 97
3.13. Influence of sonication time on crystallite sizes 97
3.14. Binding energy values determined by XPS 100
3.15. Atomic percentages for CaF_2 nanostructures, as determined by XPS . 100
3.16. ICP-MS results for doped CaF_2 101
3.17. EXAFS analysis at RE L_3 edges 101

5.1. Used chemicals 132

List of Acronyms

AOs	Atomic Orbitals
ATR	Attenuated Total Reflectance
BE	Binding Energy
CMC	Critical Micellar Concentration
CTAB	Cetyltrimethylammonium Bromide
CVD	Chemical Vapor Deposition
DLS	Dynamic Light Scattering
DLVO	Derjaguin, Landau, Verwey, and Overbeek
DRS	Diffuse Reflectance Spectroscopy
DSC	Differential Scanning Calorimetry
EDXS	Energy Dispersive X-ray Spectroscopy
ESCA	Electron Spectroscopy for Chemical Analysis
EXAFS	Extended X-ray Absorption Fine Structure
FE	Field Emission
FWHM	Full Width - Half Maximum
HLB	Hydrophilic-Lipophilic Balance
ICP-AES	Inductively Coupled Plasma - Atomic Emission Spectroscopy
ICP-MS	Inductively Coupled Plasma - Mass Spectrometry
LEDs	Light Emitting Diodes
LO	Longitudinal Optical
MBE	Molecular Beam Epitaxy

NIR	Near Infrared
NN	Nearest Neighbor
NPs	Nanoparticles
NR	Non radiative
P(E/B)-PEO	Poly(ethylene-co-butylene)-b-poly(ethylene oxide)
PAAm	Poly(acrylamide)
PAT	Photoacustic Tomography
PEO	Poly(ethylene oxide)
PHEMA	Poly(2-hydroxyethyl methacrylate)
PLE	Photoluminescence Excitation
PL	Photoluminescence
PNiPAAm	Poly(N-isopropylacrylamide)
PTFE	Poly(tetrafluoroethylene)
PVP	Polyvinylpyrrolidone
QDs	Quantum Dots
RE	Rare Earth
RT	Room temperature
SAED	Selected Area Electron Diffraction
SDS	Sodium Dodecyl Sulfate
SEM	Scanning Electron Microscopy
SP	Surface Phonon
TEM	Transmission Electron Microscopy
TGA	Thermogravimetric Analysis
TM	Transition Metal
TO	Transverse Optical

UHV	Ultra High Vacuum
VUV	Vacuum Ultraviolet
XANES	X-ray Absorption Near Edge Structures
XAFS	X-ray Absorption Fine Structure
XAS	X-ray Absorption Spectroscopy
XPS	X-ray Photoelectron Spectroscopy
XRD	X-ray Diffraction

Abstract

In this PhD thesis, several inorganic nanostructures were synthesized through a wet-chemistry synthetic route. In particular, the miniemulsion approach was exploited to induce the formation in confined space of pure and doped binary (oxides, sulfides and fluorides) and ternary (hydroxides) compounds, of metal/oxide nanocomposites and of hybrid organic/inorganic nanoparticles. Through this methodology, the investigated systems were obtained in crystalline form already at room temperature.

Various miniemulsion formulations were used to control the size and morphology of the investigated systems, achieving different emulsion stabilities and yields of crystalline powders.

The obtained materials were thoroughly characterized through a wide array of techniques from the compositional, structural and functional points of view. In particular, XRD (X-Ray Diffraction) was employed to assess the formation of crystalline materials and to calculate average crystallite sizes (through Rietveld refinement), and the data thus obtained were compared with micrographs collected through TEM (Transmission Electron Microscopy). This latter microscopy, coupled with SEM (Scanning Electron Microscopy), was also used to investigate the morphology of the synthesized nanostructures. In addition, the surface composition was explored through XPS (X-ray Photoelectron Spectroscopy) and, especially in the case of systems doped with transition metal or lanthanide ions, atomic ratios were compared to those obtained through ICP-AES (Inductively Coupled Plasma-Atomic Emission Spectroscopy) or ICP-MS (Inductively Coupled Plasma-Mass Spectroscopy). TGA-DSC (ThermoGravimetric Analysis-Differential Scanning Calorimetry) allowed to evaluate the presence and amount of residual surfactant moieties adsorbed on the materials surfaces.

In the case of the doped systems, XAS (X-ray Absorption Spectroscopy) measurements were performed in order to study in detail the local structure of the doping ions, also with respect to the hosting matrices. The obtained data were further correlated to the photoluminescence properties. These materials, also due to the biocompatibility of the selected matrices, might indeed be potentially applied for optical bioimaging. In this regard, cytotoxicity and cell viability assays were also performed on selected systems.

Abstract

In questa tesi di dottorato, diverse nanostrutture inorganiche sono state sintetizzate mediante un approccio sintetico per via umida. In particolare, l'approccio della miniemulsione è stato sfruttato per indurre la formazione in spazio confinato di composti binari (ossidi, solfuri e fluoruri) e ternari (idrossidi), sia in forma pura che drogati, e di nanocompositi metallo/ossido e nanoparticelle ibride organiche/inorganiche. Attraverso questa metodologia, i sistemi investigati sono stati ottenuti in forma cristallina già a temperatura ambiente.

Miniemulsioni con varie formulazioni sono state usate per controllare le dimensioni e la morfologia dei sistemi investigati, ottenendo emulsioni con stabilità differenti e diversa resa in termini di prodotti cristallini.

I materiali ottenuti sono stati caratterizzati in dettaglio attraverso numerose tecniche, sia dal punto di vista composizionale che da quello strutturare e funzionale. In particolare, l'XRD (X-Ray Diffraction) è stato utilizzato per valutare la formazione di materiali cristallini e, attraverso rifinimento Rietveld, calcolare le dimensioni medie dei cristalliti; i dati così ottenuti sono stati confrontati con le micrografie TEM (Transmission Electron Microscopy). Quest'ultima microscopia, affiancata al SEM (Scanning Electron Microscopy), è stata anche utilizzata per investigare la morfologia delle nanostrutture sintetizzate. In aggiunta, la composizione superficiale è stata esplorata attraverso XPS (X-ray Photoelectron Spectroscopy) e, specialmente nel caso dei sistemi drogati con ioni di metalli di transizione o lantanidi, i rapporti molari registrati sono stati confrontati con quelli ottenuti attraverso ICP-AES (Inductively Coupled Plasma-Atomic Emission Spectroscopy) o ICP-MS (Inductively Coupled Plasma-Mass Spectroscopy). Analisi TGA-DSC (ThermoGravimetric Analysis-Differential Scanning Calorimetry) hanno invece permesso di valutare la presenza e la quantità di residui di tensioattivi adsorbiti sulla superficie del materiale.

Nel caso dei sistemi drogati, sono state effettuate misure XAS (X-ray Absorption Spectroscopy) al fine di studiare in dettaglio la struttura locale intorno agli ioni droganti, in relazione alle matrici ospitanti. I dati così ottenuti sono stati inoltre correlati con le proprietà di fotoluminescenza. Questi materiali, anche grazie alla biocompatibilità delle matrici selezionate, potrebbero potenzialmente essere utilizzati nel campo del *bioimaging* ottico. A questo riguardo sono state quindi effettuate prove di citotossicità e di influenza sulla vitalità cellulare su alcuni dei sistemi sintetizzati.

Chapter 1.

Introduction

According to the IUPAC's *Gold Book*, a colloidal system corresponds to a "state of subdivision such that the molecules or polymolecular particles dispersed in a medium have at least one dimension between approximately 1 nm and 1 µm, or that in a system discontinuities are found at distances of that order" [1, 2] . Such a definition ultimately places colloids in the nanotechnology domain, a field attracting a strong and still growing interest in basic and applied research [3–5]. Among colloids, the inorganic ones are particularly exciting for their manifold functional properties, including optical, electronic, magnetic and catalytic properties [5]. A large variety of synthetic approaches for their preparation are reported in literature [6, 7]; among them, wet-chemical routes play a starring role not only because typically they are based on milder conditions, but also because the liquid phase is more versatile to orient the structural, compositional, and morphological features of the final materials and can therefore lead to a finer tuning of the desired aforementioned properties.

In this thesis, the adopted synthetic approach is the soft-templated route of miniemulsions (Chap. 2), heterophase systems characterized by the dispersion of a minor phase into an immiscible dispersing media, with mean droplets diameter ranging between 30 and 500 nm, and stabilized towards both diffusional and collision-induced degradation processes [8]. This means that, despite their thermodynamic instability (they are indeed metastable), they are able to maintain their identity on a reaction timescale, independently from the other droplets, since mass exchange is strongly hindered. In this habit, they may be exploited as "nanoreactors"; i.e. a reaction of interest can be confined within droplets cores, allowing it to take place in a parallel fashion in 10^{18}-10^{20} nanosized independent compartments, with the final particle size determined by the droplet size. Such a confinement strongly affects the crystallization process, often inducing the formation of crystalline materials at temperatures much lower than the corresponding bulk processes [9]. Despite the wide use of miniemulsions in polymerization processes [7, 9–11], their exploitation for the synthesis of inorganic materials is still rather limited [12]. One of the aims of this thesis is to make use of this powerful synthetic approach for the controlled synthesis of pure and doped binary and ternary nanocrystalline inorganic compounds such as metal oxides, hydroxides, sulfides, halogenides as well as nanocomposites. By means of inverse water-in-oil-miniemulsions, several different nanostructures have been prepared. These materials range from zinc oxide and zinc sulfide to analogous copper compounds, from magnesium and calcium hydroxides to calcium fluoride, from hollow nanospheres to ordered arrays of SnO_2 hybrid precursors. Furthermore, many of the synthesized systems (namely zinc oxide and sulfide, magnesium and calcium hydroxides, copper(II) sulfide and calcium fluoride) were doped with transition metals or rare-earth ions to obtain luminescent properties for potential application in optical bioimaging. A related aim was to optimize the synthetic parameters (such as nature and molar ratios of reagents, nature of surfactants and sonication times) in order to achieve a precise control on the systems evolution and final properties in terms of:

- crystallinity
- size and size distribution
- effective doping
- functional properties (luminescence, absence of cytotoxicity, or catalytic activity)

Each material has been carefully characterized from a compositional, structural, morphological and functional point of view. The synthesized nanostructures can be divided into two groups, based on their expected field of applications.

The former group encompasses those systems which, thanks to their low cytotoxicity and biocompatibility, coupled to fluorescence properties, may be used in optical bioimaging [13], a radiopharmacology branch apt to the identification and monitoring of molecular processes within cells, tissues and organisms using non-invasive contrast agents [14]. In the case of ZnO, for instance, its optical band gap of 3.37 eV and exciton binding energy of 60 meV ensure an efficient emission in the near UV, which can be modulated and shifted towards the visible range by introducing doping ions. The miniemulsion approach represents an appealing tool in this framework since it yields nanostructures with a small size and narrow size distribution; moreover, the peculiar conditions might lead to effective doping and crystallization even at room temperature. An additional goal of the work was to afford a comprehensive picture of the investigated systems by a synergistic interplay between different and complementary analytical tools. In fact, to optimize synthetic parameters, it is of pivotal importance the unraveling of the correlation between observed functional properties and structural/defectivity characteristics.

The latter group gathers those systems either characterized by peculiar catalytic properties or which are precursors of such a system. Again miniemulsions are very well tailored to afford a control on the final particle morphology, by promoting interfacial precipitation or confining the decomposition of a suitable precursor, or to easily obtain an ordered array of hybrid nanoparticles. The effectiveness of such an approach is clearly testified by the Au/TiO_2 nanocomposites, whose selectivity and conversion in the oxidation of 2-propanol experienced a two-fold increase when such a composite is prepared by using miniemulsions, through an original route implying the coupling of size confinement, a tailor-made single-source precursor and UV photodecomposition.

This thesis is organized in six chapters. Following the introduction, in *Chapter 2* colloidal approaches for the synthesis of inorganic material are presented, and miniemulsions are described in detail, with particular focus on the latest application in inorganic chemistry. *Chapter 3* introduces the basic principles of bioimaging and the pros and cons of inorganic contrast agents with respect to their organic counterparts. Results achieved in this habit for pure and doped nanostructures of zinc oxide and sulfide, magnesium and calcium hydroxides, copper sulfide and calcium fluoride are herein included. *Chapter 4* is devoted to systems apt for catalysis. After a general introduction and concise on basic aspects of catalysis, results obtained on tin oxide hybrid precursors, hafnia and zirconia nanocapsules, and Au/TiO_2 are thoroughly discussed. Experimental details which are not presented in the previous chapters are collected in *Chapter 5*. Finally, *Chapter 6* draws conclusions, it highlights the positive results obtained as well as perspectives disclosed by this work. Moreover, it critically discusses problems emerged in the synthetic steps and the improvements needed.

In the Appendix, the basic aspects of the characterization techniques employed are shortly reviewed.

Chapter 2.

Miniemulsions

2.1. Wet and colloidal chemistry routes for inorganic materials

Inorganic materials are particularly exciting for their manifold functional properties, including optical, electronic, magnetic, and catalytic properties. For the preparation of such a huge variety of materials, a plethora of different methods are available, many of them stemmed after the nanotechnologies dawning [3, 4].

Overall, the different synthetic approaches can be classified into three families: i) syntheses from gas phase (e.g., Chemical Vapor Deposition, CVD or Molecular Beam Epitaxy, MBE) and corresponding variants; ii) solid-state syntheses (e.g., ceramic method, ball milling, sintering, etc.); iii) wet chemistry methods (e.g. sol-gel, solvothermal, Pechini, etc.) [3, 15]. The first two are certainly valuable approaches (gas methods are essential for deposition of thin layers, while the solid state ones are usually simpler and easier to scale-up). Nevertheless they often require complex equipments, use of vacuum, tailored precursors and/or high energy consumptions. Alternatively, wet chemistry syntheses appear are more versatile with respect to the variation of structural, compositional, and morphological features of the final materials; moreover, they allow to achieve a better control of uniformity and size of the obtained materials, and they typically require lower temperatures and energy consumption [9], thus appearing the most appealing ones. Furthermore, being based on solutions or suspensions, which are inherently homogeneous systems, this homogeneity is generally retained also in the resulting materials.

Among the wet chemistry methods, colloidal routes are of special relevance. According to the IUPAC's *Gold Book*, a colloidal system is defined as a "state of subdivision such that the molecules or polymolecular particles dispersed in a medium have at least one dimension between approximately 1 nm and 1 µm, or that in a system discontinuities are found at distances of that order" [1, 2]. Therefore it is an intermediate state between a molecular solution and a heterogeneous dispersion, with a size domain almost completely overlapping with the dimensional regime of the nanotechnology world. The colloids science, dating back to the seminal Wolfgang

Ostwald's works published at the beginning of the 20th century [16, 17] (even if colloids have been used for centuries, like in the famous Lycurgus cup from the 4^{th} century A.D. [18]), is thus nowadays experiencing a sort of renaissance.

Inorganic systems may spontaneously evolve to their crystalline form; nevertheless the search for higher crystallinity and well-controlled morphology are motivated by better functional properties.

Nanocrystalline colloids are of great interest not only as functional systems, but also as controlling or structure-directing agents, and as scaffolds or templates for nanostructure assembly, thus being also interesting as versatile synthetic tools (for more details see the recent review by Muñoz-Espí *et al.* [9]).

In this framework, emulsions have found wide use in the synthesis of inorganic materials, especially through the pioneering work of the Pileni's group with macro- and microemulsion [19–21]. In this soft-templated method, generally, two emulsions containing one the metal precursor and the other a reducing/precipitating agent are combined, so that the reaction occurs after collision and coalescence of the droplets containing the reactants. If a single emulsion is used and the precipitating agent is added in the continuous phase, the precipitation may occur at the liquid–liquid interface and hollow particles are formed [7]. This kind of interfacial reactions is usually sol-gel based, and often the obtained materials are amorphous, thus requiring a successive thermal treatment in order to obtain crystallization. Nevertheless, crystalline materials have been indeed produced in macro-, mini- and microemulsion (the differences between these three classes of emulsions are discussed in the following Section), with this last case also subject of many reviews [22–25]. The use of miniemulsions in inorganic synthesis is discussed in more detail in Sec. 2.4.

2.2. Colloids and emulsion stability

When discussing colloidal systems, one key issue is their stability: a colloid is stable when it remains well dispersed and it is able to withstand breakdown processes induced by the presence of external (e.g., gravity, centrifugal[1], mechanical) or internal (attractive) forces [26]. Unstable systems might experience flocculation when weak attractive forces lead to the formation of agglomerates, which however can be reversibly disrupted, for instance by mechanical forces (e.g. stirring) or by addition of suitable peptizing agents. It is worth to note that, if attractive forces holding the agglomerates together are greater than the aforementioned mechanical forces, the aggregation process will be irreversible and it is named coagulation [1, 2]. Two or more colloidal entities may completely overcome the repulsion barrier and aggregate to form a single bigger particle; this process, driven by the minimization of the surface area, is called coalescence[1]. The interplay of attractive and repulsive components ruling colloidal particles interactions is modeled by different theories, the best established one being the DLVO theory. Shortly, this theory describes the long range attractive forces as a van der Waals potential, whereas the short range electrostatic repulsion is associated with the presence of an electrical double layer. The interest reader may refer for more details to Refs. [26–28].

---

[1] Both leading to sedimentation/creaming.

In addition to the just mentioned destabilization mechanisms, the stability of colloids is affected by a further process which, together with coalescence, is one of the most important causes of colloids destabilization: the diffusional degradation process known as "Ostwald ripening" [16, 26], arising from the Laplace pressure difference found for a curved interface having a curvature of radius r:

$$p_{Laplace} = \frac{2\gamma_{12}}{r} \tag{2.1}$$

where γ_{12} is the interfacial tension between the two phases 1 and 2. The forthcoming discussion is presented in terms of an emulsion system (liquid/liquid system), but is valid for all colloidal systems. From 2.1 it follows that the smaller the droplet, the bigger is the pressure; this means that the chemical potential increases with decreasing droplet size. This difference in chemical potential between droplets of different sizes generates a net mass flux of solute molecules from the smaller droplets, across the continuous phase, into the larger droplets. The Ostwald ripening can be minimized by narrowing the size distribution (strictly monodisperse systems do not exhibit diffusional degradation) and by adding to the disperse phase a component which is insoluble in the continuous phase. This "co-stabilizer" or "osmotically active agent" does not therefore readily diffuse between droplets and generates an inward osmotic pressure π_{osm} :

$$\pi_{\mathrm{osm}} = \frac{3nRT}{4\pi r^3} \tag{2.2}$$

where n is the number of moles of the osmotic agent and R is the universal constant of gases. This osmotic effect counteracts the outward pressure and slows down the Ostwald ripening [26].

The colloidal stability can also be achieved by means of electrostatic or steric repulsion. In the former case, as described by the forenamed DLVO theory, the presence of a surface charge (and subsequent electrostatic double layer) gives rise to a repulsion potential which might exceed the attractive potential due to van der Waals forces, stabilizing the system. This balance, on the other hand, is easily affected by the presence of inert electrolytes; these will decrease the repulsion by deshielding the electrostatic potential, therefore lowering the energy barrier that prevents aggregation. If this barrier is overcome, then flocculation occurs. In addition, such stabilization is not exploitable in non-polar solvents, due to inefficient solvation of charged particles. The latter case, where the stability is induced by the presence of an adsorbed polymers or surfactants layer, is less affected by external parameters. In the presence of adsorbed polymers, their chains create a steric hindrance, which will prevent coalescence between colloidal particles. The effectiveness of this layer depends on the conformation of the polymeric chains. A simple analytical expression for the steric interaction energy V_{ster} between two polymer-coated particles of radius a is given by:

$$\frac{V_{\mathrm{ster}}}{k_{\mathrm{B}}T} = 4\pi a\Gamma^2 N_A \frac{\overline{v}_2^2}{\overline{V}_1}\left(\frac{1}{2}-\chi\right)\left(1-\frac{D}{2L_0}\right)^2 \tag{2.3}$$

Γ is the surface coverage, $\overline{v}_2$ the partial specific volume of the polymer chain, $\overline{V}_1$ the molar volume of the solvent, χ is the Flory-Huggins enthalpic parameter [29, 30], describing the polymer-solvent interaction, D is the distance between the particles surfaces and L_0 is the polymer layer thickness [26]. An effective steric stabilization is achieved when there is high surface coverage Γ, the solvent is effective in stabilizing the chains (χ<0.5), there is strong polymer or surfactant adsorption and a low free polymer concentration. As far as this last point is concerned, an excess of polymer, not adsorbing on the surface, might lead to the so-called “depletion interaction”, an entropy-generated phenomenon that leads to flocculation [26]. Within the Asakura-Oosawa model of depletion interactions[31, 32], the particles are considered as hard spheres of diameter d, while free polymers are represented as hard spheres of diameter $2L_0$. These polymer coils do not interact with each other and therefore the osmotic pressure generated by the polymer is directly proportional to its number concentration. The polymer spheres, on the other hand, interact with the particles, and thus are excluded from a layer of thickness L_0, which is then also termed “depletion layer”. If two particles approach at a distance lower than $2L_0$, the depletion layers will overlap and the total volume available for the free polymers will increase. Due to the following change in the polymer osmotic pressure, the particles will accordingly experience an effective attraction, leading to flocculation.

Among the different colloidal systems, the emulsions are defined as dispersion of a liquid phase in a second liquid continuous phase, immiscible with the first, and are particularly interesting from the practical and synthetic point of view. The two phases are a polar component (most commonly an aqueous phase) and an apolar one (usually an hydrocarbon, generally termed oil). When the oil phase is dispersed in a larger volume of polar phase the system is termed “direct” or, when the polar phase is aqueous, “oil-in-water” (o/w) emulsion, whereas the opposite case corresponds to the so called “inverse” or “water-in-oil” emulsion [26]. Emulsions may also be classified according to their droplet size: microemulsions have droplets with size < 100 nm, miniemulsions sizes included between 30 and 500 nm [33], macroemulsions sizes in the micrometer range. This classification, on the other hand, is somehow loose; most important, as thoroughly discussed in the next section, is their thermodynamic stability: microemulsions are thermodynamically stable systems, whereas mini- and macroemulsion only achieve metastable states.

The thermodynamic stability is achieved when the emulsion free energy of formation ΔG_{form} ($\Delta G_{\text{form}} = \gamma_{ll'}\Delta A - T\Delta S$) is negative. Here $\gamma_{ll'}$ is the interfacial tension between the two liquid phases, while ΔA is the change in interfacial area upon emulsion creation and ΔS is the corresponding change in entropy. For macroemulsions, ΔS is much lower than $\gamma_{ll'}\Delta A$, leading to a positive value for ΔG_{form}. External work has to be provided to the system in order to generate the emulsion. In miniemulsion systems, the entropic term ΔS is still smaller than $\gamma_{ll'}\Delta A$ but much closer in magnitude. Finally, in microemulsions true thermodynamic stability (ΔG_{form}<0, since $\gamma_{ll'}$ is low and thereforeΔS is greater than $\gamma_{ll'}\Delta A$) is achieved and therefore the formation is spontaneous, and no external work is needed. It is noteworthy that the $\gamma_{ll'}$ term can be significantly lowered by addition of a surfactant, in concentration up to the critical micellar concentration (CMC), above which the surfactant forms micelles and stops to be adsorbed at liquid/liquid interfaces and the interfacial tension is not further lowered [33].

In addition to lowering the interfacial energy, promoting the formation of the emulsion, surfactants also increases the stability of the obtained emulsion. In the case of ionic surfactants, for example, they generate an additional electrostatic repulsion, stabilizing the emulsion against aggregation, as discussed above; again, a non-ionic surfactant will ensure a sterically-induced stabilization. Stabilization against coalescence is more complex for emulsions than in other colloidal systems, due to the presence of an adsorbed stabilizing polymer or surfactant. In the absence of the surfactant, when two droplets approach a thin layer will form between them and only upon its rupture coalescence occurs. The most likely mechanism for this rupture is the presence of oscillatory waves (generated either thermically or mechanically) in the thin layer [26].

In the presence of the surfactant, on the other hand, the formation of oscillatory waves is opposed by an increase in interfacial area of the two interfaces comprising the film. At the nodes of the waves, the expansion of these two interfaces causes a depletion of the surfactant and a consequent local increase in the interfacial tension. The displacement of surfactant is compensated by a flow of surfactant (and associated solvent) within the adjacent solution into the depleted region (phenomenon known as Marangoni effect) [26].

On this basis, it is evident that the surfactant chemical nature, its structure and amount are other key elements in determining the colloidal stability. For increasing surfactant concentration, the average droplet size decreases; on the other hand, in miniemulsion conditions (see Sec. 2.3), the surfactant adsorption equilibrium and the increasing surface tension with decreasing droplets size ensure that the free surfactant concentration is always very low, well below the CMC. In addition, smaller droplets, and subsequently particles, will require a denser surfactant layer to achieve stability. The nature of the surfactant is essential to provide sufficient stability to the emulsion. Usually ionic surfactants are better suited to stabilize direct miniemulsions whereas bulky, nonionic surfactants are more suitable for the inverse ones. This is better understood through the empirical parameter known as Hydrophilic-

Lipophilic Balance (HLB) [34, 35]. HLB quantifies the degree to which a surfactant is hydrophilic/lipophilic, based on the different chemical groups constituting the surfactant molecule. In more detail,

$$\text{HLB} = 7 + \sum(\text{group value}) \tag{2.4}$$

where at each group is associated a specific empirical increasing value in order of increasing hydrophilicity (e.g., $–CH_2–$ groups have a value of -0.475, $–SO_4^{-}Na^{+}$ of 38.7). A highly hydrophilic surfactant such as sodium dodecyl sulfate has therefore a HLB value of 40, whereas the HLB value of a lipophilic surfactant such as sorbitan tristearate (Span® 65) is as low as 2.1. The HLB value also represents a numerical correlation of the emulsifying and solubilizing properties of the different surface active agents, as reported in Tab. 2.1.

Range of HLB values	**Application**
3.5-6	W/O emulsifier
7-9	Wetting agent
8-18	O/W emulsifier
13-15	Detergent
15-18	Solubilization

Table 2.1.: Classification of surfactant according to HLB values [35]

To stabilize inverse (mini)emulsions a surfactant with low HLB value is therefore usually employed. In particular, the non-commercial block copolymer poly(ethylene-co-butylene)-b-poly(ethylene oxide) (P(E/B)-PEO) is one of the most commonly used surfactants in inverse miniemulsions because of its bulky but flexible molecular structure (it can be tuned modifying the PEO chain length), which makes it really efficient to confer colloidal stability [36, 37]. In addition, its HLB value can be tuned by changing the length of the ethylene oxide chain. The commercial Span 80 is also widely used (see Sec. 3.5), even if a much higher amount of surfactant is required in this case. As a possible alternative, a mixture of surfactants with appropriate final HLB can be used, as discussed in the Results chapters; in this case, the HLB value of the mixture is a weighted sum of the values of the single surfactants.

Another method to predict the typology of the obtained emulsion is that based on the packing parameter p [38]. Surfactants adsorbed on the droplet surface affect the curvature of the liquid/liquid interface involved and since their conformation at this oil/water interface is similar to the one they have in solution, it is possible to predict what the preferred curvature will be. This is interpreted in terms of the aforementioned packing parameter p, defined as the ratio between the area a_t of the hydrophobic tail group (determined as the ratio between the volume v of the tail and its length l_t) and the area a_h of the hydrophilic head group :

$$p = \frac{a_t}{a_h} \tag{2.5}$$

If $p > 1$ a inverse w/o emulsion is preferred, whereas for $p < 1$ a direct o/w emulsion while most probably form (for a comprehensive graphical summary, see Fig. 2.1).

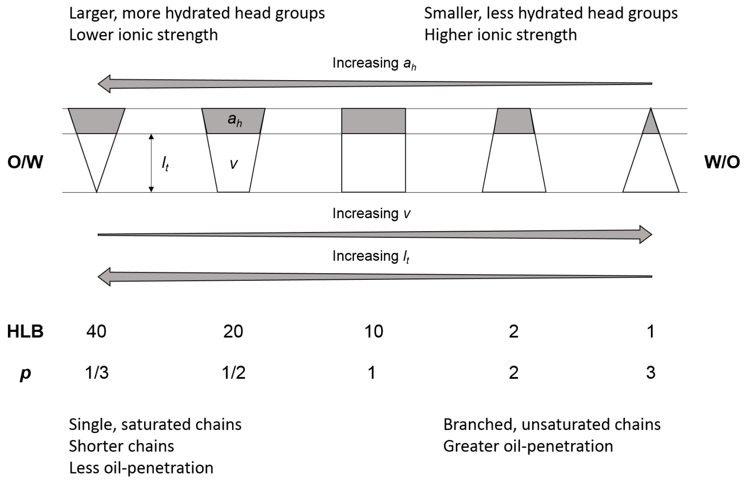
Larger, more hydrated head groups
Lower ionic strength
Smaller, less hydrated head groups
Higher ionic strength
Increasing a_h
a_h
O/W
l_t
v
W/O
Increasing v
Increasing l_t
HLB
40
20
10
2
1
p
1/3
1/2
1
2
3
Single, saturated chains
Shorter chains
Less oil-penetration
Branched, unsaturated chains
Greater oil-penetration

Figure 2.1.: Effect of molecular geometry and systems conditions on the packing parameter p and HLB values (adapted from [26])

In emulsions systems, it is possible to relate the expected droplet diameter d_{av} to the volume V_d of the phase dispersed in a continuous phase of volume V_c, in the presence of a surfactant at a concentration $\mathrm{c_s}$:

$$d_{av} = \frac{6V_d}{V_c c_s a_m N_A} \tag{2.6}$$

where $\mathrm{a_m}$ is the area occupied by a single surfactant molecule, under the assumption of a close-packed monolayer. This relation is valid if all the surfactant is dispersed in the continuous phase prior to emulsification, and after emulsification there is no free surfactant in solution.

2.3. Main features and applications of miniemulsions

Emulsions have been widely exploited for templated syntheses, since they allow a better control on the size and shape of the desired product with respect to bulk syntheses, and therefore materials can be generated using a rational structure design both on a molecular scale and on a mesoscale [8]. In this habit, a wide interest in the literature is devoted to microemulsions, which are thermodynamically stable systems with average droplets size of 5-50 nm, and are therefore optically isotropic [24]. In inorganic chemistry, for example, they are successfully used for the synthesis of several kinds of nanoparticles (metallic, oxides, calchogenides, halides,. . .) with controlled size and, in some cases, shape [22, 23, 39–45]. For inorganic synthesis, mainly w/o microemulsions are used, due to solubility issues of the precursors. On the other hand, when represented in a water/oil/surfactant triangular phase diagram (see Fig. 2.2), the inverse microemulsions are towards the oil-apex [25], meaning that the water/oil volume ratio is really low. This therefore limits the quantitative yield or, in other words, a great amount of organic solvent is required, affecting the environmental compatibility.

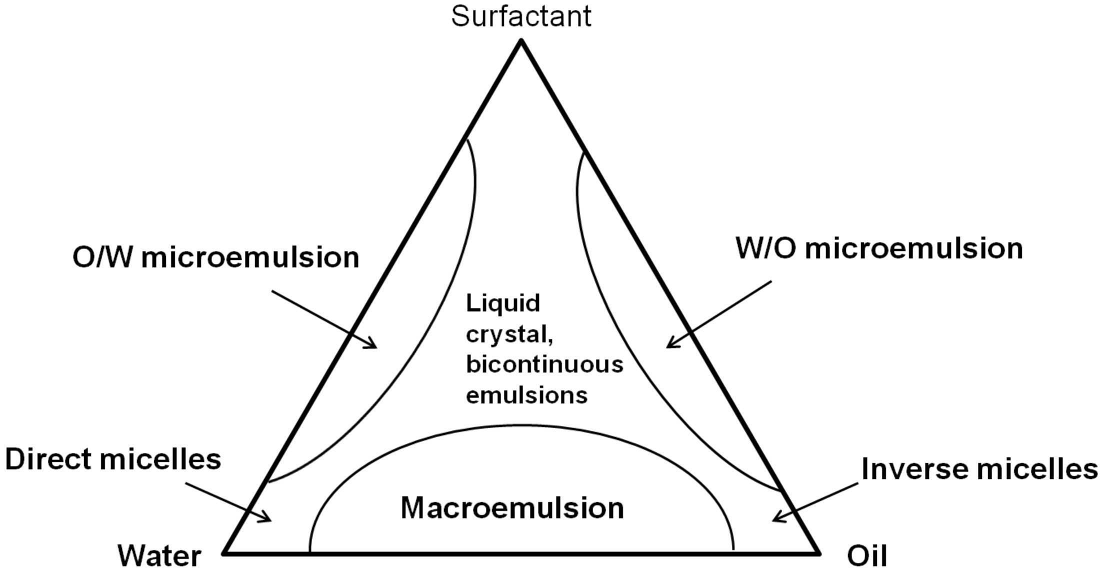

Figure 2.2.: Ternary phase diagram for a water/hydrocarbon/surfactant system

Another typical example of the use of emulsion to have a control on the size and size distribution of materials is emulsion polymerization, a process of great industrial interest since it is applied for the preparation of some synthetic rubbers (e.g., Neoprene) and plastics (e.g., PTFE) [46]. Despite emulsion polymerization being very well suited for radical homopolymerization, it is of limited value already for radical copolymerization due to kinetically controlled growth process which leads to a lack of homogeneity, and of no value for other polymer reactions. To overcome these limits, different synthetic routes have been developed (i.e microemulsions or inverse micelles), but most of them present several disadvantages such as excessive use of surfactant or insufficient stability. The “Holy Grail” in polymerization is the capability of generating small, homogenous and stable droplets of monomer which throughout the polymerization process maintain their particular identity without exchange kinetics involved. Miniemulsion systems present a great step towards this achievement and it is indeed in this framework they were firstly developed [8, 12].

As briefly mentioned before, miniemulsions are heterophase systems which are critically stabilized, and they are characterized by an average droplet size of 30 to 500 nm, being therefore usually optically turbid. With respect to microemulsions, they present higher relative water content, but the work provided by mechanical stirring is not sufficient to successfully emulsify the two phases and generate homogeneously distributed droplets. The presence of viscous resistance, which dissipates a lot of the provided energy as heat, determines the need of providing a work much greater to the surface energy $\gamma_{ll'}\Delta A$ of the newly formed interfaces. Sufficient energy is applied, in the case of miniemulsions, by using high intensity ultrasounds or, for upscaled applications, high pressure devices. An interesting "side effect" of these forces is that they also greatly lower the polydispersity of the system, since they ensure either highly turbulent flow after interface disruptions (i.e. ultrasounds) or sufficient residual time in elongational flow (high pressure homogenizer) in order to allow efficient surfactant adsorption at the newly formed droplets [8]. The longitudinal density waves of ultrasounds can give rise to several possible mechanisms of droplet formation and disruption, but the one most relevant is that of cavitation. This mechanism is associated to the implosion of bubbles that causes intense shockwaves in the surroundings and the formation of high speed liquid jets [47, 48]. It has been determined that, throughout sonication, the droplet size changes quite rapidly until it reaches a steady state, which is not further affected by the applied mechanical energy. At the beginning the polydispersity is quite high, but ultrasounds induce constant fusion and fission processes of the droplets and when the steady state is achieved, the polydispersity is greatly diminished [49] (Fig. 2.3).

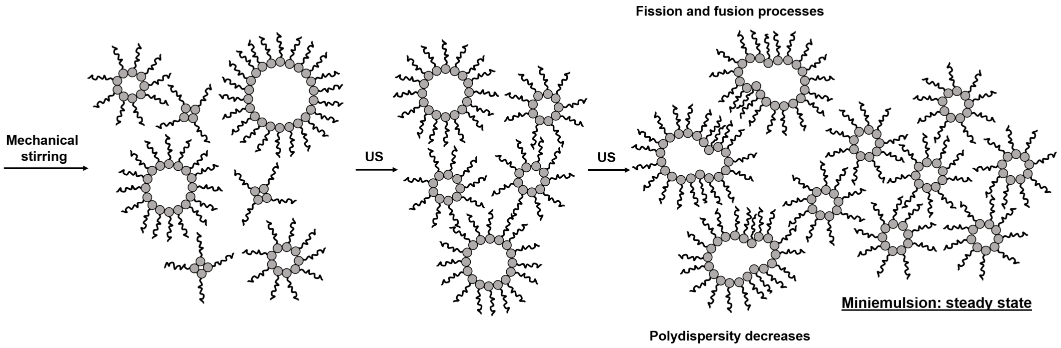

Figure 2.3.: Homogenization of a miniemulsion (adapted from [50])

At the same time, the surface tension is found to increase with decreasing droplet size, as it is intuitive since a constant amount of surfactant has to be distributed at an increasingly larger overall interface, until a plateau is reached. These and further experimental details indicate that both the miniemulsions droplet size and the size distribution are controlled by a Fokker-Planck-type dynamic rate equilibrium of fusion and fission processes [49]. This means that, after fission, droplets are very small but colloidally unstable, whereas larger droplets are more prone to be disrupted. Translated into practical terms, this indicates that droplets forming miniemulsions reach the minimal particle size under the applied conditions, and are at the critical borderline between stability and instability. They are therefore usually described as being critically stabilized, which also means they exploit the surfactant in the most efficient way.

As already mentioned, emulsions can be stabilized towards diffusional degradation by adding to the dispersed phase a “co-stabilizer” (or “osmotic pressure agent”) . This additive is a long-chain hydrocarbon (a hydrophobe, typically hexadecane) for direct emulsions, or a salt or sugar in the case of inverse ones. The Laplace pressure $p_{Laplace}$ and the osmotic pressure π_{osm} show r^{-1} and r^{-3} dependence respectively, therefore even a slight variation in dimensions disrupts the balance between the two pressures. In direct miniemulsions, the two competing pressures do not reach a real thermodynamic equilibrium but, due to the narrow polydispersity achieved, the droplets will experience the same overall effective pressure, meaning that the system is in a relative local minimum in the chemical potential. Since the Laplace pressure directly after miniemulsification is usually larger than the osmotic pressure, the miniemulsion will tend to grow on the timescale of days to weeks [51], but due to the timescale involved, this growth is usually not of relevance for synthetic applications. In addition, droplet size was found to be only negligibly affected by the amount of hydrophobe, above a minimum hydrophobe:monomer ratio necessary to build up sufficient osmotic pressure. Also in the case of inverse miniemulsions, the droplet size during the miniemulsification process reaches an equilibrium state characterized by a dynamic equilibrium between fusion and fission processes. However, in this case, the droplet size shows a dependence on the amount of osmotic agent, meaning therefore that in these systems droplets experience a real zero effective pressure ($p_{Laplace} = \pi_{osm}$), making them very stable.

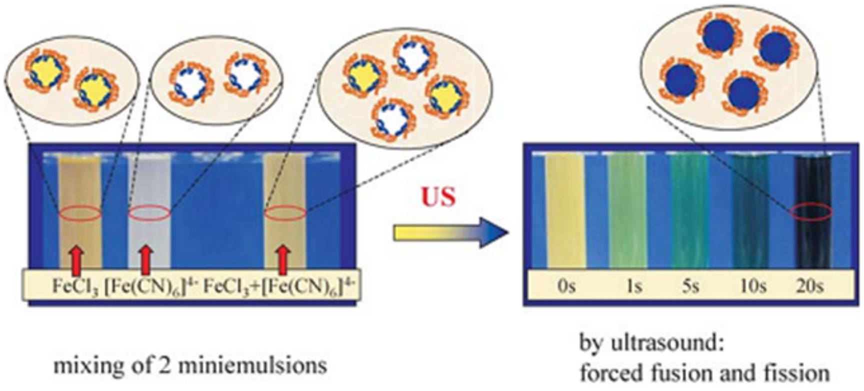
FeCl$_3$
[Fe(CN)$_6$]$^{4-}$
FeCl$_3$+[Fe(CN)$_6$]$^{4-}$
US
0s
1s
5s
10s
20s
mixing of 2 miniemulsions
by ultrasound:
forced fusion and fission

Figure 2.4.: Example of inverse miniemulsion stability: left) upon mixing of two miniemulsions, droplets remain independent; right) mixing is forced by applying ultrasounds [50]

This has a great effect on the reactions kinetics in miniemulsion systems: whereas for microemulsion mixing leads to immediate intermicellar reactants exchange (with characteristic times of the order of 10 µs–1 ms [25]), the presence of the counterbalancing osmotic pressure hinders droplets mass exchange and diffusional degradation in miniemulsions. The droplets thus maintain their identity upon mixing, and external forces (e.g., ultrasounds) are required to force fusion. The extraordinary droplet stability against exchange is exemplary represented by the suppression of the formation of Prussian Blue [50, 51] (see Fig. 2.4); when one miniemulsion containing a $FeCl_3$ aqueous solution is mixed with one containing $K_4[Fe(CN)_6]$, the obtained miniemulsion does not display any color change, meaning therefore there is no exchange between the different droplets, which remain independent. When however the coalescence of the droplets, and consequently the exchange of their contents, is triggered by ultrasounds, formation of the blue complex immediately occurs. If the same experiment is carried out with microemulsions, the formation of Prussian Blue takes place directly after mixing. Following the final homogenization step, each droplet still maintains its stability and independence towards the others, therefore each droplet can be seen as a single “nanoreactor”, in which the reaction occurs independently. In addition, the reaction space is limited to the volume of the single droplet and, as a result, the product growth is also restricted. All these effects often lead to the formation of nanocrystalline materials at temperatures significantly lower than the corresponding reaction in bulk conditions.

2.4. Miniemulsion for inorganic chemistry

The application of miniemulsion for the direct synthesis of inorganic materials is less common than that of polymer latexes, nevertheless this peculiar application is gaining a growing interest in the last few years. Among the first examples of the use of miniemulsion for the preparation of metallic nanoparticles there is a study of Willert *et al.* [52]. In their paper, the authors produced nanoparticles of pure metals (Ga, Na, Fe) or alloys (Wood’s and Rose’s metals) by using the same low-melting metals/alloys or salts ($FeCl_3$ for iron nanoparticles) as polar phase. The mentioned precursors were melted and then dispersed in cyclohexane or IsoparM® (a commercial mixture of alkanes); upon decreasing the temperature below the melting point, stable metallic nanoparticles formed.

Aside this peculiar example, many other inorganic systems, mainly oxides, were synthesized by miniemulsion exploiting the more canonical w/o approach. Several of these examples are collected in the recent review by Muñoz-Espí *et al.* [7]. The different processes involved in the miniemulsion-assisted syntheses of inorganic materials are represented in Fig. 2.5. These processes range from the i) aforementioned phase transition to ii) latex-assisted crystallization, from iii) sol-gel reactions to iv) precipitation/co-precipitation, and to v) the formation of precursor nanoparticles which can then give rise to ordered arrays of inorganic nanoparticles. A further approach, used in this work, is vi) the controlled photodecomposition of a suitable precursor in the confined space of the droplets (see Sec. 4.4)

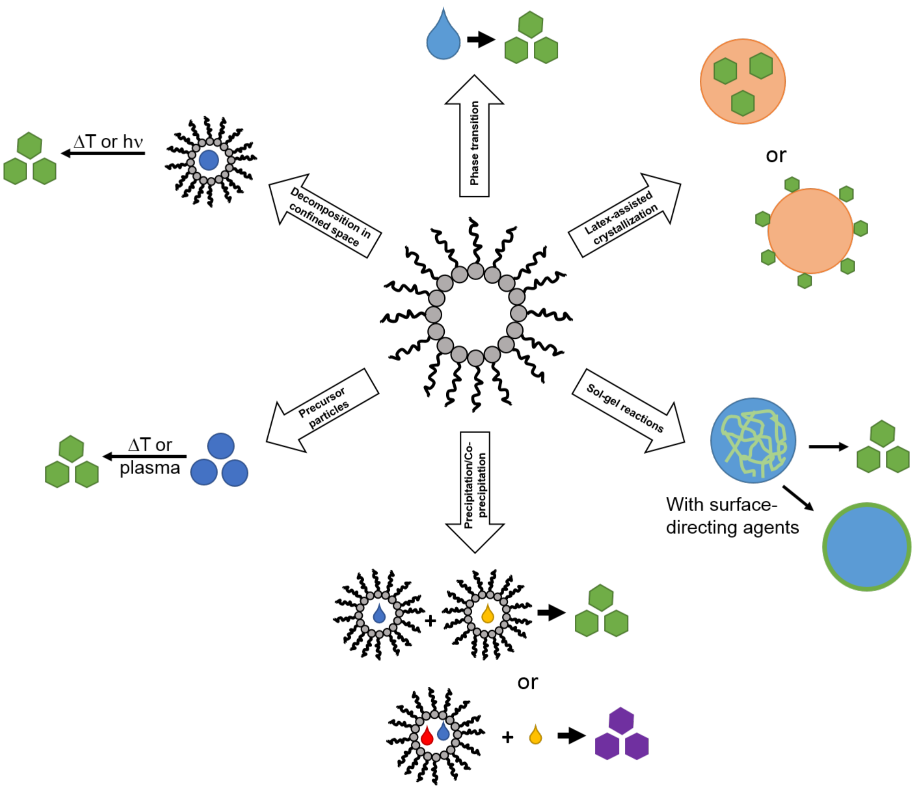
Phase transition
or
ΔT or hν
Decomposition in confined space
Latex-assisted crystallization
Precursor particles
ΔT or plasma
Sol-gel reactions
With surface-directing agents
Precipitation/Co-precipitation
+
or
+

Figure 2.5.: Processes leading to the formation of inorganic nanoparticles in miniemulsion systems (adapted from [7])

To synthesize oxide nanoparticles in a controlled fashion, it is also convenient to employ the sol-gel process, since it also enables, in the presence of proper structure-directing surfactants, the formation of porous materials, which is a key aspect for a wide variety of applications. Furthermore, the combined use of sol-gel processes with the size confinement determined by miniemulsion is particularly advantageous since it maximizes the surface-to-volume ratio of the nanoparticles. Since the droplets of inverse miniemulsions are typically aqueous solutions, hydrophobic alkoxide precursors cannot be employed; nevertheless, such a problem can be easily overcome by using pre-hydrolyzed precursor solutions. The usage of hydrophilic precursor is generally preferable, since in this case the possible structure-inducing effect of the surfactant is more favorable. This effect has been demonstrated by Schiller *et al.* [53] with the controlled synthesis of mesoporous silica nanoparticles, using silicon glycolate as precursor and cetyltrimethylammonium bromide (CTAB) as structure-directing surfactant. Along with the influence of pH within the aqueous droplets on morphology product, Schiller *et al.* also evidenced a lyotropic templating effect of CTAB. The sol-gel approach was also used for the miniemulsion synthesis of nanocrystalline TiO_2 (both rutile/anatase and pure anatase [54]) and

TiO_2/ZrO_2 [55] using glycolates and/or alkoxides as precursor; the Zr-doped particles also showed increased photocatalytic activity compared with that of pure anatase. Collins *et al.* managed to control the rate of hydrolysis and condensation of titanium ethoxide and induce the formation of hollow TiO_2 nanoparticles using formamide as dispersed phase instead of water [56]. A similar sol-gel precipitation of hafnium and zirconium hydroxides confined to the droplet interface is discussed in Sec. 4.3.

Even if a very versatile synthetic strategy is that of precipitation/co-precipitation, which can be induced temperature-dependent phase transitions, as discussed above, or by gently evaporating the solvent (binary and ternary lanthanide-base phosphors were prepared via evaporation of water in inverse miniemulsion [57]), the two most widespread approaches to binary compounds are those of a co-homogenization procedure using two miniemulsions containing the metal precursor and the precipitating agent respectively, or by adding the precipitating agent to the continuous phase (see Fig. 2.5). The results discussed in this work are mostly based on the co-homogenization approach.

The recent review by Muñoz-Espí *et al.* also suggests two indirect ways of exploiting miniemulsion for the synthesis of inorganic systems. The former methodology is inspired by biominerals (such as calcium carbonate and phosphate), whose growth is controlled by the presence of biological macromolecules, in particular proteins. In a similar way, functionalized polymers obtained in a controlled fashion by miniemulsion polymerization can assist and template the crystallization of the inorganic part. For example, ZnO naturally crystallize as hexagonal rods, but in the presence of latex particles prepared via miniemulsion, the interaction between the polar oxide surfaces and the negatively charged surface groups of the latexes induces the crystallization of the oxides with completely different morphologies [58].

The latter indirect approach is based on the use of polymer/inorganic hybrid nanoparticles containing a precursor that transforms to the desired material (metal or oxide nanoparticles, NPs) after removal of the organic component by oxidation, reduction or thermolysis of the metal precursor; the plasma assisted process is another effective method for the removal of organic components. This approach aims not only at the synthesis of the desired inorganic material, but also at arranging them in a regular pattern on solid substrates. In this case, the size of the final inorganic nanostructures is determined by the initial metal loading of the hybrid nanoparticles, while their mutual distance by the size of the initial colloids. Within this approach, metal salts can be used coupled with hydrophilic monomers (e.g. metal tetrafluoroborates in PHEMA, PNiPAAm or PAAm [37, 59]), with a salt loading higher than 50 wt % (with respect to the monomer). Better results, in terms of nanoparticles size and narrower size distribution, can be obtained by exploiting direct miniemulsions: by dispersing β-diketonate of various metals in styrene, metal loaded polystyrene nanoparticles can be obtained, and further generate, once the polymer template is removed, ordered arrays of metal nanoparticles (with the downside of achieving a much lower metal content). Such an approach was used to obtain Pt and FePt NPs

[60, 61]. In Sec. 4.2, the use of direct miniemulsion for the obtainment of ordered SnO_2 arrays is presented and discussed.

Chapter 3.

Pure and doped inorganic nanostructures for bioimaging

3.1. Basic principles of bioimaging

Bioimaging is a term encompassing several techniques devoted to the identification, characterization and measurements of biological processes at the molecular or cellular level in tissues, organs or whole organism (in vitro, in vivo or ex vivo) [62]. These different techniques (e.g. magnetic resonance imaging MRI, positron emission tomography PET, computed tomography CT, ultrasound or optical imaging, OI) are non-competitive and complementary; moreover they are characterized by different complexities, sensitivities and resolutions, as well as different demands in terms of time and costs. The choice among different imaging techniques is driven by the nature of the desired information.

With the advent of nanotechnologies (and appropriate electronics and information technology), bioimaging experienced significant advances [13]; in fact, these enabled the development of targeted contrast agents (e.g. fluorescent probes), allowing to selectively "view specific biological events and processes in both living and non-viable systems with improved detection limits, imaging modalities and engineered biomarker functionality" [13]. The two non-invasive imaging techniques which benefited mostly from these advances are optical (luminescence) and magnetic resonance imaging, also as a consequence of the development of multimodal contrast agents. These multimodal contrast agents are usually inorganic or hybrid nanoparticles which can be detected simultaneously by OI and MRI thanks to the presence of both a luminescent core and paramagnetic ions, thus coupling the high sensitivity of optical detection with the potential of true 3D imaging of biological processes at cellular resolution achieved by MRI.

Our attention has been herein mainly focalized on inorganic nanostructures for optical bioimaging. Light, mainly in the Vis-Near Infrared (NIR) range, is a very versatile imaging radiation, since it is non-invasive and it can create contrast by many effects (i.e. absorption, intensity, polarization, coherence, interference, lifetime and nonlinear optical effects), achieving different resolutions and penetration depths, as summarized in Tab. 3.1.

Technique	**Contrast factor**	**Penetration depth**	**Wavelength**	**Clinical potential**
Microscopic resolution				
Epi (back-emitted photons)	A, F	20 µm	Visible	Not yet assessed
Confocal	F	500 µm	Visible	Not yet assessed
Two-photon	F	800 µm	Visible	Yes
Mesoscopic resolution				
Optical projection tomography	A, F	15 mm	Visible	No
Optical coherence tomography	S	2 mm	Visible, NIR	Yes
Laser speckle imaging	S	1 mm	Visible, NIR	Yes
Macroscopic resolution (intrinsic contrast)				
Hyperspectral imaging	A, S, F	< 5 mm	Visible	Yes
Endoscopy	A, S, F	< 5 mm	Visible	Yes
Polarization imaging	A, S	< 1.5 cm	Visible, NIR	Yes
Fluorescence reflectance imaging	A, F	< 7 mm	NIR	Yes
Diffuse optical tomography	A, F	< 20 cm	NIR	Yes
Macroscopic resolution (molecular contrast)				
Fluorescence resonance imaging	A, F	< 7 mm	NIR	Yes
Fluorescence molecular tomography	F	< 20 cm	NIR	Yes
Bioluminescence imaging	E	< 3 cm	500–600 nm	No

Table 3.1.: Different optical imaging techniques (A: absorption, E: emission, F: fluorescence, S: scattering) [13, 63]

Among the different effects used to create contrast, the most common and powerful one is fluorescence. Organelles, cells or tissues are selectively marked with an appropriate fluorophore (e.g. organic dyes, luminescent complexes, inorganic nanoparticles) which, when irradiated with photons of appropriate wavelength, can absorb it and re-emit it as a slightly lower energy photon (due to the Stoke shift [64], a non-radiative decay to lower energy roto-vibrational levels of the excited state).

A good fluorescent marker for both in vitro and in vivo applications must satisfy particular requirements, such as a high quantum efficiency and high photon cross section. The former is the ratio between the emitted and absorbed photons, and is directly correlated to the emission intensity; the latter is a measure of the quantity of absorbed photons of those impinging the fluorophore. Furthermore, the fluorophore must be physically and chemically stable in physiologically environment and should be stable upon irradiation, without loss of fluorescence due to radiation-induced damage (photobleaching). In addition, it should not alter the biological functions of the investigated specimen and be not cytotoxic. In this regard, critical issues encountered for tissue imaging are the presence of scattering events, autofluorescence and, for the mid-visible range, high absorption due to hemoglobin. These effects strongly affect the radiation penetration depth and the maximum depth (in the orders of centimeters [63]) is achieved for the near infrared region on the 650-900 nm range, since this window corresponds to a minimum in the absorption due to tissues (in particular of hemoglobin and lipids) [63] and where radiation penetrates deeply within tissues, without causing photochemical damage [65].

3.2. Inorganic systems for bioimaging: state of the art

Exogenous contrast agents, the most common contrast agents in bioimaging, can be divided between organic fluorescent dyes and inorganic systems. Even though the use of the former is quite widespread, they are affected by several limitations, namely the lower chemical and thermal stability, the sensitivity to rapid photobleaching, the low suitability for multicolor imaging (due to broad emission bands, which lead to undesired superimpositions), the sensitivity to changes in local chemical environment (e.g., pH) and the overlapping of some emission bands with fluorescence deriving from tissues [66]. Inorganic contrast agents, typically in form of nanoparticles, are able to overcome most or all of these limits, either by exploiting intrinsically fluorescent or optically active NPs (quantum dots, gold NPs, phosphors NPs) or by using host NPs with an encapsulated organic dye (e.g. dye-doped silica NPs), so as to enhance its stability. The following key elements need to be considered when designing nanoparticles for bioimaging applications:

- Optical core: the key element, is itself optically active or encapsulates the fluorophore. Due to their versatility, microemulsions and miniemulsions are perfectly suited for the synthesis of these materials since they can be used to finely tune the NPs to the desired characteristics.
- Shell: might serve to enhance photostability and optical properties, providing at the same time further possibility for surface modification. It can also prevent the leakage of toxic ions (e.g. Cd^{II} ions from CdS quantum dots [67]).
- Surface modification: used to prevent particles aggregation by modifying the surface with appropriate dispersing agents, to achieve appropriate dispersibility in physiological environment.
- Bioconjugation and targeting: modification of the surface with appropriate molecules and biomolecules can increase biocompatibility and induce selective affinity for recognition and interaction with specific cells or tissues.

Among the different nanoparticles-based imaging agents, gold nanoparticles have attracted special attention due to their biocompatibility, easiness of conjugation to biomolecules and interesting optical properties [3, 68–71], ascribed to a strong surface plasmon resonance. By playing with synthetic conditions, nanoparticles with different sizes, shapes and consequently different surface plasmonic resonances, corresponding to different emissions, can be prepared. Nanorods are particularly appealing since their longitudinal resonance usually lies in the aforementioned NIR window [65]. Incidentally their absorption can be finely tuned by changing their aspect ratio (length/width ratio), whose increase is followed by an absorption red shift toward the NIR region [65, 72]. In addition, their absorption and scattering coefficients are one order of magnitude higher than those of spherical NPs [73]. Other extensively used inorganic systems for bioimaging are quantum dots (QDs) and nanophosphors, which are stable, highly fluorescent, tunable and can be easily functionalized. QDs are typically II-VI (e.g CdSe, CdTe) or III-V (e.g. InAs, InP) semiconductors NPs, with sizes of few nm (typically 2-10 nm), which can absorb in a wide spectral region but, at variance to organic fluorophores, they emit in symmetrical and narrow bands, with size-dependent emission maxima [74]. The strong interest for QDs is also related to the possibility of exciting simultaneously QDs of different sizes which will emit with distinctly different colors, allowing for concurrent labeling of different molecules/tissues. On the other hand, they often require a capping with a shell of another wide band-gap inorganic material (i.e. ZnS or SiO_2), which has the double function of both enhancing the quantum yield (by confining the exciton in the QD core) and preventing the release of toxic ions (e.g., Cd^{II}) [67]. Another kind of widely used nanophosphors is that of mixed lanthanide oxides, which present similar exciting luminescent properties as QDs and have been already conveniently prepared by miniemulsion [57]. A third category, slightly different from quantum dots and nanophosphors, is that of doped semiconductors NPs, where the luminescent properties are not ascribed to the matrix, but rather they are generated by the presence of doping ions, or embedded organic dyes. In this framework, fluoride materials doped with lanthanide ions (especially Er^{III} and Yb^{III}) often exhibit up-converting properties [75], meaning they undergo a two-photon event, with wavelength in the optimal IR window, and subsequent emission in the visible range.

The first practical issue to address for the use of NPs for bioimaging is the dispersibility of the NPs in water or, even better, in physiological environment. In order to achieve this, NPs' surfaces are functionalized with molecules able to ensure the desired solubility, usually polar or charged molecules. Such a molecule is selected depending on the nature of the nanoparticles, of the targeted system and their dimension, but overall it should meet several requirements:

i. easy to synthesize in good quantity;
ii. reduce length, so as to avoid NPs with a too large hydrodynamic diameter;
iii. easily modifiable to introduce a second functional group, in order to obtain bioconjugation (see Tab. 3.2 below);
iv. minimal interaction with biomolecules different from the target ;
v. low or no cytotoxicity;
vi. little or no effect on the NPs functional properties.

Its function is therefore not only to ensure dispersibility, but also should not induce additional toxicity and should conceal the NPs from the immune system (stealth

NPs), with the purpose of avoiding degradation or rejection of the contrast agent. A key aspect in NPs-based molecular imaging is the selective binding of the contrast agent to the biological molecule of interest, property known as bioconjugation (see Fig. 3.1). In order to achieve this, the nanostructures surface is conveniently modified by physi- or chemisorption of appropriate molecules carrying functional groups capable of selectively binding to the target (e.g antibody, oligonucleotide or protein).

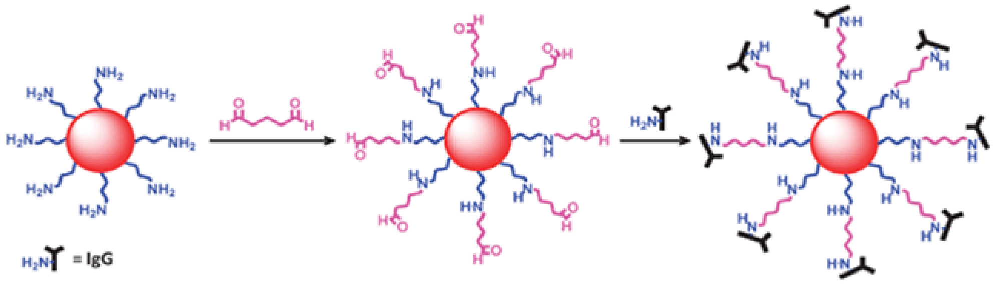

Figure 3.1.: Bioconjugation basic principles: a functionalized NP reacts with a bifunctional ligand, which enables the binding with the target biomolecule [76]

This binding can be covalent or non covalent (see Tab. 3.2), with the former preferable when a stable conjugation is desired. The first approach encompasses the direct chemisorption of the biomolecule on the nanoparticle surface or linking through a bifunctional ligand (often a bulky polymeric ligand, in order to minimize unwanted adsorptions). The second approach relies on hydrogen bonds and/or electrostatic interaction between the nanoparticle and the target biomolecule, and is particularly common when the targets are proteins, even if upon adsorption denaturation might occur, with the consequent loss of biological properties [77].

Functionalized NPs	**Substrate**	**Reaction**	**NP attached to substrate**	**Interaction**
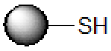	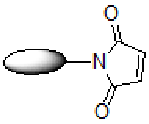	Michael's addition	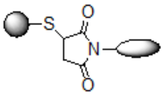	Covalent
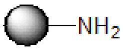	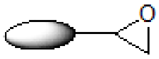	Epoxide opening	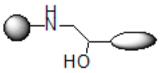	Covalent
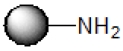	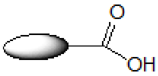	Amide bond formation	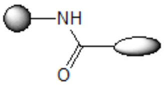	Covalent
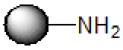	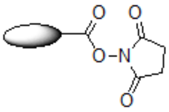	Amidation	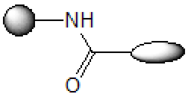	Covalent
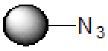	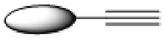	Click chemistry	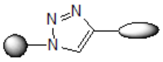	Covalent
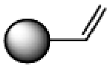	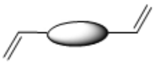	Ring-closing or opening metathesis	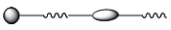	Covalent
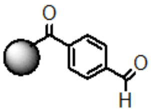	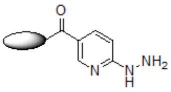	Hydrazone formation	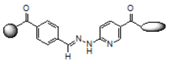	Covalent
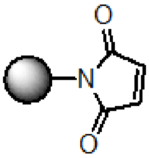	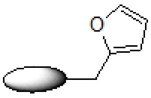	Diels-Alder reaction	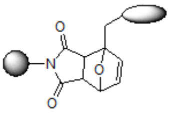	Covalent
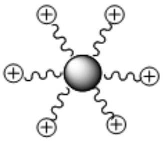	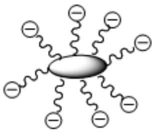	Electrostatic interacion	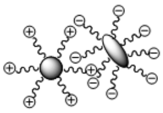	Non covalent
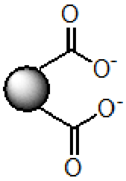	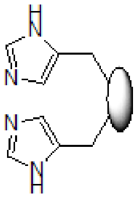	Metallic coordination	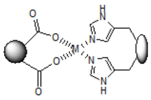	Non covalent

Table 3.2.: Bioconjugation chemistry for nanoparticles (adapted from [76])

Journal of
Materials Chemistry

Dynamic Article Links

Cite this: *J. Mater. Chem.*, 2012, **22**, 1620

www.rsc.org/materials

PAPER

Miniemulsions as chemical nanoreactors for the room temperature synthesis of inorganic crystalline nanostructures: ZnO colloids†‡

Paolo Dolcet,[a] Maurizio Casarin,[ab] Chiara Maccato,[a] Laura Bovo,[ac] Gloria Ischia,[d] Stefano Gialanella,[d] Fabrizio Mancin,[a] Eugenio Tondello[ab] and Silvia Gross*[ab]

Received 14th July 2011, Accepted 20th October 2011
DOI: 10.1039/c1jm13301b

We successfully explored, for the first time, the use of the w/o inverse miniemulsion route to prepare surfactant-functionalised nanocrystalline ZnO colloids. The adopted route exploits the micelles as nanoreactors for the precipitation of the desired oxide in a confined space. Triton X-100 (TritX-), sodium dodecyl sulfate (SDS-) and polyvinylpyrrolidone (PVP-) coated ZnO crystalline nanoparticles (NPs) have been obtained at room temperature (RT) with no need for post-treatment, by precipitation of zinc chloride with ammonium or sodium hydroxide into w/o inverse micelles. Their hydrodynamic diameter, evaluated by Dynamic Light Scattering (DLS), is about 35 nm. X-Ray Photoelectron Spectroscopy (XPS), X-ray Diffraction (XRD), Scanning Electron Microscopy (SEM), Transmission Electron Microscopy (TEM), Inductively Coupled Plasma Atomic Emission Spectrometry (ICP-AES), Fourier Transform Infrared (FT-IR) spectroscopy and Thermogravimetric Analysis (TGA) have been used to characterize powders separated by miniemulsions. The NP inorganic core is constituted of wurtzite ZnO, with a high degree of crystallinity, as determined by XRD. XRD data and TEM images revealed the formation, in the case of ZnO^{TritX}, of anisotropic plate-like crystallites, with an average diameter of 72 nm and a thickness of 15–20 nm. The RT photo-luminescent (PL) spectrum of ZnO^{PVP} NPs shows a strong UV emission band, attributed to the free exciton recombination, with a relevant tail in the Vis region due to the presence of structural defects. The morphology of these systems, investigated by SEM, corresponds to a homogeneous dispersion of globular sponge structures in a compact and fibrous matrix.

Introduction

ZnO nanostructures of different shapes and morphologies have been the focus of intense research efforts in the last 10 years.[1] Nanosized ZnO displays in fact interesting optical properties[2] as well as outstanding electronic properties and functional performances,[3] in many cases related to its defectivity,[4] such as photocatalytic activity[5] and luminescence.[1a,6]

ZnO nanoparticles (NPs) have been obtained both by classical methods of colloid chemistry[7] and by solvo- and hydrothermal methods.[8] There is a plethora of different synthesis approaches to ZnO colloids and many of them have been reviewed by Sphanel.[6c,9]

Moreover, in the last few years, the Niederberger group has developed an effective and easy non-aqueous sol–gel route to prepare crystalline metal oxide NPs, including ZnO.[10] Very recently, some of us addressed the synthesis of ZnO by using a facile, cost-effective and reproducible wet-synthesis route based on the use of zinc acetylacetonate as the precursor.[11]

Now, the goal is the preparation of nanosized ZnO colloids with an improved control of their size and size-dispersion. With this aim in mind, we switched to miniemulsion (ME), a more sophisticated method for the preparation of inorganic nanostructures. Among the "green" approaches to NPs, recently reviewed by Dahl *et al.*,[12] MEs[13] are spurring a growing interest not only for their easy preparation routes, low energy and low reactant consumption (reactions leading to the NP formation occur in a confined space), but mainly because of their outstanding versatility as well as for the wide and exciting synthetic possibilities and perspectives disclosed by the

---

[a] *Dipartimento di Scienze Chimiche, Università degli Studi di Padova, via Marzolo, 1, I-35131 Padova, Italy. E-mail: silvia.gross@unipd.it*
[b] *Istituto di Scienze e Tecnologie Molecolari, ISTM-CNR, via Marzolo, 1, I-35131 Padova, Italy*
[c] *Current address: London Centre for Nanotechnology, 17-19 Gordon Street, London, WC1H 0AH*
[d] *Dipartimento di Ingegneria dei Materiali e Tecnologie Industriali, Via Mesiano 77, 38123 Trento, Italy*

† Dedicated to the memory of Professor Klaus Müller who unexpectedly and prematurely passed away on 1.4.2011. He was Full Professor of Chemistry at the University of Trento and a very appreciated and internationally known solid state NMR spectroscopist.

‡ Electronic supplementary information (ESI) available. See DOI: 10.1039/c1jm13301b

This journal is © The Royal Society of Chemistry 2012

fascinating world of the colloidal state.[14] MEs are defined as stable emulsions of very fine droplets (dispersed phase) in another immiscible liquid (continuous phase).[13] According to the nature of the dispersing/dispersed phase, oil-in-water (o/w) or water-in-oil (w/o) ME—the latter also called inverse micelles—can be prepared.

The wide range of possibilities of carrying out reactions in MEs has been the topic of extensive reviews by Landfester and Antonietti.[13b–f] This approach allows the obtainment of polymers, inorganic materials (metals, ceramics, semiconductors), hybrid and core–shell NPs with a size ranging between 20 and 300 nm through a careful optimisation of the experimental parameters. Moreover, MEs have been extensively used for the preparation of single[13b,15] and mixed oxides,[16] metal NPs,[17] polymer dispersions and encapsulation of different substances in polymeric particles,[18] but not yet, to the best of our knowledge, for ZnO-based systems.

Despite MEs, and in particular the ME polymerisation, having been already used to prepare different types of ZnO–polymer nanocomposites,[19] this is the first study devoted to the synthesis of pure ZnO by using MEs as nanoreactors for a controlled and confined growth of NPs. In this framework, the main goal of the present work has been the development of a facile, reproducible, cost effective, RT and fast synthesis route for the production of monodispersed ZnO colloidal suspensions. A related purpose was also to investigate the effect of the chemical–physical nature of different surfactants on the colloids' formation and evolution.

In the present contribution we then present the results pertaining to the synthesis of surfactant-functionalised ZnO NPs by using w/o ME, which are perfectly suited nanoreactors as a consequence of their stability coupled with the possibility of achieving a uniform size distribution. Triton X-100 (hereafter, ZnO^{TritX}), sodium dodecyl sulfate (hereafter, ZnO^{SDS}) and polyvinylpyrrolidone (hereafter, ZnO^{PVP}) coated ZnO nanoparticles have been obtained by precipitation of zinc salts with ammonium or sodium hydroxide at RT into the confined space of w/o inverse micelles. The synthetic approach used is sketched in Scheme 1.

It should be underlined that the different surfactants, characterized by different hydrophilic–lipophilic balance (HLB)[20] values, are expected to yield miniemulsions with different stabilities. This has in turn an effect also on the NP morphology and size. The higher the HLB value, the more hydrophilic the surfactant is, thus stabilizing better the direct emulsions rather than the inverse ones. In our case, as follows, we expect a better miniemulsion stability with Triton X-100 (HLB = 13.4) than with SDS (HLB = 40). The obtained suspensions have been characterised by Dynamic Light Scattering (DLS) and afterwards centrifuged and washed with ethanol to obtain a white powder. Chemical–physical and structural characterisations of the achieved materials have been carried out by X-ray Diffraction (XRD), X-ray Photoelectron Spectroscopy (XPS), Inductively Coupled Plasma Atomic Emission Spectrometry (ICP-AES) and Fourier Transform Infrared (FT-IR) spectroscopy, while the morphology and the optical properties of these systems have been investigated by Scanning Electron Microscopy (SEM), Transmission Electron Microscopy (TEM) and photoluminescence measurements, respectively.

Experimental section

Chemicals

Zinc chloride ($ZnCl_2$), sodium hydroxide (NaOH), ammonium hydroxide (NH_4OH, 28–30%), polyvinylpyrrolidone (PVP, $(C_6H_9NO)_n$, M_w = ~4000), sodium dodecyl sulfate (SDS, $NaC_{12}H_{25}SO_4$), ethanol (C_2H_5OH), 1-butanol (C_4H_9OH), 1-pentanol ($C_5H_{11}OH$), and *n*-heptane (C_7H_{16}) have been purchased from Aldrich. Triton X-100 ($C_{14}H_{22}O(C_2H_4O)_n$, n = 9–10) and cyclohexane (C_6H_{12}) have been obtained from Alfa-Aesar. Anhydrous KBr has been purchased from Merck GmbH, Germany and anhydrified in vacuum at 200 °C for 24 h before use. All other chemicals have been used without further purification.

Procedures

Synthesis of ZnO with Triton X-100 (ZnO^{TritX}). Two identical mixtures, A and B, have been prepared by dispersing 3 mL of Triton X-100 (5.1×10^{-3} mol) and 1 mL of pentanol (9.2×10^{-3} mol) in 28 mL of cyclohexane. Subsequently, 1 mL of 0.2 M $ZnCl_2$ (2.0×10^{-4} mol) has been added to mixture A and stirred, giving emulsion A′ (pH = 3.4), while 1 mL of 1 M NaOH (1.0×10^{-3} mol) has been added to mixture B to generate, after mechanical stirring, emulsion B′ (pH = 14). Both emulsions have been then sonicated for 3 minutes by using a Sartorious Stedim LabsonicP homogenizer, mounting a 3 mm titanium tip and operating at an amplitude of 70%, corresponding to an acoustic power of 322 W cm^{-2}. The resulting miniemulsions, both transparent, have been mixed together and sonicated again, with unchanged time and amplitude. The final pH was determined to be 13.4. A floc appeared in the miniemulsion after a few minutes and the mixture was allowed to stand for one night. The white precipitate that formed has been separated by centrifugation/filtration (10 000 rpm for 15 minutes) and washed with ethanol and water.

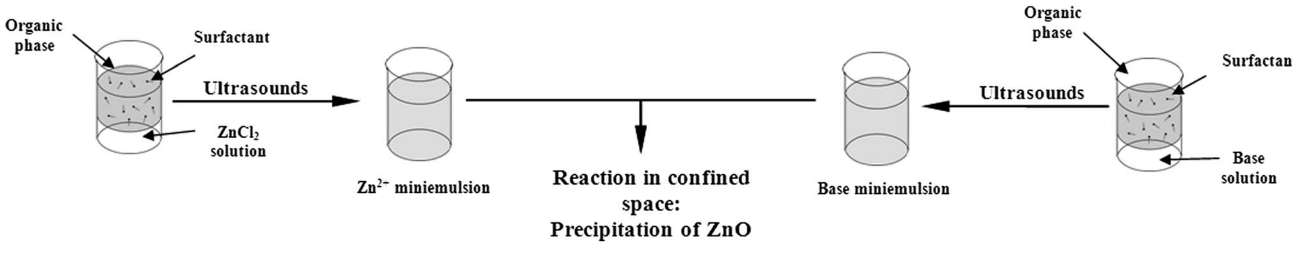

Scheme 1 General synthesis approach.

Synthesis of ZnO with PVP (ZnO^{PVP}). In a typical synthesis, 5 g of polyvinylpyrrolidone (PVP) have been dissolved in 14 mL of 1-butanol. To this solution 70 mL of 0.025 M $ZnCl_2$ (1.8×10^{-3} mol) have been added. A similar emulsion has been prepared by using 0.5 g of PVP, 1.4 mL of butanol and 7 mL of 1 M NH_4OH (7.0×10^{-3} mol). Both emulsions are optically transparent and they have been sonicated separately for 3 min, with an acoustic power of 322 W cm^{-2}. After the miniemulsification, the two miniemulsions have been mixed and the resulting mixture has been sonicated again, using the same parameters as mentioned before. The final miniemulsions appeared slightly turbid due to the formation of a floc, and they have been allowed to stand overnight. The obtained white precipitate was separated by centrifugation/filtration (10 000 rpm for 30 minutes) and washed with ethanol and water.

Synthesis of ZnO with SDS (ZnO^{SDS}). In a typical experiment, 2.0 g of sodium dodecyl sulfate (SDS) (6.9×10^{-3} mol) and 4.0 g of pentanol (3.7×10^{-2} mol) have been dispersed in 10.0 g of heptane (6.8×10^{-2} mol), giving mixture A; a second similar mixture, B, was prepared using twice the amounts of the reagents. To mixture A, 4.0 g of 0.1 M $ZnCl_2$ (4.0×10^{-4} mol) have been added, while 8.0 g of 0.2 M NH_4OH (1.6×10^{-3} mol) have been added to mixture B. After mixing the precursor solutions, the resulting emulsions appeared optically transparent. The two suspensions have been then separately sonicated for 3 minutes, with an acoustic power of 322 W cm^{-2} and subsequently mixed. The resulting emulsion has also been sonicated, using unchanged parameters, generating the final miniemulsion, which has been allowed to stand overnight. The white precipitate that formed has been separated by centrifugation/filtration and washed with water and ethanol.

Characterisation methods

FT-IR analysis. FT-IR experiments have been performed with a NEXUS 870 FT-IR (NICOLET), operating in the transmission range of 400–4000 cm^{-1}, collecting 64 scans with a spectral resolution of 4 cm^{-1}. The measurements have been recorded by dispersing the powders in anhydrous KBr.

XPS analysis. The powders have been investigated by XPS with a Perkin-Elmer Φ 5600ci instrument using standard Al-K$_\alpha$ radiation (1486.6 eV) operating at 350 W. The working pressure was $\leq 5 \times 10^{-8}$ Pa $\sim 10^{-11}$ Torr. The calibration was based on the binding energy (BE) of the Au4f$_{7/2}$ line at 83.9 eV with respect to the Fermi level. The standard deviation for the BE values was 0.15 eV. The reported BEs have been corrected for the BE charging effects, assigning the BE value of 284.6 eV to the C1s line of carbon.[21] Survey scans have been obtained in the 0–1350 eV range (pass energy 187.5 eV, 1.0 eV per step, 25 ms per step). Detailed scans (58.7 eV pass energy, 0.1 eV per step, 50–150 ms per step) have been recorded for the O1s, C1s, Zn2p, ZnLMM, and Na1s regions. The atomic composition, after a Shirley-type background subtraction,[22] was evaluated using sensitivity factors supplied by Perkin-Elmer.[23] Charge effects have been partially compensated by using a charge neutraliser (flood gun). Peak assignment was carried out according to literature data.[24]

Thermogravimetric analysis. The thermogravimetric analyses (TGA) have been performed in air on a LabSys Setarm SDT 2960 instrument in the temperature range of 20–800 °C using a heating rate of 10 °C min^{-1}.

X-Ray diffraction. The XRD data have been collected with a Bruker D8 Advance Diffractometer equipped with a Göbel mirror by using the CuK$_\alpha$ radiation. The angular accuracy was 0.001° and the angular resolution was better than 0.01°. All experimental data were analyzed using the Material Analysis Using Diffraction (MAUD) software package,[25] an original software used to work out quantitative crystallographic and microstructural information[26] using a Rietveld code.

SEM analysis. The morphology of three ZnO samples, prepared from different surfactants as described above, and their composition have been analysed using SEM and Energy Dispersive X-ray Spectroscopy (EDXS). Measurements have been performed using a Field Emission (FE-SEM) Zeiss SUPRA 40VP with a primary beam acceleration voltage of 5 kV, a conventional secondary electron detector for the SEM investigations and an Oxford INCA x-sight X-ray detector for EDXS analysis.

TEM analysis. TEM analysis was carried out using a Philips CM12 microscope operating at 120 keV and equipped with an EDXS, which allows localized chemical analyses.

For each sample, both images and Selected Area Electron Diffraction (SAED) patterns have been collected as well as EDXS chemical analyses in order to investigate the morphology and dimensions of ZnO NPs, their crystalline nature and local chemical composition.

Photoluminescence measurements. Room temperature photoluminescence (PL) measurements have been performed by using a Xenon UV-lamp (450 W, Edinburgh Instruments Ltd.) with an excitation wavelength of 300 nm. Spectra have been recorded using a Horiba Jobin Yvon T64000 triple monochromator coupled with an intensified charge-coupled device (CCD; Andor iStar).

Results and discussion

The three samples obtained by using the different surfactants (hereafter, ZnO^{PVP}, ZnO^{TritX} and ZnO^{SDS}) have been thoroughly investigated by different and complementary techniques to look into their chemical–physical, structural, morphological and optical properties.

The obtained MEs have been firstly characterised by Dynamic Light Scattering (DLS), giving an average diameter of about 35 ± 5 nm and evidencing an appreciable degree of monodispersion (see Fig. S1 in the ESI‡).

To assess the actual formation of the desired ZnO phase, XRD measurements have been carried out. The wurtzite polymorph at RT has been assessed for ZnO^{PVP} and ZnO^{TritX}, JCPDS 79-207 (2θ: 31.7, 34.4, 36.18, 47.46, 56.5, 62.8, 66.2, 67.8, 68.9, 76.8); at variance to that, the complete crystallisation of ZnO^{SDS} needed a mild thermal treatment at 200 °C. Diffraction patterns of the three samples are shown in Fig. 1, whereas obtained structural

This journal is © The Royal Society of Chemistry 2012

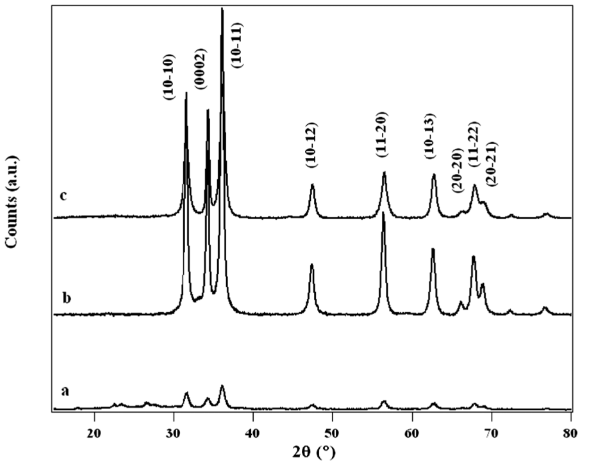

Fig. 1 XRD patterns of the samples: (a) ZnO^{SDS} (after calcination at 200 °C for 4 h), (b) ZnO^{PVP} and (c) ZnO^{TritX}.

parameters are summarised in Table 1. The Rietveld refinement on the XRD patterns of the synthesized ZnO^{TritX} NPs revealed anisotropic growth of the crystalline domains, in particular along the [0002] axis. This direction is characterized by a crystallite size of 72 nm, whereas along the other directions the average crystallite size is 15–20 nm. In the case of the ZnO^{PVP}, the sample shows an average crystallite size of 25–30 nm but with an anisotropic growth along the [110] direction, with a size of 54 nm. It has to be outlined that these results are not conflicting with those obtained by DLS, since these latter refer to the as-prepared fresh suspensions, whereas the former refer to aged and dried powders, in which preferential growth has likely occurred upon aging.

These XRD results are particularly interesting because they ultimately demonstrate the formation of crystalline ZnO at RT without the need for any thermal treatment, at least in the case of PVP and Triton X-100-assisted synthesis of ZnO.

In basic or neutral media (in our case the pH of the final miniemulsion was determined to be 13.4), Zn(II) ions form the amphoteric hydroxide species, $ZnO_x(OH)_g(OH_2)_z$ in a colloidal state, which forms as amorphous or crystalline species. This species spontaneously evolves to crystalline wurtzite ZnO not only under the action of heating or irradiation, through a dehydration process, but also upon prolonged storing and aging in its mother liquor.[27] This second pathway to ZnO is the most likely involved in this process, since the confined space of micelles is filled with the aqueous precursor solution, the mother liquor, and aging can reasonably occur. XRD, SAED and XPS (see below) data confirm the tendency of the colloidal phase to form the crystalline one for the favorable entropy and enthalpy conditions.

Table 1 Average crystallite diameters as determined by the Rietveld refinement on the XRD pattern

Sample	Crystalline phase	Average diameter/nm	Preferential growth direction
ZnO^{TritX}	Wurtzite	15–20	[002] (72 nm)
ZnO^{PVP}	Wurtzite	25–30	[110] (54 nm)
ZnO^{SDS}	Wurtzite + hydroxide	13	—

XPS has been then used to get information about the surface atomic composition of nanocrystalline powders and the chemical environment of the different species (Fig. S2‡, the survey spectrum of ZnO^{TritX} is exemplarily reported). Before proceeding, it deserves to be mentioned that selected regions of interest (Zn2p, O1s, C1s, ZnLMM) have been also acquired with higher resolution for quantitative purposes and for the evaluation of the binding energies (BEs) of the main peaks (see Table 2 and Fig. 2 where C1s, O1s and Zn2p regions of ZnO^{TritX} nanoparticles are plotted).

The inspection of the figure reveals some broadening of the C1s and O1s peaks, suggesting the presence of different chemical environments both for C and O. Chemical information may be gained by looking into these features through a peak deconvolution. For instance, the ZnO^{TritX} C1s peak can be fitted with three components lying at 284.6, 286.2 and 288.7 eV (Fig. 2a) due to contamination and to the aliphatic chains of the surfactant (the first), to C atoms of the surfactant polyether chain[28] (the second), and to an oxidized carbon, probably due to partial carbonatation of the sample upon exposure to air (the third). Similar considerations hold for the O1s peak. As a matter of fact, it can be deconvoluted in two components lying at 530.1 and 531.7 eV (Fig. 2b), attributed to ZnO oxide ions[11] and to O atoms of the surfactant polyglycolic chains,[21,28] respectively. As far as the

Table 2 BE (eV) values for $Zn2p_{3/2}$ and O1s and atomic percentage ratios of the four ZnO samples. Values of BE have been corrected considering charging effects

Sample	BE C1s	BE O1s	BE $Zn2p_{3/2}$	% O	% C	% Zn
ZnO^{PVP}	284.6	531.5, 529.8	1021.4	25.9	65.2	8.9
ZnO^{TritX}	284.6	530.1, 531.7	1021.2	46.4	20.7	32.9
ZnO^{SDS}	284.6	530.3	1021.8	37.0	49.7	13.3

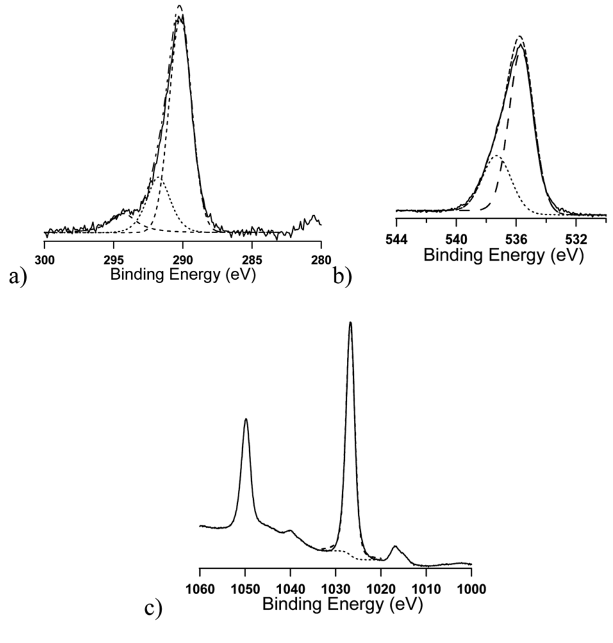

Fig. 2 Peaks of (a) C1s, (b) O1s, and (c) Zn2p for ZnO^{TritX} (graphs shown are not corrected for surface charging effects).

$Zn2p_{3/2}$ peak (1021.2 eV) is concerned, its BE has the typical ZnO value[11,23] (Fig. 2c). The same arguments can be extended to ZnO^{SDS} and ZnO^{PVP}, although slight differences could be observed in the O1s and C1s components, which have to be ultimately ascribed to the different surfactants (see S3 and S4, ESI‡).

The analysis of atomic percentages reported in Table 2 testifies that oxygen, in ZnO^{TritX}, is the predominant species (46.4%), as expected by considering its presence both in ZnO and in the surfactant polyether chain. From the comparison of this value with the Zn atomic percentage (32.9%) it can be concluded that most of the oxygen is present as ZnO, while the amount of surfactant on the NP surface is rather limited.

This is confirmed by TGA analysis (see Fig. 3) overlapped with the corresponding DSC curve. At ~70 °C a first, non-relevant (1%) weight loss was detected straightforwardly ascribed to the release of water and/or ethanol physisorbed on the sample surface. The recorded calorimetric curve fits well with that reported by Mitsuda *et al.* for Triton X-100 decomposition.[29] The minima at 210 °C and 343 °C correspond to subsequent oxidative decompositions of the surfactant molecules which, in the presence of oxygen, easily undergo oxidation of the C–O–C bond of the polyether moiety. These decompositions determine a weight loss of about 7%. The remaining part of the surfactant, the hydrophobic part, is then pyrolised at higher temperatures [350–800 °C], with a further weight loss of 4%. The residual weight (88%) corresponds to ZnO. Similar results have been obtained also in the case of PVP- and SDS-assisted synthesis (see S5, ESI‡).

Photoluminescence properties of a selected ZnO sample (ZnO^{PVP}) have been preliminarily investigated (Fig. 4). The PL spectrum presents a strong UV emission band, centred around 388 nm, displaying a quite strong tail at higher wavelengths in the visible region. This UV-signal can be ascribed to the near band-edge emission of ZnO, originated from free-exciton recombination.[6c,30] On the other hand, the emission in the visible region could be traced back to the combined contribution of various kinds of structural defects, even though their exact nature can be hardly deduced from the present spectrum. In fact, the asymmetry of the signal reveals the presence of different contributions that need further investigation to clearly ascribe them.

Materials characterised by the same chemical composition but having different morphologies can show different functional properties,[1a,b] therefore a systematic SEM investigation, as a function of the synthesis conditions, has been carried out in order to verify the influence of the various surfactants on the final material features.

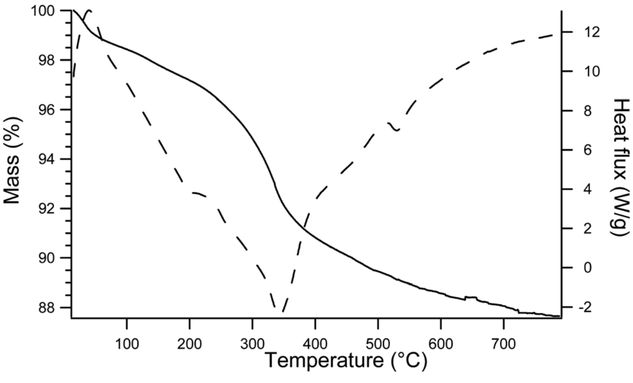

Fig. 3 Thermogram (solid line) and calorimetry (dashed line) of ZnO^{TritX}.

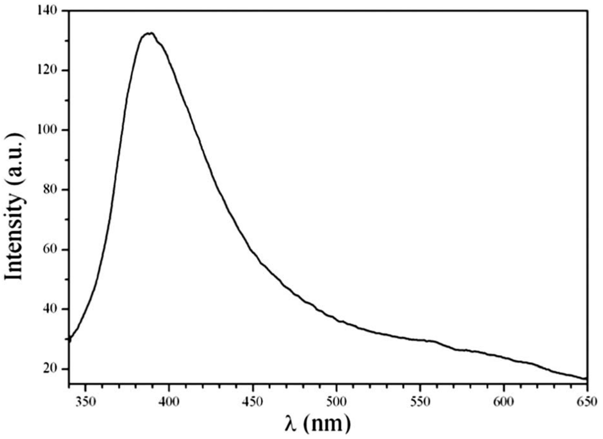

Fig. 4 Photoluminescence spectrum of ZnO^{PVP}.

In a recent paper by Pai and Pillai[31] devoted to the synthesis of calcium carbonate by an approach similar to that used in the present contribution (mixing of two miniemulsions each containing one of the salt precursors), it was reported that particular experimental conditions (in this case the nature and concentration of the surfactant) can rule also the morphological and structural evolution of the final system. In particular, the authors outline that the relevant role played by the surfactant molecules which, being characterised by a preferential absorption on one less stable polymorph of the calcium carbonate, is supposed to balance the loss in the crystallisation energy with respect to the most stable form (calcite) and determine the formation of the vaterite, a less stable polymorph. It could be expected that, also in our case, a complex interplay of different parameters (nature of the surfactants, relative concentration of precursors in the micelle, pH) can affect at least the morphological fate of the micelles, which in turn influences the size and shape of the forming nanoparticles.

In Fig. 5a the SEM micrographs of ZnO^{TritX} sample are reported. These powders are characterised by intertwined ZnO micro-platelets with a height size distribution ranging from 200 to 600 nm and an average thickness of 25 nm. The resulting material is characterised by a high porosity due to its peculiar morphology.

The morphology evidenced by SEM was also confirmed by TEM. Fig. 5b shows indeed the presence of platelets that tend to agglomerate. It is therefore likely that, upon drying, the crystallites aggregate and form the larger features observed in the SEM pictures. The crystalline structure, the morphology and the actual size of the crystallites, as imaged by TEM, are in excellent agreement with the XRD findings. The discrete diffraction spots in the relevant SAED pattern, that can be indexed according to the ZnO wurtzite phase, confirm that grains in Fig. 5b are mostly monocrystalline. Incidentally, TEM images displayed the presence of carbonaceous residuals of the micelles, appearing as rod-like structures (see the central region of the TEM micrograph in Fig. 5b).

In Fig. 6 ZnO^{PVP} SEM micrographs are reported. Highly porous globular features (sizes ranging between 0.25 μm and 1.5

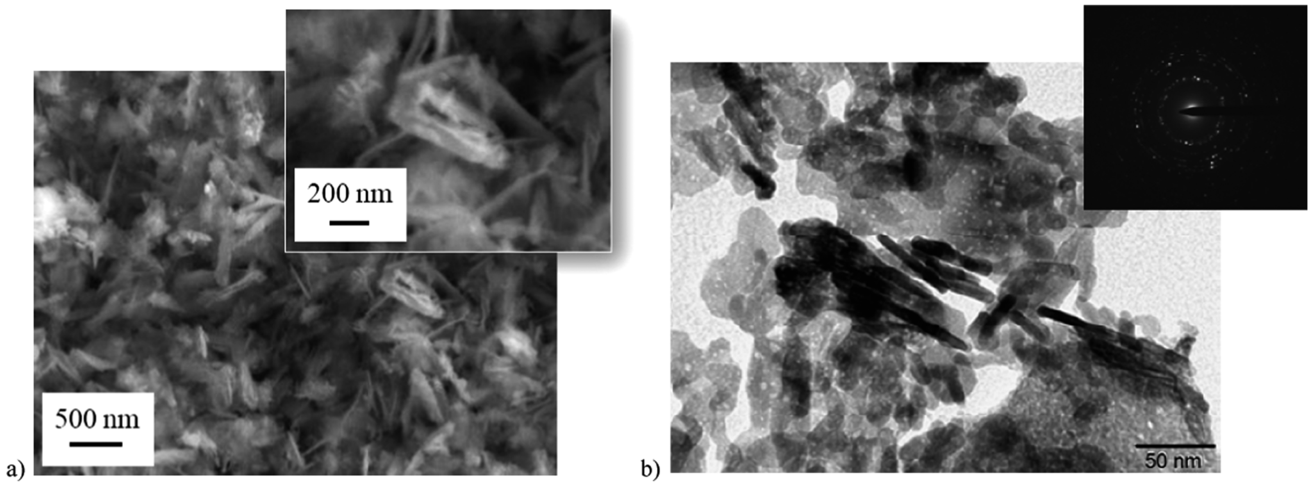

Fig. 5 (a) SEM and (b) TEM micrographs of ZnO^{TritX}. Insets: (a) higher magnification view of the SEM sample and (b) SAED.

μm) result homogeneously distributed over an underlying compact and fibrous matrix probably deriving from the used surfactant. The collected compositional EDXS maps (see S6, ESI‡) confirmed the uniform intermixing between the oxide aggregates and the organic polymeric matrix.

The miniemulsions prepared with sodium dodecyl sulfate, as expected, have been the least stable among the investigated ones. This is likely due to the high HLB value of the surfactant (HLB = 40), making it less suitable for stabilizing inverse emulsions. The stability zone of these systems was found to be very narrow, as experimentally determined by systematically changing the components' molar ratio.

The XRD diffractogram of the as-prepared sample revealed only weak signals due to ordered crystalline phases (wurtzite), so the powder was heated to 200 °C for 4 h.

After the thermal treatment the crystallinity of the sample dramatically increased (see Fig. S7, ESI‡). The indexed reflexes correspond to the wurtzite structure. Furthermore other reflexes at lower angles have been detected, which are probably due to lamellar zinc hydroxides.

The XPS analysis showed similar results as the previous samples and confirmed the formation of ZnO (see S4‡).

All the obtained powders have been further characterised by FT-IR to assess the actual chemical nature of the groups on the surface of the micelles. In the case of ZnO^{TritX}, for example, the presence of zinc oxide was confirmed by the strong absorption at 420 cm^{-1}, corresponding to the Zn–O *stretching* and the band at 3450 cm^{-1}, corresponding to the O–H *stretching* of surface hydroxide[32] (see S8, ESI‡).

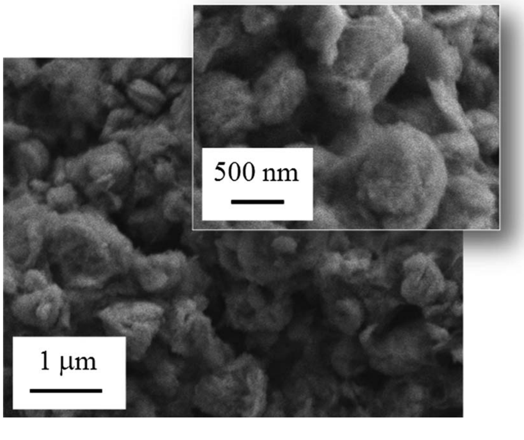

Fig. 6 SEM micrograph of ZnO^{PVP}.

Conclusions

We successfully exploited miniemulsions as nanoreactors for the controlled synthesis of nanostuctured material. Zinc oxide plate-like nanoparticles, with nanometric crystallite size, homogeneous in size distribution, have been obtained in crystalline form (wurtzite) already at RT, without any need for high temperature thermal treatment.

Different surfactants have been compared, and the ones having the lower HLB values have been found to be, as expected, the best performing ones in terms of suspension stability and the final obtained structure. As a final remark, SEM investigations seem to point out that the use of different surfactants in the synthesis paths allows the obtainment of materials endowed with peculiar morphological features as well as with tunable size.

Acknowledgements

Stefano Diodati is acknowledged for the Rietveld refining of XRD data. Prof. Vito Di Noto and Dr Roberta Saini (Università di Padova) are kindly acknowledged for ICP-AES and TGA analyses, respectively. The authors would also like to thank Gabriele Dal Ben for his collaboration in the synthesis of the materials. The University of Padua, the Italian INSTM and the National Research Council (CNR) are acknowledged for financial support.

Notes and references

1 (*a*) H. Morkoç and Ü. Özgür, *Zinc Oxide: Materials Preparation, Properties, and Devices*, Wiley VCH, Weinheim, 2008; (*b*) Z. L. Wong, *Mater. Today*, 2004, **7**, 26–33; (*c*) L. Yichun and T. Yanhong, *J. Nanosci. Nanotechnol.*, 2008, **8**, 1101–1109; (*d*) K. Ellmer and A. Klein, *Springer Ser. Mater. Sci.*, 2008, **104**, 1–33; (*e*) C. Klingshirn, *ChemPhysChem*, 2007, **8**, 782–803; (*f*) C. Klingshirn, R. Hauschild, H. Priller, M. Decker, J. Zeller and H. Kalt, *Superlattices Microstruct.*, 2005, **38**, 209–222; (*g*) Z. Fan

and J. G. Lu, *J. Nanosci. Nanotechnol.*, 2005, **5**, 1561–1573; (*h*) U. Ozgur, Y. Alivov, C. Liu, A. Teke, M. A. Reshchikov, S. Dogan, V. Avrutin, S. J. Cho and H. Morkoç, *J. Appl. Phys.*, 2005, **98**, 1–103; (*i*) S. J. Pearton, D. P. Norton, K. Ip, Y. W. Heo and T. Steiner, *Prog. Mater. Sci.*, 2005, **50**, 293–340; (*j*) Y. Lu and J. Zhong, *Semiconductor Nanostructures for Optoelectronic Applications*, Artech House Publishers, Norwood, 2004, p. 187; (*k*) Z. L. Wang, *J. Phys.: Condens. Matter*, 2004, **16**, R829–R858; (*l*) D. C. Look, *Mater. Sci. Eng., B*, 2001, **80**, 383–387; (*m*) S. Kwon and T. Hyeon, *Acc. Chem. Res.*, 2008, **41**, 1696–1709; (*n*) C. Klingshirn, J. Fallert, H. Zhou, J. Sartor, C. Thiele, F. Maier-Flaig, D. Schneider and H. Kalt, *Phys. Status Solidi B*, 2010, **247**, 1424–1447; (*o*) A. Umar, and Y. B. Hahn, *Metal Oxide Nanostructures and Their Applications, Volume 5: ZnO Nanostructures and Nanodevices*, American Scientific Publisher, Stevenson Ranch, CA, 2010.

2 (*a*) C. Bundesmann, R. Schmidt-Grund and M. Schubert, *Springer Ser. Mater. Sci.*, 2008, **104**, 79–124; (*b*) J. Muth, A. Osinsky, G. F. Neumark, I. L. Kuskovsky and H. Jiang, *Wide Bandgap Light Emitting Materials and Devices*, Wiley-VCH Verlag GmbH & Co. KGaA, Weinheim, 2007, p. 179; (*c*) A. K. Sood, Y. R. Puri, R. Yash, C. Lao, W. Mai, P. Gao, S. Xu, Z. L. Wang, D. L. Polla, M. B. Soprano and N. K. Dhar, *Proc. SPIE–Int. Soc. Opt. Eng.*, 2007, **6768**, 676803; (*d*) T. W. Kang, S. U. Yuldashev, G. N. Panin and A. A. Balandin, *Handbook of Semiconductor Nanostructures and Nanodevices*, American Scientific Publishers, Stevenson Ranch CA, 1st edn, 2006, vol. 4, p. 159; (*e*) A. B. Djurisic and Y. H. Leung, *Small*, 2006, **2**, 944–961; (*f*) R. Bertoncello, M. Bettinelli, M. Casarin, A. Gulino, E. Tondello and A. Vittadini, *Inorg. Chem.*, 1992, **31**, 1558–1565; (*g*) T. Andelman, Y. Gong, M. Polking, M. Yin, I. Kuskovsky, G. Neumark and S. O'Brien, *J. Phys. Chem. B*, 2005, **109**, 14314; (*h*) D. W.Bahnemann, C. Kormann and M. R. Hoffmann, *J. Phys. Chem.*, 1987, **91**, 3789–3798.

3 (*a*) D. C. Look, *J. Electron. Mater.*, 2006, **35**, 1299–1305; (*b*) C. Klingshirn, H. Priller, M. Decker, J. Brueckner, H. Kalt, R. Hauschild, J. Zeller, A. Waag, A. Bakin, H. Wehmann, K. Thonke, R. Sauer, R. Kling, F. Reuss and C. Kirchner, *Adv. Solid State Phys.*, 2006, **45**, 275–287; (*c*) M. Ahmad and J. Zhu, *J. Mater. Chem.*, 2011, **21**, 599–614.

4 (*a*) A. A. Sokol, S. A. French, S. T. Bromley, C. R. A. Catlow, H. J. J. van Dam and P. Sherwood, *Faraday Discuss.*, 2007, **134**, 267–282; (*b*) S. Polarz, J. Strunk, V. Ischenko, M. W. E. van den Berg, O. Hinrichsen, M. Muhler and M. Driess, *Angew. Chem., Int. Ed.*, 2006, **45**, 2965–2969; (*c*) C. Y. Chen, M. W. Chen, J. J. Ke, C. A. Lin, J. R. Retamal and J. H. He, *Pure Appl. Chem.*, 2010, **82**, 2055–2073; (*d*) M. D. McCluskey and S. J. Jokela, *J. Appl. Phys.*, 2009, **106**, 071101.

5 (*a*) C. Hariharan, *Appl. Catal., A*, 2006, **304**, 55–61; (*b*) Q. Zhang, C. S. Dandeneau, X. Zhou and G. Cao, *Adv. Mater.*, 2009, **21**, 4087–4108.

6 (*a*) X. Sui, Y. Liu, C. Shao, Y. Liu and C. Xu, *Chem. Phys. Lett.*, 2006, **424**, 340–344; (*b*) N. H. Nickel and E. Terukov, *Zinc Oxide—a Material for Micro- and Optoelectronic Applications*, Springer, Dodrecht, The Netherlands, 2005; (*c*) L. Spanhel and M. A. Anderson, *J. Am. Chem. Soc.*, 1991, **113**, 2826; (*d*) A. B. Djurišić, A. M. C. Ng and X. Y. Chen, *Prog. Quantum Electron.*, 2010, **34**, 491; (*e*) H. M. Xiong, *J. Mater. Chem.*, 2010, **20**, 4251–4262.

7 H. Weller, *Philos. Trans. R. Soc. London, Ser. A*, 2003, **361**, 229–240.

8 (*a*) K. P. Loh and S. J. Chua, *Top. Appl. Phys.*, 2007, **109**, 92–117; (*b*) D. Ehrentraut, H. Sato, Y. Kagamitani, H. Sato, A. Yoshikawa and T. Fukuda, *Prog. Cryst. Growth Charact. Mater.*, 2006, **52**, 280–335.

9 (*a*) L. Spanhel, *J. Sol-Gel Sci. Technol.*, 2006, **39**, 7–24; (*b*) B. Weintraub, Z. Zhou, Y. Li and Y. Deng, *Nanoscale*, 2010, **2**, 1573–1587.

10 (*a*) M. Niederberger, G. Garnweitner, N. Pinna and G. Neri, *Prog. Solid State Chem.*, 2006, **33**, 59–70; (*b*) I. Bilecka, I. Djerdj and M. Niederberger, *Chem. Commun.*, 2008, 886–888; (*c*) J. Buha, I. Djerdj and M. Niederberger, *Cryst. Growth Des.*, 2007, **7**, 113–116.

11 A. Famengo, S. Anantharaman, G. Ischia, V. Causin, H. Bertagnolli, M. Natile, C. Maccato, E. Tondello and S. Gross, *Eur. J. Inorg. Chem.*, 2009, **33**, 5017–5028.

12 J. A. Dahl, B. L. S. Maddux and J. E. Hutchinson, *Chem. Rev.*, 2007, **107**, 2228.

13 (*a*) Y. J. Chou, M. S. El-Aasser and J. W. Vanderhoff, *J. Dispersion Sci. Technol.*, 1980, **1**, 129; (*b*) K. Landfester and M. Antonietti, in *Colloids and Colloid Assemblies*, ed. F. Caruso, Wiley-VCH, Weinheim, 2004; (*c*) K. Landfester, *Annu. Rev. Mater. Res.*, 2006, **36**, 231; (*d*) K. Landfester, *Top. Curr. Chem.*, 2003, **75**, 227; (*e*) K. Landfester, *Macromol. Symp.*, 2000, **150**, 171; (*f*) K. Landfester and M. Antonietti, *Prog. Polym. Sci.*, 2002, **27**, 689.

14 (*a*) H. D. Dörfler, *Grenzflächen und kolloid-disperse Systeme-Physik und Chemie*, Springer Verlag, Berlin, 1994; (*b*) D. H. Everett, *Basic principles of Colloid Science*, RSC Paperbacks, London, 1989; (*c*) D. J. Shaw, *Colloid and Surface Chemistry*, Butterworth-Heinemann Ltd, Oxford, 1992; (*d*) R. J. Hunter, *Foundation of Colloid Science*, Clarendon Press, Oxford 1989; (*e*) W. Ostwald, *Grundrisse der Kolloidchemie*, 1910; (*f*) R. J. Hunter, *Introduction to Modern Colloid Science*, Oxford Sci Publ, 1993; (*g*) W. Ostwald, *Die Welt der Vernachlässigten Dimension*, 1919.

15 (*a*) W. Que, Y. Zhou, C. H. Kam, Y. L. Lam, Y. C. Chan, L. H. Gan and G. Deen Roshan, *Mater. Res. Bull.*, 2001, **36**, 889; (*b*) R. Rossmanith, C. K. Weiss, J. Geserick, N. Hüsing, U. Hörmann, U. Kaiser and K. Landfester, *Chem. Mater.*, 2008, **20**, 5768; (*c*) W. Lu, M. Chen and L. Wu, *J. Colloid Interface Sci.*, 2008, **324**, 220–224.

16 A. Taden, M. Antonietti, A. Heilig and K. Landfester, *Chem. Mater.*, 2004, **16**, 5081.

17 M. Willert, R. Rothe, K. Landfester and M. Antonietti, *Chem. Mater.*, 2001, **13**, 4681.

18 (*a*) K. Landfester, F. Tiarks, H. P. Hentze and M. Antonietti, *Macromol. Chem. Phys.*, 2000, **201**, 1; (*b*) K. Landfester, N. Bechthold, F. Tiarks and M. Antonietti, *Macromolecules*, 1999, **32**, 5222; (*c*) K. Landfester, *Eur. Coat. J.*, 2005, **12**, 120.

19 (*a*) E. Kobitskaya, D. Ekinci, A. Manzke, A. Plettl, U. Wiedwald, P. Ziemann, J. Biskupek, U. Kaiser, U. Ziener and K. Landfester, *Macromolecules*, 2010, **43**, 3294–3305; (*b*) E. Tang and S. Dong, *Colloid Polym. Sci.*, 2009, **287**, 1025–1032; (*c*) R. Munoz-Espi, G. Jeschke, I. Lieberwirth, C. M. Gomez and G. Wegner, *J. Phys. Chem. B*, 2007, **111**, 697–707; (*d*) R. Munoz-Espi, Y. Qi, I. Lieberwirth, C. M. Gomez and G. Wegner, *Chem.–Eur. J.*, 2006, **12**, 118–129; (*e*) J. J. Zhang, G. Gao, M. Zhang, D. Zhang, C. Wang, D. Zhao and F. Q. Liu, *J. Colloid Interface Sci.*, 2006, **301**, 78–84.

20 (*a*) J. T. Davies, *Proceedings of the 2nd International Congress of Surface Activity*, 1957, pp. 426–438; (*b*) J. Goodwin, *Colloids and Interfaces With Surfactants and Polymers: an Introduction*, John Wiley and Sons, Chichester, 2004.

21 D. Briggs and M. P. Seah, *Practical Surface Analysis*, J. Wiley & Sons, New York, 1990.

22 A. Shirley, *Phys. Rev. B: Solid State*, 1972, **5**, 4709–4713.

23 J. F. Moulder, W. F. Stickle, P. E. Sobol and K. D. Bomben, *Handbook of X-Ray Photoelectron Spectroscopy*, ed. J. Chastain, Perkin-Elemer Corp, Eden Prairie, 1992.

24 (*a*) NIST XPS Database X-ray Photoelectron Spectroscopy Database 20, Version 3.5, 2007; (*b*) Z. G. Wang, X. T. Zu, S. Zhu and L. M. Wang, *Phys. E.*, 2006, **35**, 199–202.

25 L. Lutterotti, S. Matthies, H. R. Wenk and M. Goodwin, *J. Appl. Phys.*, 1997, **81**, 594–600.

26 I. Lonardelli, H. R. Wenk, L. Lutterotti and M. Goodwin, *J. Synchrotron Radiat.*, 2005, **12**, 354–360.

27 R. Fricke, K. Mreyring, *Z. Anorg. Ch.*, 1937, 230, 366–374, in *Gmelins Handbuch der Anorganischen Chemie*, Edited by Gmelin-Institut für anorganische Chemie und Grenzgebiete, Zn-Band, 1956, vol. 32, p. 776.

28 P. Louette, F. Bodino and J. Pireaux, *Surf. Sci. Spectra*, 2005, **12**, 59.

29 K. Mitsuda, H. Kimura and T. Murahashi, *J. Mater. Sci.*, 1989, **24**, 413–419.

30 (*a*) M. Anpo and Y. J. Kubokawa, *J. Phys. Chem.*, 1984, **88**, 5556; (*b*) L. Armelao, F. Heigl, A. Jurgensen, R. I. R. Blyth, T. Regier, X. T. Zhou and T. K. Sham, *J. Phys. Chem. C*, 2007, **111**, 10194–10200; (*c*) X. H. Sun, S. Lam, T. K. Sham, F. Heigl, A. Jurgensen and N. B. Wong, *J. Phys. Chem. B*, 2005, **109**, 3120–3125; (*d*) T. Hirai, Y. Harada, S. Hashimoto, K. Edamatsu and T. Itho, *J. Lumin.*, 2001, **94–95**, 261; (*e*) A. Van Dijken, E. Meulenkamp, D. Vanmaeklenbergh and A. Meijerink, *J. Lumin.*, 2000, **90**, 123; (*f*) X. W. Zheng, J. L. Yuan and L. Zhang, *J. Phys. Chem. C*, 2008, **112**, 3505.

31 R. K. Pai and S. Pillai, *CrystEngComm*, 2008, **10**, 865.

32 K. Nakamoto, *Infrared and Raman Spectra of Inorganic and Coordination Compounds*, Wiley VCH, Weinheim, 2009.

EurJIC European Journal of Inorganic Chemistry
ChemPubSoc Europe
FULL PAPER

DOI:10.1002/ejic.201201474

Inorganic Chemistry in a Nanoreactor: Doped ZnO Nanostructures by Miniemulsion

Paolo Dolcet,[a] Francesca Latini,[a] Maurizio Casarin,[a] Adolfo Speghini,[b] Eugenio Tondello,[a] Cristina Foss,[c,d] Stefano Diodati,[a] Lucia Verin,[c,d] Antonella Motta,[c,d] and Silvia Gross*[a,e]

Keywords: Colloids / Nanoparticles / Doping / Zinc / Luminescence / Cytotoxicity

Doped M:ZnO nanoparticles (Zn/M = 50:1 or 20:1; M = Ag^{I}, Co^{II}, Cu^{II}, Eu^{III}, Mg^{II}, Mn^{II}) have been produced by an easy, reproducible, and fast inverse miniemulsion approach, enabling the co-precipitation of the nanocrystalline oxide in a confined space. Unexpectedly, the formation of crystalline materials took place at room temperature. Suspensions were characterized by dynamic light scattering and UV/Vis spectroscopy, whereas precipitated powders were characterized by X-ray photoelectron spectroscopy, X-ray diffraction, transmission electron microscopy, inductively coupled plasma atomic emission spectrometry, and thermogravimetric analysis. The particles obtained showed preferential growth along the [0002] direction with a size of 70 nm, whereas along the other directions average sizes of between 26 and 33 nm were determined. The analyses confirmed successful doping in all cases but one: In fact, the Ag-doped sample is a nanocomposite consisting of metallic silver clusters dispersed in the ZnO matrix. Red emission from the ZnO:Eu sample was evidenced upon excitation at around 465 nm.

Introduction

Zinc oxide has been the subject of renewed intense research in the last few years as a consequence of its unique properties.[1–4] In particular, its wide band-gap (3.37 eV) and high exciton binding energy (60 meV),[5] which incidentally generates efficient excitonic emission even at room temperature, make ZnO a material perfectly suited to use in blue-light-emitting diodes, ultraviolet laser diodes, and photodiodes. Further applications are in the field of catalysis,[6,7] sensing,[8] and photovoltaics.[9]

Doping ZnO with transition-metal ions greatly enriches its appealing functional properties and performance. In particular, doping with rare-earth ions enhances its optical properties, whereas paramagnetic ions lead to outstanding magnetic properties. One of the most exciting applications for doped ZnO is related to spintronics,[1,2,5,10] an emerging field that focuses on manipulating the spin of charge carriers instead of the charge carriers themselves for information storage. Among the materials that have potential for use as spintronics devices there are the so-called diluted magnetic semiconductors (DMS),[11–14] characterized, even at room temperature, by ferromagnetic behavior. DMS are semiconductors doped with transition-metal ions having a magnetic moment, such as Mn^{II} and Co^{II},[15,16] but also Fe^{II}, Cu^{II}, or Ni^{II}.[17] The particular magnetic properties associated with these materials are strongly related to the adopted synthetic strategy.[18] Furthermore, they are extremely sensitive to the operating conditions. Fundamental issues are the solubility of the specific dopant in the ZnO host matrix (usually achieved with cations with an ionic radius R_M such that $R_{Zn^{II}}/R_M \approx 1$) and the ferromagnetism generated by doping (usually associated with a second phase M_xO_y rather than a solid solution M:ZnO[19]). Moreover, the optical and magnetic properties of doped ZnO nanostructures may also be conveniently used in biomedicine, in particular for bioimaging in which the low cytotoxicity and biocompatibility also represent a competitive advantage. In particular, the emission properties of doped ZnO of ZnO can be exploited for both in vitro and in vivo bioimaging.[20–22] In this regard, it is noteworthy that the doping of ZnO is

---

[a] Dipartimento di Scienze Chimiche, Università degli Studi di Padova,
via Marzolo 1, 35131 Padova, Italy
[b] Dipartimento di Biotecnologie, Università degli Studi di Verona and INSTM, UdR Verona,
Strada Le Grazie 15, 37134 Verona, Italy
[c] Department of Industrial Engineering and Biotech Research Center, University of Trento,
38100 Trento, Italy
[d] European Institute of Excellence on Tissue Engineering and Regenerative Medicine, and INSTM,
38100 Trento, Italy
[e] Istituto di Scienze e Tecnologie Molecolari, ISTM-CNR and INSTM, UdR Padova,
via Marzolo 1, 35131 Padova, Italy
E-mail: silvia.gross@unipd.it
Homepage: http://www.chimica.unipd.it

Supporting information for this article is available on the WWW under http://dx.doi.org/10.1002/ejic.201201474.

© 0000 Wiley-VCH Verlag GmbH & Co. KGaA, Weinheim

widely used to tune its photoluminescence characteristics by shifting its emission in the visible range.[22]

Pure and doped ZnO nanoparticles (NPs) can be obtained through different wet-chemistry methods involving either colloidal, sol–gel,[23] or solvo/hydrothermal methods, as has been extensively reviewed.[24] The crystallization of ZnO nanostructures at low temperature (60 °C)[25–28] or at room temperature[29] has previously been achieved. Despite the fact that the microemulsion method has been used for the synthesis of ZnO[30–32] and other oxides,[33–38] to the best of our knowledge, a miniemulsion method has never been used to synthesize doped ZnO NPs. In this regard, it can be useful to remember that microemulsions are formed by the simple vigorous stirring of appropriate water/oil/surfactant mixtures, whereas miniemulsions (MEs) are generated by applying to such systems intense shear forces through high-power ultrasonication or high-pressure homogenization to obtain smaller particles (the average droplet size ranges from 30–500 nm) as well as better control over their dimensions.[39]

MEs have been the topic of extensive reviews by Landfester and Antonietti.[39–42] They have been widely employed in the synthesis of polymer dispersions or hybrid systems.[43–45] Nevertheless, it has to be noted that they have limited applications in purely inorganic systems[46–49] compared with much wider applications in polymer synthesis and, to the best of our knowledge, only our group has successfully applied this method to the synthesis of ZnO NPs.[50] In this contribution we hence report an easy, fast, reproducible, and cost-effective synthetic route to the production of monodispersed, doped ZnO colloidal suspensions at room temperature by the co-precipitation of M:ZnO (with M = Ag^{I}, Co^{II}, Cu^{II}, Eu^{III}, Mg^{II}, Mn^{II}) in a confined space within the droplets of inverse (water-in-oil w/o) miniemulsions.

To evaluate possible cytotoxic effects (as mentioned above, doped ZnO may find application in the field of in vitro and in vivo bioimaging), the synthesized NPs have also been subjected to the lactate dehydrogenase (LDH) activity test[51] by using the human fibroblast cell line MRC5.

Furthermore, in view of their application as bioimaging contrast agents, we also assessed the luminescence of the samples doped with lanthanide ions, which are usually characterized by strong emissions.[52]

Results and Discussion

The nature and compositions of the miniemulsions were investigated by dynamic light scattering (DLS) and UV/Vis spectroscopy immediately after the mixing and sonication that yielded the final MEs. DLS allowed the hydrodynamic diameters of the w/o droplets to be determined, with average values of 32–40 nm (see Figure 1 and Table 1), confirming the high reproducibility of the synthetic route. Their absorption properties (in particular for those samples with a Zn/M ratio of 50:1) were determined by UV/Vis spectroscopy (Figure 1, right).

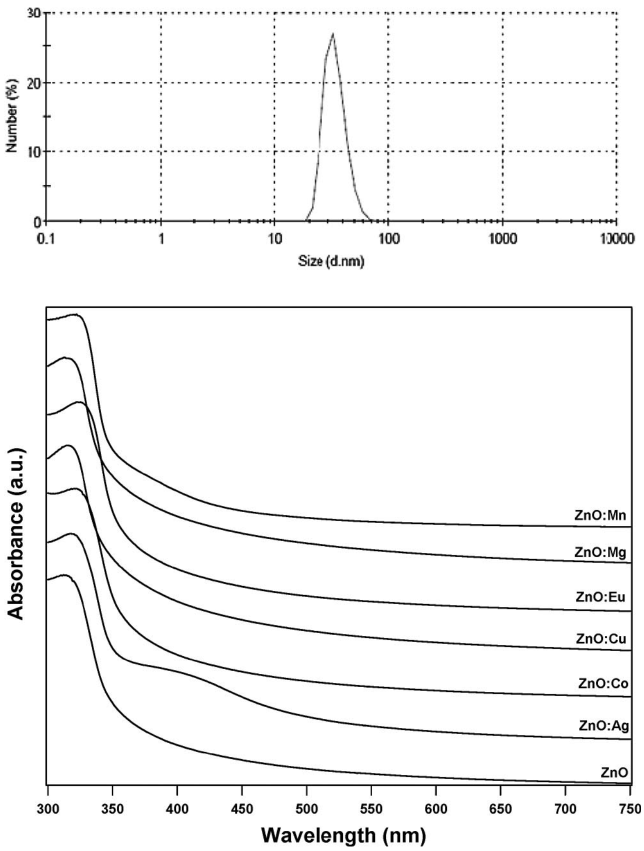

Figure 1. Top: Typical size distribution diagrams obtained from DLS (ZnO:Cu 50:1), bottom: UV/Vis spectra for samples with atomic ratio of Zn/M = 50:1.

Table 1. Average hydrodynamic diameters for 50:1 samples of ZnO:M determined by DLS.

Sample	D_{hydr} [nm]
ZnO:Ag	37 ± 4
ZnO:Co	37 ± 5
ZnO:Cu	32 ± 3
ZnO:Eu	33 ± 4
ZnO:Mg	40 ± 4
ZnO:Mn	39 ± 3

All the samples were characterized by an intense absorption in the UV region with an onset at 360 nm associated with the ZnO energy gap.[1,53] Moreover, both the low concentration and the Laporte selection rule concur to the absence of any additional band in the visible region for all the samples but one; the UV/Vis spectrum of ZnO:Ag is characterized by the presence of an additional broad absorption band at 410 nm. This is a value typical of the surface plasmon resonance of metallic silver[54,55] and therefore might be quite confidently associated with the presence of reduced silver NPs, as confirmed by the TEM analysis (see below).

Powders separated by centrifugation of the miniemulsions were investigated by X-ray diffraction to obtain information about the possible formation of crystalline materi-

© 0000 Wiley-VCH Verlag GmbH & Co. KGaA, Weinheim

als. The X-ray diffraction patterns for the Zn:M = 50:1 samples (hereafter ZnO:M 50:1) are displayed in Figure 2 in which the ZnO wurtzite reflections are indexed. Interestingly, for all the samples, the ZnO wurtzite polymorph is present at room temperature without the need for any further thermal treatment. Moreover, inspection of Figure 2 clearly testifies that 1) the only ZnO phase present in all the different samples is wurtzite and 2) no phase due to domains generated by dopant ions is detectable. This latter result may be ascribed either to a homogeneous distribution of dopants in the host lattice or to the intrinsically low detection limit of the technique. A tentative rationale for the unexpected formation of crystalline ZnO at room temperature relies on the generation, in basic or neutral media, of amphoteric hydroxide species, $ZnO_x(OH)_y(OH_2)_z$. These are initially formed in the colloidal state as amorphous species, and they spontaneously evolve, through a dehydration process, to crystalline wurtzite ZnO, not only through the action of heating or irradiation but also, as in our case, upon prolonged storing and aging in their mother liquor.[56] At pH > 9, which corresponds to our operating conditions, the high concentration of OH^- induces dehydration of the initially formed $Zn(OH)_2$ or $Zn(OH)_4^{2-}$ species, which favors the growth of the ZnO crystal structure.[50,57]

The average crystallite size (15–20 nm) was determined by using the Scherrer equation. Successive Rietveld refinement revealed average diameters ranging from 26 nm (as pure ZnO, and for samples doped with Co, Cu, and Mn) to 33 nm (for samples containing Ag and Eu) and also showed, in all cases, a preferential growth along the [0002] direction, thus leading to the formation of anisotropic structures. The crystallites have dimensions ranging from 56 to 78 nm along this axis.

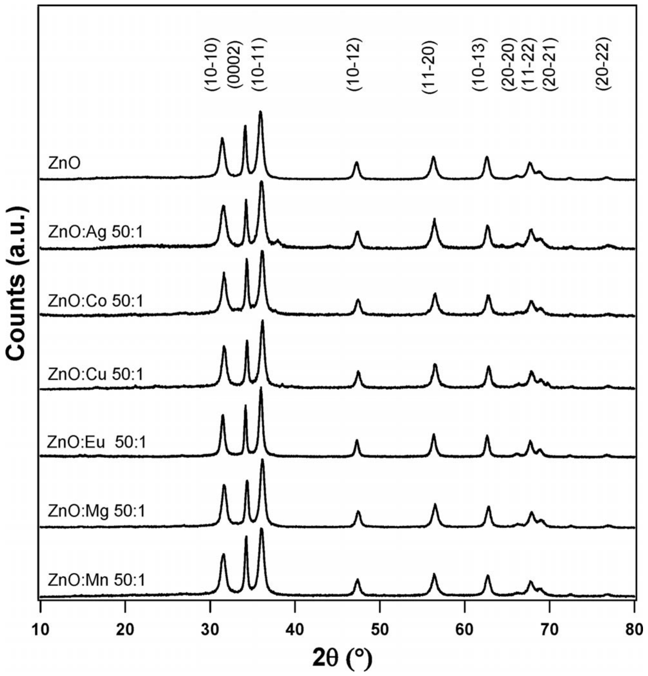

Figure 2. Diffractograms of powder samples with Zn/M = 50:1.

Table 2. XPS data for the powder samples obtained by centrifugation of the suspensions.[a]

	BE C1s [eV]	BE O1s [eV]	BE $Zn2p_{3/2}$ [eV]	Auger parameter α' [eV]	BE dopant [eV]	C [%]	O [%]	Zn [%]	M [%]	Zn/M atomic ratio (XPS)	Powder color
ZnO:Ag 50:1	284.6 286.0	529.9 532.3	1021.0	2010.4	$Ag3d_{5/2}$ 367.0	65.1	31.8	3.0	0.1	25:1	black
ZnO:Ag 20:1	284.6 286.3 289.5	530.0 531.5	1021.3	2010.0	$Ag3d_{5/2}$ 366.9 367.5	23.7	60.1	16.1	0.1	98:1	brown
ZnO:Co 50:1	284.6 285.9	530.1 532.0	1021.1	2009.9	$Co2p_{3/2}$ 780.2	43.1	46.3	10.0	0.6	17:1	brown
ZnO:Co 20:1	284.6 285.0 288.5	529.8 531.2	1021.3	2010.1	$Co2p_{3/2}$ 779.8	26.2	57.7	15.2	1.0	16:1	brown
ZnO:Cu 50:1	284.6 286.0	530.1 531.2 532.5	1021.2	2009.9	$Cu2p_{3/2}$ 933.7	57.0	37.1	5.7	0.2	35:1	green
ZnO:Cu 20:1	284.6 286.2	529.7 532.1	1020.9	2010.0	$Cu2p_{3/2}$ 931.9	59.2	37.1	3.5	0.2	16:1	green
ZnO:Eu 50:1	284.6 285.3 288.6	529.7 531.5	1020.7	2010.5	$Eu3d_{5/2}$ 1133.8	44.3	47.6	7.0	1.1	6:1	white
ZnO:Eu 20:1	284.6 286.1 289.5	530.1 531.7	1021.5	2010.2	$Eu3d_{5/2}$ 1133.8 1136.1	47.9	43.0	7.4	1.7	4:1	white
ZnO:Mg 50:1	284.6 286.1	529.6 532.0	1020.7	2010.3	Mg2p –	65.2	31.2	3.1	0.4	7:1	white
ZnO:Mn 50:1	284.6 286.9 289.7	530.3 532.1	1021.3	2009.8	$Mn2p_{3/2}$ 640.5	52.2	41.2	6.3	0.3	20:1	brown
ZnO:Mn 20:1	284.6 287.8	530.1 531.5	1021.3	2010.1	$Mn2p_{3/2}$ 641.0	31.6	54.4	13.6	0.5	29:1	brown

[a] BE data is corrected for charging effects.

© 0000 Wiley-VCH Verlag GmbH & Co. KGaA, Weinheim

The surface composition and the actual oxidation states of the surface species in our powder samples were determined by X-ray photoelectron spectroscopy. Detailed scans were recorded for O1s, C1s, Zn2p, ZnLMM, and significant dopant binding energy (BE) regions (including Auger peaks). The BE values and atomic percentages are pre-

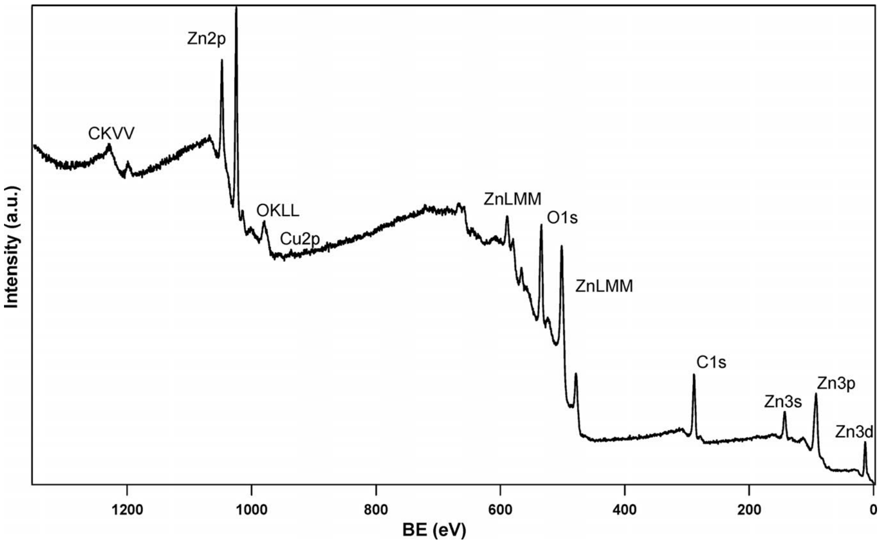

Figure 3. XPS survey spectrum of the ZnO:Cu 20:1 sample (not corrected for charging effects).

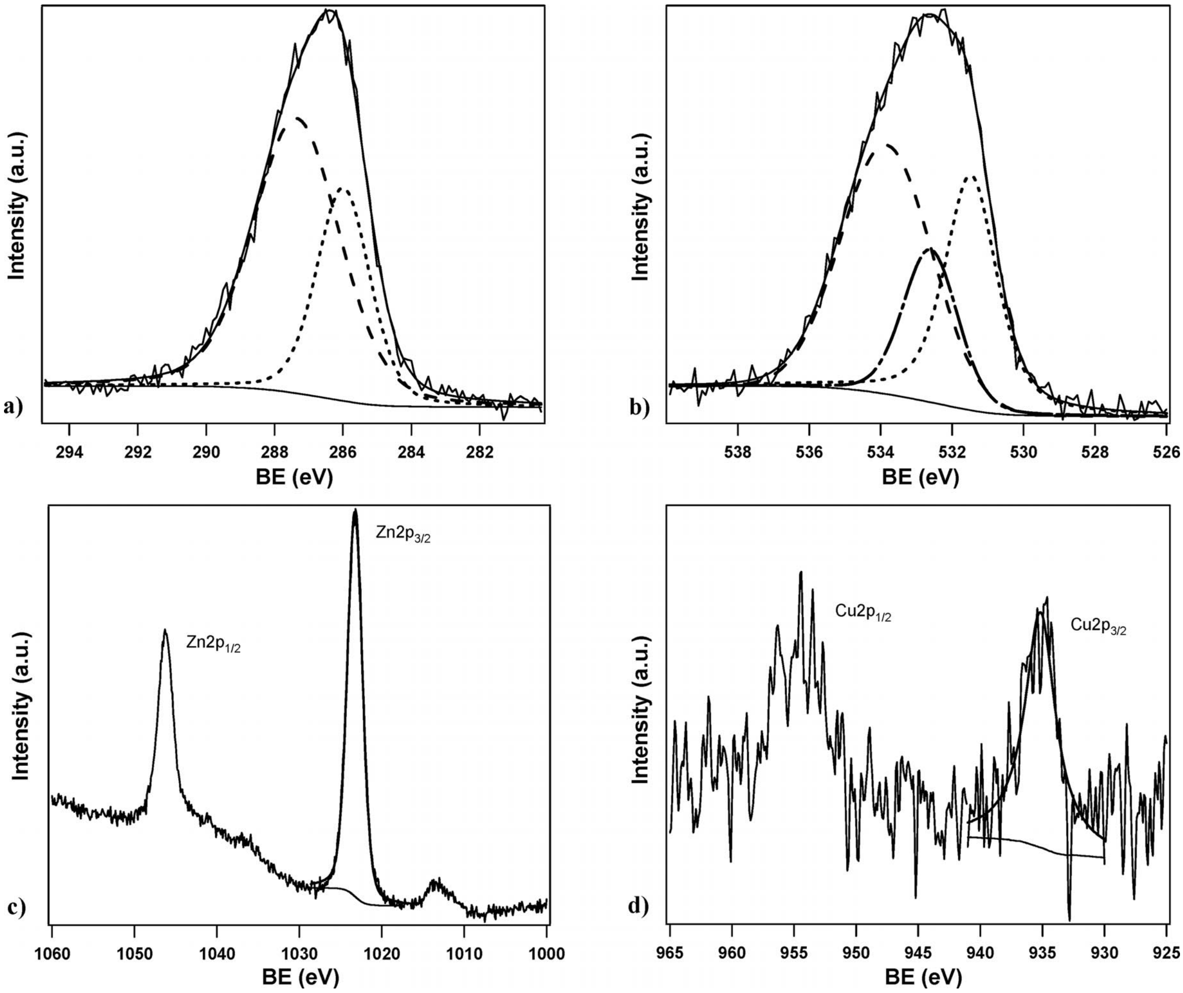

Figure 4. XPS peaks for ZnO:Cu 50:1. a) C1s, b) O1s, c) Zn2p$_{3/2}$, and d) Cu2p$_{3/2}$ (the peaks in the spectra are not corrected for charging effects).

sented in Table 2, whereas the XPS survey spectrum and selected BE regions for ZnO:Cu 50:1 are exemplarily reported in Figure 3 and Figure 4, respectively (the other spectra are presented in the Supporting Information).

For all the samples, the C1s and O1s peaks are characterized by some broadening, which suggests the presence of different chemical environments for these two elements. As far as the carbon peak is concerned, along with the standard signal at 284.6 eV (due to external contamination), the contribution at around 286 eV can be readily assigned to residual surfactant from the synthesis procedure. More specifically, the spectral feature at higher BEs can be ascribed to the C atoms of the hydrophilic chain.[58] The third contribution (at ca. 289 eV) characterizing the ZnO:Eu and ZnO:Mn spectra have been ascribed in both cases to partial carbonation of the samples due to absorption of CO_2. Moving to the oxygen O1s region, the two different contributions correspond to the oxygen atoms in the ZnO lattice (ca. 530 eV)[29,59,60] as well as to the surfactant (at 532.0 eV).[58] Both the Zn2p$_{3/2}$ signal (ca. 1021 eV) and the modified Auger parameter α' (α' = 2009.8–2010.5 eV), evaluated according to Wagner,[61] are in good agreement with typical literature ZnO values.[29,59,60,62,63] As far as the dopants are concerned, even though most of the BEs in the detected regions agree with the presence of dopant ions in an oxidic environment (Zn/M = 50:1: Co2p$_{3/2}$ = 780.2 eV, Cu2p$_{3/2}$ = 933.7 eV, Eu3d$_{5/2}$ = 1133.8 eV, Mn2p$_{3/2}$ = 640.5 eV; Zn/M = 20:1: Co2p$_{3/2}$ = 779.8 eV; Mn2p$_{3/2}$ = 641.0 eV), some discrepancies exist. For example, in the ZnO:Ag samples, the signal pertaining to the Ag3d$_{5/2}$ peak lies at 366.9–367.0 eV, a value lower than that usually found for elemental Ag or Ag_2O.[59,64] Such a shift may be explained in terms of a strong interfacial interaction between Ag and ZnO. Because the metal has a higher Fermi energy level than the semiconductor, efficient Ag→ZnO electron transfer may occur at the interface to equilibrate the Fermi level. This phenomenon induces a partial oxidation of the surface of the metal nanoparticles and is therefore at the origin of the observed shift in BE.[65,66] Moreover, an additional component at 376.5 eV (characteristic of Ag^{I} ions in an oxidic environment) is observed in the ZnO:Ag 20:1 sample.

In the case of the samples doped with copper, the BEs of the Cu2p$_{3/2}$ peak are 931.9 and 933.7 eV for Zn:Cu 20:1 and Zn:Cu 50:1, respectively. In this regard it is noteworthy that such a low value for the former is consistent with the presence of Cu^{I} ions, which suggests a partial reduction from Cu^{II} to Cu^{I}. This reduction is also confirmed by the corresponding α' value (1848.8 eV),[67,68] even if the low signal-to-noise ratio in the Auger region prevents an accurate evaluation of the parameter itself. The latter, on the other hand, corresponds to Cu^{II} in an oxidic environment.[68]

The Eu3d$_{5/2}$ peak for the sample with the higher lanthanide concentration (Zn/Eu = 20:1) consists of two components, one at 1133.8 eV and the other at 1136.1 eV, accompanied by two satellite peaks at 1124.2 and 1126.0 eV. This is consistent with Eu^{III} ions coordinated by oxides and traces of the nitrate precursor, respectively.[69] Finally, the Mg2p signal of the ZnO:Mg 50:1 sample has such a low intensity that any discrimination from the noise was prevented.

Before continuing, it has to be emphasized that the experimental Zn:M atomic ratios, as determined by XPS, are always lower than those expected (see Table 2), which suggests the possible segregation of dopants on the surface. Bulk Zn:M ratios were determined by inductively coupled plasma atomic emission spectrometry (ICP-AES) for selected samples and these were consistent with the expected nominal ratio, which proves the efficiency of the chosen doping strategies based on the simultaneous embedding of the doping ions in the nucleating host structure.

Despite the absence of any specific UV/Vis absorption, apart from that generated by the ZnO matrix, the doped samples are all distinguished by their color (see Table 2 for details). For this reason, for some of the powders obtained, diffuse UV/Vis reflectance spectra in the range 300–800 nm were recorded (ZnO:Ag and ZnO:Mn were too dark to perform a reliable analysis). The spectrum of ZnO:Co 50:1 is characterized by four minima centered at 350 nm (due to the ZnO matrix) and 560, 616, and 658 nm (due to the dopant; Figure 5). According to literature data, these latter absorptions are associated with the ν_3 [$^4A_2 \rightarrow {}^4T_1(P)$] ligand field band characteristic of tetrahedral Co^{2+} species.[70] Different mechanisms contribute to the shape of this band:

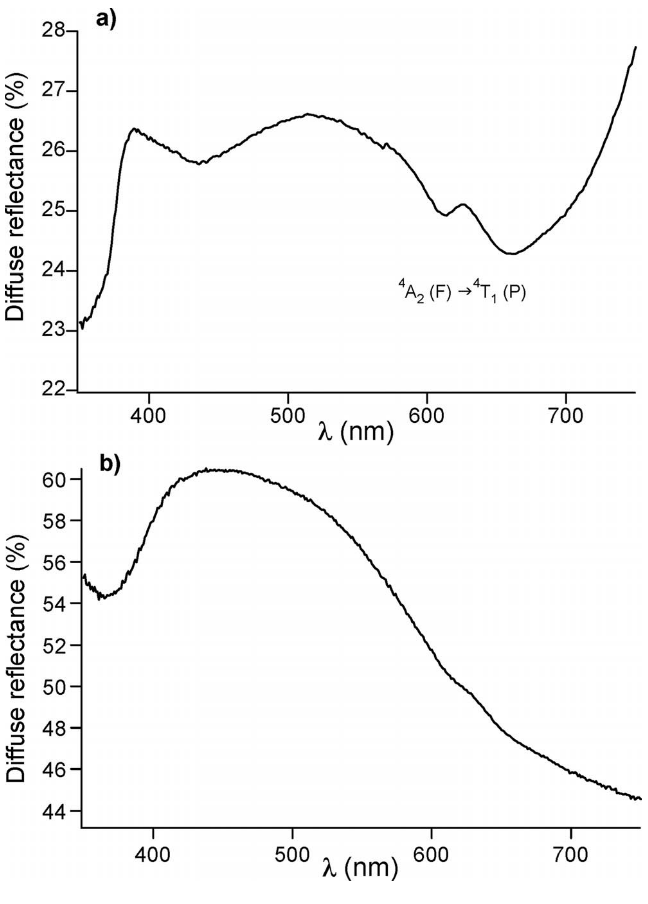

Figure 5. UV/Vis reflectance spectra of Zn/M = 50:1 samples: a) ZnO:Co and b) ZnO:Cu.

© 0000 Wiley-VCH Verlag GmbH & Co. KGaA, Weinheim

1) Vibronic coupling, 2) a first-order spin–orbit coupling ($\zeta_{Co}{}^{2+}$ free ion = 515 cm^{-1}) splits the tetrahedral ^{4}T states into three spinor components, and 3) spin–orbit mixing of the ^{4}T state with close doublet states arising from the doublet ^{2}G free-ion term.[71,72] In the spectrum of ZnO:Cu 50:1, there is a broad band stretching towards high wavelengths, typical of CuO,[73] in accordance with the XPS observations. The other samples did not show increased absorbance due to the presence of doping ions and the corresponding spectra are therefore reported only in the Supporting Information.

As already mentioned, in the UV/Vis spectrum of the suspension of the ZnO:Ag 50:1 sample, alongside the main absorption peak at 360 nm, a broad band centered at 410 nm is present corresponding to the surface plasmon resonance of metallic silver,[54,55] which corroborates the hypothesis of the presence of reduced silver clusters. To confirm such a hypothesis, transmission electron microscopy (TEM) and selected area electron diffraction (SAED) were performed and the results obtained are displayed in Figure 6. The recorded micrograph shows the presence of ZnO nanostructures (mainly as nanoplatelets, with an average length of ca. 200 nm and thickness of 15 nm, along with nanorods of similar length, consistent with what was found for the other samples, see Figure S4 in the Supporting Information) and Ag spherical particles (average diameter of ca. 20 nm). Moreover, in agreement with the Rietveld refinement of the XRD patterns, the shape of the oxide matrix confirms the presence of anisotropic structures. As far as the spherical particles are concerned, their metallic nature was confirmed by electron diffraction [the highlighted spots in Figure 6 (b) correspond to the (111) plane of metallic silver] and energy-dispersive X-ray spectroscopy (EDX), which strengthens our hypothesis concerning the formation of an Ag/ZnO nanocomposite. In this regard, it has to be noted that the generation of Ag/ZnO is not particularly surprising because a similar co-precipitation method has previously been reported for the synthesis of Ag/ZnO heterostructures. In fact, Ag_2O, readily obtained by basic precipitation, easily undergoes photolysis to generate metallic silver.[74]

The residual surfactant on the surfaces of the NPs was estimated by thermogravimetric analysis (TGA) of the Ag-doped nanostructures (the TGA-DSC measurement for ZnO:Ag 50:1 is presented in Figure 7). Adsorbed water is released up to 200 °C (leading to a weight loss of about

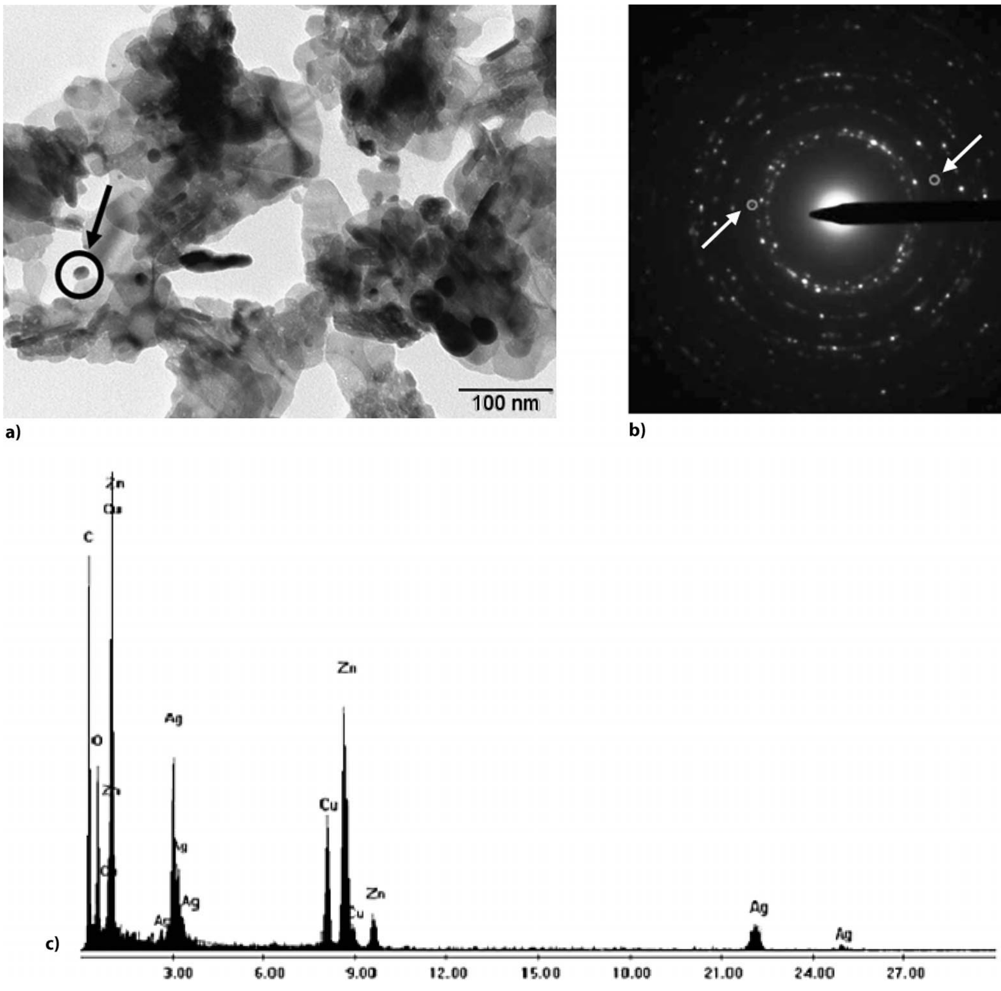

Figure 6. a) TEM image (arrow shows an Ag NP), b) SAED pattern [highlighted spots correspond to Ag (111) reflections], and c) EDX spectrum of ZnO:Ag 50:1.

© 0000 Wiley-VCH Verlag GmbH & Co. KGaA, Weinheim

2%) and on further heating the surfactant Triton X-100 decomposes between 200 and 300 °C leading to a further weight loss of 20.7%. The remaining 77.3% corresponds to the inorganic nanocomposite.

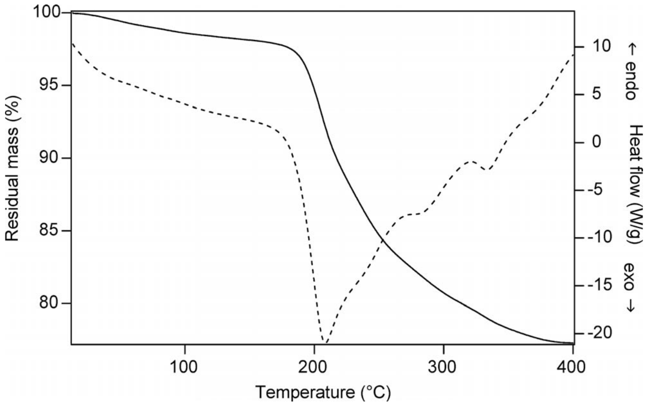

Figure 7. DSC-TGA for the ZnO:Ag 50:1 sample.

As already outlined, the interesting luminescence properties coupled with low cytotoxicity make doped ZnO nanosystems particularly interesting for bioimaging applications, both in vitro and in vivo.[20–22] Within this framework, the cytotoxicity of selected samples was assessed. In particular, the lactate dehydrogenase (LDH) assay was performed by seeding the human fibroblast cell line MRC5. The LDH test is a simple photometric test, and its working principle is depicted in Figure 8. Upon stressing or membrane lysis, cells release an increased amount of lactate, which is then oxidized to pyruvate by the enzyme LDH, at the same time reducing NAD to NADH + H$^+$. This latter process is then reversed through the use of a dye (found in the reactive set), which is yellow in the oxidized form and red in the reduced form. By evaluating the absorption at 490 nm (λ_{max} of the red form), the cytotoxicity can be evaluated by comparison with a blank control. Two of our samples, pure ZnO and ZnO:Co 50:1, were tested and showed LDH activities comparable to the enzyme activity in the negative control, which indicates that these materials are not significantly cytotoxic (see Figure 8). Although cytotoxicity was not expected for pure ZnO, the result obtained with the Co-doped sample is remarkable and shows the possibility of applying these systems at least for in vitro applications.

In this regard, the luminescence of the proposed nanostructures was also assessed. With this aim, luminescence spectra were acquired for samples doped with the lanthanide ion. The emission spectrum of the ZnO:Eu 50:1 sample at room temperature upon excitation at 465 nm is displayed in Figure 9 in the 550–750 nm wavelength range. The emission bands can be assigned to $^5D_0 \rightarrow {}^7F_J$ (J = 0, 1, 2, 3, 4) transitions of the Eu^{3+} ion. The strongest emission band at 609 nm, which clearly dominates the spectrum, is due to the hypersensitive $^5D_0 \rightarrow {}^7F_2$ transition. The $^5D_0 \rightarrow {}^7F_2$ band is much stronger than the magnetic dipole $^5D_0 \rightarrow {}^7F_1$ band, which shows that the Eu^{3+} ions are located at low-symmetry sites without inversion symmetry. Moreover, the pres-

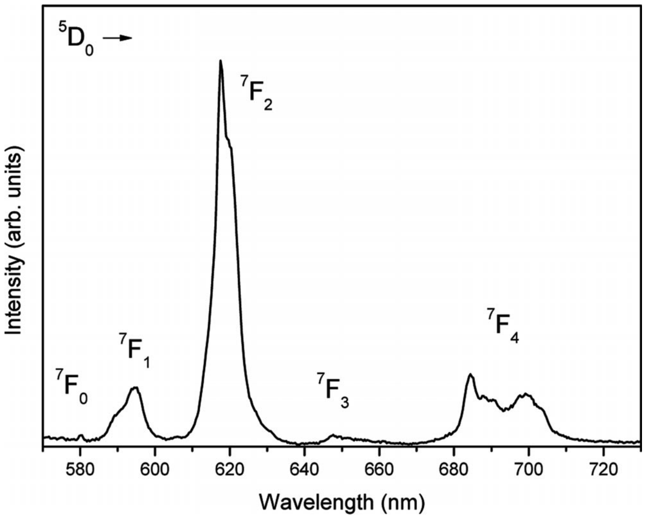

Figure 9. Emission spectrum for the ZnO:Eu 50:1 sample at room temperature (λ_{exc} = 465 nm).

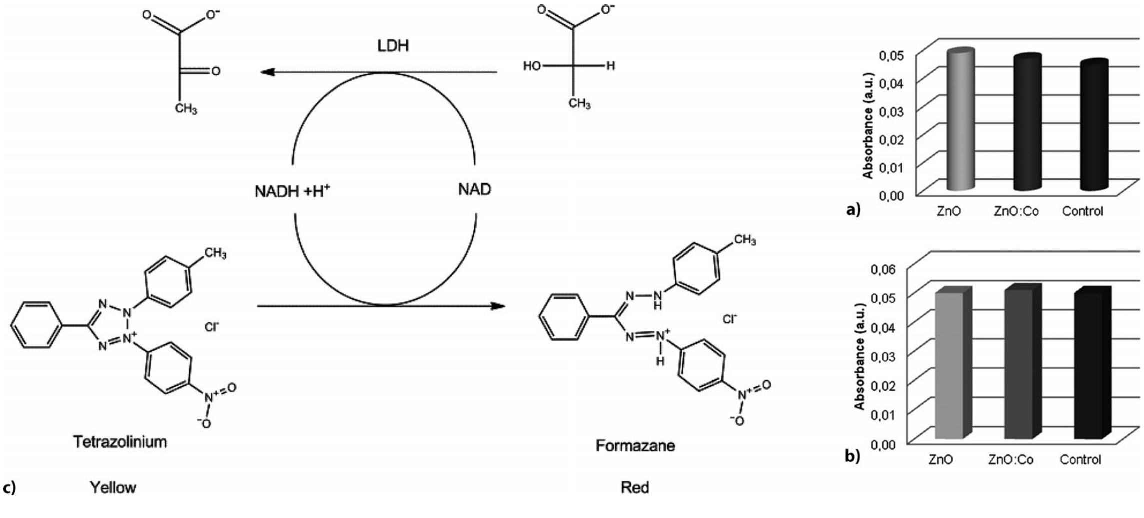

Figure 8. a) Working principle and reaction involved in the LDH assay. LDH activity for a negative control and ZnO and Zn:Co 50:1 NPs at concentrations of b) 30 and c) 100 µg/mL.

© 0000 Wiley-VCH Verlag GmbH & Co. KGaA, Weinheim

ence of a weak but clearly visible $^5D_0 \rightarrow {}^7F_0$ band in the emission spectrum indicates that the Eu^{3+} ions are accommodated at sites with C_s, C_1, C_n, or C_{nv} (n = 2, 3, 4, 6) point symmetry, in accord with the electric dipole selection rules for lanthanide ions.[75] The emission spectrum shows that not all the Stark components of the emission transitions are resolved and that some bands overlap. This behavior points to a small crystal-field splitting and to significant broadening of the emission bands, probably due to structural disorder around the Eu^{3+} ions. The emission decay (Figure 10) has a slightly nonexponential behavior, which confirms the presence of disorder around the lanthanide ions. The effective decay time, t_{eff}, was calculated by using Equation (1)[76] in which $I(t)$ is the luminescence intensity at time t corrected for the background and the integrals are evaluated in the range $0 < t < t_{max}$ with $t_{max} >> \tau_{eff}$. The value of τ_{eff} is 1.43 ± 0.01 ms, which is compatible with that obtained for Eu^{3+} ions incorporated in a ZnO nanocrystalline host,[77] which confirms the effectiveness of our synthetic approach for controlled doping.

$$\tau_{\mathrm{eff}} = \int \frac{tI(t)\mathrm{d}t}{I(t)\mathrm{d}t} \qquad (1)$$

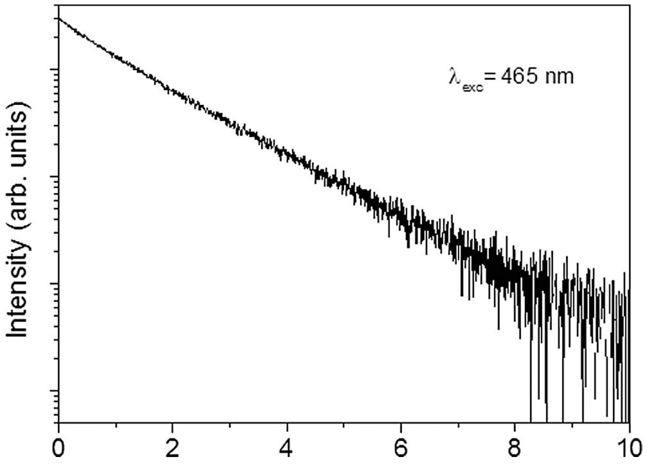

Figure 10. Emission decay for the ZnO:Eu 50:1 sample at room temperature (λ_{exc} = 465 nm, λ_{em} = 612 nm).

Conclusions

In this contribution we have reported an easy, reproducible, and effective method for the preparation of doped nanocrystalline ZnO particles at room temperature without any need for successive thermal treatment. The method developed produces fine polycrystalline platelets with an average crystallite size of 15–20 nm and preferred growth along the [0002] direction. The morphologies and compositions of the nanoparticles were investigated in detail by using different and complementary techniques. In particular, doping ions were found to be embedded in crystalline ZnO. XPS analyses revealed the tendency of dopants to migrate towards the surfaces for all samples but one; in the ZnO:Ag material, silver is reduced and generates metallic NPs, as confirmed by the TEM measurements.

In view of their possible applications in the field of bioimaging, the synthesized NPs were subjected to the LDH assay and showed no significant cytotoxic effect.

A strong red luminescence was observed for the europium-doped ZnO nanocrystals, which suggests a possible use of these materials for in vitro and in vivo biomedical applications as red light is not strongly absorbed by biological tissues and can be efficiently detected by using cheap CCD devices.

Experimental Section

General: Zinc nitrate hexahydrate [$Zn(NO_3)_2 \cdot 6H_2O$], copper(II) chloride dihydrate ($CuCl_2 \cdot 2H_2O$), silver nitrate ($AgNO_3$), manganese(II) nitrate [$Mn(NO_3)_2$], europium(III) nitrate pentahydrate [$Eu(NO_3)_3 \cdot 5H_2O$], magnesium nitrate hexahydrate [$Mg(NO_3)_2 \cdot 6H_2O$], sodium hydroxide (NaOH), 1-pentanol ($C_5H_{11}OH$), and Triton X-100® [$C_{14}H_{22}O(C_2H_4O)_n$, n = 9–10] were purchased from Aldrich. Cyclohexane (C_6H_{12}) was obtained from Alfa-Aesar. Cobalt(II) chloride hexahydrate ($CoCl_2 \cdot 6H_2O$) was purchased from Carlo Erba Reagenti. All chemicals were used without further purification.

Nanoparticle Synthesis: The investigated ZnO NPs were synthesized according to a previously reported method.[50] In a typical synthesis, two identical mixtures, A and B, were prepared by dispersing Triton X-100 (5.1×10^{-3} mol, 3 mL) and pentanol (9.2×10^{-3} mol, 1 mL) in cyclohexane (28 mL). Subsequently, an aqueous precursor solution (1 mL) containing 0.2 M $Zn(NO_3)_2 \cdot 6H_2O$ (2.0×10^{-4} mol) and 4 mM dopant precursor (4.0×10^{-6} mol, Zn/M = 50:1; or 10 mM in the case of the Zn/M = 20:1 samples) was added to mixture A and stirred to yield emulsion A′. A 0.1 M solution of NaOH (1.0×10^{-3} mol, 1 mL) was added to mixture B to generate, after mechanical stirring, emulsion B′. Both emulsions were then separately sonicated for 3 min by using a Sartorious Stedim LabsonicP homogenizer, mounting a 3 mm titanium tip, and operating at an amplitude of 70 %, which corresponds to an acoustic power of 322 W/cm^2. The resulting miniemulsions A′ and B′ were mixed together and sonicated again for the same time and amplitude. Flocculation appeared in the miniemulsion after a few minutes and the mixture was allowed to stand overnight. The white precipitate that formed was separated by centrifugation (10 krpm for 15 min) and washed several times with deionized water.

Methods of Characterization

DLS Analysis: DLS analyses were carried out on the as-prepared suspensions with a Malvern Zetasizer Nano S at a temperature of 20 °C.

UV/Vis and Reflectance Spectroscopy: Absorbance spectra were recorded with a Varian UV-CARY 5E spectrophotometer in the spectral range 280–800 nm. For the reflectance measurements, the instrument was equipped with an integrating sphere coated with poly(tetrafluoroethylene) (PTFE). The geometry used allowed the specular component of the reflected light to be excluded. The spectra were collected within the range 300–2000 nm with a spectral resolution of 1 nm.

XPS Analysis: Powder samples were investigated by XPS with a Perkin–Elmer Φ 5600ci instrument using standard Al-K_α radiation (1486.6 eV) operating at 350 W. The working pressure was

© 0000 Wiley-VCH Verlag GmbH & Co. KGaA, Weinheim

$<5 \times 10^{-8}$ Pa or ca. 10^{-11} Torr. The instrument was calibrated by reference to the binding energy (BE) of the Au $4f_{7/2}$ line at 83.9 eV with respect to the Fermi level. The standard deviation of the BE values was 0.15 eV. Reported BEs were corrected for charging effects, assigning the BE value of 284.6 eV to the C1s line of carbon.[78] Survey scans were obtained in the 0–1350 eV range (pass energy 187.5 eV, 1.0 eV/step, 25 ms/step). Detailed scans (pass energy 29.35 eV, 0.1 eV/step, 50–150 ms/step) were recorded for the O1s, C1s, Zn2p, ZnLMM, Ag3d, Co2p, Cu2p, Eu3d, Mg2p, Mn2p, and dopant Auger regions. The atomic compositions, after a Shirley-type background subtraction,[79] were evaluated by using sensitivity factors supplied by Perkin–Elmer.[59] Charge effects were partially compensated by using a charge neutralizer (flood gun). Peak assignments were carried out according to literature data.[59]

X-ray Diffraction: The XRD data were collected with a Bruker D8 Avance Diffractometer equipped with a Göbel mirror and by using Cu-K_α radiation. The angular accuracy was 0.001° and the angular resolution was better than 0.01°. All the experimental data were analyzed by using the Material Analysis Using Diffraction (MAUD) software package,[80] an original software used to deduce quantitative crystallographic and microstructural information[81] by using a Rietveld code.

TEM Analysis: TEM analysis was carried out by using a Philips CM12 microscope operating at 120 keV and equipped with an EDXS, which allows localized chemical analyses. For each sample, both TEM images and SAED patterns were collected as well as EDXS chemical analyses to determine the morphologies and dimensions of ZnO NPs, their crystalline nature, and local chemical compositions.

Luminescence Spectroscopy: Luminescence spectroscopy was performed with a tunable dye laser pumped by a Nd:YAG laser as the excitation source. The emission signal was analyzed by a half-meter monochromator (HR460, Jobin Yvon) equipped with a 150 lines/mm grating and detected with a CCD detector (Spectrum One, Jobin Yvon) or with a photomultiplier. The spectral resolution of the emission spectrum was about 0.4 nm. The emission decay curves were recorded upon pulsed laser excitation and detected with a GaAs photomultiplier (Hamamatsu) and a 500 MHz digital oscilloscope (WaveRunner, LeCroy).

ICP-AES Analysis: The metal composition of the samples was determined by using a Spectroflame Modula sequential and simultaneous ICP-AES spectrometer equipped with a capillary cross-flow nebulizer (Spectro Analytical, Kleve, Germany). Analytical determinations were performed by using a plasma power of 1.2 kW, a radiofrequency generator of 27.12 MHz, and an argon gas flow with nebulizer and a coolant set at 1, 0.5, and 14 L/min, respectively. The materials were mineralized by treating appropriate amounts of the samples (in the order of 50–100 mg) with a solution (2 mL) consisting of 54 vol-% HNO_3 (70%), 31 vol-% HCl (37%), and 15 vol-% H_2O. The solution obtained was diluted to 25 mL with 1% HCl.

Cytotoxicity LDH Test: An MRC5 human fibroblast suspension at a concentration of 2×10^4 cells/cm^2 was plated in 24-well plates and incubated in 5% CO_2 at 37 °C. The cells were cultured in RPMI-1640 (1.5 mL) with 10% inactivated fetal bovine serum, 2 mM L-glutamine, nonessential amino acids, 1 mM sodium pyruvate, and antibiotics for 72 h. Then the cells were incubated in the nanoparticle suspension in culture medium (1.5 mL) at a concentration of 30 or 100 µg/mL of the NPs. At the same time, a group of samples was exposed to nanoparticle extract (400 µL) in the culture medium (1.1 mL). Extracts were previously obtained by incubating nanoparticles in D-PBS at 37 °C at a concentration of 1 mg/mL for 72 h. Samples in fresh medium without nanoparticles or with D-PBS (400 µL) were used as negative controls. After 24 h of incubation, the LDH assay (Sigma kinetic method kit, St. Louis, MO, USA) was performed on the supernatants according to manufacturer's instructions. $N = 3$ samples per kind were analyzed and the Student *t*-test was used to evaluate the statistical significance of differences between the results.

Supporting Information (see footnote on the first page of this article): UV/Vis diffuse reflectance spectra, XPS spectra, and TEM micrographs.

Acknowledgments

The authors would like to thank Prof. Vito Di Noto and Dr. Roberta Saini, University of Padova, for ICP-AES and TGA measurements, respectively. Dr. Gloria Ischia, University of Trento, is acknowledged for TEM measurements.

---

[1] H. Morkoç, Ü. Özgür, *Zinc Oxide: Fundamentals, Materials and Device Technology*, Wiley-VCH, Weinheim, Germany, **2009**.
[2] Ü. Özgür, Y. I. Alivov, C. Liu, A. Teke, M. A. Reshchikov, S. Doan, V. Avrutin, S. Cho, H. Morko, *J. Appl. Phys.* **2005**, *98*, 1–103.
[3] C. Klingshirn, R. Hauschild, H. Priller, M. Decker, J. Zeller, H. Kalt, *Superlattices Microstruct.* **2005**, *38*, 209–222.
[4] C. Klingshirn, J. Fallert, H. Zhou, J. Sartor, C. Thiele, F. Maier-Flaig, D. Schneider, H. Kalt, *Phys. Status Solidi B* **2010**, *247*, 1424–1447.
[5] C. Klingshirn, *Phys. Status Solidi B* **2007**, *244*, 3027–3073.
[6] Y. Li, W. Xie, X. Hu, G. Shen, X. Zhou, Y. Xiang, X. Zhao, P. Fang, *Langmuir* **2010**, *26*, 591–597.
[7] N. Daneshvar, D. Salari, A. R. Khataee, *J. Photochem. Photobiol. A: Chem.* **2004**, *162*, 317–322.
[8] S. J. Pearton, F. Ren, Y. Wang, B. H. Chu, K. H. Chen, C. Y. Chang, W. Lim, J. Lin, D. P. Norton, *Prog. Mater. Sci.* **2010**, *55*, 1–59.
[9] Q. Zhang, C. S. Dandeneau, X. Zhou, G. Cao, *Adv. Mater.* **2009**, *21*, 4087–4108.
[10] C. Chien, S. H. Chiou, G. Y. Guo, Y. Yao, *J. Magn. Magn. Mater.* **2004**, *282*, 275–278.
[11] R. Janisch, P. Gopal, N. A. Spaldin, *J. Phys. Condens. Matter* **2005**, *17*, R657.
[12] S. J. Pearton, W. H. Heo, M. Ivill, D. P. Norton, T. Steiner, *Semicond. Sci. Technol.* **2004**, *19*, R59.
[13] W. Prellier, A. Fouchet, B. Mercey, *J. Phys. Condens. Matter* **2003**, *15*, R1583.
[14] S. Ram, *Curr. Opin. Solid State Mater. Sci.* **2005**, *9*, 1–7.
[15] S. Han, T. Jang, Y. B. Kim, B. Park, J. Park, Y. H. Jeong, *Appl. Phys. Lett.* **2003**, *83*, 920–922.
[16] S. K. Mandal, A. K. Das, T. K. Nath, D. Karmakar, B. Satpati, *J. Appl. Phys.* **2006**, *100*, 104315.
[17] K. Ando, H. Saito, Z. Jin, T. Fukumura, M. Kawasaki, Y. Matsumoto, H. Koinuma, *J. Appl. Phys.* **2001**, *89*, 7284–7286.
[18] K. Ueda, H. Tabata, T. Kawai, *Appl. Phys. Lett.* **2001**, *79*, 988–990.
[19] J. H. Yang, Y. Cheng, Y. Liu, X. Ding, Y. X. Wang, Y. J. Zhang, H. L. Liu, *Solid State Commun.* **2009**, *149*, 1164–1167.
[20] H. Jiang, H. Wang, X. Wang, *Appl. Surf. Sci.* **2011**, *257*, 6991–6995.
[21] A. V. Kachynski, A. N. Kuzmin, M. Nyk, I. Roy, P. N. Prasad, *J. Phys. Chem. C* **2008**, *112*, 10721–10724.
[22] Y. L. Wu, C. S. Lim, S. Fu, A. I. Y. Tok, H. M. Lau, F. Y. C. Boey, X. T. Zeng, *Nanotechnology* **2007**, *18*.
[23] L. Armelao, G. Bottaro, M. Pascolini, M. Sessolo, E. Tondello, M. Bettinelli, A. Speghini, *J. Phys. Chem. C* **2008**, *112*, 4049–4054.

[24] B. Weintraub, Z. Zhou, Y. Li, Y. Deng, *Nanoscale* **2010**, *2*, 1573–1587.
[25] Y. Masuda, N. Kinoshita, F. Sato, K. Koumoto, *Cryst. Growth Des.* **2006**, *6*, 75–78.
[26] Y. Masuda, K. Kato, *Cryst. Growth Des.* **2008**, *8*, 275–279.
[27] Y. Masuda, K. Kato, *Cryst. Growth Des.* **2008**, *8*, 2633–2637.
[28] Y. Masuda, K. Kato, *Cryst. Growth Des.* **2009**, *9*, 3083–3088.
[29] A. Famengo, S. Anantharaman, G. Ischia, V. Causin, M. M. Natile, C. Maccato, E. Tondello, H. Bertagnolli, S. Gross, *Eur. J. Inorg. Chem.* **2009**, 5017–5028.
[30] S. Hingorani, V. Pillai, P. Kumar, M. S. Multani, D. O. Shah, *Mater. Res. Bull.* **1993**, *28*, 1303–1310.
[31] X. Sui, Y. Liu, C. Shao, Y. Liu, C. Xu, *Chem. Phys. Lett.* **2006**, *424*, 340–344.
[32] J. Xu, Q. Pan, Y. Shun, Z. Tian, *Sensor Actuators, B - Chem.* **2000**, *66*, 277–279.
[33] L. M. Gan, L. H. Zhang, H. S. O. Chan, C. H. Chew, B. H. Loo, *J. Mater. Sci.* **1996**, *31*, 1071–1079.
[34] M. Lee, S. Oh, S. Yi, *J. Colloid Interface Sci.* **2000**, *226*, 65–70.
[35] J. A. Lopez Perez, M. A. Lopez Quintela, J. Mira, J. Rivas, S. W. Charles, *J. Phys. Chem. B* **1997**, *101*, 8045–8047.
[36] T. Masui, K. Fujiwara, K. Machida, G. Adachi, T. Sakata, H. Mori, *Chem. Mater.* **1997**, *9*, 2197–2204.
[37] T. Masui, K. Fujiwara, Y. Peng, T. Sakata, K. Machida, H. Mori, G. Adachi, *J. Alloys Compd.* **1998**, *269*, 116–122.
[38] Y. Pang, X. Bao, *J. Mater. Chem.* **2002**, *12*, 3699–3704.
[39] K. Landfester, *Adv. Mater.* **2001**, *13*, 765–768.
[40] M. Antonietti, K. Landfester, *Prog. Polym. Sci.* **2002**, *27*, 689–757.
[41] K. Landfester, *Macromol. Rapid Commun.* **2001**, *22*, 896–936.
[42] K. Landfester, *Ann. Rev. Mater. Res.* **2006**, *36*, 231–279.
[43] N. Bechthold, F. Tiarks, M. Willert, K. Landfester, M. Antonietti, *Macromol. Symp.* **2000**, *151*, 549–555.
[44] K. Landfester, N. Bechthold, F. Tiarks, M. Antonietti, *Macromolecules* **1999**, *32*, 5222–5228.
[45] K. Landfester, *Eur. Coat. J.* **2005**, 20–25.
[46] A. Taden, M. Antonietti, A. Heilig, K. Landfester, *Chem. Mater.* **2004**, *16*, 5081–5087.
[47] M. Willert, R. Rothe, K. Landfester, M. Antonietti, *Chem. Mater.* **2001**, *13*, 4681–4685.
[48] R. Rossmanith, C. K. Weiss, J. Geserick, N. Hüsing, U. Hörmann, U. Kaiser, K. Landfester, *Chem. Mater.* **2008**, *20*, 5768–5780.
[49] R. Schiller, C. K. Weiss, J. Geserick, N. Hüsing, K. Landfester, *Chem. Mater.* **2009**, *21*, 5088–5098.
[50] P. Dolcet, M. Casarin, C. Maccato, L. Bovo, G. Ischia, S. Gialanella, F. Mancin, E. Tondello, S. Gross, *J. Mater. Chem.* **2012**, *22*, 1620–1626.
[51] X. Han, R. Gelein, N. Corson, P. Wade-Mercer, J. Jiang, P. Biswas, J. N. Finkelstein, A. Elder, G. Oberdörster, *Toxicology* **2011**, *287*, 99–104.
[52] Y. Liu, K. Ai, Q. Yuan, L. Lu, *Biomaterials* **2011**, *32*, 1185–1192.
[53] A. B. Djurišić, Y. H. Leung, *Small* **2006**, *2*, 944–961.
[54] A. Hilger, M. Tenfelde, U. Kreibig, *Appl. Phys. B* **2001**, *73*, 361–372.
[55] U. Kreibig, M. Vollmer, *Optical properties of metal clusters*, Springer, Heidelberg, Germany, **1995**.
[56] R. Fricke, K. Meyring, *Z. Anorg. Allg. Chem.* **1937**, *230*, 366–374.
[57] S. Yamabi, H. Imai, *J. Mater. Chem.* **2002**, *12*, 3773.
[58] P. Louette, F. Bodino, J. Pireaux, *Surf. Sci. Spectra* **2005**, *12*, 59–63.
[59] J. F. Moulder, W. F. Stickle, P. E. Sobol, K. D. Bomben, *Handbook of X-ray photoelectron spectroscopy: a reference book of standard spectra for identification and interpretation of XPS data*, Physical Electronics Division, Perkin–Elmer Corp, Eden Prairie, MN, **1992**.
[60] M. Casarin, T. Devic, A. Famengo, D. Forrer, S. Gross, E. Tondello, A. Vittadini, *Inorg. Chem.* **2010**, *49*, 4099.
[61] C. D. Wagner, *Anal. Chem.* **1975**, *47*, 1201–1203.
[62] X. Feng, *J. Phys. Condens. Matter* **2004**, *16*, 4251–4259.
[63] P. T. Hsieh, Y. C. Chen, K. S. Kao, C. M. Wang, *Appl. Phys. A* **2008**, *90*, 317–321.
[64] Y. Zheng, C. Chen, Y. Zhan, X. Lin, Q. Zheng, K. Wei, J. Zhu, *J. Phys. Chem. C* **2008**, *112*, 10773–10777.
[65] Y. Zheng, L. Zheng, Y. Zhan, X. Lin, Q. Zheng, K. Wei, *Inorg. Chem.* **2007**, *46*, 6980–6986.
[66] T. Alammar, A. Mudring, *J. Mater. Sci.* **2009**, *44*, 3218–3222.
[67] L. Armelao, D. Barreca, M. Bertapelle, G. Bottaro, C. Sada, E. Tondello, *Thin Solid Films* **2003**, *442*, 48–52.
[68] S. Poulston, P. M. Parlett, P. Stone, M. Bowker, *Surf. Interface Anal.* **1996**, *24*, 811–820.
[69] F. Mercier, C. Alliot, L. Bion, N. Thromat, P. Toulhoat, *J. Electron Spectrosc. Relat. Phenom.* **2006**, *150*, 21–26.
[70] P. V. Radovanovic, D. R. Gamelin, *J. Am. Chem. Soc.* **2001**, *123*, 12207–12214.
[71] N. El Habra, L. Crociani, C. Sada, P. Zanella, M. Casarin, G. Rossetto, G. Carta, G. Paolucci, *Chem. Mater.* **2007**, *19*, 3381–3386.
[72] D. Dell′Amico Belli, H. Bertagnolli, F. Calderazzo, M. D′Arienzo, S. Gross, L. Labella, M. Rancan, R. Scotti, B. M. Smarsly, R. Supplit, E. Tondello, E. Wendel, *Chem. Eur. J.* **2009**, *15*, 4931–4943.
[73] M. Yang, J. He, *J. Colloid Interface Sci.* **2011**, *355*, 15–22.
[74] Y. Zheng, C. Chen, Y. Zhan, X. Lin, Q. Zheng, K. Wei, J. Zhu, *J. Phys. Chem. C* **2008**, *112*, 10773–10777.
[75] R. Peacock, *The Intensities of Lanthanide f-f Transitions*, in: *Structure and Bonding*, vol. 22, Springer, Heidelberg, pp. 83–122.
[76] E. Nakazawa, *Fundamentals of Luminescence*, in: *Phosphors Handbook* (Eds.: W. M. Yen, S. Shionoya), CRC Press, Boca Raton, FL, **1999**, p. 102.
[77] Y. Liu, W. Luo, R. Li, G. Liu, M. R. Antonio, X. Chen, *J. Phys. Chem. C* **2008**, *112*, 686–694.
[78] D. Briggs, M. P. Seah, *Practical Surface Analysis: Auger and X-ray photoelectron spectroscopy*, Wiley, New York, **1990**.
[79] D. A. Shirley, *Phys. Rev. B* **1972**, *5*, 4709.
[80] L. Lutterotti, S. Matthies, H.-R. Wenk, A. S. Schultz, J. J. W. Richardson, *J. Appl. Phys.* **1997**, *81*, 594–600.
[81] I. Lonardelli, H. R. Wenk, L. Lutterotti, M. Goodwin, *J. Synchrotron Radiat.* **2005**, *12*, 354–360.

Received: December 6, 2012
Published Online: ■

Submitted to J. Mater. Chem. B

Dynamic Article Links ►

Cite this: DOI: 10.1039/c0xx00000x

www.rsc.org/xxxxxx

ARTICLE TYPE

Simple, Common but Functional: Biocompatible and Luminescent Rare-Earth Doped Magnesium and Calcium Hydroxides from Miniemulsion

Erika Butturini[a,b], Paolo Dolcet[a], Maurizio Casarin[a], Adolfo Speghini[c], Marco Pedroni[c], Cristina Foss[d], Antonella Motta[d], Denis Badocco[a], Paolo Pastore[a], Stefano Diodati[a,b], Luciano Pandolfo[a] and Silvia Gross[a,b*]

Received (in XXX, XXX) Xth XXXXXXXXX 20XX, Accepted Xth XXXXXXXXX 20XX
DOI: 10.1039/b000000x

Nanostructured (d ~ 20-35 nm) and highly luminescent Ca(OH)2:Ln and Mg(OH)2:Ln (Ln = Eu(III), Sm(III), Tb(III), Mg(Ca)/Ln = 20:1) nanostructures were obtained in inverse (water in oil - w/o) miniemulsion (ME), by exploiting the nanosized compartments of the droplets to spatially confine the hydroxides precipitation in basic environment (NaOH). The functional nanostructures were prepared by using different surfactants (Span80 (span) and a mixture of Igepal co-630 and Brij52 (mix)) to optimise the ME stability and hydroxides' biocompatibility as well as to tune the droplets sizes. X-ray Diffraction (XRD) analyses testify the achievement of pure brucite-$Mg(OH)_2$-phase and pure portlandite- $Ca(OH)_2$-phase with a high degree of crystallinity. Besides structural characterisations, the products were thoroughly characterised by means of several and complementary techniques (Dynamic Light Scattering (DLS), X-ray Photoelectron Spectroscopy (XPS), Thermogravimetric Analysis (TGA) and Differential Scanning Calorimetry (DSC), Micro-Raman spectroscopy, Inductively Coupled Plasma Mass Spectrometry (ICP-MS) and Fourier Transform Infrared spectroscopy (FT-IR)) to assess their chemico-physical properties and microstructural features. The stoichiometry of the doped systems was confirmed by ICP-MS measurements. Finally, in-vitro cytotoxicity and viability tests were carried out and the biocompatibility of the doped hydroxides was proved. As far as the luminescence properties are concerned, the Eu-doped and Tb-doped materials show a strong luminescence around 620 nm and 540 nm respectively, further strengthen their possible use as biocompatible materials for bioimaging.

Introduction

In the last years, bioimaging and drug delivery based on nanostructures (i.e. nanoparticles, vesicles, dendrimers, etc) have gained an impressing interest, as witnessed by several studies and patents.[1-4] As a matter of fact, if these nanostructures are suitably functionalised with fluorescent organic dyes or doped with luminescent ions, they can be used for molecular bioimaging. For instance, polymeric NPs functionalised with organic dyes find several applications in targeting and imaging in living cells.[5] As inorganic alternative to organic fluorophores, quantum dots (QDs), semiconductor and metal NPs have also been intensively studied for these applications.[6] Although QDs display good luminescent properties and a greater chemical and photochemical stability compared with organic dyes, they are usually based on toxic metals (i.e. Cd, Pb) which strongly decrease their biocompatibility and limit their possible use in nanomedicine.[7] As far as metal NPs, such as for instance Au NPs, are concerned, their optical and magnetic properties make them suitable for imaging, targeting and photothermal therapy but cytotoxicity is still topic of debate.[8-10]

At variance to the just mentioned NPs, those based on Mg and Ca oxide, hydroxide, phosphate and carbonate are particularly appealing for their higher biocompatibility and stability in cellular environment.[11-14] Furthermore, due to the chemical nature of their surface, they can be easily functionalised with molecules endowing them with lock-and-key binding specificity and they can be easily doped with lanthanides (Ln) ions which confer them luminescent properties.[15-17] As far as calcium and magnesium hydroxides are concerned, they are currently extensively used in biomedical applications: magnesium hydroxide is used for instance as antacid in stomach diseases, calcium hydroxide for

---

[a] *Dipartimento di Scienze Chimiche, Università degli Studi di Padova, via Marzolo, 1, I-35131, Padova, Italy*
E-mail: silvia.gross@unipd.it
[b] *Istituto per l'Energetica e le Interfasi, IENI-CNR and INSTM, UdR, via Marzolo, 1, I-35131, Padova, Italy*
[c] *Dipartimento di Biotecnologie, Università degli Studi di Verona, Strada Le Grazie 15, 37314 Verona, Italy and INSTM, UdR Verona*
[d] *University of Trento, Department of Industrial Engineering and BIOtech Research Center, Trento, Italy; European Institute of Excellence on Tissue Engineering and Regenerative Medicine, Trento, Italy*

† Electronic Supplementary Information (ESI) available: Figures E.S.I. 1-4. See DOI: 10.1039/b000000x/

endodontic therapy.[18, 19] Despite these features make Ln-doped Mg and Ca hydroxides potential candidates for application as contrast agents for bioimaging, they have not yet been used, to the best of our knowledge, for this purpose. In the literature, only reports on luminescent layered double hydroxide[20] and on rare-earth doped or rare-earth based nanoparticles[21] are extensively reported, but no study on rare-earth doped magnesium and calcium hydroxide has been reported yet. These hydroxide systems can be addressed either by solid state or by wet chemistry approaches. Among the latter, the MEs one is particularly appealing being an easy, fast, reproducible and cost effective method. Particularly, it is mostly exploited for the syntheses of polymeric[22-24] and hybrid NPs, whereas it was less intensively used for crystallisation of inorganic systems.[25-28] Nevertheless, it has recently been assessed the effectiveness of the inverse ME for the synthesis of different inorganic systems, ranging from pure and doped ZnO,[29, 30] to iron oxide, calcium carbonate, zirconium dioxide,[31] lanthanides oxides,[32] titania,[33] silica, ceria,[27] hydrous zirconia and hafnia.[34, 35] In this regard, it is noteworthy that Muñoz-Espì et al. have recently described progresses in the achievements of crystalline inorganic nanostructures by ME without the need of any subsequent thermal treatment.[28] ME droplets act as nanoreactors, thus enabling to perform the desired precipitation in a confined space, with a good control over the material final size and crystallinity. Furthermore, MEs allow an easy route to functionalise the surface of the NPs by ligand exchange methods or post-reaction functionalisation for nanomedicine applications. Incidentally, MEs, or nanoemulsions, have already been investigated for human trial of intranasal vaccines, confirming the possibility of application of NPs and MEs in nanomedicine.[36]

In this study we addressed the controlled growth of lanthanide-doped $Mg(OH)_2$ and $Ca(OH)_2$ NPs to be used as luminescent contrast agent in bioimaging applications.

More specifically, we optimised a fast, easy, low temperature and cost effective method for the ME based synthesis of pure and doped magnesium and calcium hydroxides in a confined space. Furthermore, the synthesis was complemented by a thorough chemico-physical characterisation of the products, as well as by a functional assessments in terms i) of optical properties of the doped nanostructures and ii) of the evaluation of the cytotoxic behaviour in view of the application of these NPs as contrast agents for both in-vitro and in-vivo bioimaging.

Experimental Section

Chemicals

Magnesium nitrate hexahydrate ($Mg(NO_3)_2 \cdot 6H_2O$), europium (III) nitrate pentahydrate ($Eu(NO_3)_3 \cdot 5H_2O$), terbium (III) nitrate hexahydrate ($Tb(NO_3)_3 \cdot 5H_2O$), sodium hydroxide (NaOH), Igepal co-630 ($(C_2H_4O)_n \cdot C_{15}H_{24}O$, n=9-10), Brij 52 ($C_{16}H_{33}(OCH_2CH_2)_nOH$, n~2), Span 80 ($C_{24}H_{44}O_6$) and cyclohexane ($C_6H_{12}$) were purchased from Aldrich, Milan, Italy. Samarium (III) acetate hydrate ($C_6H_9O_6Sm \cdot H_2O$) was obtained from Strem chemicals, Newburyport, Massachusetts. Calcium nitrate tetrahydrate ($Ca(NO_3)_2 \cdot 4H_2O$) was purchased from Carlo Erba Reagenti, Milan, Italy. All chemicals were used without further purification.

Nanoparticles synthesis

$Mg(OH)_2$ nanoparticles (NPs) were synthesised by miniemulsion (ME) technique using two different surfactant systems (Span 80 (span) and a mixture of Brij52:Igepal co-630 (mix), weight ratio 3:1 (3:1 mix)), whereas $Ca(OH)_2$ NPs were obtained only with the mixture of Brij52:Igepal co-630 3:1.

For NPs synthesised by using the mix, two identical suspensions were prepared by dispersing the surfactant mixture (0.8 g) in cyclohexane (8 g). Then an aqueous 0.5 M solution of $Mg(NO_3)_2 \cdot 6H_2O$ (3 mL, 1.5 mmol) were added to mixture A and an aqueous 1 M solution of NaOH (3 mL, 3 mmol) to mixture B, to get a Mg:NaOH molar ratio of 1:2. Both emulsions were then separately sonicated for 3 minutes, by using a Sartorious Stedim LabsonicP homogeniser, mounting a 3 mm titanium tip and operating at amplitude of 70%, corresponding to an acoustic power of 322 Wcm^{-2}, giving MEs A' and B', respectively. These MEs were then mixed, stirred and sonicated again for 3' thus yielding ME C. The same method was used for the synthesis of $Ca(OH)_2$ NPs. A schematic representation of the synthesis procedure is reported in **Scheme 1**.

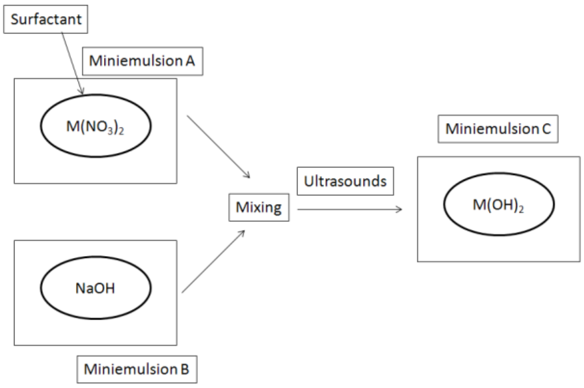

Scheme 1 Schematic representation of the synthesis procedure

The procedure for synthesising NPs with Span 80 was the same, although different concentrations, due to the different HLB value of the surfactant, were used. Indeed MEs A and B were prepared by dispersing Span 80 (0.75 g) in cyclohexane (24 g). Then, an aqueous solution of $Mg(NO_3)_2 \cdot 6H_2O$ 0.5 M (6 ml, 3 mmol) and an aqueous solution of NaOH 1 M (6 ml 6 mmol) (molar ratio Mg:OH 1:2) were added to ME A and ME B, respectively, using the amount of substances reported by Landfester et al.[37] Subsequently the two MEs were mixed, stirred and sonicated for 3'as in the previous case. In both cases ME C were allowed to stand overnight. The white precipitate formed was separated by centrifugation (10000 rpm for 10 minutes) and washed 3 times with deionised water and, in the case of Span 80 ME, also with ethanol. For the preparation of lanthanides doped $Mg(OH)_2$ and $Ca(OH)_2$, an appropriate amount of Eu(III), Sm(III) or Tb (III) was added at mixture A to achieve the atomic ratios Mg/Ca:M (M=Eu, Sm, Tb) of 20:1 and then the procedure described above was carried out.

Characterisation methods

DLS analysis

DLS analyses on the as-prepared suspensions were carried out using a Malvern Zetasizer Nano S, at a temperature of 20 °C.

This journal is © The Royal Society of Chemistry [year]

FT-IR analysis

FT-IR and FT-IR/ATR experiments were performed with a NEXUS 870 FT-IR (NICOLET), operating in the transmission range 4000-400 cm^{-1}, collecting 64 scans with a spectral resolution of 4 cm^{-1}. The measurements were recorded by dispersing the powders in anhydrous KBr.

Thermogravimetric analysis:

The thermogravimetric analyses (TGA) were performed in air on a LabSys Setarm SDT 2960 instrument in the temperature range 20-800 ° C using a heating rate of 10° C min^{-1}.

Raman analysis

Raman experiments were performed with a Thermo Scientific DXR Raman microscope operating in the range 100-6000 cm^{-1}, with a solid state laser of wavelength of 532 nm^{-1} and a 10x objective. All spectra were normalised to 1 before plotting them.

XPS analysis

The powders were investigated by XPS with a Perkin-Elmer Φ 5600ci instrument using standard Al-K_α radiation (1486.6 eV) operating at 350 W. The working pressure was $< 5\cdot10^{-8}$ Pa $\sim10^{-11}$ torr. The calibration was based on the binding energy (BE) of the $Au4f_{7/2}$ line at 83.9 eV with respect to the Fermi level. The standard deviation for the BE values was 0.15 eV. The reported BE's were corrected for the BE's charging effects, assigning the BE value of 284.6 eV to the C1s line of carbon.[38] Survey scans were obtained in the 0 - 1350 eV range (pass energy 187.5 eV, 1.0 eV/step, 25 ms/step). Detailed scans (29.35 eV pass energy, 0.1 eV/step, 50-150 ms/step) were recorded for the O1s, C1s, Mg2s, Mg1s, Mg 2p, Mg KLL, Ca2p, Ca2s, Eu3d, Sm3d, Sm4d, Tb3d and 4d regions. The atomic composition, after a Shirley-type[39] background subtraction was evaluated using sensitivity factors supplied by Perkin-Elmer.[40] Charge effects were partially compensated by using a charge neutraliser (flood gun). Peak assignment was carried out according to literature data.

X-Ray diffraction

XRD data was collected with a Bruker D8 Advance diffractometer equipped with a Göbel mirror and employing the CuK_α (λ = 0.15405 nm) radiation. The angular accuracy was 0.001° and the angular resolution was better than 0.01°. All patterns were recorded in the range 10-80° with a scan step of 0.03 (2θ) and a 7 secs/step acquisition interval.

ICP-MS Chemicals and procedure: All reagents were of analytical grade and were used as purchased: HNO_3 (CAS Number 7697-37-2) 70%, purified by redistillation, ≥99.999% (Sigma Aldrich), $HClO_4$ 70% RP Normapur (Prolabo, France). Ca (1000 mg/l) and Mg (10 mg/l) were present in the multi-element standard Solution CPAchem ICP-MS Calibration Standard Ref N: MS19EB.10.2N.L1. Eu, Sm and Tb (all 1 mg/l) were present in the ICP-MS Calibration Standard Ref N: MS98B2.1.2N.L1. All solutions were prepared in milliQ ultrapure water obtained with a Millipore Plus System (Milan, Italy, resistivity 18.2 Mohm cm^{-1}). The ICP-MS was tuned daily using a 1 μg/l tuning solution containing ^{140}Ce, ^{7}Li, ^{205}Tl and ^{89}Y (Agilent Technologies, UK). A 100 μg/l solution of ^{45}Sc and ^{115}In (Aristar®, BDH, UK) prepared in 2% (v/v) nitric acid was used as an internal standard through addition to the sample solution via a T-junction.

Solution setup for ICP-MS

Multielement standard solutions were prepared in 2% v/v HNO_3. The calibration solutions were prepared by gravimetric serial dilution from multi-element standard solutions, at six different concentrations (min. 10 ppb–max. 1000 ppb). Calibration plots were obtained with an internal standard. In particular, Ca and Mg refer to the ^{45}Sc internal standard; Eu, Sm and Tb refer to the ^{115}In internal standard. All regressions were linear with a determination coefficient larger than 0.9999. To check for instrumental drift, one of the multi-element standards was analyzed every 10 samples. The internal standard concentration of both In and Sc was 100 ppb in all samples and blanks. Blank samples of ultrapure water and reagents were also prepared using the same procedures as for the samples. All blank levels obtained were subtracted appropriately.

NPs digestion for ICP-MS

NPs doped samples (50 mg) were placed in a 25 ml digestion vials and added with 3 ml of 70% HNO_3 and 3 ml 60% $HClO_4$. Vials were heated on a hot plate at 200 ± 10 °C for 150 min. A PTFE cap was used to minimise sample loss from the vial. Vials were then cooled and the obtained solution was diluted with 2% v/v HNO_3.

All the elements were measured by using inductively coupled plasma coupled to a mass spectrometer (ICP-MS) Agilent Technologies 7700x ICP-MS system (Agilent Technologies International Japan, Ltd., Tokyo, Japan), equipped with an octupole collision cell operated in kinetic energy discrimination mode. The instrument was optimised daily to achieve optimum sensitivity and stability according to manufacturer recommendations. Typical operating conditions and data acquisition parameters are summarised in **Table 1**. All parameters were checked daily using an in-house optimisation program.

Table 1 Instrumental operation conditions for ICP-MS

Instrumental	Agilent 7700x ICP-MS
RF power	1550 W
RF matching	1.8 V
Plasma gas flow rate	15 l min−1 Ar
Auxiliary gas flow rate	1.0 l min−1 Ar
Carrier gas flow rate	1.05 l min−1 Ar
Make-up gas flow rate	0.0 l min−1 Ar
He gas flow	4.3 ml/min
CeO+/Ce+	0.902%
Ratio(2+) 70/140	0.944%
Nebulizer	Microflow PFA nebulizer
Spray chamber	Scott double-pass type at 2 °C
Torch	Quartz glass torch
Sample uptake rate	0.1 ml min−1
Sample cone Nickel	1.0 mm aperture i.d.
Skimmer cone Nickel	0.5 mm aperture i.d.
Sampling depth	8.5 mm
Detector mode	Dual (pulse and analog counting)
Dwell time/mass	100 ms
Scan type	Peak hopping, three sweeps per reading and three reading per replicate

Photoluminescence measurements

Luminescence measurements were performed using a tunable dye laser pumped by a Nd:YAG laser as the excitation source. The emission signal was analyzed by a half-meter monochromator (HR460, Jobin Yvon) equipped with a 150 or 1200 lines/mm grating and detected with a CCD detector (Spectrum One, Jobin Yvon) or with a photomultiplier. The spectral resolution of the emission spectrum is about 0.2 nm. The emission decay curves were recorded upon pulsed laser excitation and detected with a GaAs photomultiplier (Hamamatsu) and a 500 MHz digital oscilloscope (WaveRunner, LeCroy).

Viability and Cytotoxicity LDH tests

Cell culture

Human ovarian carcinoma cells ES2 were cultured in T75 flasks until confluence in RPMI-1860 (Euroclone, Italy) supplemented with 10% inactivated fetal bovine serum, 2 mM L-Glutamine and penicillin-streptomycin (Invitrogen, US). Then, cells were trypsinised and seeded in 48-well plates at a density of $2\cdot10^4$ cells/cm^2 in 1 ml of medium. 24 hours after seeding, cells started to be cultured in full medium with Ca_mix or Mg_mix NPs, Mg_span, or Mg_Eu_mix and Mg_Sm_mix NPs. Two concentrations were chosen to evaluate the influence of each NP on cell behaviour: 100 µg/ml (high concentration) and 30 µg/ml (low concentration). As a negative control for the following tests, a group of samples were kept in NP-free medium.

Before use, NPs were incubated in ethanol 70% (Roth, Germany) overnight at 4°C. Subsequently, after a centrifugation for 5 minutes at 3000 rpm, NP were resuspended in sterile distilled water and centrifuged again three times to completely remove the ethanol. After the last centrifugation, NPs were dispersed in full media at the appropriate concentrations.

AlamarBlue assay

Cell viability was evaluated after 2, 24 and 48 hours of incubation in medium with NPs. To this purpose, AlamarBlue assay (Invitrogen, US) was performed according to manufacturer's instructions. Briefly, culture medium (with or without NP) was removed from samples and substituted with 1 ml of full medium with 10% v/v of AlamarBlue solution. Cells were incubated at 37°C for 3 hours and subsequently, 100 µl of the supernatant were transferred in a black 96-well plate. The amount of AlamarBlue reduced by viable cells was assessed measuring the corresponding fluorescence signal (excitation wavelength: 565 nm; emission wavelength: 595 nm) with a micro plate reader (Tecan Infinite M200 Pro). 10% v/v AlamarBlue solution was also incubated as a control and its fluorescence was subtracted from those of samples.

Lactate dehydrogenase assay

Cytotoxicity of $Ca(OH)_2$ and $Mg(OH)_2$ NPs at high and low concentration was evaluated after 24 hours of incubation. A lactate dehydrogenase-based (LDH) assay was used (*in vitro* toxicology assay kit, Sigma-Aldrich, US) following the provided instructions. In short, LDH enzymes are released by cells into the external environment when the cellular membrane is damaged. Therefore, the activity of LDH in the culture medium is a measure of cell necrosis and/or apoptosis and can be evaluated by means of a colorimetric reaction involving the reduction of NAD and the subsequent conversion of a tetrazolium salt into a colored compound. The amount of this product after the enzymatic reaction in the sample culture media was assessed measuring the absorbance of the supernatant at 490 nm, using the absorbance at 690 nm as a reference to normalise the measurements.

Statistical analysis

Each test was performed on N = 3 independent determinations per data point. Results are presented as mean ± standard error and were subjected to one-way or two-way ANOVA with Tukey post-test. Before applying the tests, the equality of variances was verified. All statistical analyses were performed using GraphPad Prism 4.0 (GraphPad software, US). Significance was assigned at p-values less than 0.05.

Results and discussion

i)

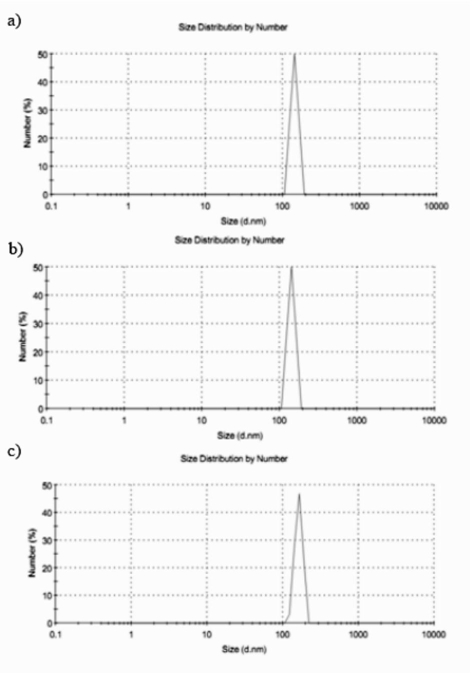

ii)

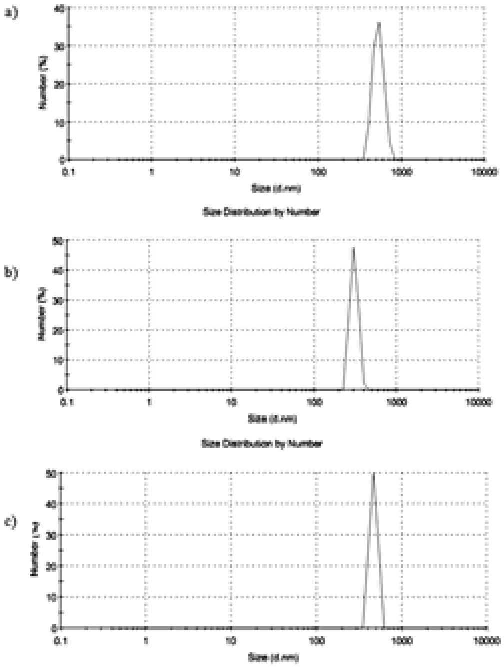

Fig. 1 i) DLS results for Mg_span NPs. Average hydrodynamic diameter: a) 162 nm, b) 142 nm, c) 142 nm ii) DLS results for Mg_mix NPs. Average hydrodynamic diameter: a) 520, b) 300, c) 460 nm

As extensively described in the Experimental Section, the final ME was achieved by sonication of the two precursors MEs (one containing metal salt and the other NaOH), thus affording the precipitation of the hydroxides in the nanodroplets produced by ultrasound shear forces. Immediately after the sonication, the average hydrodynamic diameter of w/o droplets was investigated by Dynamic Light Scattering (DLS). In the case of MEs prepared with Span 80, the average hydrodynamic diameter always resulted to be ~130 nm (Figure 1. a), with a good reproducibility. Analogous results were found for lanthanide doped NPs. At variance, the average hydrodynamic diameter of both MEs prepared with the mix for $Mg(OH)_2$ (Mg_mix) and $Ca(OH)_2$ (Ca_mix) NPs, was not completely reproducible (Figure 1. b). A tentative explanation of such a finding could be the different distribution in suspension of Igepal CO-630 and Brij 52 which thus generate a polydispersed suspension.

Once separated the powder from the suspension, the crystallographic structure and the average NPs' crystallite size were obtained by XRD analyses (see **Figure 2** and **Table 2**).

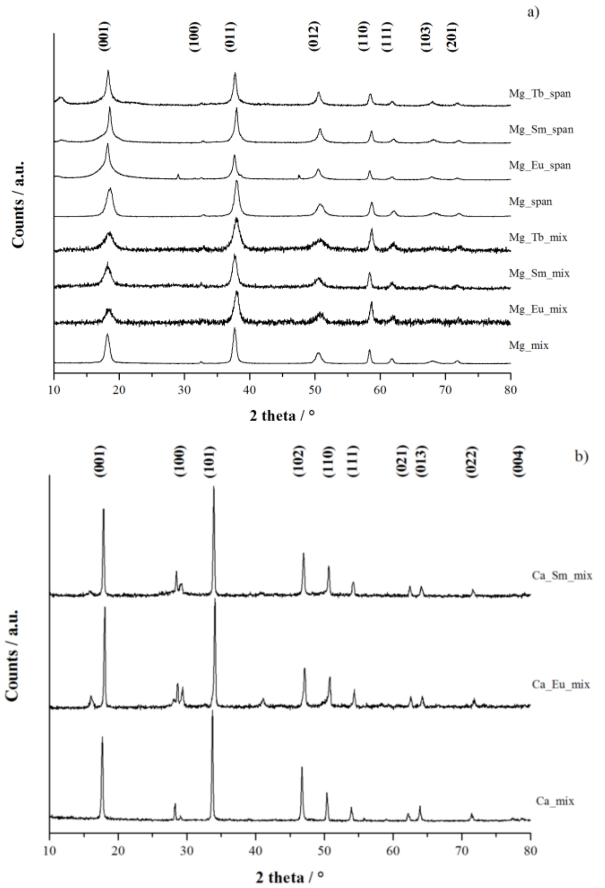

Fig. 2 XRD diffractograms of pure and doped $Mg(OH)_2$ (a)and $Ca(OH)_2$ (b)

Independently from the used surfactant, the crystallographic structure of $Mg(OH)_2$, both pure and doped, was *brucite* (Powder Diffraction File, PDF: 01-083-0114) while the crystallite size, calculated with the Scherrer equation,[41] was for both class of systems ~20 nm. In $Ca(OH)_2$ NPs, characterised by the *portlandite* structure (PDF: 00-001-1079), the average size, for both pure and doped NPs, was about 35 nm. Calcium hydroxide X-ray powder patterns of both pure as well as doped systems and those of doped Mg_span are characterised by the presence of further phases. These phases are due to the formation of crystalline $Eu(OH)_3$ (PDF: 01-083-2305) in Mg_Eu_mix NPs, $Sm(OH)_3$ (PDF: 01-083-2036) in Sm doped Ca_Sm_span and Mg_Sm_span and finally $Tb(OH)_3$ (PDF: 01-083-2038) and Tb_5O_9 (PDF: 00-048-1601) in Mg_Tb_span and Mg_Tb_mix NPs respectively. The XRD reported results prove the effective formation of a crystalline phase even at room temperature (RT) and without the need of subsequent thermal treatments. Furthermore, these results are consistent with a good reproducibility of the crystalline phase and of the average crystallite dimensions.

Table 2a Crystallographic data of brucite $Mg(OH)_2$ and $Ca(OH)_2$ hexagonal P-3m1

	$Mg(OH)_2$	**$Ca(OH)_2$**
Lattice parameters (PDF) [Å]	a=b=3.1477, c=4.7717	a=b=3.5890, c=4.9110
Volume (CD) (PDF) [Å^3]	40.94	54.78
Ionic radius (Mg^{2+}/Ca^{2+}) [pm]$^{a)}$	72	100

Table 2b Average crystallite size of brucite $Mg(OH)_2$ and $Ca(OH)_2$

Sample	Scherrer [nm]	Crystallographic phase
Ca_mix	40	Portlandite
Ca_Eu_mix	36	Portlandite
Ca_Sm_mix	38	Portlandite
Mg_mix	15	Brucite
Mg_Eu_mix	12	Brucite
Mg_Sm_mix	11	Brucite
Mg_ mix	8	Brucite
Mg_span	11	Brucite
Mg_Eu_span	20	Brucite
Mg_Sm_span	21	Brucite
Mg_Tb_span 80	12	Brucite

Since it is the surface of these systems which is expected to interact with the cellular environment in biological applications, the surface composition and the oxidation state of surface species were investigated by means of XPS measurements. In **Figure 3**, the survey spectra of Mg_Sm_mix and Ca_Sm_mix are displayed. Detailed scans were recorded for the regions of interest, as reported in the Experimental Section, to obtain more accurate binding energy (BE) values and to perform the quantitative analysis (see **Table 3**).

Table 3 XPS BE values and quantitative data. Values of BE were corrected considering charging effects

BE [eV]	**C1s**	**O1s**	**Mg 2p/Ca2 p$_{3/2}$**	**Dopant**	**% C**	**% O**	**% Mg/ Ca**	**% Sm**
Mg_Sm _mix	284.6 285.5 286.3	530.3	49.7	Sm3 d$_{5//2}$ 1083.2	56.3	31.6	11.4	0.7
Ca_Sm _mix	284.6 285.8 288.7	530.9	346.7	Sm3d$_{5/2}$ 1083.0	66.3	24.3	8.8	0.6

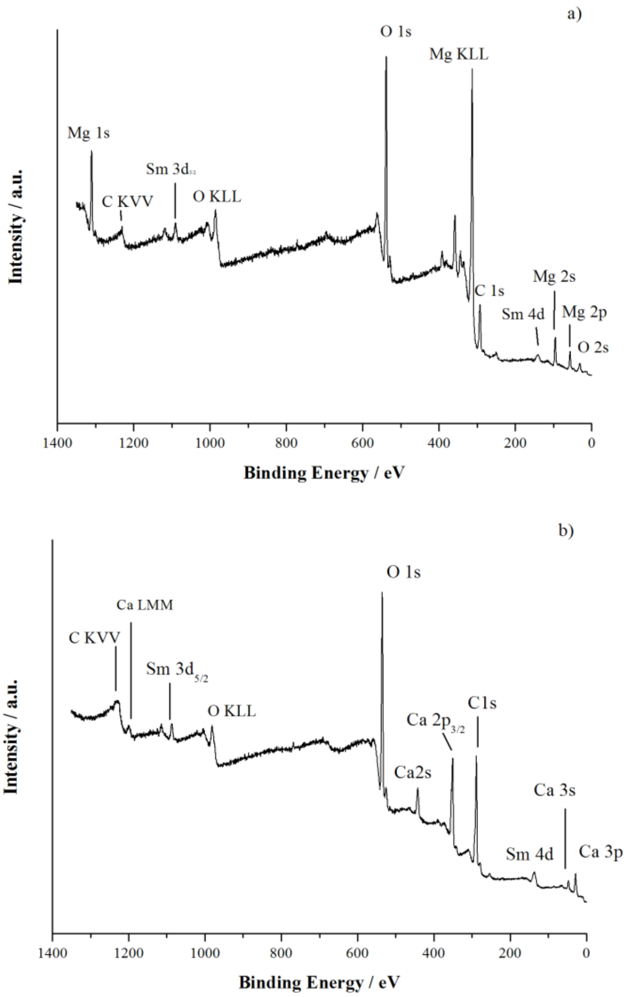

Fig. 3 XPS survey spectra of Mg_Sm_mix (a) and Ca_Sm_mix (b) (graphs shown are not corrected for surface charging effects)

The high carbon and oxygen percentages detected on the surface of all the systems are reasonably ascribed to the presence of the surfactant on the NPs surface, particularly carbon derived from the aliphatic chain and oxygen from the polar head of these molecules. With specific reference to the carbon C1s spectrum (see **Figure 4**), a contribution at 284.6 eV due to alkyl groups and, partially, to external contamination is always present. A further contribution due to surfactants aliphatic chains is detected at 285.5 eV, whereas contribution due to polar chains (C-O-C, C-OH) is, according to literature, peaked at 286.7 eV, for all the samples (see **Figure 4**).[42-44]

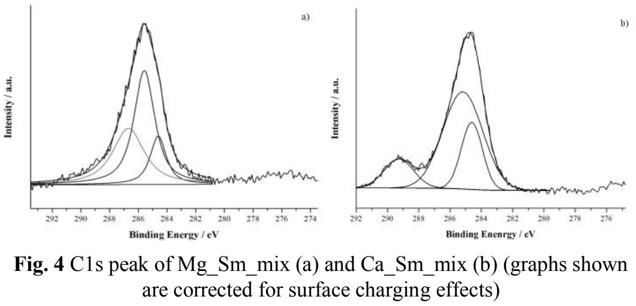

Fig. 4 C1s peak of Mg_Sm_mix (a) and Ca_Sm_mix (b) (graphs shown are corrected for surface charging effects)

The presence of the surfactant was also confirmed by FT-IR and TGA data (vide infra). The comparison of BEs with literature data indicates that Ca2p$_{3/2}$, Mg1s and Mg2s regions have the typical binding energyvalues of calcium and magnesium hydroxides, whereas doping elements have BE, typical of these ions in an oxidic environment, as shown in **Table 3** for Mg_Sm_mix and Ca_Sm_mix NPs, thus corroborating XRD outputs.[45, 46] In these samples, Mg 2p is found at 49.7 eV, i. e. the typical value for Mg(OH)$_2$,[40, 47, 48] whereas Ca2p$_{3/2}$ is found at 346.7 eV which is a typical value for Ca(OH)$_2$.[40, 46-49] Due to the low atomic concentrations involved, Mg/Ca_Sm_mix samples are the only two for which the dopant is clearly visible. The BE value for Sm 3d$_{5/2}$ (1083.0 eV) confirms the presence of samarium in oxidic environment.[40, 45, 46]

To accurately assess the actual atomic ratios in the doped systems, ICP-MS measurements were carried out. Expected and found stoichiometric atomic ratios for calcium and magnesium and the doping elements (Eu, Sm and Tb) are reported in **Table 4**. Experimental evidences herein reported statistically coincide with the expected values for all but one (Mg_Ln_span) sample series, for which the Mg:Ln ratios in Mg_Ln_span are larger than the expected ones. Since the Mg amount is in agreement with nominal values, these samples are likely characterised by a lanthanides leakage. As a whole, ICP results highlight the effectiveness of the adopted synthetic route to accurately control the stoichiometry and the actual doping level of final products.

Table 4 Calculated (second column) and experimental (third column) atomic ratios between Mg and Ca with the doping elements (Eu, Sm and Tb) characterising the NPs, as determined by ICP-MS. The used surfactants are reported in the last column. In column 3 the expanded uncertainty obtained by using a coverage factor k=2, corresponding to a coverage probability of approximately 95% for a normal distribution, is also reported

Sample	Calculated atomic ratio	Experimental atomic ratio ± expanded uncertainty	Surfactant
Mg_Eu_mix	20	19±2	Mix
Mg_Sm_mix	20	22±3	Mix
Mg_Tb_mix	20	19±3	Mix
Mg_Eu_mix	100	97±6	Mix
Mg_Eu_span	20	209±13	Span 80
Mg_Sm_span	20	303±20	Span 80
Mg_Tb_span	20	96±5	Span 80
Ca_Eu_mix	20	16±5	Mix
Ca_Sm_mix	20	16±5	Mix

The expected presence of the surfactant on the NPs surface was confirmed by FT-IR spectra recorded for pure Mg_mix, Ca_mix NPs and for pure Mg_span NPs. In the first two cases, vibrational bands are observed at 3700 and 3400 cm^{-1}. These bands are straightforwardly ascribed to the stretching of –OH groups, particularly of free –OH (the sharp one at higher wavenumbers), and of H-bonded hydroxyl groups (the broad one at lower wavenumbers), which are assignable to the surfactant and the hydroxides, respectively. Further bands characteristic of surfactants are those at 2920 and 2850 cm^{-1} (ν CH$_2$), at 1645, 1520, 1260 cm^{-1} (ν (C=C) aromatic and δ (=C-H)) typical of Igepal co-630. In the Ca_mix case, the two further bands at 875 and 785 cm^{-1} are characteristic of aromatic out-of-plane deformations. Finally bands at about 1100 cm^{-1} and 1020 cm^{-1} are due to C-O-C vibration of ether moieties of Brij 52.[50] Spectra are shown in Figure E.S.I. 1 a, b). FT-IR Attenuated Total Reflectance (ATR) spectra of pure surfactants are also reported in SI (Figure E.S.I. 1 cI)).

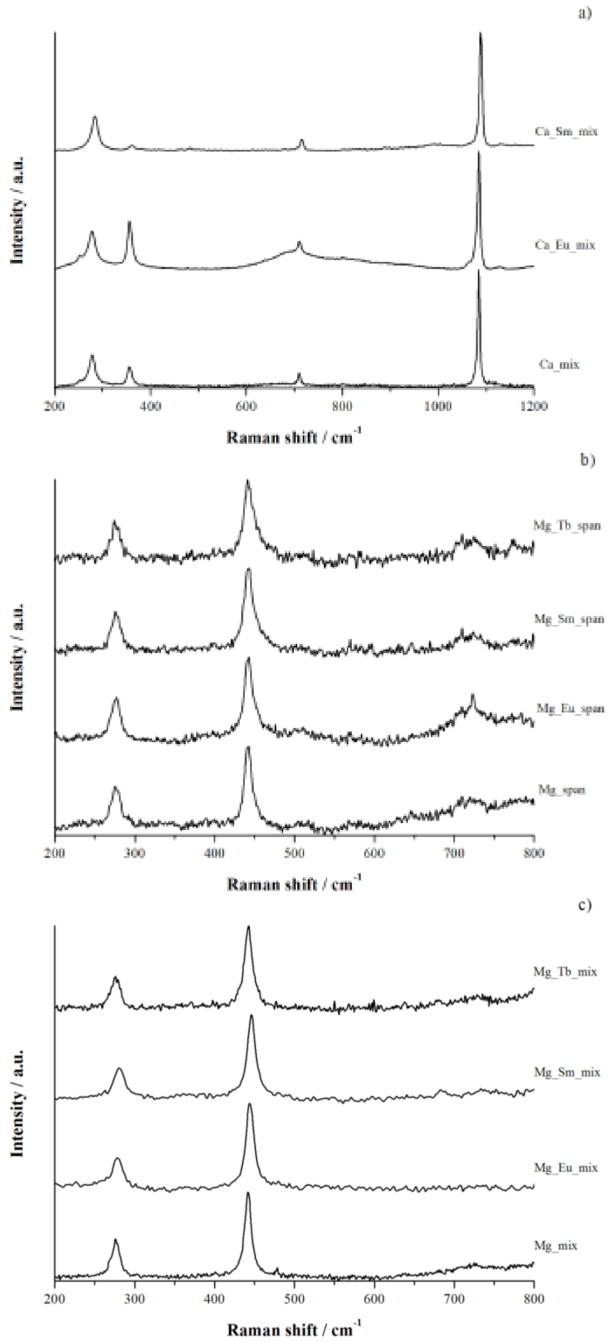

Fig. 5 Normalised Raman spectra of: a) pure and doped Ca_mix, b) pure and doped Mg_span, c) Mg_mix samples

A further hint on the composition of the prepared samples was provided by Micro-Raman analyses. This technique is indeed extensively used for the analysis of nanostructured materials, since it allows to analyze their composition, the presence and nature of crystalline phases contemporary present as well as the domain dimensions.[51, 52] Spectra recorded for pure and doped Ca_mix NPs show the presence of characteristic peaks of portlandite-calcium hydroxide, particularly of the Ca-O stretching (253 cm^{-1}, 355 cm^{-1}) as shown in **Figure 5**. Further peaks at higher Raman shifts are ascribed to the surfactants used in these synthesis (Igepal co630 and Brij 52), whose spectra are reported in Figure E.S.I. 2. These samples show evidence of carbonations and characteristic peaks of aragonite $CaCO_3$ at 278, 711 and 1085 cm^{-1} are present in all the spectra.[53-57] Pure and doped $Mg(OH)_2$ samples, obtained using both Span 80 and the surfactant mix show typical brucite Mg-O vibration peaks in $Mg(OH)_2$ at 275, 442 and 721 cm^{-1}.[58, 59] Other peaks are ascribed to Span 80, Igepal CO-630 and Brij 52 (Figure E.S.I. 2).

To evaluate quantitatively the amount residual surfactant on NPs, TGA-DSC analyses were also carried out on Mg_mix (**Figure 6**). In the range up to 200 °C, a weight loss of ~ 3%, due to the release of physisorbed water was revealed. Above this temperature and up to ~ 340°C another weight loss of ~ 7% takes place, which is associated to the decomposition of the two surfactant molecules (Igepal co-630 and Brij 52). This is confirmed by the exothermic peak at 305 °C, observed in the DSC trace, and by the comparison with the thermogravimetric curves recorded for the pure surfactants (Figure E.S.I. 3). In the temperatures range 340-400°C a further weight loss of about 27%, due to the dehydration of $Mg(OH)_2$, according to equation (1) and confirmed by the endothermic peak at 387 °C, is detected. This weight loss is in agreement with the final residual weight.[60]

$$Mg(OH)_2 + 84.5\,\text{kJ/mol} \rightarrow MgO + H_2O \qquad (1)$$

In view of the already mentioned bioimaging applications, cell viability, cytotoxicity tests and luminescence measurements were performed to assess both the biocompatibility and the luminescence of our products.

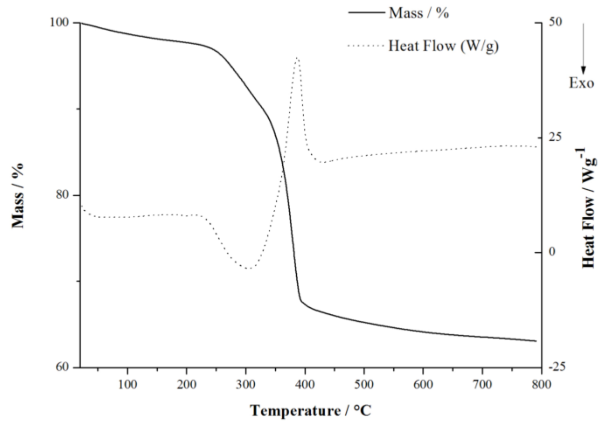

Fig. 6 TGA-DSC curve of Mg_mix NPs

Ovarian carcinoma cells (ES2 cells) were used as an *in vitro* model and incubated with NPs at two different concentrations (100 µg/ml and 30 µg/ml). Cell viability was monitored through the Alamar Blue assay, while the LDH (lactate dehydrogenase)-based test was then employed to estimate the possible NPs induced cell death after 24 hours of culture. In more detail, the effect on cell response of the surfactant used and of the doping ions was assessed. Results for $Mg(OH)_2$ NPs are shown in **Figure 7**: (A), (C) and (E) refer to the cytotoxicity measurements for Mg_mix, Mg_span and Mg_Eu_mix, respectively. These three systems were evaluated to test both the effect of the surfactant as well as of the dopant. It is in fact well known that also the surfactant can affect the biocompatibility.[61] The absorbance values are proportional to the amount of the LDH enzyme released by dead cells exposed to a high or low concentration of NPs. Cells cultured with NP-free full medium were used as a control. The absence of any significant difference between the absorbance of samples cultured with or without NPs, regardless of the NPs concentration, ultimately testifies that $Mg(OH)_2$ NPs are not cytotoxic at the used concentrations. Moreover, neither the employed surfactant nor the doping ions influence this evidence. Similar results were also observed when Sm(III) ions were used to dope $Mg(OH)_2$ NPs (Figure E.S.I. 4). Results pertaining $Ca(OH)_2$ NPs were analogous to those collected for $Mg(OH)_2$: no cytotoxicity at the applied concentrations after 24 hours of culture was revealed (Figure E.S.I. 4).

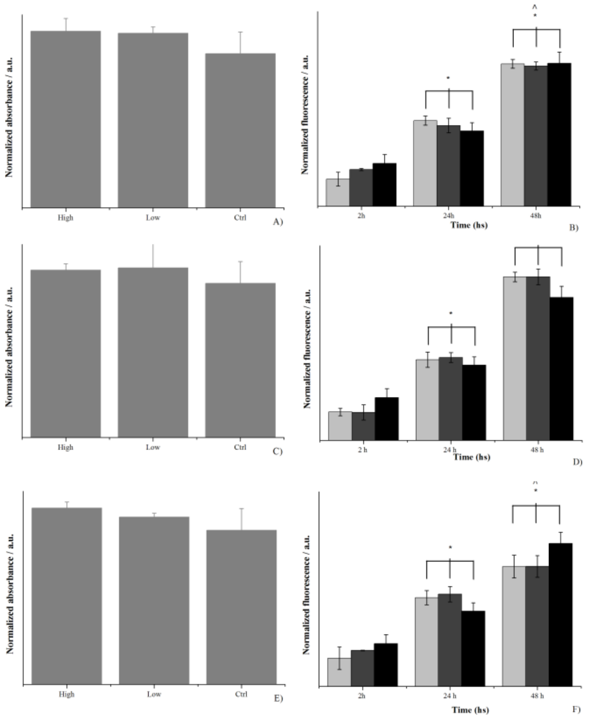

Fig. 7 Results of the LDH-based assay (A, C, E) and the AlamarBlue assay (B, D, F) for Mg_mix (A, B), Mg_span (C, D) and Mg_Eu_mix (E, F) NPs

A further test to assess the incubated cells viability, based on the Alamar Blue assay, was performed. **Figure 7** (B), (D) and (F) display the results of cell viability measurements after 2, 24 and 48 hours of incubation with $Mg(OH)_2$ NPs at high and low concentrations. At each time point, results are compared with the viability of cells cultured in a NP-free medium, used as blank reference The fluorescence values are proportional to the number of viable cells in the corresponding sample. No differences were detected among pure or Eu(III) doped Mg_mix, Mg_span NPs: for all samples, regardless of the concentrations used, NPs did not influence cell viability at earlier or later culture times. In fact, cells proliferated significantly after 24 and 48 hours culture and the number of viable cells was comparable among samples cultured with or without NPs. Similar outcomes were obtained for $Mg(OH)_2$ NPs doped with Sm(III) and for undoped $Ca(OH)_2$ nanostructures (Figure E.S.I. 4). Therefore, doped $Mg(OH)_2$ NPs can be potentially employed in the bioimaging field, since they showed neither cytotoxicity nor influence on cell viability at concentrations lower than 100 µg/ml, regardless of the used surfactant. In addition, the doping process with Eu(III) or Sm(III) did not influence these outcomes.

The possibility to apply these systems in bioimaging applications entails an efficient and stable luminescence. In this regard, RT emission spectra of Mg_Eu_mix, Mg_Eu_span and Ca_Eu_mix samples upon laser excitation at 465 nm are shown in **Figure 8** in the 550-750 nm wavelength range.

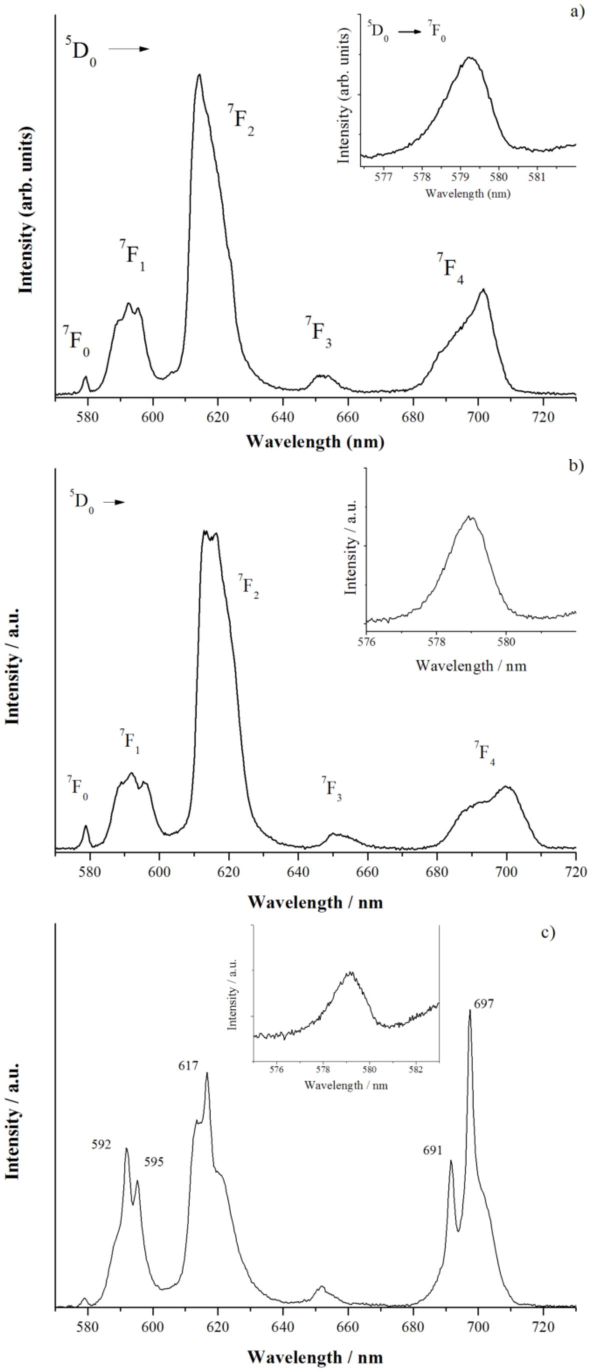

Fig. 8 Room temperature emission spectra of Mg_Eu_mix (a), Mg_Eu_span (b), Ca_Eu_mix (c)

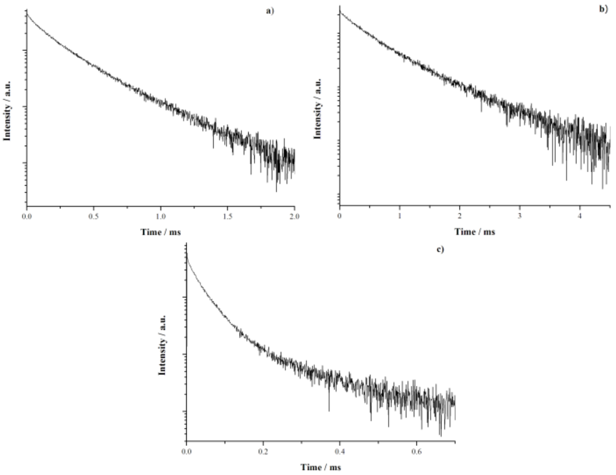

Fig. 9 Room temperature emission decays for Mg_Eu_mix (a), Mg_Eu_span (b), Ca_Eu_mix (c)

The emission bands can be assigned to Eu(III) $^5D_0 \rightarrow {}^7F_J$ (J=0, 1, 2, 3, 4) transitions (the transitions relative to J=5, 6 should also be mentioned, but, due to their wavelength falling in the IR region, they could not be experimentally detected). For both Eu(III) doped $Mg(OH)_2$ samples, prepared by using different surfactants, the strongest emission band is peaked at ~ 620 nm, and it is due to the hypersensitive $^5D_0 \rightarrow {}^7F_2$ transition, which clearly dominates the spectra. The allowed $^5D_0 \rightarrow {}^7F_2$ band is stronger than the magnetic dipole $^5D_0 \rightarrow {}^7F_1$ one, suggesting that Eu(III) ions are located in low symmetry sites, without inversion symmetry. Moreover, the degeneracy of the $^7F_1$ level is completely lifted, since three $^5D_0 \rightarrow {}^7F_1$ bands are clearly visible in the emission spectra, although overlapping each other. This behaviour suggests the presence of a significant broadening of the emission bands, probably due to structural disorder around Eu(III) ions, also confirmed by the full width at half maximum (FWHM) of the $^5D_0 \rightarrow {}^7F_0$ (0-0) band, similar to that of Eu(III) doped glass systems. The Eu(III) asymmetry ratios R = $I(^5D_0 \rightarrow {}^7F_2)/I(^5D_0 \rightarrow {}^7F_1)$, where I represents the emission integrated intensity of the corresponding band, for the Mg_Eu_span and Mg_Eu_mix samples, result to be 4.36 and 3.84, respectively.[62] These quite high values confirmed the low symmetry of the sites accommodating Eu(III) ions. On the other hand, the emission spectrum for Ca_Eu_mix sample clearly evidences the presence of europium hydroxide, impurity that is confirmed also by the X-ray diffraction patterns of this sample (see **Figure 2b**). In fact, some sharp bands, indicated with the wavelength positions, in **Figure 8(c)**, are typical of $Eu(OH)_3$, as found by different authors.[63, 64] Before going on, it has to be remarked that the Eu(III) site symmetry in europium hydroxide is relatively low (C_{3h}), explaining the similarity between the emission intensities of the electric dipole allowed $^5D_0 \rightarrow {}^7F_2$ and the magnetic dipole allowed $^5D_0 \rightarrow {}^7F_1$ bands. In the C_{3h} point symmetry, the $^5D_0 \rightarrow {}^7F_0$ band is forbidden, and in fact no such band was observed for europium hydroxide. Therefore, the presence of a weak but clearly visible 0-0 band in the emission spectrum indicates that some Eu(III) ions are accommodated in sites with lower point symmetries (C_s, C_1, C_n or C_{nv}, n=2, 3, 4, 6) with respect to C_{3h}, according to the electric dipole selection rules for lanthanide ions.[65] It is interesting to note that the point symmetry of calcium ions in calcium hydroxide is D_{3d} and therefore no (0-0) should be observed if Eu(III) would substitute Ca(II) ions in the lattice sites. Nonetheless, the presence of distortions of the coordination polyhedron around the Eu(III) ions or the presence of defects might lift this selection rule and making partially allowed the weak 0-0 band, as observed for the present sample. The emission decays, shown in **Figure 9**, present a different behaviour for the Eu(III) doped $Mg(OH)_2$ or $Ca(OH)_2$ samples. In particular, a slightly non-exponential behaviour is observed for the $Mg(OH)_2$ sample, confirming the presence of disorder around the lanthanide ions. The effective decay times, τ_{eff}, was calculated using the equation:[66]

$$\tau_{eff} = \frac{\int tI(t)dt}{\int I(t)dt}$$

where $I(t)$ represents the luminescence intensity at time t corrected for the background, while the integrals are evaluated in the range $0<t<t^{max}$ with $t^{max} \gg \tau_{eff}$. The τ_{eff} for the Mg_Eu_mix and Mg_Eu_span are 0.30±0.01 ms and 0.70±0.01 ms, respectively. This different behaviour can be explained by considering that for the Mg_Eu_mix sample the asymmetry ratio (4.36) is higher than for the Mg_Eu_span (3.84) and therefore the lower point symmetry of the Eu(III) sites implies longer lifetimes of the $^5D_0$ level (if non-radiative relaxation processes as multiphonon relaxation processes are similar for the samples as in the present case). The emission decay behaviour for the Eu(III) doped $Ca(OH)_2$ differs from that of $Mg(OH)_2$. In fact, in Eu(III) doped $Ca(OH)_2$, the emission decay can be fit using two exponential curves, thus obtaining two different lifetimes: τ_1=0.035±0.001 ms and τ_2=0.277±0.001 ms. The τ_2 value is very similar to the one pertinent to europium hydroxide (0.22 ms),[67] thus confirming the presence of $Eu(OH)_3$ in Ca_Eu_mix NPs. As far as the τ_1 value is concerned, it is quite short and consistent with a slightly distorted site for Eu(III) as well as a strong non-radiative relaxation due to the high energy phonons of the hydroxide ions surrounding the lanthanide ions. We tentatively assign this lifetime to Eu(III) ions substituting the Ca(II) ones in the $Ca(OH)_2$ lattice, substitution which is facilitated by the similarity of Ca(II) (126 pm, in eight-fold coordination) and Eu(III) (120.6 pm, in eight-fold coordination) ionic radii.

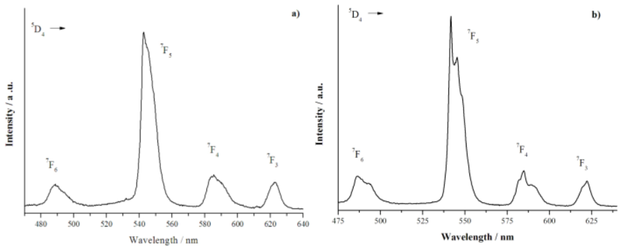

Fig. 10 Room temperature emission spectrum of Mg_Tb_span (a) and Mg_Tb_mix (b)

The same experiment was carried out on Tb-doped systems. RT emission spectra of Mg_Tb_span and Mg_Tb_mix samples upon laser excitation at 355 nm are shown in **Figure 10** in the 470-640 nm wavelength range. The emission bands can be assigned to $^5D_4 \rightarrow {}^7F_J$ (J=6, 5, 4, 3) transitions typical of the Tb(III) ion. Both the spectra are dominated by the $^5D_4 \rightarrow {}^7F_5$ emission bands.

Analogously to Eu(III) doped samples bands are quite broad, suggesting even for Tb(III) ions, a significant structural disorder around them. In **Figure 11** are shown Mg_Eu_mix (the red one) and Mg_Tb_mix (the green one) samples irradiated with UV radiation.

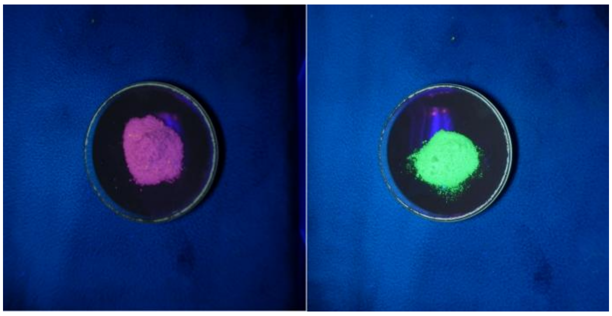

Fig. 11 Mg_Eu_mix (left) and Mg_Tb_mix (right) samples irradiated with UV radiation

Conclusions

In this contribution an easy, reproducible, fast and effective method to prepare nanocrystalline pure and doped magnesium and calcium hydroxides NPs which crystallise already at room temperature, without any need of successive thermal treatment, was optimised and described. This approach affords a very precise control on the stoichiometry, structure and size of the obtained NPs. The MEs method allowed to achieve polycrystalline powder with an average crystallite size ~ 20 nm for $Mg(OH)_2$ systems and ~ 35 nm for $Ca(OH)_2$ systems, without particular difference between pure and doped NPs. The NPs characterisation was carried out by exploiting different and complementary techniques. The role of the used surfactant (or mixture thereof) on the stability of the achieved suspension and on the final features of the nanostructures was assessed. As far as the functionality of the addressed systems is concerned, no significant cytotoxicity or influence on the viability of ES2 cells was revealed after 48 hours of culture, regardless of NPs concentration and doping. Finally, good luminescence performances were observed for the Eu(III) (in the red) and Tb(III) (in the green) doped magnesium and calcium hydroxides, which candidates these materials for in-vitro and in-vivo biomedical applications.

Acknowledgements

The University of Padua, Italy and the Italian National Research Council (CNR) are acknowledged for financial support. Prof. Fabrizio Mancin (Dipartimento di Scienze Chimiche, Università degli Studi di Padova) is gratefully acknowledged for DLS measurements. Dr. Roberta Saini (Dipartimento di Scienze Chimiche, Università degli Studi di Padova) is gratefully thanked for TGA-DSC measurements. Dr. Massimiliano Rocchia and Thermo Fischer are gratefully acknowledged for help in recording and processing Raman data. A.S. and M.P. acknowledge Fondazione Cariverona (Verona, Italy), project Verona Nanomedicine Initiative, for financial support.

References

1. T. M. Fahmy, P. M. Fong, J. Park, T. Constable and W. M. Saltzman, *AAPS J.*, 2007, **9**, E171-E180.
2. V. J. Pansare, S. Hejazi, W. J. Faenza and R. K. Prud'homme, *Chem. Mater.*, 2012, **24**, 812-827.
3. J.-C. G. Bünzli, *Chem. Rev. (Washington, DC, U. S.)*, 2010, **110**, 2729-2755.
4. P. Sharma, S. Brown, G. Walter, S. Santra and B. Moudgil, *Adv. Colloid Interface Sci.*, 2006, **123-126**, 471-485.
5. K. Landfester, A. Musyanovych and V. Mailaender, *J. Polym. Sci., Part A: Polym. Chem.*, 2010, **48**, 493-515.
6. V. Biju, T. Itoh, A. Anas, A. Sujith and M. Ishikawa, *Anal. Bioanal. Chem.*, 2008, **391**, 2469-2495.
7. Y. Su, F. Peng, Z. Jiang, Y. Zhong, Y. Lu, X. Jiang, Q. Huang, C. Fan, S.-T. Lee and Y. He, *Biomaterials*, 2011, **32**, 5855-5862.
8. A. Llevot and D. Astruc, *Chem. Soc. Rev.*, 2012, **41**, 242-257.
9. S. J. Soenen, P. Rivera-Gil, J.-M. Montenegro, W. J. Parak, S. S. C. De and K. Braeckmans, *Nano Today*, 2011, **6**, 446-465.
10. N. Khlebtsov and L. Dykman, *Chem. Soc. Rev.*, 2011, **40**, 1647-1671.
11. C. Martinez-Boubeta, L. Balcells, R. Cristofol, C. Sanfeliu, E. Rodriguez, R. Weissleder, S. Lope-Piedrafita, K. Simeonidis, M. Angelakeris, F. Sandiumenge, A. Calleja, L. Casas, C. Monty and B. Martinez, *Nanomedicine (Philadelphia, PA, U. S.)*, 2010, **6**, 362-370.
12. F. Tamimi, N. D. Le, D. C. Bassett, S. Ibasco, U. Gbureck, J. Knowles, A. Wright, A. Flynn, S. V. Komarova and J. E. Barralet, *Acta Biomater.*, 2011, **7**, 2678-2685.
13. Y. Yu, J. Wang, C. Liu, B. Zhang, H. Chen, H. Guo, G. Zhong, W. Qu, S. Jiang and H. Huang, *Colloids Surf., B*, 2010, **76**, 496-504.
14. A. Doat, F. Pelle, N. Gardant and A. Lebugle, *J. Solid State Chem.*, 2004, **177**, 1179-1187.
15. H.-C. Huang, S. Barua, G. Sharma, S. K. Dey and K. Rege, *J. Controlled Release*, 2011, **155**, 344-357.
16. F. Chen, Y.-J. Zhu, K.-H. Zhang, J. Wu, K.-W. Wang, Q.-L. Tang and X.-M. Mo, *Nanoscale Res. Lett.*, 2011, **6**, 67, 69 pp.
17. V. Sokolova and M. Epple, *Angew. Chem., Int. Ed.*, 2008, **47**, 1382-1395.
18. P. J. Neuvonen and K. T. Kivisto, *Eur. J. Clin. Pharmacol.*, 1988, **35**, 495-501.
19. T. Okiji and K. Yoshiba, *Int J Dent*, 2009, **2009**, 464280.
20. X. Gao, M. Hu, L. Lei, D. O'Hare, C. Markland, Y. Sun and S. Faulkner, *Chem. Commun. (Cambridge, U. K.)*, 2011, **47**, 2104-2106.
21. C. Bouzigues, T. Gacoin and A. Alexandrou, *ACS Nano*, 2011, **5**, 8488-8505.
22. K. Landfester, N. Bechthold, F. Tiarks and M. Antonietti, *Macromolecules*, 1999, **32**, 5222-5228.
23. F. J. Schork, Y. Luo, W. Smulders, J. P. Russum, A. Butte and K. Fontenot, *Adv. Polym. Sci.*, 2005, **175**, 129-255.
24. M. Antonietti and K. Landfester, *Prog. Polym. Sci.*, 2002, **27**, 689-757.
25. A. Ethirajan and K. Landfester, *Chem. - Eur. J.*, 2010, **16**, 9398-9412.
26. K. Landfester, *Angew. Chem., Int. Ed.*, 2009, **48**, 4488-4507.
27. R. Muñoz-Espì, C. K. Weiss and K. Landfester, *Curr. Opin. Colloid Interface Sci.*, 2012, **17**, 212-224.
28. R. Muñoz-Espì, Y. Mastai, S. Gross and K. Landfester, *CrystEngComm*, 2013, **15**, 2175-2191.
29. P. Dolcet, M. Casarin, C. Maccato, L. Bovo, G. Ischia, S. Gialanella, F. Mancin, E. Tondello and S. Gross, *J. Mater. Chem.*, 2012, **22**, 1620-1626.
30. P. Dolcet, F. Latini, M. Casarin, A. Speghini, E. Tondello, C. Foss, S. Diodati, L. Verin, A. Motta and S. Gross, *Eur. J. Inorg. Chem.*, 2013, **2013**, 2291-2300.
31. M. Willert, R. Rothe, K. Landfester and M. Antonietti, *Chem. Mater.*, 2001, **13**, 4681-4685.
32. A. Taden, M. Antonietti, A. Heilig and K. Landfester, *Chem. Mater.*, 2004, **16**, 5081-5087.
33. C. Saiwan, S. Krathong, T. Anukulprasert and E. A. O'Rear, III, *J. Chem. Eng. Jpn.*, 2004, **37**, 279-285.
34. M. Hajir, P. Dolcet, V. Fischer, J. Holzinger, K. Landfester and R. Munoz-Espi, *J. Mater. Chem.*, 2012, **22**, 5622-5628.

35. F. Caruso, *Colloids and Colloid Assemblies - Synthesis, Modification, Organization and Utilization of Colloid Particles, 1st Ed.*, Wiley-VCH, Weinheim, 2004.
36. B. S. Zolnik, A. Gonzalez-Fernandez, N. Sadrieh and M. A. Dobrovolskaia, *Endocrinology*, 2010, **151**, 458-465.
37. K. Landfester, M. Willert and M. Antonietti, *Macromolecules*, 2000, **33**, 2370-2376.
38. D. Briggs and M. P. Seah, *Practical Surface Analysis - Volume 1 - Auger and X-ray Photoelectron Spectroscopy, 2nd Ed.*, John Wiley & Sons, New York, 1990.
39. D. A. Shirley, *Phys. Rev. B*, 1972, **5**, 4709-4713.
40. J. F. Moulder, W. F. Stickle, P. E. Sobol and K. D. Bomben, *Handbook of X-Ray Photoelectron Spectroscopy - A Reference Book of Standard Spectra for Identification and Interpretation of XPS Data*, Perkin-Elmer Corp., Eden Prarie, Minnesota, 1992.
41. H. P. Klug and L. E. Alexander, *X-Ray Diffraction Procedures for Polycrystalline and Amorphous Materials*, J. Wiley & Sons, New York, 1974.
42. T. L. Barr and S. Seal, *J. Vac. Sci. Technol., A*, 1995, **13**, 1239-1246.
43. M. R. Alexander, S. Payan and T. M. Duc, *Surf. Interface Anal.*, 1998, **26**, 961-973.
44. R. Xu and H. C. Zeng, *Langmuir*, 2004, **20**, 9780-9790.
45. M. J. Capitàn, M. A. Centeno, P. Malet, I. Carrizosa, J. A. Odriozola, A. Marquez and S. J. Fernandez, *J. Phys. Chem.*, 1995, **99**, 4655-4660.
46. P. Ghods, O. B. Isgor, J. R. Brown, F. Bensebaa and D. Kingston, *Appl. Surf. Sci.*, 2011, **257**, 4669-4677.
47. D. E. Haycock, C. J. Nicholls, D. S. Urch, M. J. Webber and G. Wiech, *J. Chem. Soc., Dalton Trans.*, 1978, 1791-1796.
48. S. Ardizzone, C. L. Bianchi, M. Fadoni and B. Vercelli, *Appl. Surf. Sci.*, 1997, **119**, 253-259.
49. T. Sugama, L. E. Kukacka, N. Carciello and N. J. Hocker, *Cem. Concr. Res.*, 1989, **19**, 857-867.
50. G. Socrates, *Infrared and Raman Characteristic Group Frequencies: Tables and Charts, 3rd Ed.*, John Wiley & Sons, Chichester, UK, 2004.
51. G. Gouadec and P. Colomban, *Prog. Cryst. Growth Charact. Mater.*, 2007, **53**, 1-56.
52. G. Gouadec and P. Colomban, *J. Raman Spectrosc.*, 2007, **38**, 598-603.
53. R. Frech, E. C. Wang and J. B. Bates, *Spectrochim. Acta, Part A*, 1980, **36A**, 915-919.
54. K. Suito, J. Namba, T. Horikawa, Y. Taniguchi, N. Sakurai, M. Kobayashi, A. Onodera, O. Shimomura and T. Kikegawa, *Am. Mineral.*, 2001, **86**, 997-1002.
55. D. Nave, S. Rosenwaks, R. Vago and I. Bar, *J. Appl. Phys.*, 2004, **95**, 8309-8313.
56. A. Aminzadeh, *Spectrochim. Acta, Part A*, 1997, **53A**, 693-697.
57. S. Martìnez-Ramìrez and M. Frias, *Appl. Clay Sci.*, 2011, **51**, 283-286.
58. P. S. Braterman and R. T. Cygan, *Am. Mineral.*, 2006, **91**, 1188-1196.
59. V. Drozd, S. Saxena, S. V. Garimella and A. Durygin, *Int. J. Hydrogen Energy*, 2007, **32**, 3370-3375.
60. E. Riedel, *Anorganische Chemie*, Walter de Gruyter, Berlin, 1994.
61. S. T. Kim, K. Saha, C. Kim and V. M. Rotello, *Acc. Chem. Res.*, 2013, **46**, 681-691.
62. R. Reisfeld, E. Zigansky and M. Gaft, *Mol. Phys.*, 2004, **102**, 1319-1330.
63. Q. G. Zeng, Z. J. Ding, Z. M. Zhang and Y. Q. Sheng, *J. Phys. Chem. C*, 2010, **114**, 4895-4900.
64. R. L. Cone and R. Faulhaber, *J. Chem. Phys.*, 1971, **55**, 5198-5206.
65. R. D. Peacock, *Struct. Bonding*, 1975, **22**, 83-122.
66. S. Shionoya and W. M. Yen, *Phosphor Handbook, 1st Ed.*, CRC Press, Boca Raton, FL, 1999.
67. I. Pointeau, B. Piriou, M. Fedoroff, M.-G. Barthes, N. Marmier and F. Fromage, *J. Colloid Interface Sci.*, 2001, **236**, 252-259.
68. *WebElements: the periodic table on the web, http://www.webelements.com/*.
69. *Shannon Radii - Atomistic Simulation Group, http://abulafia.mt.ic.ac.uk/shannon/ptable.php*.

3.6. Zinc sulfide

3.6.1. Introduction

Zinc sulfide is a II–VI semiconductor with a direct band gap of about 3.6 eV at room temperature and an exciton binding energy of 40 meV. It has two known crystallographic structures: the hexagonal wurtzite and the cubic sphalerite (or zinc blende). The hexagonal phase is thermodynamically metastable and it is stable at temperatures higher than 1020°C [78], whereas the cubic phase is the stable form at room temperature (RT). ZnS displays good luminescent properties, and it is therefore used for example in displays, sensors and lasers [79]. When downsizing the systems, exciting properties emerge: zinc sulfide NPs and quantum dots (QDs) have been widely explored as alternatives to CdSe QDs for bioimaging applications, due to their lower toxicity and enhanced thermal and environmental stability [80, 81][1]. Furthermore, due to its large band gap, it can easily host different transition metal and rare earth ions as luminescent centers [83], engineering the band gap as needed. Luminescence characteristics of doped ZnS nanostructures differ markedly from those of bulk ZnS, with mechanism related to the position of the dopant in the host lattice. Since Bhargava's work in 1994 [84], who claimed that Mn^{II} doped ZnS NPs could yield both high quantum luminescence efficiency and lifetime shortening at the same time, contemporary suggesting that these NPs corresponded to a new class of luminescent materials, doped zinc sulfide nanocrystals are focus of great interest, even if controversies are still present [79]. Manganese doped ZnS nanostructures represent the most attractive and studied family among these luminescent materials, but a wide variety of examples are present in literature, involving either transition metal ($TM=Cu^{II}$, Fe^{II}, Pb^{II}, Ni^{II}, Cd^{II}, Co^{II}) or rare earths ($RE=Eu^{III}$, Sm^{III}, Tb^{III}, Er^{III}) dopants [79]. Zinc sulfide NPs have been prepared by many different wet chemistry routes, for examples by chemical precipitation,decomposition of organometallic compunds, sol–gel and other colloidal methods, or by ions implantation (e.g., see the review by Hu *et al.* [79] and references therein). Microemulsions have as well been exploited, also coupled to hydrothermal treatment, leading to the formation of nanocrystals with sizes as low as 3 nm [85]; on the other hand, no account of ZnS nanostructures prepared by miniemulsions has been reported so far in the literature.

3.6.2. Results and discussion

In this work, the synthesis of zinc sulfide NPs was attempted by a two-emulsion approach, using both sodium sulfide and thioacetamide as sulfur sources[2]. Whereas the use of Na_2S easily afforded the formation of a crystalline precipitate, thioacetamide was not successful in promoting the formation of the desired product and was therefore not further investigated. We focused our attention on both pure ZnS and ZnS doped with M=Cu^{II}, Mn^{II}, Sm^{III}, Gd^{III} and Tb^{III}, with a Zn:M atomic ratio of 50:1.

---

[1] For example, ZnS QDs showed no cytotoxic effect on human endothelial cells even after more than 6 days[82]

[2] The latter is labile towards acid hydrolysis, which promotes the decomposition to acetic acid, with release of H_2S, the true active species. This decomposition is usually favored for pH<4 and temperature ranging from 60 to 80°C [86].

In order to follow the growth of the nanostructures, UV-Vis spectra were collected on the suspensions at different time after sonication of the final colloidal suspension (Fig. 3.2). As it can be seen (5 minutes curve), the absorption onset is initially centered at about 320 nm showing a slight blue shift with respect to the value reported for bulk ZnS (338 nm). Moreover, the onset is ill-defined, hinting towards high polydispersity and/or aggregation of particles. Spectra registered after 10, 30 and 60 minutes do not present a shift in the absorption edge, rather a progressive decrease in intensity coupled with increased baseline absorption are well evident; both phenomena can be rationalized in terms of particles flocculation.

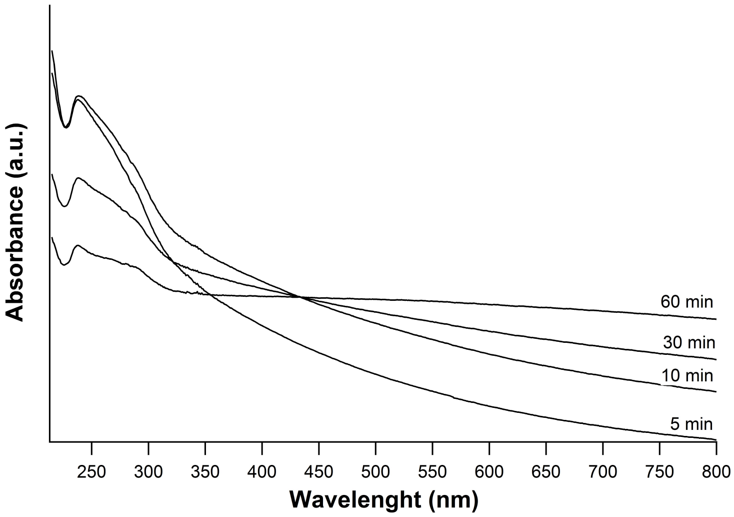

Figure 3.2.: UV-Vis of pure ZnS suspension

The powders obtained by centrifugation of suspensions were firstly characterized by X-ray diffraction (XRD), which confirmed the formation of nanocrystalline ZnS with cubic sphalerite structure (JCSD PDF 01-080-0020). With respect to the undoped sample, diffractograms of the doped ones show a slight reflections shift towards higher angles. Such an effect is more evident for the Mn doped sample. This can be taken as an indication of lattice contractions, the origin of which, on the other hand, is still under investigation. These contractions should indeed arise when Zn^{II} is substituted by an ion with a smaller ionic radius, nevertheless this is the case only for Cu^{II} (in a T_d coordination: Zn^{II}=0.6 Å, Cu^{II}=0.57 Å, Mn^{II}=0.66 Å; in a O_h coordination: Sm^{III}=0.958 Å, Gd^{III}=0.935 Å, Tb^{III}=0.923 Å [87]), for which, incidentally, the shift is minimal. Due to the broadness and overlapping of the reflections, the crystallite size could not be reliably evaluated by using the

Scherrer equation. Nevertheless, the crystallite size could be estimated by Transmission Electron Microscopy (TEM) analyses (an example of which is reported in Fig. 3.3, together with the corresponding Selected Area Electron Diffraction (SAED) pattern), which indicated a mean size of 5-10 nm.

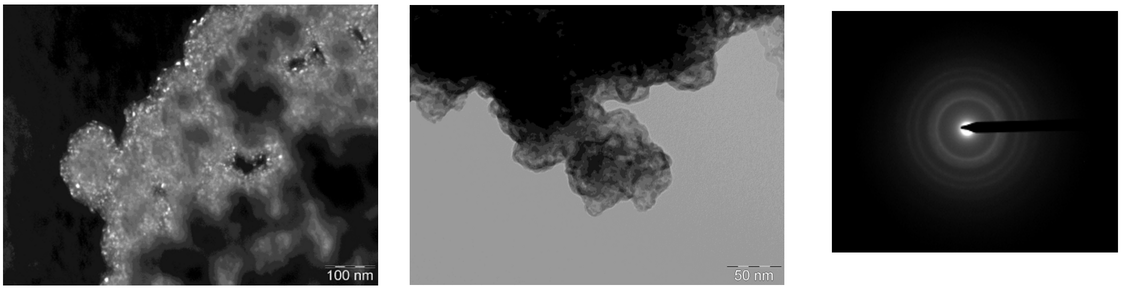

Figure 3.3.: Dark (left) and bright (center) field TEM images of pure ZnS nanostructures and corresponding SAED pattern (right)

In all samples the SAED patterns display a substantially continuous distribution of the diffracted intensity along the diffraction rings and this is an indication of an extremely reduced domain size. The Dark Field image, acquired using a portion of the innermost diffraction rings, clearly displays, in the form of brighter speckles, a uniform distribution of coherently scattering domains, having an average size in the 5-10 nm range. These crystallites are further organized on a larger scale as grains (50-100 nm) forming a continuous porous network. A better description of these agglomerates has been provided by Scanning Electron Microscopy (SEM) micrographs (see Fig. 3.4). The agglomerates, with an average dimension of hundreds of nanometers, are indeed formed by very small quasi-spherical particles, with size compatible with that of the grains imaged in TEM micrographs.

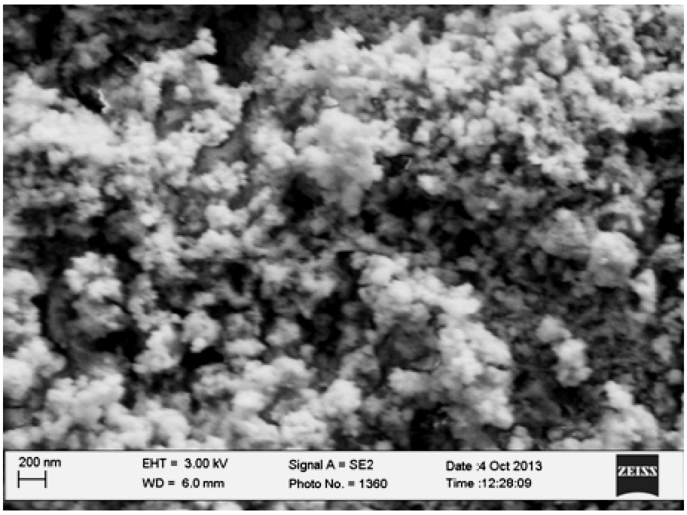

Figure 3.4.: SEM micrograph of pure ZnS nanostructures

XRD diffractograms were similar for all the samples (see Fig. 3.5). In this regard, it deserves to be stressed that the Cu and RE doped samples showed reflections only due to sphalerite, while the Mn doped sample is characterized by additional weak reflections, ascribable to traces of hetaerotite $ZnMn_2O_4$ (JCSD PDF 01-071-2499). It is worth mentioning that SAED patterns of these materials evidence the presence of ZnO diffraction rings in association with the ZnS phase in all samples. The apparent discrepancy between XRD and TEM data can be reasonably explained in terms of the formation of a very thin surface layer present on the sulfide grains, with an overall volume fraction fraction below the XRD detectability limit, and thus not sufficient to provide adequate diffraction intensity. This latter hypothesis seems more reliable and backed by X-ray Absorption Fine Structure (XAFS) data (*vide infra*), showing the presence of only sulfur in the zinc first coordination shell. Coherently with this picture, it is has to be considered that SAED patterns are acquired in transmission. Therefore, due to limited electron beam penetration, the collected signal will be mainly representative of the outer surface layers of the investigated samples.

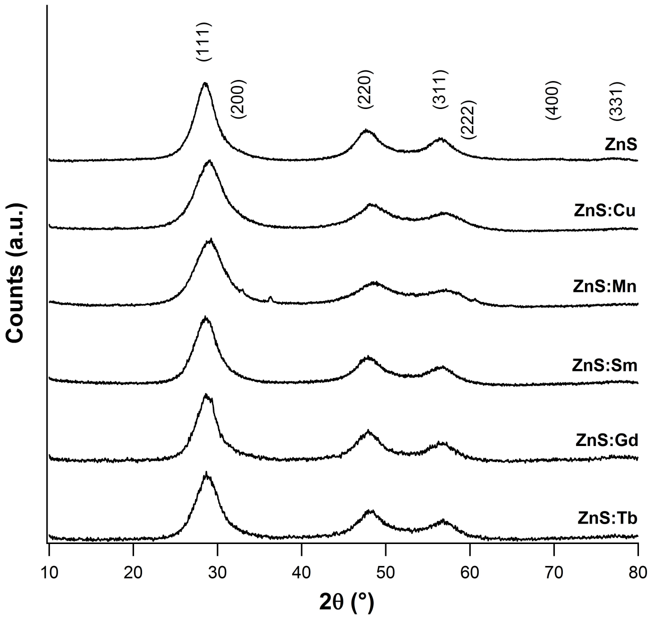

Figure 3.5.: XRD diffractograms of pure and doped ZnS NPs

The UV-Vis absorption properties of the synthesized samples were also evaluated for the dried powders by means of Diffuse Reflectance Spectroscopy (DRS). The spectrum reported in Fig. 3.6 for pure ZnS (black line) has an absorption onset centered at 374 nm, with a slight shift with respect to bulk ZnS (about 350 nm). Such a shift may be tentatively explained in terms of structural defectivity, which determines the presence of additional energy levels within the band-gap, with its subsequent narrowing (see Scheme 3.1). Such an effect is even more pronounced in doped samples, since the absorption edges are less defined and further shifted, or covered by dopant-induced absorption features. Furthermore, the Sm^{III} doped sample shows an extra

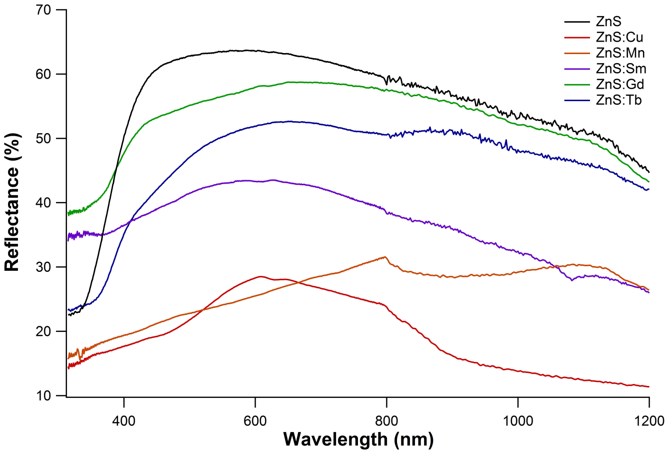

Figure 3.6.: Diffuse Reflectance UV-Vis spectra of the obtained powders

absorption peak in the NIR range, at 1082 nm, compatible with the $^6H_{5/2} \rightarrow ^6F_{9/2}$ transition of this ion [88]. A close inspection of this spectrum reveals a further less intense peak at 950 nm, assigned to the$^6H_{5/2} \rightarrow ^6F_{11/2}$ transition typical of Sm^{III}, whereas signals in the UV-Vis range are too weak to be clearly identified. The photoluminescence (PL) spectrum (λ_{exc} = 325 nm) of undoped ZnS nanostructures (recorded in cooperation with Prof. Speghini at Università di Verona) similarly shows a typical defect-related shape (see Fig. 3.7), with a broad band centered at 409 nm and a long tail extending up to 600 nm. In the literature, this band is most commonly considered as a “self activated” band composed of different components due to emission processes mainly involving sulfur vacancies (therefore not needing the presence of any dopant), as depicted in Scheme 3.1 (NR: non-radiative process; V_s: sulfur vacancy; V_{Zn}: zinc vacancy; SS: surface states [89]).

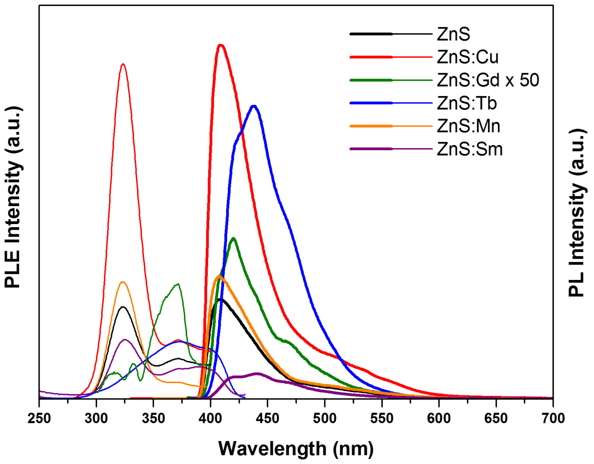

Figure 3.7.: Excitation (thin) and emission (thick) spectra

Despite a modulation of the fluorescence intensity, particularly evident in the Cu

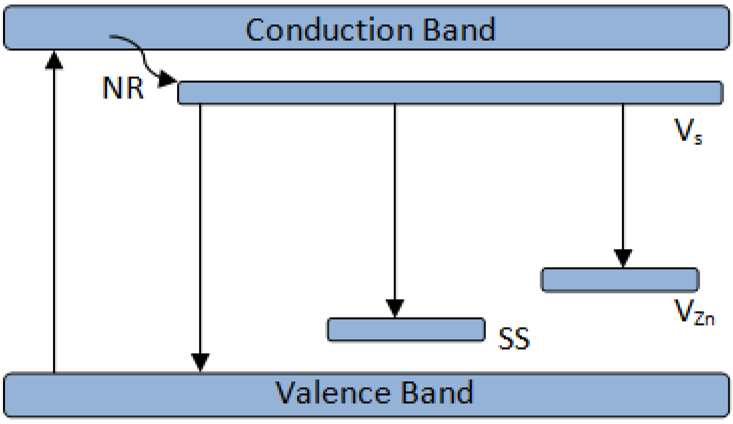

Scheme 3.1: Emission processes for ZnS nanoparticles (adapted from [89])

doped sample, the spectra shape is negligibly affected by the presence of transition metal or rare earth impurities, no extra band is in fact present in any of the spectra. Since the excitation was performed at the matrix maximum absorption, the absence of these extra bands might evidence that there is no charge transfer from the matrix to the doping ions [79, 90, 91], thus suggesting a not effective embedding of the latter. At variance to TM doped specimens, the spectra shape of the lanthanide doped ones is significantly modified upon doping and, in ZnS:Gd, the emission is strongly quenched (see in Fig. 3.7 the corresponding curves, multiplied by 50). These modifications can be ascribed with confidence to structural modifications induced by the formation of lanthanide oxide clusters (see Extended X-ray Absorption Fine Structure - EXAFS - data) in the zinc sulfide matrix. In fact these ions are known to be difficult to incorporate in such matrices and often high temperatures are needed to accomplish this [91]. Despite the absence of any doping ions typical bands/line, the dopants presence is confirmed by Inductively Coupled Plasma-Mass Spectrometry (ICP-MS) measurements (see Tab. 3.3), which show excellent agreement with the expected nominal atom ratio.

Sample	**Nominal atomic ratio**	**Experimental atomic ratio**
ZnS:Cu	50:1	45 ± 6
ZnS:Mn	50:1	41 ± 10
ZnS:Sm	50:1	50 ± 5
ZnS:Gd	50:1	51 ± 6
ZnS:Tb	50:1	50 ± 3

Table 3.3.: ICP-MS measurements (Confidence interval: 95%)

NPs were also analyzed by X-ray photoelectron spectroscopy (XPS) to evaluate the possibility of dopants segregation on the surface, a consequence of the already indicated incorporation difficulties in sulfides matrices. In all samples, the Zn2p$_{3/2}$ signal is found at 1021.5-1022.0 eV, while the corresponding Auger parameter is in the range 2011.1-2011.3 eV. Both values are compatible with zinc sulfide (Zn2p$_{3/2}$=1022.0 eV, Auger parameter= 2011.5 eV [92, 93]). Also the binding energy values for the S2p main components (S2p$_{3/2}$=161.3-162 eV) are in agreement with data reported in the literature (S2p$_{3/2}$=161.6 eV [93]).

As far as the Mn doped sample is concerned, the S2p signal showed the presence of two contributions, the former compatible with ZnS, the latter, at 166.3 eV, probably due to the presence of partially oxidized surface sulfur species (in particular SO_3^{2-}, which could be generated from simple oxidation or by oxidation of HS^- by $OH\cdot$ radicals generated by water sonolysis during the emulsification process [94]). Moving to the dopants peaks, the signal-to-noise ratios are too low to clearly distinguish dopant signals and assign them. Such an evidence could mean that an effective incorporation of the TM doping ions in the host matrix took place (also strengthened by ICP-MS analysis), and no clustering or surface segregation of dopants occurred. On the other hand, it could be simply related to XPS detection limits. Due to the presence of adsorbed surfactant (see thermogravimetric analysis, TGA) and surface contamination, the detected atomic percentage for Zn is at most 10-12 % (see Tab. 3.4), leading to an expected dopant maximum atomic percentage of about 0.2-0.3 %, close to the detection limit. As it can be seen from the semi-quantitative analysis results presented in Tab. 3.4, all spectra are dominated by the surfactants signals. Also attenuated total reflectance (ATR) data (*vide infra*) confirmed the presence of the adsorbed surfactants.

Sample	**C %**	**O %**	**Zn %**	**S %**	**Zn:S**
ZnS	57.5	17.8	12.4	12.3	1
ZnS:Cu	68.7	29.3	1	1	1
ZnS:Mn	69.7	25.9	1.9	2.4	0.8
ZnS:Sm	63.4	17.8	10.6	8.2	1.3
ZnS:Gd	57.4	23.8	10.4	8.4	1.2

Table 3.4.: XPS semi-quantitative analysis results

With the intent of tailoring the desired characteristics, it is important to correlate the observed functional properties (i.e., luminescence) with the structural ones. This, in fact, may help the tuning of the synthetic parameters in order to achieve the desired results. In this regard, further insights into the doping ions local environment were gained through XAFS measurements at S, Zn and dopant K or L$_3$ edges, performed during dedicated beamtimes, in order to get a full description of the samples. The

X-ray Absorption Near Edge Structure (XANES) region for selected S K-edges is compared with data pertaining to bulk sphalerite ZnS in Fig. 3.8. The main features characterizing the edge (arising from S 1s → 3p-like transitions [95]) are obviously the same along the whole series, even though less defined for the synthesized samples, thus evidencing a certain degree of distortion of the tetrahedral coordination. In all the spectra, a feature at 2482 eV is always present, which however is an artifact generated by the measuring apparatus [3]. Similarly to S K-edge spectra, the Zn K-edge features (see Fig. 3.8) do not show significant variation along the whole series, thus confirming that the Zn^{II} environment is negligibly affected upon doping. As far as the poorer peak definition (particularly evident in the lanthanide doped samples) is concerned, this is likely due to an higher local disorder of the synthesized samples with respect to the reference.

The data pertaining the fitting of Zn K-edges EXAFS functions within a sphalerite model are collected in Tab. 3.5. The data reported evidence that the coordination numbers for the first shell are higher than what expected from the sphalerite crystal structure and, in addition, the nearest neighbors (NN) numbers for undoped and Cu-doped samples are higher than for the other samples. Such discrepancies indicate that, as hinted by XANES spectra, the samples are indeed characterized by an average local disorder, which might be related to the presence of amorphous or spurious phases, not detected by XRD. Even if the presence of an oxide spurious phase was confirmed by SAED, any attempt to include it in the fitting procedure did not lead to physically acceptable results. Such a disorder is also reflected on the higher shells, which are affected by very relevant NN errors.

Particularly interesting are the data concerning the fitting of the dopant edges (see Tab. 3.6). Starting with the ZnS:Cu sample, the corresponding EXAFS function (not shown) presents a monomodal decay, indicating the presence of only one coordination shell. This is confirmed by the fitting of the matching Fourier transform, revealing a coordination number of about 2 S nearest neighbors . Such a low NN number indicates that Cu ions are likely only adsorbed on the surface of ZnS nanostructures and are not embedded in the crystalline structure, neither as a dopant nor as a Cu-rich secondary phase. Such a behaviorcould be related to the absence of Cu bands in the PL spectrum (Cu^{II} usually presents a band in the red region [96], while Cu^{I} gives rise to a band around 472 nm [89]), but the reason of it is still unclear and under investigation.

In addition, the first derivative spectrum of the XANES region for this dopant closely resembles that of chalcocite Cu_2S (see Fig. 3.8c) [97], thus indicating that the Cu is indeed a Cu^{I} rather than Cu^{II}. This is also confirmed by the absence of a pre-edge peak, which, on the other hand, is usually found in transition metals with unoccupied 3d levels.

Moving to ZnS:Mn, structural evidences are consistent with a substitutional char-

---

[3] In particular it is due to the presence of traces of sulfate in the Kapton windows of the ionization chambers.

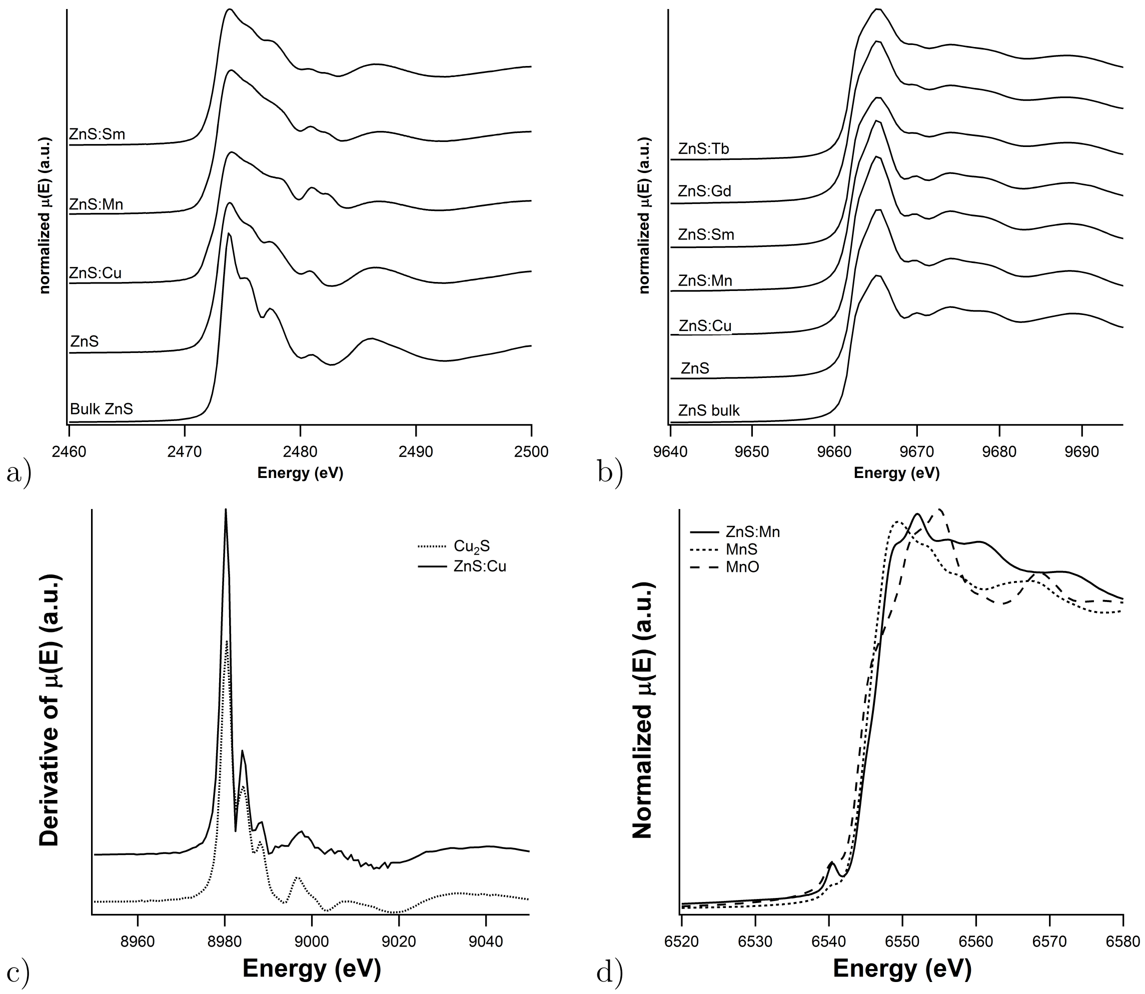

Figure 3.8.: a) S, b) Zn and d) Mn K-edge XANES spectra for doped ZnS nanostructures; c) first derivative Cu K-edge XANES spectra for ZnS:Cu and Cu_2S reference

acter of Mn impurities in the sphalerite structure, in good agreement with other examples present in the literature [98]. The substitutional nature of Mn^{II} ions is further confirmed by the XANES region, where the intensity of the pre-edge peak is higher than in MnS or MnO (see Fig. 3.8d), ultimately testifying the Mn tetrahedral coordination (as in sphalerite), rather than an octahedral environment as in MnS or MnO [99]. Conversely, this is in contrast with what revealed by PL spectroscopy, where Mn related bands were absent, even though in this case such a behavior might be due to a strong luminescence quenching.

L_3-edge XANES spectra of lanthanides doped samples are dominated, as expected for these species, by intense white lines (dipole-allowed transitions from p to empty s and d orbitals, with the latter 50 times more probable than the former) [100]. The corresponding EXAFS functions, when fitted by using a sulfide first shell, do

Sample	**Neighbor**	**Coordination number**	**Distance/Å**	**Debye-Waller factor/Å^{-2}**
Bulk ZnS	S	4	2.35 ±0.01	0.002 ±0.001
	Zn	12	3.83 ±0.01	0.009 ±0.003
	S	12	4.49 ±0.01	0.008 ±0.004
Undoped ZnS	S	6.0 ±0.4	2.34 ±0.01	0.007 ±0.001
	Zn	10.3 ±5.6	3.81 ±0.01	0.018 ±0.006
	S	10.3 ±5.6	4.47 ±0.01	0.016 ±0.010
ZnS:Cu	S	5.7 ±0.4	2.34 ±0.01	0.007 ±0.001
	Zn	10.3 ±5.6	3.82 ±0.01	0.017 ±0.006
	S	10.3 ±5.6	4.48 ±0.01	0.015 ±0.010
ZnS:Mn	S	4.7 ±0.5	2.34 ±0.01	0.006 ±0.002
	Zn	7.0 ±4.0	3.82 ±0.01	0.014 ±0.006
	S	7.0 ±4.0	4.47 ±0.02	0.012 ±0.010
ZnS:Sm	S	4.7 ±0.2	2.33 ±0.01	0.006 ±0.001
	Zn	6.6 ±3.3	3.81 ±0.01	0.016 ±0.005
	S	6.6 ±3.3	4.46 ±0.01	0.017 ±0.011
ZnS:Gd	S	4.6 ±0.4	2.33 ±0.01	0.007 ±0.001
	Zn	4.2 ±3.0	3.81 ±0.01	0.014 ±0.008
	S	4.2 ±3.0	4.46 ±0.02	0.008 ±0.011
ZnS:Tb	S	4.8 ±0.2	2.33 ±0.01	0.006 ±0.001
	Zn	6.6 ±4.1	3.80 ±0.01	0.017 ±0.006
	S	6.6 ±4.1	4.46 ±0.01	0.018 ±0.014

Table 3.5.: EXAFS analysis at Zn K-edge

not yield satisfactory results, which are indeed obtained through the assumption of an oxide environment. The NN numbers is higher than seven for all lanthanides and are as high as 9 for the Sm- and Tb-containing sample. Incidentally, such high coordination numbers are quite common for lanthanides [101]. All lanthanide ions therefore do not disperse as ions into the host matrix, but rather form separated oxidic domains.

To investigate vibrational properties of the doped nanocrystallites, contemporary validating the nanometer-sized particles formation, micro-Raman measurements were performed at room temperature. The transverse optical (TO) and longitudinal optical (LO) first-order phonons for bulk cubic ZnS are reported in literature at ~271 and ~352 cm^{-1}, respectively [102]. In Fig. 3.9, the Raman spectra recorded for the samples are displayed and corresponding peaks positions are reported in Tab. 3.7. As it can be seen, the phonons shift to lower energy in all samples and

Sample	**Edge**	**Neighbor**	**Coordination number**	**Distance/Å**	**Debye-Waller factor/Å^{-2}**
ZnS:Cu	Cu K	S	2.5±0.3	2.24 ±0.01	0.006
ZnS:Mn	Mn K	S	4.0±0.4	2.40 ±0.02	0.009
		Zn	6.0±2.9	3.79 ±0.02	0.017
		S	6.0±2.9	4.44 ±0.03	0.015
ZnS:Sm	Sm L_3	O	8.8±1.7	2.44 ±0.02	0.011
ZnS:Gd	Gd L_3	O	7.3±1.1	2.41 ±0.02	0.008
ZnS:Tb	Tb L_3	O	8.6±1.4	2.38 ±0.03	0.011

Table 3.6.: EXAFS analyses at dopant edges

are affected by substantial broadening. Both evidences are associated to quantum confinement effects arising from the reduced crystallite size. A further important outcome is the overall presence of a weak shoulder of the LO mode, at about 315 cm^{-1}, due to surface vibration, therefore associated to a surface phonon (SP), only occurring in nanostructures, characterized by a high surface/volume ratio [102].

The Raman spectra provide also additional confirmation of the presence of a superficial ZnO layer, as hinted by SAED patterns, since a peak at roughly 430 cm^{-1}, associated with the E_2 mode of hexagonal wurtzite, is found in all samples.

Sample	**TO (cm^{-1})**	**LO (cm^{-1})**	**SP (cm^{-1})**	**ZnO (cm^{-1})**
ZnS bulk[a]	271	352	-	-
ZnS	257	348	315	435
ZnS:Cu	260	345	314	-
ZnS:Mn	262	345	317	428
ZnS:Sm	256	345	316	427
ZnS:Gd	260	346	315	427
ZnS:Tb	257	346	314	430

Table 3.7.: Significant Raman phonons in ZnS nanoparticles: [a] See Ref. [102]

To assess the nature and amount of adsorbed surfactants molecules on the synthesized nanostructures, attenuated total reflectance and thermogravimetric analyses (TGA) were carried out. The ATR spectra (not shown) show all the characteristic peaks for the surfactants, even if, due to extensive similarity, it is not possible to identify specifically the different contributions of the two surfactants used (a 3:1 Brij® 52/Igepal® CO-630 weight ratio). As expected, a very broad band centered at 3300 cm^{-1} is present in the all samples, compatible with the O-H stretching due

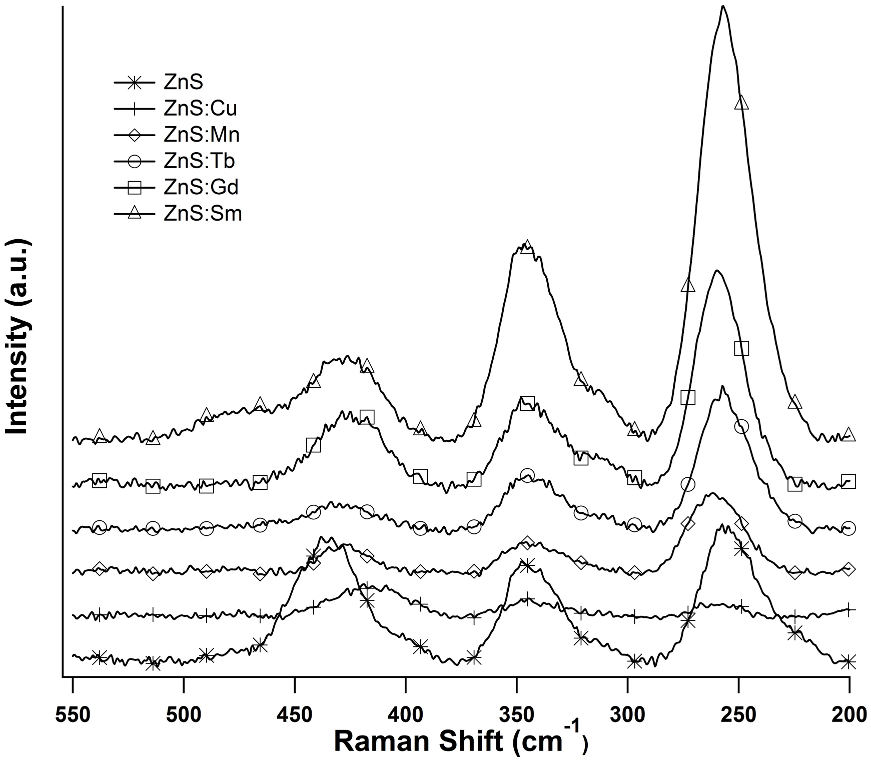

Figure 3.9.: Raman spectra of different ZnS samples

both to the hydroxyl groups of the surfactants as well as to the presence of adsorbed water molecules or surface hydroxyl group on ZnO domains/surface layers. In addition, sharp C-H stretching bands are found in the 2800-3100 cm^{-1} range, while the fingerprint region is characterized by the overlapping of different C-C, C-O and ring modes. In all the samples a sharp peak appears at 1008 cm^{-1}, which is not due to the organic molecules, but rather could be attributed to stretching modes of SO_3^{2-} [103], whose presence was evidenced by XPS and confirmed by micro-Raman.

The actual amount of surfactants adsorbed on the synthesized NPs was determined by Thermogravimetric Analysis - Differential Scanning Calorimetry (TGA-DSC) measurements, carried out in air (Fig. 3.10). Up to 120°C there is an initial 6 % endothermic weight loss due to adsorbed water, followed by exothermic processes in the range 120-500°C, adding up to a further 5 %, consistent with the pyrolysis of the adsorbed surfactants molecules. Subsequently, a weight loss of 2 % is present, whose nature is unclear and it is still under investigation. Above 700°C there is a slight increase in the mass, corresponding to the gradual oxidation of sulfide to oxide, with the intermediate mass gain due to formation of sulfate [104].

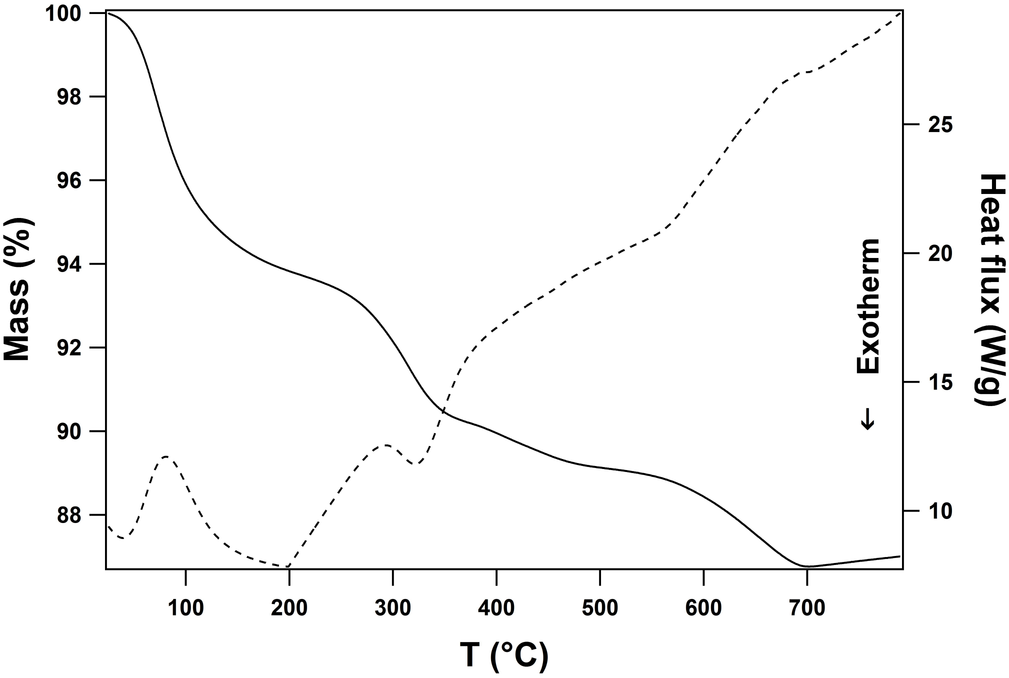

Figure 3.10.: TGA (solid) and DSC (dashed) of ZnS NPs

3.6.3. Conclusions

Pure and TM- and RE-doped ZnS nanostructures were prepared through an easy and reproducible way. The nanoparticles obtained were determined to be crystalline cubic ZnS, characterized by an average crystallite diameter ranging 5-10 nm, with the presence of a superficial crystalline ZnO layer. These nanostructures further aggregate to form a continuous network of aggregates with a size of hundreds of nm, as shown by SEM. XPS and SAED outcomes are consistent with the presence of an oxide surface phase and also of traces of surface sulfite, in particular in the Mn-doped sample. In addition, no XPS features due to dopants were detected. This is probably due to the presence of surfactant adsorbed on the surface (about 5% w/w remains adsorbed on the nanostructures, as determined by TGA measurements; see also ATR), lowering the overall dopant atomic concentration below the detection limit. The presence of TM and RE was indeed confirmed with ICP-MS, showing an excellent agreement between the nominal and the experimental molar ratios. Photoluminescence spectra were dominated by a broad band, characteristics of sulfur vacancies, but no further signal related to the dopants is present in the spectra, possibly meaning that they were not successfully embedded in the host matrix. This is confirmed by EXAFS measurements, which, in Cu doped sample, clearly indicates that copper decorates the surface of the nanostructures, whereas lanthanides tend to form segregated oxide phases. At variance to that, controversial results were obtained for ZnS:Mn. In this case EXAFS outcomes are consistent with substitutional doping (with Mn^{II} found in V_{Zn}), therefore also possibly indicating strong dopant-related luminescence quenching. Overall, the chosen methodology was successful in promoting the room temperature formation of crystalline ZnS nanostructures, but further optimization is needed in order to improve the dopants-induced luminescence.

3.7. Copper sulfide

3.7.1. Introduction

Copper(II) sulfide is a semiconductor with a bandgap of 1.2-2.0 eV and an electric resistivity of 10^{-6} Ωm, giving the material a metallic character [105]. It is usually found as covellite [99], having a complex hexagonal structure (space group $P6_{3/mmc}$) characterized by the presence of layers generated by trigonal planar CuS_3 units separated by tetrahedral CuS_4 units [106] (see Fig. 3.11). Copper (sulfur) ions of CuS_3 units have the +2 (-2) formal oxidation state, while CuS_4 tetrahedral units are assumed to be constituted by Cu^I and S_2^{2-} species. As a whole, among the six Cu ions present in the covellite unit cell, four (two) of them have a tetrahedral (trigonal planar) coordination, while the six sulfur atoms generate two S_2^{2-} and two S^{2-} ions, respectively.

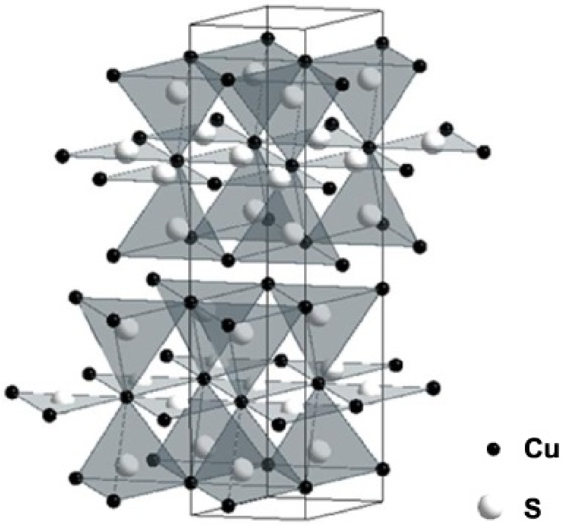

Figure 3.11.: Covellite crystal structure

At the industrial level, copper sulfide is widely used as a cathode material for lithium battery [107], as broad emission band phosphor in LEDs, and in infrared sensors [108], due to a strong absorption in the 800-1400 nm window [109]. CuS is also exploited in the biomedical field, for example benefiting of its catalytic activity in redox reduction to mimic the enzyme peroxidase [110], commonly used for the colorimetric estimation of human blood glucose level. CuS is able to overcome the limitations of this enzyme, namely its lack of stability, difficulty to be produced in large quantities and easiness of denaturation in conditions like strong acidic, basic medium and high temperature. Furthermore, when in form of nanoparticles, CuS is also used as both a diagnostic and a therapeutic medium. Exploiting the low cytotoxicity and IR absorption properties of the CuS NPs [111], it is possible to use them as contrast agents in photoacustic tomography (PAT) of deep tissues [112][4]. The NIR absorption of CuS can also be exploited for photothermal therapy, in particular for photothermal ablation of tumor cells [113]. The use of CuS nanoparticles for biomedical applications has been extensively reviewed in a very recent work [111]. CuS nanostructures have been prepared with a variety of different methods, such as hydro/solvothermal [114, 115], microwave assisted [116, 117] and sonochemical [108, 118] syntheses. They have also been approached by classical colloidal routes [119–121]. Among emulsion-based methods, microemulsions are the most commonly used for the preparation of CuS nanoparticles or nanostructures [122–124], with also some particular cases like water-in-CO_2 microemulsions [125].

In this thesis, the miniemulsion approach was successfully applied for the first time to the synthesis of pure and doped CuS nanostructures. In the present case, syntheses were carried out by employing different sulfur sources, as depicted in Scheme 3.2, to evaluate their effect on the nanostructures composition, crystallinity and morphology. Similarly, also the copper precursor was changed, although in this case the effect was expected to be less important.

3.7.2. Results and discussion

Copper(II) sulfide nanostructures were synthesized *via* miniemulsion by means of different sulfide precursors, such as thiourea (NH_2CSNH_2), thioacetamide (CH_3CSNH_2), thioacetic acid (CH_3COSH), ammonium thioglycolate ($SHCH_2COONH_4$) and sodium sulfide (Na_2S). In this regard, it has to be remarked that Na_2S is widely used as precipitating agent, and it leads to the immediate precipitation of the desired product, whereas the other precursors need controlled conditions (mostly in terms of pH) to release sulfur . For instance, thiourea requires a pH≥8 or thermal/microwave treatment in order to hydrolyze [117]. The formation of active sulfur species (S^{2-}, HS^-, or H_2S) will depend on the pH of the solution; for pH<6.99 hydrogen sulfide is favored, while for pH>17.4 the sulfide is the likely species [127]. In addition, an alternative copper precursor ($CuCl_2$ instead of $Cu(NO_3)_2$) was also employed in selected tests, as well as different Cu:S molar ratios.

To gain an estimate of the average droplet size, the obtained milky suspensions were firstly characterized through Dynamic Light Scattering (DLS) measurements. These measurements were carried out on selected miniemulsions (pure and Eu^{III} doped CuS, obtained by using Na_2S and $Cu(NO_3)_2$, as discussed in more detail below),

---

[4] Unlike other optical imaging modalities, (e.g., confocal microscopy, two-photon microscopy; see Sec. 3.1), PAT relies on both diffused and ballistic light and thus can be used to image deeper biological tissues. Due to overwhelming scattering effects of biological tissues irradiated by light, near-infrared (NIR) radiation must be used, since it shows a relatively low absorption coefficient and a low scattering coefficient. In this regard, CuS NPs are an attractive choice as contrast agents for this imaging techniques since they strongly absorb in the desired region (most commonly a 1064 nm laser is used) and by selectively delivering the NPs to the desired tissues they can enhance the PAT signal intensity.

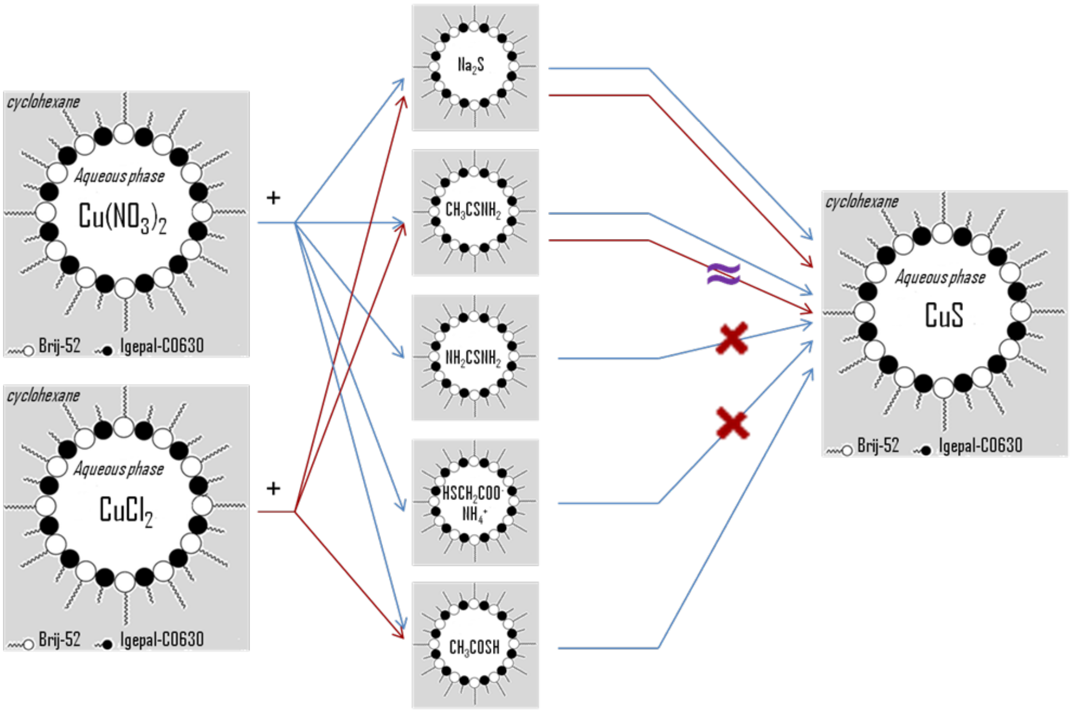
cyclohexane
Aqueous phase
Cu(NO3)2
Brij-52
Igepal-CO630
cyclohexane
Aqueous phase
CuCl2
Brij-52
Igepal-CO630
+
+
Na2S
CH3CSNH2
NH2CSNH2
HSCH2COO NH4+
CH3COSH
cyclohexane
Aqueous phase
CuS
Brij-52
Igepal-CO630

Scheme 3.2: Different reaction pathways tested [126]

being the overall composition (aqueous phase/cyclohexane/surfactants) unchanged between the different samples. Mean hydrodynamic diameters in the two samples were found to be comparable within the experimental error (360 ± 21 nm for CuS, 398 ± 43 nm for Eu^{III} doped sample, see Fig. 3.12).

Powders obtained after suspensions precipitation and centrifugation were firstly investigated by X-ray diffraction (see Fig. 3.13 and Tab. 3.8).

Cu^{II} precursor	Sulfur source	Crystalline phase(s)	Average crystallite size
$Cu(NO_3)_2$	Na_2S	covellite	14 nm
	CH_3CSNH_2	covellite	13 nm
	CH_3COSH	covellite	15 nm
	$SHCH_2COONH_4$	not determined	-
	NH_2CSNH_2	not determined	-
$CuCl_2$	Na_2S	covellite	12 nm
	CH_3CSNH_2	covellite + not determined	-

Table 3.8.: Experiments with different copper and sulfur sources

As it can be seen, the use of Na_2S leads to the formation of covellite (JCSD PDF N. 00-001-1281) regardless of the nature of the copper precursor. This is not particu-

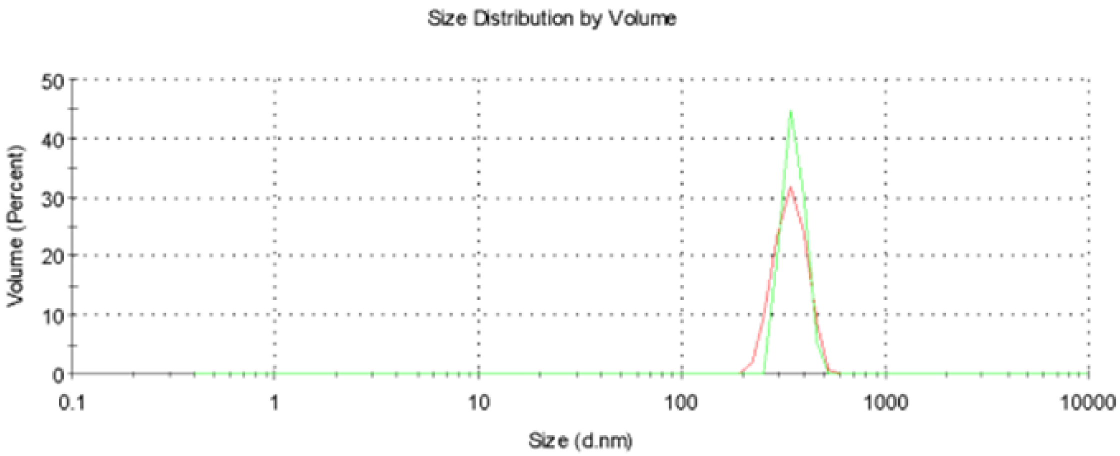

Figure 3.12.: DLS curves for pure CuS (red line) and CuS:Eu (green line)

larly surprising because S^{2-} ions are readily available and CuS is quite insoluble ($K_{sp} = 6 \cdot 10^{-16}$ [128]). Whereas thioacetamide and $Cu(NO_3)_2$ yielded pure covellite, when thioacetamide reacted with copper chloride further phases appeared along with covellite. A rationale of such evidence has not yet been found and further investigations are needed.

Thioacetic acid, ammonium thioglycolate and thiourea were tested only in combination with $Cu(NO_3)_2$. Among them, only thioacetic acid induced the CuS formation. As a matter of fact, thiourea produced an amorphous green precipitate (CuS is usually brown) rich in the organosulfur precursor, as determined by FT-IR (data not shown). This is probably due to the fact that the final miniemulsion had a pH value in the 2.5-3.0 range, too acidic to induce an efficient thiourea hydrolysis [108, 117]. Also in the case of ammonium thioglycolate, no formation of any crystalline material was achieved since, similarly to thiourea, its hydrolysis is favored for basic pH values.

Further experiments were also carried out by varying the Cu-precursor/S-precursor molar ratios (see Tab. 3.9). Briefly, XRD data point out that the Cu:S molar ratio mainly influences the purity of the crystalline phases, and that an excess of S-containing species is preferable. A stoichiometric ratio usually led to the presence of a spurious phase which, in the case of samples prepared with thioacetamide, was identified as calcantite $CuSO_4$. The sulfate ion might be generated by oxidation of HS^- by $OH\cdot$ radicals generated by water sonolysis during the emulsification process [94].

When formed, covellite average crystallite sizes, determined by using the Scherrer equation [129, 130], were all in the range 11-15 nm, regardless of the sulfur source used. This indicates that the determining factor for the crystallite size is the emulsification process, and not the reaction pathway. In this regard, it can be useful to underline that these results cannot be compared with the DLS ones. The outcomes

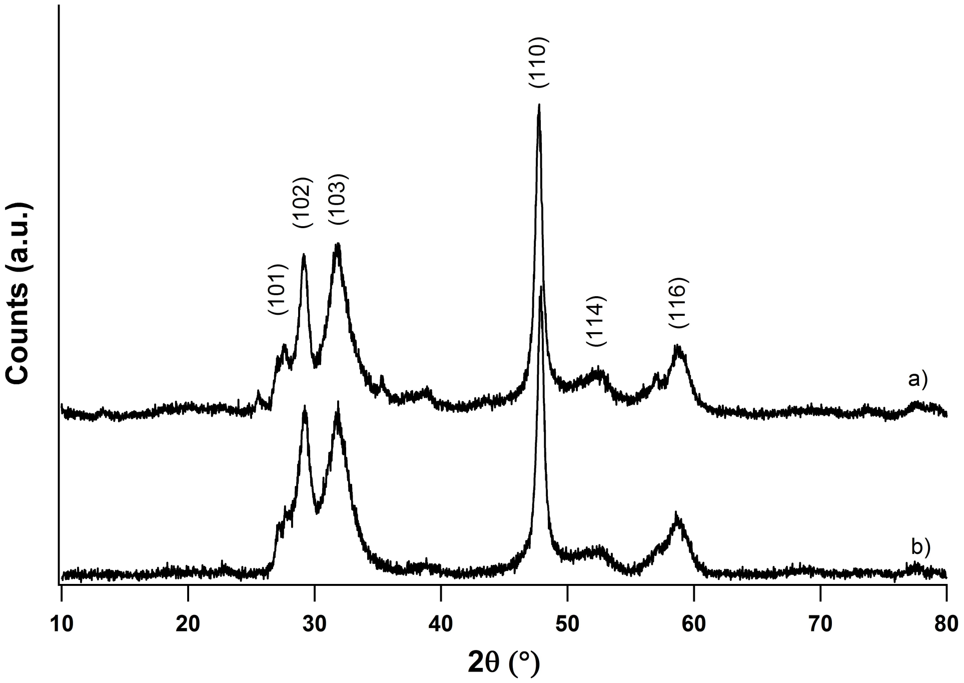

Figure 3.13.: XRD diffractograms for samples obtained from Na_2S and different copper sources: a) $CuCl_2$; b) $Cu(NO_3)_2$

collected by using the Scherrer equation simply state that within each droplet there are several crystallites of similar dimension, while DLS determines the size of the crystallite aggregates including the surfactants shells. The best results in terms of reproducibility and crystallinity were obtained by using sodium sulfide and copper nitrate, in a 2:1 molar ratio. The following discussion therefore refers to specimens obtained by using these precursors.

TEM and SEM microscopies (Fig. 3.14) were used to better evaluate the morphology of the synthesized nanostructures. Moreover, SAED, coupled with TEM measurements, allowed a further insight about the samples crystallinity. Both TEM and SEM micrographs evidence that samples are formed by aggregates of nanoflakes, a behavior already reported in the literature [117, 131]. The formation of these flat structures is likely due to the intrinsic anisotropic characteristics of CuS [132]. The covellite crystal structure can also be seen as alternating CuS_3–CuS_3–CuS_3 layers and S–S layers along the c axis, with the interactions in the latter layer being weaker and involving longer distances [133]. This anisotropy might therefore affect the crystal growth rate along this axis.

These nanostructures are represented by sheets with a width of several hundreds of nanometers, which organize in flake-like structures. The darker rod-like structures can be interpreted as clustered tilted flakes, showing therefore a thickness of less than 10 nm. Furthermore, even though SAED confirmed that the main phase is

Cu^{II} precursor	S^{2-} **precursor**	**Cu:S molar ratio**	**Crystalline phase**	**Average crystallite size**
$Cu(NO_3)_2$	Na_2S	2:1	covellite	11 nm
$Cu(NO_3)_2$	Na_2S	1:1	covellite + not identified	13 nm
$Cu(NO_3)_2$	Na_2S	1:2	covellite	14 nm
$Cu(NO_3)_2$	CH_3CSNH_2	1:1	covellite/calcantite	12 nm
$Cu(NO_3)_2$	CH_3CSNH_2	1:2	covellite	13 nm
$Cu(NO_3)_2$	CH_3COSH	1:2	covellite	15 nm
$CuCl_2$	Na_2S	1:1	covellite	11 nm
$CuCl_2$	Na_2S	1:2	covellite	12 nm
$CuCl_2$	CH_3CSNH_2	1:2	covellite + not identified	-

Table 3.9.: Experiments with different Cu:S precursors molar ratios

that of covellite, it also hinted towards the presence of amorphous or poorly crystallized nanometric copper oxide domains; in fact, a diffused halo with maxima corresponding to tenorite CuO reflections is present in all samples. The presence of this contaminant might be due to superficial oxidation of the flakes. As in the previously discussed case (see Sec. 3.6), the formation of this oxide is assumed to be limited to the surface.

In addition to pure CuS nanostructures, nanocrystalline covellite particles incorporating Mn^{II}, Sm^{III}, Eu^{III}, Gd^{III} or Tb^{III} were prepared with a Cu:M atomic ratio of 50:1. The doping ions did not induce relevant lattice distortion, since no shift in the XRD reflections (see Fig. 3.15) was determined, apart in the case of CuS:Mn and CuS:Gd, for which a slight shift of 0.1° towards lower angles was found. Furthermore, no additional spurious crystalline phases were revealed.

With the aim of investigating their surface chemical composition and evaluate the incorporation of the dopants in the materials, samples were investigated by XPS. In all the samples, the S 2p signal (see Fig. 3.16) might be deconvoluted in the two main contributions, one due to the S^{2-} (161.7-161.9 eV), the other to S_2^{2-} (163.0-163.5 eV), typically found in the covellite crystal structure [92, 134]. Even if reference to the covellite crystal structure would imply a S_2^{2-}:S^{2-} area ratio of 2:1, the one experimentally found was 1:2.6. In addition, some samples showed the presence of a further peak at 168.3-168.5 eV, symptomatic of S^{VI}, due to the presence on the surface of a small fraction of $CuSO_4$.

As far as the Cu 2p signal is concerned, the doublet components are centered at 932.0 eV ($2p_{3/2}$) and 952.0 eV ($2p_{1/2}$) respectively. Focusing on the $2p_{3/2}$, this can be fitted with three different contributions, the main one lying at 932.1 eV, and two smaller components at 933.6 and 934.9 eV. The feature at 932.1 eV (area %: 85) corresponds to CuS, while the other two components may be ascribed to CuO (area %: 13) and $CuSO_4$ (area %: 2), in order of increasing binding energy [92, 93]. The presence of an oxidic surface layer is in agreement with what determined by SAED, and

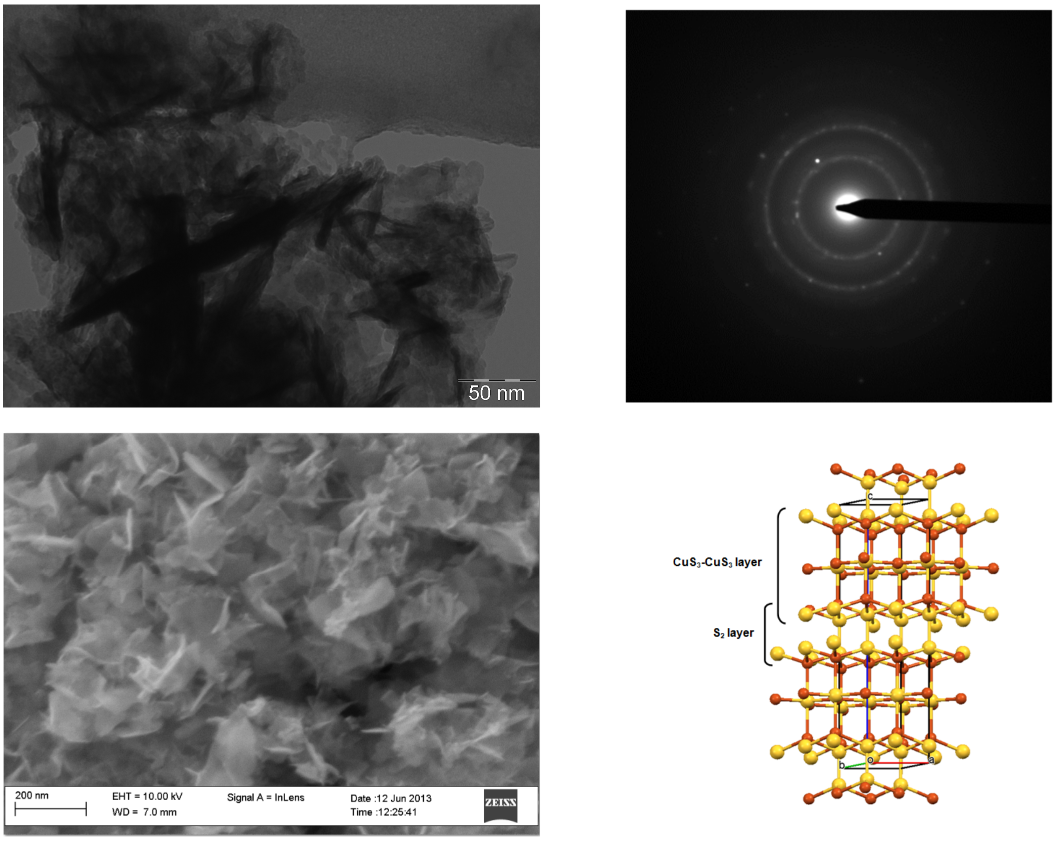

Figure 3.14.: top: TEM (left) micrograph and corresponding SAED (right) for pure CuS sample; bottom: SEM (left) , and layered structure (right)

its presence is further confirmed by calculating the corresponding modified Auger parameters α', defined as $\alpha' = BE_{Cu2p_{3/2}} + (1486.6 - BE_{Auger})$ [135]. The experimental values are 1850.3 and 1851.8 eV for CuS and CuO respectively, compatible with literature values [92, 93]. A semi-quantitive analysis (Tab. 3.10) of the surface composition confirms a Cu:S atomic ratio of about 1, as expected from stoichiometry, even if a relevant amount of copper is in the form of CuO. The high amount of carbon and oxygen is mainly due to the presence of adsorbed surfactants and surface contamination. Despite the deconvolution of the O 1s peak could give further information on the oxide and sulfate phases, the signals of these species (in particular of the sulfate phases) overlaps with that of the surfactants ether chains and a careful determination of the different contributions was substantially prevented.

The detailed investigation of the dopant regions (in particular, the Eu doped sample was investigated) did not show any appreciable signal, probably due to the low atomic concentration of this species (assuming the absence of clustering phenomena, an atomic percentage of about 0.1% is expected, below the detecting limit of 0.2%). In order to confirm the effective presence of the Eu as well as of the other dopant species, ICP-MS measurements were performed. The results summarized in

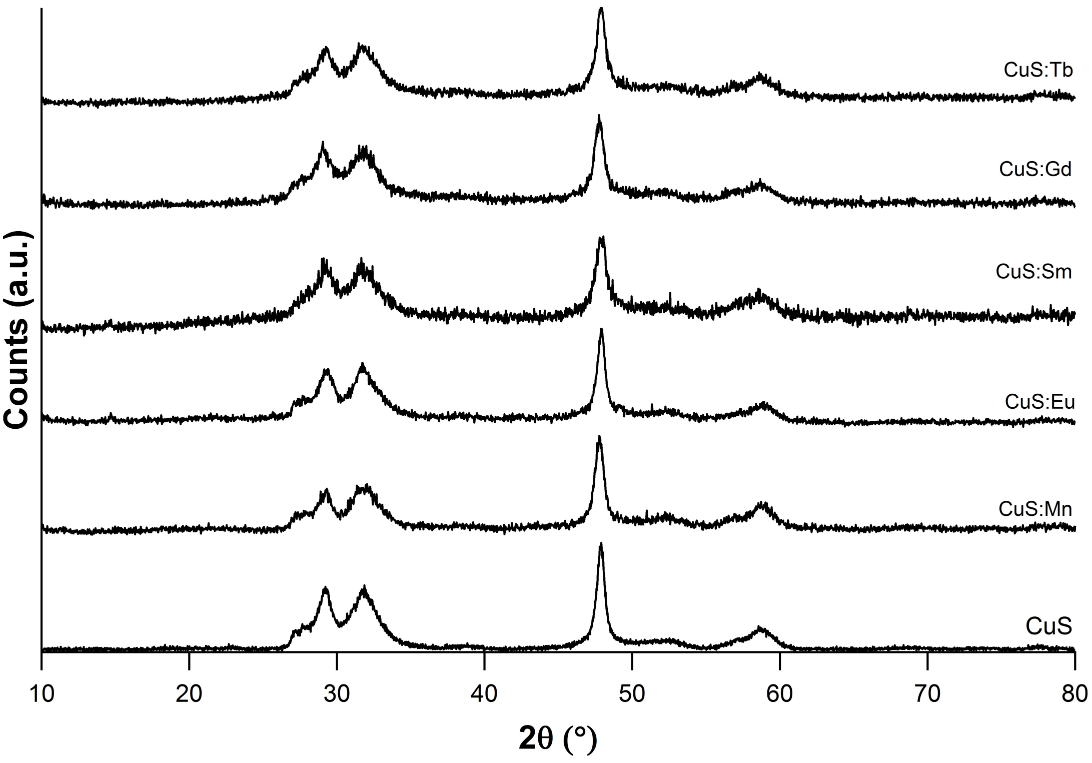

Figure 3.15.: XRD diffractograms of pure and doped CuS nanostructures

Sample	%O	%C	%Cu	%S	Cu/S
CuS	15.3	71.7	6.3	6.7	0.9
CuS:Eu	23.0	64.3	6.7	6.0	1.1

Table 3.10.: Atomic percentages for CuS and CuS:Eu

Tab. 3.11 show excellent agreement between the nominal and experimental values, evidencing a successful doping process of the sulfide nanostructures.

Insights into the local coordination environment of doping species in the hosting structure were gained by carrying out a series of X-ray Absorption Fine Structure experiments at Elettra (at S K-edge) and Swiss Light Source, SLS (at metals K- or L_3-edges).

The Cu K-edge XANES spectrum for the pure CuS sample is compared, in Fig. 3.17a, with those of reference CuS and CuO, the latter to possibly rule out the presence of bulk oxidic domains. The spectrum of reference CuS shows a peak at 8987 eV, characteristic of a tetrahedrically coordinated domain [97]. Even though less prominent, the same feature in present in the synthesized sample. Fig. 3.17b shows the k^2-weighted EXAFS functions for the Cu K-edge of different samples (a) pure

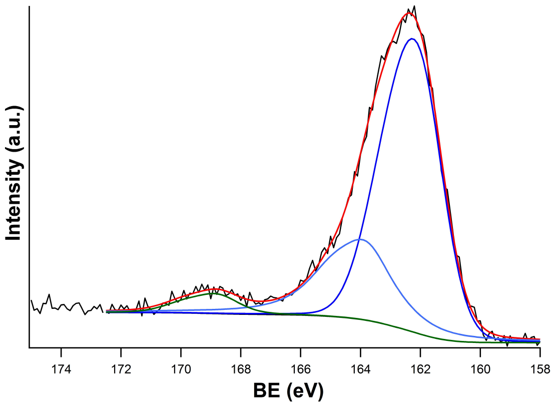

Figure 3.16.: S 2p signal for pure CuS sample

Sample	Nominal atomic ratio	Experimental atomic ratio
CuS:Eu	50:1	49.6 ± 3.5
CuS:Sm	50:1	51.6 ± 3.7
CuS:Tb	50:1	50.2 ± 4.1
CuS:Mn	50:1	47.9 ± 4.8
CuS:Gd	50:1	47.9 ± 4.8

Table 3.11.: ICP-MS measurement on doped CuS samples (Confidence interval: 95%)

CuS, b) CuS:Eu, c) CuS:Mn, d) Cu:Sm) along with those of reference CuS and CuO. The inspection of Fig. 3.17b clearly testifies that spectra of our samples are significantly different from the reference CuS and CuO ones. In particular, they show a monomodal evolution, indicating a short range disorder. Interestingly, the fitting of the EXAFS data with a mixed sulfide/oxide shell does not provide good results, while the assumption of a purely sulfide shell results in a satisfactory fitting, with an average coordination number of 4.3 ± 0.6 and a Cu-S bond length of 2.23 ± 0.03 Å. This confirms that the tenorite CuO domains are only on the outer layers.

XAFS spectra were also recorded at sulfur K-edge (see Fig. 3.18a). As far as the XANES region is concerned, it does not change along the different samples, thus indicating the negligible perturbation induced by doping at this edge. Moreover, the recorded spectra are very similar to those reported in literature for covellite [97, 133, 136]. In particular, the main peak can be assigned to S 1s → 3p-like transitions, whereas the pre-edges peaks labeled “a” and “b” in Fig. 3.18a are due to transitions to 3p states hybridized with Cu 3d atomic orbitals (AOs) in CuS_3 and CuS_4 covellite domains, respectively [97, 136]. Incidentally, all XANES spectra are

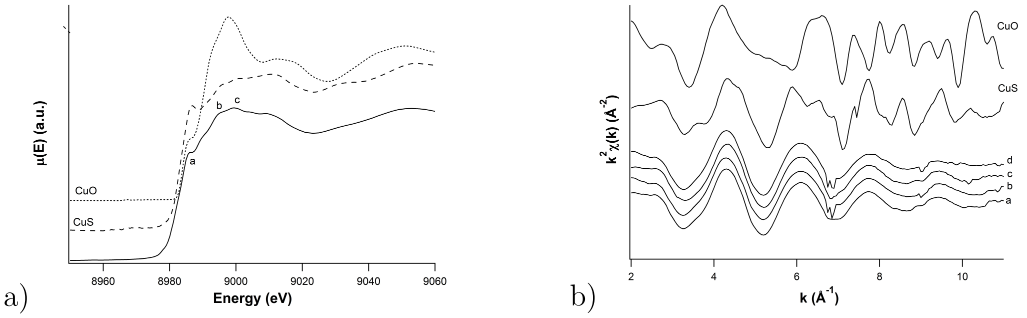

Figure 3.17.: a) XANES and b) EXAFS spectra (a) pure CuS; b) CuS:Eu; c) CuS:Mn; d) Cu:Sm) at Cu K-edge for the synthesized samples, compared to bulk CuS and CuO

characterized by an intense absorption at about 2482 eV, due to a problem in the measuring apparatus.

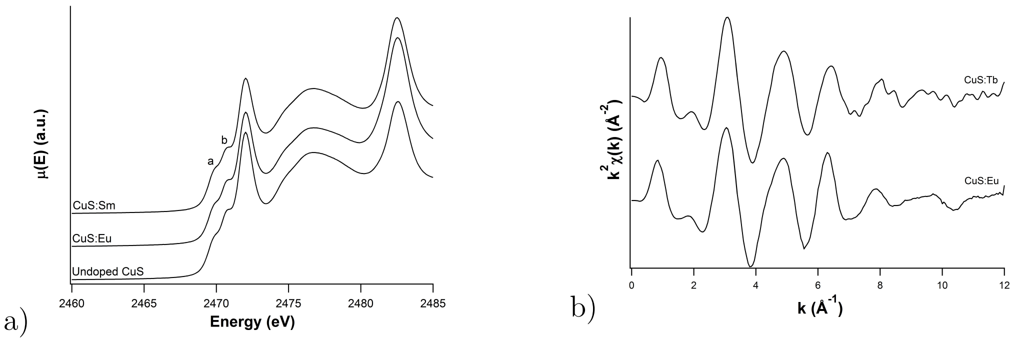

Figure 3.18.: a) XANES spectra at S K-edge for CuS samples; b) EXAFS spectra for lanthanide L_3-edges

As far as the dopants are concerned, Eu and Tb L_3 edges (Fig. 3.18b) give rise to almost identical EXAFS functions, indicating a similar coordination environment. This is not particularly surprising because these lanthanide ions are known to have similar size and chemical behavior. On the other hand, first shell fittings reveal that both lanthanides are found in an oxidic environment, with a coordination number of 10.1 ± 1.2 oxygen atoms placed at 2.42 ± 0.03 Å in the case of the Eu doped sample. It can be useful to remind that such a high coordination number is not unusual for lanthanides [101]. The formation of these oxidic domains is understandable in terms of the higher affinity of lanthanides towards oxygen rather than sulfur [99].

These materials were also characterized by a functional point of view, in particular by acquiring photoluminescence spectra (λ_{exc}=325 nm) in the UV-Vis range (see Fig. 3.19). The emission spectra are all characterized by a broad band in the UV region, centered at 365 nm, whose attribution is still controversial. The photoluminescence behavior of CuS is not yet fully understood, but it was found to be strongly influenced by morphology and inherent microstructures [137, 138][5]. The sharp peaks typical of the lanthanide emissions could not be observed, and this might be due to a strong luminescence quenching induced either by the residual organic species adsorbed on the surface, by the highly absorbing dark matrix or by its defectivity.

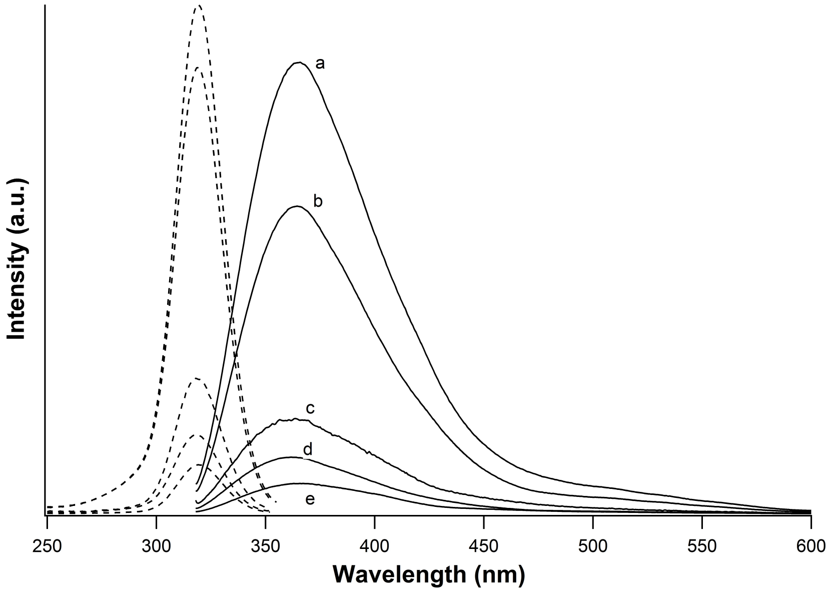

Figure 3.19.: Emission (solid line) and excitation (dashed) spectra for a) CuS;Mn (emission spectrum scaled 1/10); b) CuS:Gd; c) CuS:Tb; d) CuS:Sm; e) CuS:Eu

The quantity of adsorbed surfactants remaining on the surface was estimated by thermogravimetric analysis, coupled with differential scanning calorimetry, performed under nitrogen atmosphere. The solid curve in Fig. 3.20 evidences an initial 4 % weight loss up to about 150°C, corresponding to water desorption, followed by an exothermic multistep-wise loss of 19 %, in the 150-400°C range, due to pyrolysis of the surfactants. The final 7 % weight loss might be due to the decomposition of the covellite to digenite $Cu_{1.8}S$ and/or chalcocite Cu_2S [141, 142].

3.7.3. Conclusions

Pure and doped covellite CuS nanostructures were synthesized at room temperature in the controlled space of droplets produced by miniemulsion, using different precursors for both Cu and S. Most sulfide precursors successfully induced the generation of nanocrystalline materials, while neither ammonium thioglycolate nor thiourea allowed the precipitation of CuS or other crystalline materials, probably due to the

---

[5] For example, besides the tail of the broad band, the 400 –600 nm wavelength range does not include any signal, as is commonly observed for elongated CuS nanostructures[137, 139], whereas polycrystalline hollow spheres present a broad band at 530 nm [140].

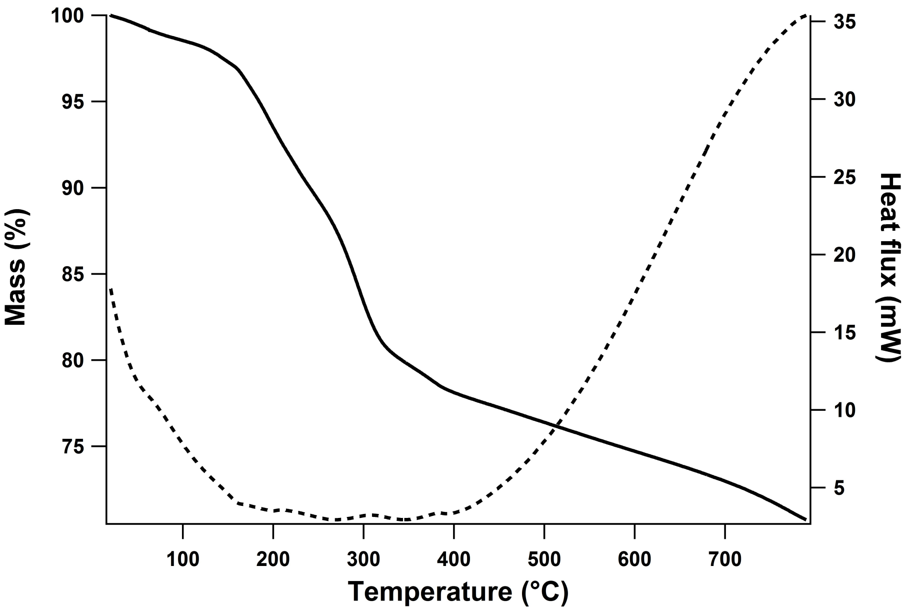

Figure 3.20.: TGA-DSC curve of undoped CuS

fact that the acidic conditions present in the droplets did not favor the decomposition of these precursors. Best results in terms of reproducibility, product purity and yield were obtained by using copper nitrate and sodium sulfide, in a molar ratio of 1:2. This combination was also used to prepare a series of CuS:M (Mn^{II}, Sm^{III}, Eu^{III}, Gd^{III} and Tb^{III}) doped nanostructures with a Cu:M ratio of 50:1 (average crystallite size 12-15 nm). The obtained powders were found to have platelet morphology, with an average diameter of hundreds of nanometer and a thickness of few nanometers, a morphology already reported in the literature. XPS and SAED outcomes were consistent with the presence of an oxide spurious surface layer and traces of surface sulfate. The dopants were not revealed by XPS, but their presence was confirmed by ICP-MS, showing very good agreement between experimental and nominal ratios. None of the dopant was found as a substitute for copper, but EXAFS analysis evidenced that lanthanides tend to form segregated oxide phases. Luminescence spectra were dominated by a strong broad band, but did not show any peak associated to the dopant, probably due to intense quenching phenomena, associated with a 19 wt% of surfactants adsorbed on the surface, or due to the highly absorbing dark matrix. The reason for the observed flake-like morphology can be traced back to the mentioned anisotropic characteristics of covellite. The nanostructures nucleate and grow in the quite big ($\approx$ 300 nm) droplets formed by the miniemulsification process, and the confined space plays a relevant role in determining the structural evolution of the copper sulfide. In this regard, it should be highlighted that the same reaction, carried out with the same precursors and molar ratio in a batch instead of in miniemulsion droplets did not eventually lead to the formation of crystalline covellite, but rather of amorphous species.

3.8. Calcium fluoride

3.8.1. Introduction

Similarly to their oxide- and sulfur-based counterparts, rare earth-doped metal fluoride compounds are very attractive materials for a wide variety of potential applications, including advanced phosphor, photonic, display monitors, bioimaging, light amplification, anti-fraud labeling [143], and optical bioimaging, as seen in previous Sections. On the other hand, metal fluorides present additional advantages, in particular a high transparency in a wider wavelength window, ranging from infrared to vacuum ultraviolet (VUV), low defectivity, and a low phonon energy, resulting in a decreased non-radiative transition probability of the embedded luminescent ions and better luminescent properties [143]. In addition, these ions may show near infrared (NIR) to red or NIR to NIR upconversion properties, of particular importance for biomedical purposes. In fact, an excitation in the NIR region (around 1000 nm) coupled with emission also in the NIR (or in the red) is very advantageous, due to the high transparency of the biological fluids in this region, together with a low tissues damage and an almost total absence of autofluorescence [144].

Among the fluoride compounds, CaF_2 is particularly appealing thanks to its stability and non-hygroscopic behavior, and thanks to its fluorite crystal structure (consisting of a simple cubic array of fluoride ions with every alternate cube occupied by the divalent cation Ca), it is a good host for doping ions, also in high concentrations [145]. In addition, it shows an excellent biocompatibility [146].

Ln-doped CaF_2 nanostructures have been prepared by a wide variety of methods such as sol-gel [147], solvo/hydrothermal methods [144, 148, 149], polyol-mediated [150], thermal decomposition of precursors [151], and colloidal techniques, such as microemulsion [23, 143].

In this framework, it is here reported the synthesis of rare earth-doped calcium fluoride nanoparticles (Ln=Sm^{III}, Gd^{III} and Tb^{III}, with Ca:Ln=50:1), prepared by a inverse miniemulsion approach, by simple co-precipitation in confined space.

3.8.2. Results and discussion

The nanostructures were prepared using NaF as a simple fluoride source, and calcium nitrate. The miniemulsions produced by mixing and ultrasonication of the two starting emulsions were firstly analyzed by DLS, in order to investigate the average size of the droplets obtained by these method. Such analyses, performed for pure CaF_2 samples, revealed a mean hydrodynamic radius of 180 nm, showing also a good reproducibility of the method proposed. After aging overnight, the nanoparticles formed a precipitate and the corresponding powders were separated by centrifugation (for more details see Chap. 5). These powders were firstly characterized by X-ray diffraction, with the aim of examining the possible formation of crystalline materials. All samples showed the formation of crystalline fluorite (JCSD PDF N: 77-2093), at the same time evidencing the absence of any spurious amorphous phases and, in the case of the doped materials, of secondary phases due to the doping ions (see Fig. 3.21).

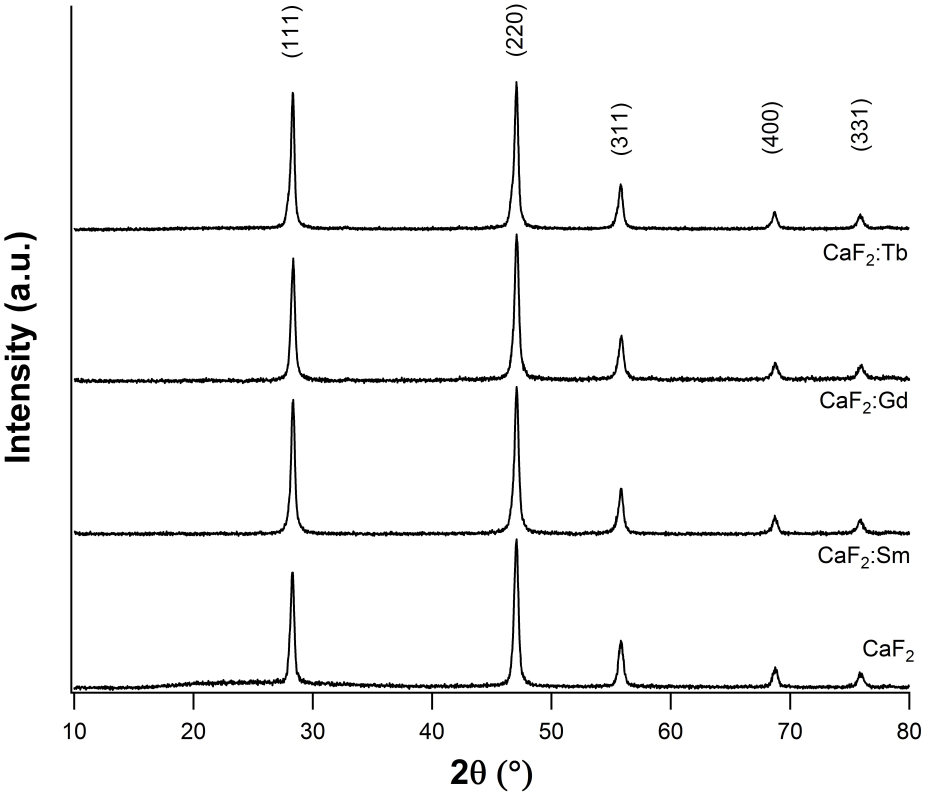

Figure 3.21.: XRD diffractograms for pure and doped CaF_2 nanostructures

In Tab. 3.12 the crystallite sizes, determined by using the Rietveld refinement method [152, 153], are reported, showing an average value of 36-37 nm. In the Tab. 3.12, the lattice constants *a*, are also listed. Upon insertion of the doping ions in the lattice, slight distortions in the lattice are induced, and correspondingly XRD reflections shift to higher angles; the difference is more evident in the case of the sample doped with terbium. This is not surprising, since terbium has the shortest ionic radius of the three dopants [87, 154].

As reported in Sec. 2.3, the ultrasonication process, by producing high shear forces, induces many fission and fusion events between droplets, affecting the average droplet size. In this experiment, in order to investigate how the final dimensions of the NPs crystallites are influenced by this homogenization process, the ultrasonication time was varied (t=40, 60, 120 and 180 s), both for the preparation of the starting miniemulsions and the final one. The obtained powders were examined by

Sample	**Average crystallite size (nm)**	**a (Å)**	**Ionic radius (pm)**
CaF_2	36.9±0.5	5.4653	Ca^{II}: 1.12
CaF_2:Sm	35.6±0.5	5.4674	Sm^{III}: 1.079
CaF_2:Gd	37.0±0.5	5.4682	Gd^{III}: 1.053
CaF_2:Tb	37.3±0.5	5.4688	Tb^{III}: 1.04

Table 3.12.: Average crystallite size, as determined by Rietveld method, lattice constants and cations ionic radii for a 8 coordination

XRD, and the average crystallite sizes, as determined by Rietveld refinement are shown in Tab. 3.13, together with corresponding lattice parameter a.

Sonication time	**Average crystallite size (nm)**
40 s	77.8±1.5
60 s	63.1±0.5
120 s	39.9±0.5
180 s	36.9±0.5

Table 3.13.: Influence of sonication time on crystallite sizes

Fascinatingly, the crystallite size show a decrease with increasing sonication time (increasing the sonication time from 40 s to 180 s yields a decrease in the crystallite diameter down to less than half the initial value,see Fig. 3.22). This is a very important result, confirming the key role played by the ultrasounds in forming and stabilizing the nanodroplets, which therefore act as nanoreactors.

The microstructure and morphology of the obtained nanostructures were investigated by means of TEM and SEM microscopy; the TEM micrographs collected for these samples (see Fig. 3.23) showed a common morphology characterized by the presence of grains with a size in the 60-100 nm range on which smaller, darker domains are found. Selected area diffractograms of the grains showed bright spots corresponding to the fluorite structure, in agreement with XRD results, but also evidenced the presence of a second phase, displayed as continuous, homogeneous rings, which was identified as CaO (JCSD PDF N: 77-2010).

Dark field images registered by using a portion of the oxide diffraction rings evidenced that the darker domains seen in bright field are indeed oxide portions, highlighting therefore the presence of an oxide layer on the fluorite grains. SEM micrographs (see Fig. 3.24) were consistent with TEM findings, and showed agglomerates of quasi-spherical nanoparticles whose average size is 50-100 nm. This size,

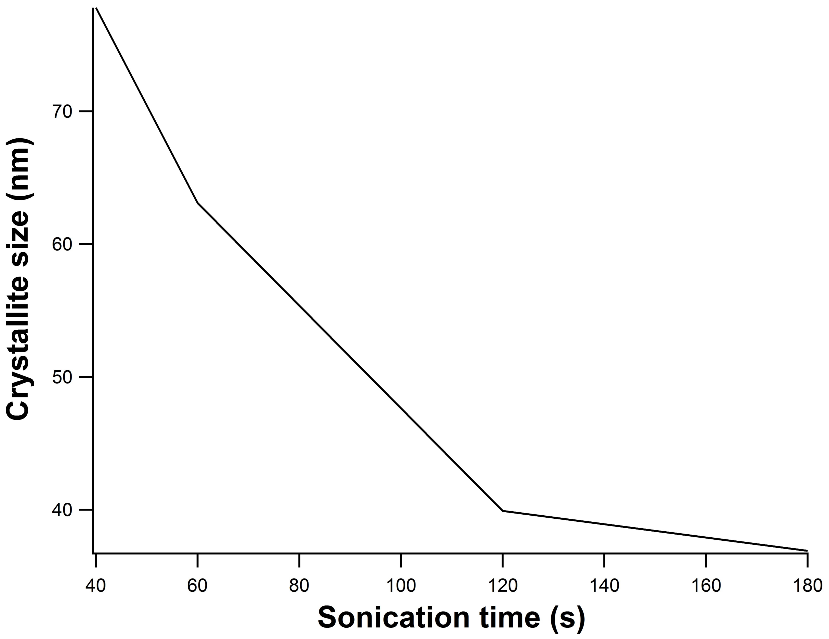

Figure 3.22.: Average crystallite size vs sonication time

comparable with the the average crystallite size of around 40 nm, could mean that the particles were composed of few crystallites.

A further confirmation of the presence of an oxide surface layer comes from XPS analysis, performed on pure and doped CaF_2 samples, the results of which are summarized in Tab. 3.14. The $Ca2p_{3/2}$ peaks present two components, one centered at 346.9-347.4 eV, compatible with the oxide ($Ca2p_{3/2}$=346.7-347.3 eV [93]), and a second major one (see percentages reported in Tab. 3.14), lying at 347.5-348.2, representing the fluoride ($Ca2p_{3/2}$=347.8-348.1 eV [93]). The F1s signals are found at 684.3-684.5 eV, values typical of calcium fluoride (F1s=684.6 eV [92]). The O1s peak can be deconvoluted into two contributions, one at about 530-531 eV, compatible with CaO, and a second one at higher binding energy (532-532.5 eV), due to the ethylene glycol chains in the surfactants. As for the dopant signals, the binding energy values for Sm and Gd $3d_{5/2}$ peaks are compatible with a Ln^{III} ion in a fluoridic environment, while, for the Tb doped sample, the signal-to-noise ratio is too low to discriminate accurately the $3d_{5/2}$ signal. Interestingly, the Tb doped sample is also the one for which the CaO components of the $Ca2p_{3/2}$ peak is more relevant.

Through a XPS semi-quantitative analysis (see Tab. 3.15), the amount of each detected element was determined. As it can be seen from Tab. 3.15, all samples present high amounts of carbon, due to the presence of surfactants adsorbed on the surface and external contamination. The Ca:F atomic ratio was determined to be in accordance to the nominal 1:2 ratio, within the experimental error. Fascinatingly, the better accordance is found for the Sm doped sample, which presents a lower carbon

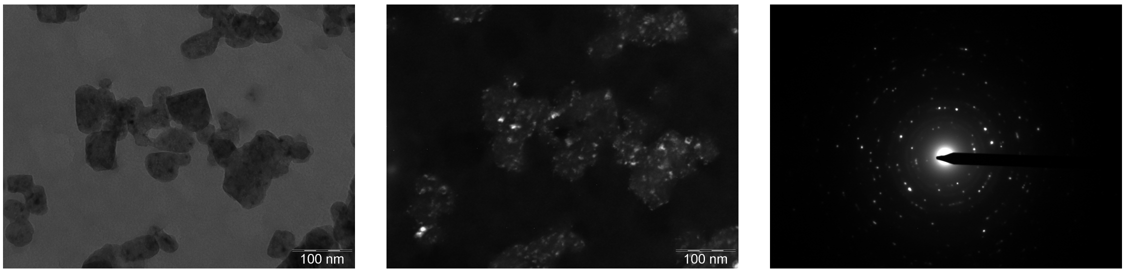

Figure 3.23.: Bright (left) and dark (center) field TEM micrographs. Dark field images were recorded using a portion of the continuous rings found in the SAED diffractogram (right)

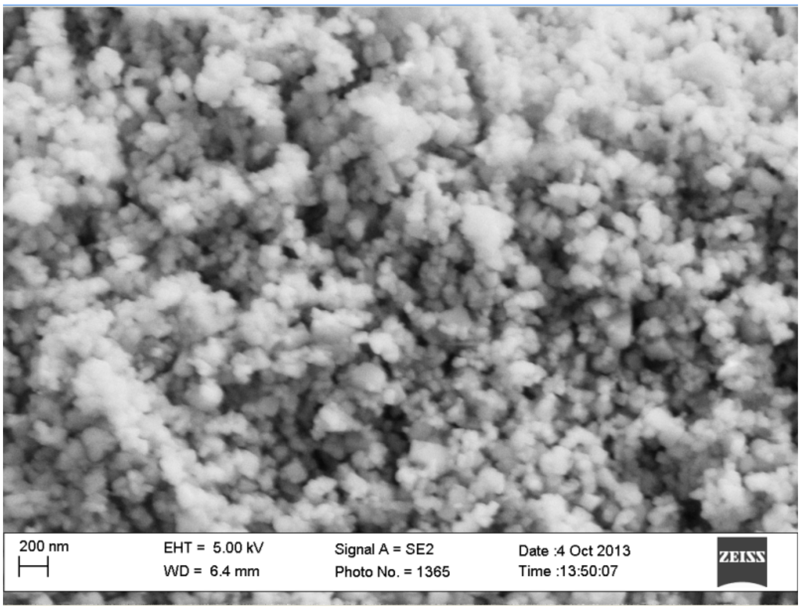

Figure 3.24.: SEM micrograph of CaF_2 nanoparticles obtained by miniemulsion

content. On contrary, for the Gd sample this content is higher, thus partially explaining the higher CaO content and low signal-to-noise ratio for Gd, since, due to surface specificity of XPS, the analysis is strongly affected by contamination.

The successful embedding of gadolinium and of the other dopants was confirmed also by ICP-MS, revealing an excellent agreement between nominal and experimental atomic ratios, as reported in Tab. 3.16.

The obtained powders were also investigated by Raman spectroscopy (λ_{exc}=532 nm), in order to assess the effect of the dopants presence on the crystal lattices. The spectra are characterized by an intense signal at around 320-325 cm^{-1} (see Fig. 3.28), distinctive phonon vibrational band of cubic CaF_2, corresponding to the T_{2g} vibrational mode and due to fluorine ions oscillating towards each other [155]. For pure CaF_2 and CaF_2:Gd this signal is found at 325 cm^{-1}, while for the other samples this peak

Sample	**$Ca2p_{3/2}$ (eV)**	**F1s (eV)**	**Dopant $3d_{5/2}$ (eV)**	**O1s (eV)**
CaF_2	347.4 (34 %) 348.1 (66 %)	684.5	-	531.0 532.4
CaF_2:Sm	346.9 (16 %) 347.6 (84 %)	684.3	1083.5	531.5 532.5
CaF_2:Gd	346.7 (25 %) 347.5 (75 %)	684.4	1187.0	530.6 532.2
CaF_2:Tb	347.4 (48 %) 348.2 (52 %)	684.5	Not available	530.0 532.1

Table 3.14.: Binding energy values determined by XPS

Sample	**C %**	**O %**	**Ca %**	**F %**	**Ca:F**	**Dopant %**
CaF_2	65.0	12.3	8.4	14.3	1.7	-
CaF_2:Sm	58.6	11.5	10.0	19.6	2.0	0.3
CaF_2:Gd	66.2	11.1	7.9	14.6	1.9	0.1
CaF_2:Tb	65.6	11.2	7.3	15.9	2.2	Not available

Table 3.15.: Atomic percentages for CaF_2 nanostructures, as determined by XPS

is at 322 cm^{-1}. The fact that for the Gd doped sample the peak is found at the same position as the pure fluoride, coupled to a slight peak broadening ($FWHM_{CaF_2}$=14 cm^{-1}, $FWHM_{CaF_2:Gd}$=15.0 cm^{-1}), means that the dopant ions do not induce relevant lattice distortions, thus possibly meaning an efficient dilution of the Ln ion in the host matrix or, on the other hand, hinting to possible segregation effects. In the other two samples, the signal is indeed slightly shifted to lower wavenumbers, thus strengthening the hypothesis of lattice distortions, which is further confirmed by the broadening of the peaks ($FWHM_{CaF_2:Sm}$=15 cm^{-1}, $FWHM_{CaF_2:Tb}$=18 cm^{-1}). Consistently with what determined by XRD, the greater distortions were determined for the sample doped with terbium.

To shed light on the incorporation and actual local environment of the dopant, its valence and coordination geometry in the matrix, influencing also the PL behavior (*vide infra*), X-ray Absorption (XAS) experiments (XANES and EXAFS) were performed at the dopants L_3-edges at Swiss Light Source synchrotron. In Fig. 3.27, XANES spectra of Gd and Tb L_3-edges are reported.

Sm, Gd and Tb XANES spectra are dominated by intense white lines, since the transition involved is $2p_{3/2} \rightarrow 5d$, towards empty d orbitals. Furthermore, the 2p core holes lifetime broadening is relevant (3.5-4.5 eV), and therefore much of the near-edge structure is lost. On the other hand, the three edges are asymmetrical,

Sample	**Nominal ratio**	**Experimental ration**
CaF_2:Sm	50:1	51 ± 4
CaF_2:Gd	50:1	49 ± 4
CaF_2:Tb	50:1	55 ± 6

Table 3.16.: ICP-MS results for doped CaF_2(Confidence interval: 95 %)

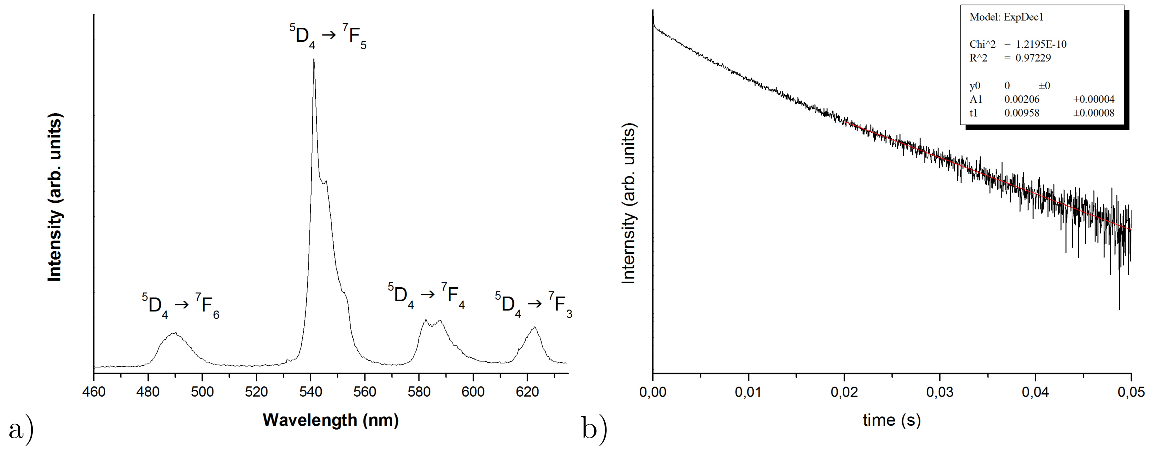

Figure 3.25.: a) Emission spectrum and b) RT emission decay for CaF_2:Tb

symptomatic of the presence of two underlying components describing the crystal field splitting of the 5d states, with the t_{2g} states energetically higher than the e_g states, assuming, for simplicity, local cubic (T_d) symmetry [100].

As far as the EXAFS region is concerned, the corresponding functions are reported in Fig. 3.27c, and their behavior is similar, evidencing therefore analogous coordination environment. First shell fitting (Tab. 3.17) revealed that the lanthanide ions are indeed found in a fluoridic environment, with coordination number compatible, within the experimental error, with the picture of substitutional doping, since in the fluorite structure Ca ions are surrounded by 8 fluoride anions [99]. For the Gd-doped sample, the lower quality of the data registered is reflected in higher uncertainties.

Sample	**Coordination number**	**Ln-F Distance (Å)**	**Debye-Waller factor (Å^{-2})**
CaF_2:Sm	9.4 ± 1.1	2.34 ± 0.01	0.013 ± 0.002
CaF_2:Gd	12.9 ± 3.2	2.34± 0.03	0.016 ± 0.005
CaF_2:Tb	8.7 ± 1.6	2.31 ± 0.02	0.013 ± 0.002

Table 3.17.: EXAFS analysis at RE L_3 edges

As already mentioned, these materials are interesting for their optical properties,

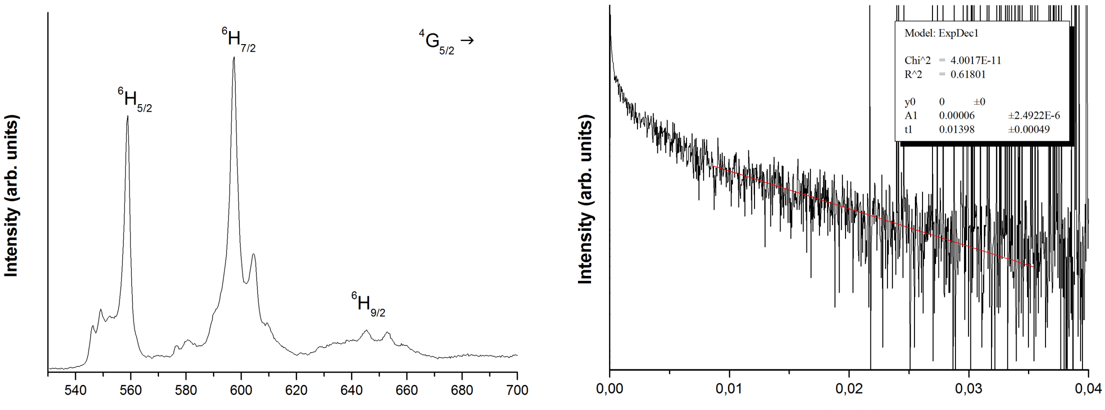

a) b)

Figure 3.26.: a) Emission spectrum and b) RT emission decay for CaF_2:Sm

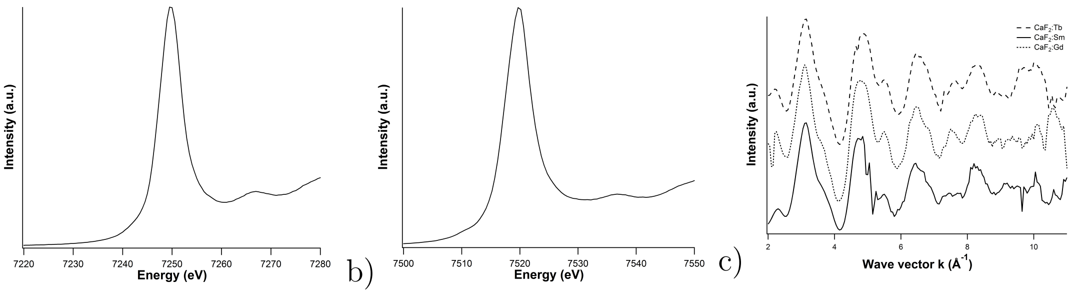

a) b) c)

Figure 3.27.: Dopant L_3-edge XANES spectra of a) Gd- and b) Tb-doped CaF_2 nanoparticles, and c) corresponding EXAFS functions

being calcium fluoride an excellent matrix for the lanthanide ions. The photoluminescence (PL) spectrum (λ_{exc} = 355 nm) of CaF_2:Tb sample is characterized by the typical Tb^{III} spectral lines [156] and involving transitions from the excited $^5D_4$ state to the different ^7F_J states (J = 3, 4, 5 and 6), as labeled in Fig. 3.25a. The spectrum, similarly to the case of the doped hydroxides (see Sec. 3.5), is dominated by the transition to the $^7F_5$ state but, in contrast to the aforementioned cases, the bands are narrower, showing an higher degree of order. The corresponding emission decay (Fig. 3.25b) presents a radiative lifetime of 9.6 ms, in accordance with values reported in the literature for such ion [157].

Similarly, the PL spectrum (Fig. 3.26a) of CaF_2:Sm presents the spectral lines involving the transition from the excited $^4G_{5/2}$to ^6H_J states (J = 5/2, 7/2 and 9/2) states. The intensity of the transition to the $^6H_{9/2}$ state is much lower to that usually reported in the literature [158], and the reason of this behavior is still unclear, since it is not an hypersensitive transition, whose intensity is modulated by change in coordination environment. In addition, the observed radiative lifetime of 14 ms is sensibly higher than the average value found in literature (6 ms) [158].

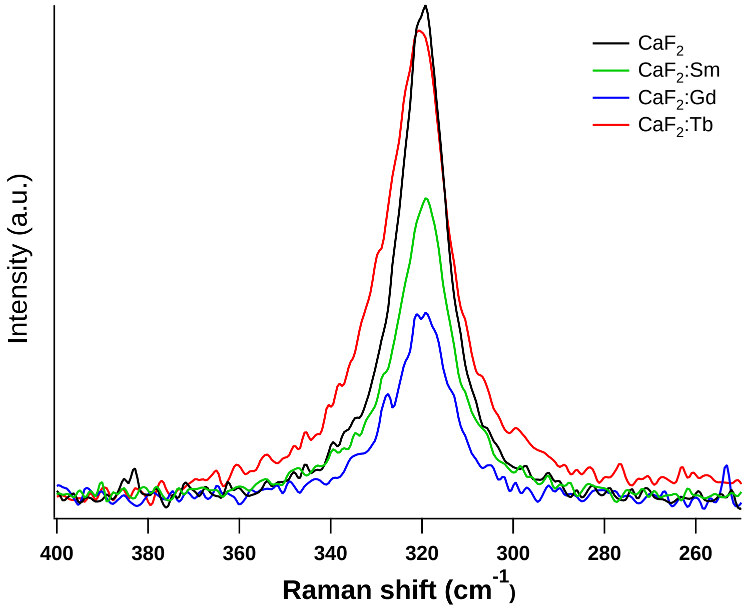

Figure 3.28.: Raman spectra for pure and doped nanoparticles

3.8.3. Conclusions

Lanthanide doped CaF_2 nanostructures were synthesized by co-precipitation in the confined space of miniemulsion droplets. This approach achieves an average crystallite size of 37 nm, which was determined to be dependent on sonication time (increasing it leads to a decrease in the crystallite size). SEM and TEM micrographs evidenced the formation of aggregates of nanoparticles with sizes of about 50-100 nm. SAED also revealed the presence of a secondary phase consisting in an oxide surface layer, as also confirmed by photoelectron spectroscopy. Micro-Raman data suggested lattice distortion induced by lanthanide ions, and EXAFS spectroscopy indeed confirmed that these ions are surrounded by about 8 fluoride ions, compatible with a successful substitutional doping. Accordingly, all samples showed to be luminescent, with properties consistent with typical emissions for the Tb doped sample, whereas in the case of the Sm doped sample a strong quenching of the transition to the $^6H_{9/2}$ state was observed. Interestingly, the sonication time was found to be a key aspect in determining the crystallite size.

Chapter 4.

Inorganic nanostructures for catalysis

4.1. Introduction and general approaches

A catalyst is a substance which increases the rate of a chemical reaction, without being consumed during the process. A catalyst does not modify the Gibbs free energy of reaction, but rather it lowers the activation energy [159]. The catalyzed reaction is a cyclic process: as a general simplified scheme, the reactant(s) and the catalyst form a complex which lowers the energy of the transient state, or alternatively provides a more convenient path, generating the products. The catalyst is then released and can start another cycle. If the catalyst and the reactant(s) (or their solutions) are both present in the same phase, then the reaction is said to be homogeneously catalyzed, otherwise it is termed heterogeneous. In this work, the attention is focused on this latter case, since inorganic solids such as metals, oxides, sulfides are common examples of heterogeneous catalysts, also for large-scale processes. A good number of solid catalyst are simple in composition (e.g., metallic Ni, TiO_2), but most of them rather consist of several components and polymorphs, making therefore challenging to assess a catalytic material's structure. Regardless on the exact structure, on the other hand, one of the key aspects in catalysis is the size of the active species. Generally, the smaller the size, the higher the activity is, due to an increase in the surface-to-volume ratio. Especially in the case of metallic nanoparticles, in addition, differently sized NPs may present different active sites, and these might correspond to variations in catalytic activity.

It is then straightforward that a key issue when developing a catalyst is to use synthetic strategies that enable the formation of nanosized particles, with a narrow size distribution. Additionally, in the case of catalyst working at low temperatures, the need of thermal treatments during the synthetic process should be avoided, in order to prevent particles coalescence.

In this framework, microemulsions have been widely used for the preparation of mono- and bimetallic catalysts, simple and mixed metal oxides and also of nanocomposites of metal NPs coated by oxides, as extensively reviewed by Boutennet *et al.* [22]. The use of miniemulsions in this field, on the other hand, is still quite limited, but some remarkable examples can be found [55, 160].

ACS APPLIED MATERIALS & INTERFACES

RESEARCH ARTICLE

www.acsami.org

Tin(IV) Oxide Coatings from Hybrid Organotin/Polymer Nanoparticles

Rafael Muñoz-Espí,* Paolo Dolcet,[†,‡] Torsten Rossow,[†] Manfred Wagner, Katharina Landfester, and Daniel Crespy*

Max Planck Institute for Polymer Research, Ackermannweg 10, 55128 Mainz, Germany

S *Supporting Information*

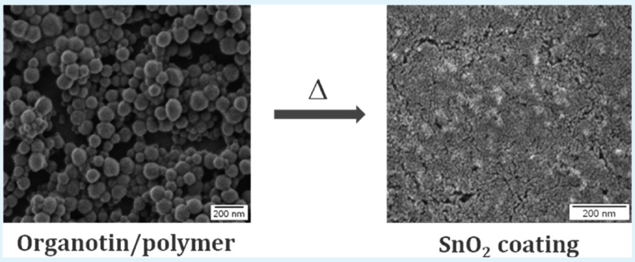

ABSTRACT: Tin dioxide coatings are widely applied in glasses and ceramics to improve not only optical, but also mechanical properties. In this work, we report a new method to prepare SnO_2 coatings from aqueous dispersions of polymer/organotin hybrid nanoparticles. Various liquid organotin compounds were encapsulated in polymeric nanoparticles synthesized by miniemulsion polymerization. Large amounts of tetrabutyltin and bis(tributyltin) could be successfully incorporated in cross-linked and noncross-linked polystyrene nanoparticles that served as sacrificial templates for the formation of tin oxide coatings after etching with oxygen plasma or calcination. Cross-linked polystyrene particles containing bis(tributyltin)—selected for having a high boiling point—were found to be especially suited for the oxide coating formation. The content of metal in the particles was up to 12 wt %, and estimations by thermogravimetrical indicated that at least 96% of the total organotin compound was converted to SnO_2. The resulting coatings were mainly identified as tetragonal SnO_2 (cassiterite) by X-ray diffraction, although a coexistence of this phase with orthorhombic SnO_2 was observed for samples prepared with bis(tributyltin).

KEYWORDS: encapsulation, miniemulsion, nanoparticles, organotin, tin oxide

INTRODUCTION

Tin oxide colloids have been used as pigments since ancient times. For instance, in Antic Rome they were already used in cosmetic creams, as discovered during an archeological excavation in London.[1] Tin(IV) oxide is highly transparent in the visible region of the electromagnetic spectrum, but it reflects the infrared light; combined with its low electrical resistance, these features make of SnO_2 a suitable material not only for advanced optoelectronic applications, such as solar cells or light emitting diodes, but also as a pigment in glasses and ceramic glazes.[2,3] In glasses and ceramics, SnO_2 films of different thicknesses can be applied to increase the resistance to abrasion (films of <0.1 μm),[4,5] to obtain iridescent colored layers (0.1−1.0 μm),[4] and to improve the thermal isolation (>1 μm).[4] Furthermore, SnO_2 is one of the most used metal oxides in gas sensors applications due to its chemical and thermal stability and its high sensibility,[6−9] and it has been also applied as catalyst support.[6,10−15]

Films of SnO_2 can be prepared by a variety of techniques, including wet chemical approaches,[16−19] and physical methods such as vapor deposition[20−22] or laser ablation.[23,24] It is known that when ignited, organotin compounds burn to SnO_2, H_2O, and CO_2.[2] Accordingly, the pyrolysis under an oxidative atmosphere of solid molecular[9,25,26] and polymeric[27,28] organotin precursors has also been applied to obtain SnO_2 nanoparticles. Alkynylorgantin was also used as precursor for the fabrication of self-assembled bridged hybrid materials[29] and thin films.[30] The relative amount of metal in organotin polymers can be as high as >40 wt %,[27] but the synthetic pathway of such precursors requires several demanding steps. Although liquid organotin molecular compounds can also be potentially used for the same purpose, their low flash points represent a clear limitation. This restriction could, however, be overcome by encapsulation of the liquid precursors in a polymer matrix. In this sense, the miniemulsion polymerization is probably now the most versatile method to produce functionalized polymer nanoparticles and nanocapsules.[31]

Hydrophobic[32−35] but also hydrophilic substances[36−39] can be encapsulated either in a polymer matrix ("nanoparticle"),[32−35,38,39] or dissolved or dispersed in the liquid core of a core/shell nanoparticle ("nanocapsule").[36,37] Previous work showed that silver nanoparticles can be produced in situ in miniemulsion droplets by the reduction of a silver salt. The interface of the droplets was used to perform polyaddition and polycondensation reactions,[36] or the entire volume of the droplets was subsequently polymerized by free-radical polymerization.[38] The latter method was used to encapsulate hydrophilic cobalt(II), iron(II), iron(III), nickel(II), zinc(II), and copper(II) salts in poly(2-hydroxyethyl methacrylate) particles in water-in-oil miniemulsions.[39] Owing to their rather low solubility, hydrophobic metal complexes are encapsulated in much lower amounts in oil-in-water miniemulsions (with an aqueous continuous phase) compared to their hydrophilic counterparts. This is a known problem, also typically encountered in the encapsulation of metallopharmaceutics.[40]

Received: July 22, 2011
Accepted: September 28, 2011
Published: September 28, 2011

ACS Publications © 2011 American Chemical Society

The encapsulation of metal complexes in hydrophobic particles is particularly interesting because it makes possible the use in aqueous-based systems. Moreover, oil-in-water dispersions are usually easier to stabilize than water-in-oil ones. Hydrophobic complexes of platinum(II), indium(III), zinc(II), chromium(III), and iron(III) were encapsulated and used further for colloid lithography applications.[34,41] Almost 1 wt % of platinum(II) acetylacetonate was located in polystyrene nanoparticles fabricated in miniemulsion.[41] One strategy to increase the amount of not well-soluble substance in the disperse phase of an emulsion is to dilute the monomer and the substance to be encapsulated in a solvent that can be emulsified and later evaporated. This strategy was used to improve the dielectric constant of polyaniline/polydivinylbenzene hybrid particles.[35]

This work presents a novel approach for the formation of SnO_2 coatings from encapsulated liquid organotin precursors. We report for the first time—to the best of our knowledge—the encapsulation of very large amounts (up to more than 12 wt % of metal in the particles) of liquid organotin precursors in polymer nanoparticles synthesized by miniemulsion polymerization. We investigate the stability of the prepared dispersions and their suitability to form tin oxide coatings by calcination or etching with oxygen plasma.

■ EXPERIMENTAL SECTION

Materials. Di-*n*-butyltin dilaurate (DBTDL, 95%, Sigma Aldrich), bis(2-ethyl hexanoate) tin(II) (BEHT, 95%, ABCR), tetra-*n*-butyltin (TBT, 95%, Merck), bis(tri-*n*-butyltin) (BTBT, 95%, Sigma Aldrich), bis(tri-*n*-butyltin) oxide (BTBTO, 96%, Acros Organics), α,α'-azoisobutyronitrile (AIBN, 98%, Fluka), and sodium dodecylsulfate (SDS, 99%, Roth) were used without further purification. Styrene (S, 99%, Merck) and divinylbenzene (DVB, 80%, Sigma Aldrich) were passed through an aluminum oxide column before use. The chemical structures of the different organotin compounds used in the work are displayed in Figure 1 and Figure S1 (for DBTDL and BEHT). ***Caution!*** *Tributyltin, bis(tri-n-butyltin), and bis(tri-n-butyltin) oxide are toxic chemicals and are hazardous for the health and the aquatic environment. Thus, these chemicals must be handled and disposed with care.*

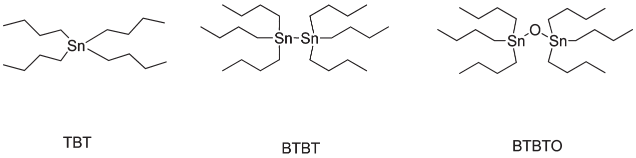

Figure 1. Chemical structures of the organotin precursors used in the synthesis: tetra-*n*-butyl tin (TBT), bis(tri-*n*-butyltin) (BTBT), and bis (tri-*n*-butyltin) oxide (BTBTO).

Synthesis of Hybrid Organotin–Polymer Nanoparticles. The monomers (styrene and divinylbenzene) were mixed with the organotin compound according to the amounts given in Table 1. After dissolving AIBN (98 ± 2 mg) in the monomer/organotin mixture, an aqueous solution of SDS (30 g of solution, 1.00 ± 0.02 $g \cdot L^{-1}$) was added. Afterward, the mixture was stirred for 1 h and ultrasonicated for 2 min with a Branson Sonifier W450 Digital (1/2 in. tip, 90% amplitude, 1 s pulse/0.1 s pause) under cooling in an ice–water bath. The resulting miniemulsion was stirred at 72 °C for 24 h in a closed round flask, cooled at room temperature, and filtered. As a representative sample for estimating the polymerization yield, the dispersion prepared with styrene and BTBT (sample **3**) was precipitated in an excess of methanol and filtered. The precipitate was dissolved in toluene, reprecipitated in methanol, and dried under vacuum. The polymerization yield was determined gravimetrically from the weight of the dry precipitate.

Formation of SnO_2 Coatings. The coatings were prepared by simple drop-casting on silicon wafers from dilutions of the miniemulsions. The silicon wafers used for the plasma etching experiments were previously treated by immersion for 2 h at 60 °C in a 3:1 mixture of concentrated ammonia with hydrogen peroxide. Plasma etching of the samples (15 sccm, 50 W power, 30 min) was performed in a plasma oven (Diener electronic Femto) and the calcination took place in a muffle furnace (Nabertherm Controller P330 LT 5/13) according to the following heating program: 25 → 500 °C with a heating rate of 3 $°C \cdot min^{-1}$, plateau of 3 h at 500 °C, and annealing to room temperature.

Analytical Methods. The morphology of the samples was investigated by scanning electron microscopy (Zeiss 1530 LEO Gemini, operated up to 2 kV) and transmission electron microscopy (Zeiss EM902, operated at 80 kV). The apparent molecular weight was determined by GPC using THF as an eluent and a calibration with polystyrene standards. The measurements were performed on a Waters 515 pump coupled with a refractive index detector (ERC RI 101), using 10 μm 0.8 × 30 cm SDV columns (PSS, Mainz, Germany) with 106, 104, and 500 Å with a flow rate of 1 $mL \cdot min^{-1}$ at 30 °C. Thermogravimetric analysis (TGA) was carried out with a thermobalance Mettler Toledo ThermoSTAR TGA/SDTA 851 under an air atmosphere (30 $mL \cdot min^{-1}$) with a heating rate of 10 $°C \cdot min^{-1}$ from room temperature to 900 °C. X-ray diffraction patterns were recorded on a Bruker D8 Advance 2 diffractometer with Cu Kα radiation (λ = 1.54 Å, 40 kV, 30 mA) in the range 2θ = 5–65° ($\Delta 2\theta$ = 0.02°, Δt = 15 s).

The ^{119}Sn NMR spectra were performed on a Bruker Avance III 700 spectrometer at 261 MHz at 298.3 K using the topspin 3.0 software (Bruker). Quantitative tin measurement were carried out with inverse gated decoupling technique using a 30° flip angle of 6.3 μs and a recovery

Table 1. Composition of the Organotin-Containing Dispersions, Coagulum Separated after Polymerization, and Fraction of Dispersed Phase $f_{d\varphi}$ Measured after Freeze-Drying of the Resulting Miniemulsions

	organotin		monomers [g]			
sample	compound	mass [g]	styrene	DVB	coagulum[a] [g]	$f_{d\varphi}$[b] [wt %]
1	TBT	2.00	4.04	0	0.27	15.5
2	TBT	2.00	3.84	0.16	0.44	12.8
3	BTBT	2.00	4.00	0	0.49	15.0
4	BTBT	2.00	3.85	0.16	0.32	16.6
5	BTBTO	2.10	4.05	0	1.99	n.d.[c]
6	BTBTO	2.00	3.84	0.16	1.89	9.9

[a] Coagulum measured after drying the feed of the filtration. [b] Fraction of dispersed phase measured by freeze-drying the filtrate and defined as the ratio of the weights of organotin + polymer + surfactant in the dispersed phase (excluding the coagulum) to the total weight of the dispersion. [c] Not determined.

Table 2. Characteristics of Organotin−Polymer Hybrid Minimemulsions

sample	composition	D_h	molecular weight of polymer[a] M_n	molecular weight of polymer[a] M_w	PDI[b]	organotin in the dispersed phase[c] [wt %]	organotin converted to SnO_2 after calcination[d] [%]
1	PS/TBT	161 ± 75	55 500	292 000	5.3	32.6	45.0
2	P(S-*co*-DVB)/TBT	178 ± 72	cross-linked			26.0	5.3
3	PS/BTBT	142 ± 51	52 500	302 000	5.8	27.1	54.9
4	P(S-*co*-DVB)/BTBT	133 ± 52	cross-linked			32.2	96.0
5	PS/BTBTO	147 ± 25	221 500	710 500	3.2	10.4	nd[e]
6	P(S-*co*-DVB)/BTBTO	270 ± 160	cross-linked			6.2	48.0

[a] Determined by GPC. [b] Polydispersity index (PDI) determined by GPC. [c] Measured by ^{119}Sn-NMR spectroscopy. [d] Estimation from the residue remaining after calcination from the TGA measurements (cf. Figure 4). [e] Not determined.

delay of 20 s. The ^{119}Sn NMR spectra were referenced against tetrabutyltin (TBT) at −7 ppm. All the signals were obtained in the same spectral width window of 300 ppm to allow measurements under comparable conditions. A 200 mg portion of the freeze-dried samples was dissolved in 2 g of a 90:10 toluene−toluene-d_8 mixture in the presence of a defined amount of another organotin was taken as an internal standard (between 2 and 4 × 10^{-4} mol). BTBTO was used as standard for hybrid materials containing TBT, whereas TBT was the standard for samples containing BTBTO and BTBT. After optimizing the relaxation delay and the spectral width the ^{119}Sn nuclei were integrated against the reference compound. The ^{119}Sn chemical shifts for the tetrabutyltin, bis(tri-*n*-butyltin), and bis(tri-*n*-butyltin) oxide are −7, −80, and +85 ppm, respectively with $\delta = 0$ ppm for tetramethyltin.

RESULTS AND DISCUSSION

1. Colloidal Stability of the Miniemulsions and Dispersions. Miniemulsions with at least 30 wt % (with respect to styrene) of the different organotin compounds shown in Figure 1 were prepared in the absence and presence of divinylbenzene, used as a cross-linker. Samples prepared with DBTDL or BEHT were found to be unstable, i.e. phase separation was observed after polymerization (Supporting Information, Table S1). Differently from the other organotin compounds used in this study, DBTDL and BEHT are ionic. The destabilization may be, therefore, caused by a salting out effect resulting from the relative high ionic strength present in the system. It is known that dibutyltin dilaurate is partly hydrolyzed to lauric acid and dibutyltin dihydroxide even at room temperature, leading also to charged carboxylate species.[42]

The miniemulsions with BTBTO did also not yield stable dispersions, as can be deduced from the high amount of coagulum (cf. Table 1). This is attributed to the higher polarity and, thus, solubility of BTBTO in the continuous phase compared to TBT and BTBT. In a different manner, miniemulsions containing TBT and BTBT were found to be particularly stable.

As reported in Table 2, the hydrodynamic diameters (D_h) of the nanoparticles with TBT were larger than those for BTBT. TBT has a lower density (1.06 g·cm^{-3} at 25 °C) than BTBT (1.15 g·cm^{-3} at 25 °C) and, therefore, an equal mass of organotin in the dispersion lead to a larger droplet volume for TBT. The sizes of cross-linked nanoparticles were not significantly different from the noncross-linked analogous nanoparticles.

2. Polymerization of the Monomers in the Presence of the Organotins. Tetraalkyltin molecules can react with free radicals at a hydrogen center of an alkyl ligand to form stannylalkyl radicals, which can undergo a β-scission of a Sn−C bond.[43] Moreover, at temperatures as low as 100 °C, the Sn−Sn bond of some distannanes can break irreversibly and form alkyl radicals.[44] In principle, these radicals can react further with double bonds to yield new alkyl radicals or recombine to yield distannanes.[45] The chemical structure of the organotin was verified to remain intact under our experimental conditions by ^{119}Sn NMR spectroscopy (see below), and no tin compound could be detected in the chain of polystyrene.

Taken as a representative sample, the polymerization yield of the sample prepared with styrene and BTBT (sample **3**) was estimated to be >90% from reprecipitation experiments. The molecular weight of the polymer present in stable samples, contained in Table 2, was found to be 55 500 and 52 500 g·mol^{-1} for the samples with TBT (sample **1**) and BTBT (sample **3**), respectively. These values are in the typical range measured for nanocapsules produced by free-radical polymerization of styrene in miniemulsion considering the initiator concentration that was used.

3. Encapsulation of a High Amount of Tin Oxide Precursors. After polymerization, the organotin-containing colloids were analyzed by electron microscopy. Micrographs of the samples prepared with TBT, BTBT, and BTBTO are shown in Figure 2. No significant discrepancy was observed between the particle sizes measured by light scattering data and electron microscopy. Noncross-linked nanoparticles of TBT and BTBT displayed two kinds of morphologies: a majority of spherical nanoparticles and occasionally half-spherical larger particles (cf. insets in Figure 2). The latter morphology is explained by the different chemical composition of the droplets. In particular, droplets with higher amount of organotin can lead to acornlike droplets that transform to half spheres after the evaporation of the organotin-containing hemisphere.

The selected organotin compounds possess a high amount of tin in their chemical structures (34.2 and 40.9 wt % of Sn for TBT and BTBT, respectively). The theoretical amount of tin metal was calculated to be between 1.9 wt % (samples with TBT, **1** and **2**) and 2.3 wt % (samples with BTBT, **3** and **4**) in the aqueous dispersion. The amount of tin from TBT and BTBT precursors in the dispersed phase was determined to be between 26 and 33 wt % by ^{119}Sn-NMR spectroscopy, that is, close to the theoretical amount of 33 wt % (Table 2, representative spectra are shown in Figure S2 of the Supporting Information). The amount was found to be much lower when BTBTO was used as precursor. Indeed, 10.4 and 6.2 wt % of BTBTO were found in the freeze-dried dispersions of PS/BTBTO and P(S-*co*-

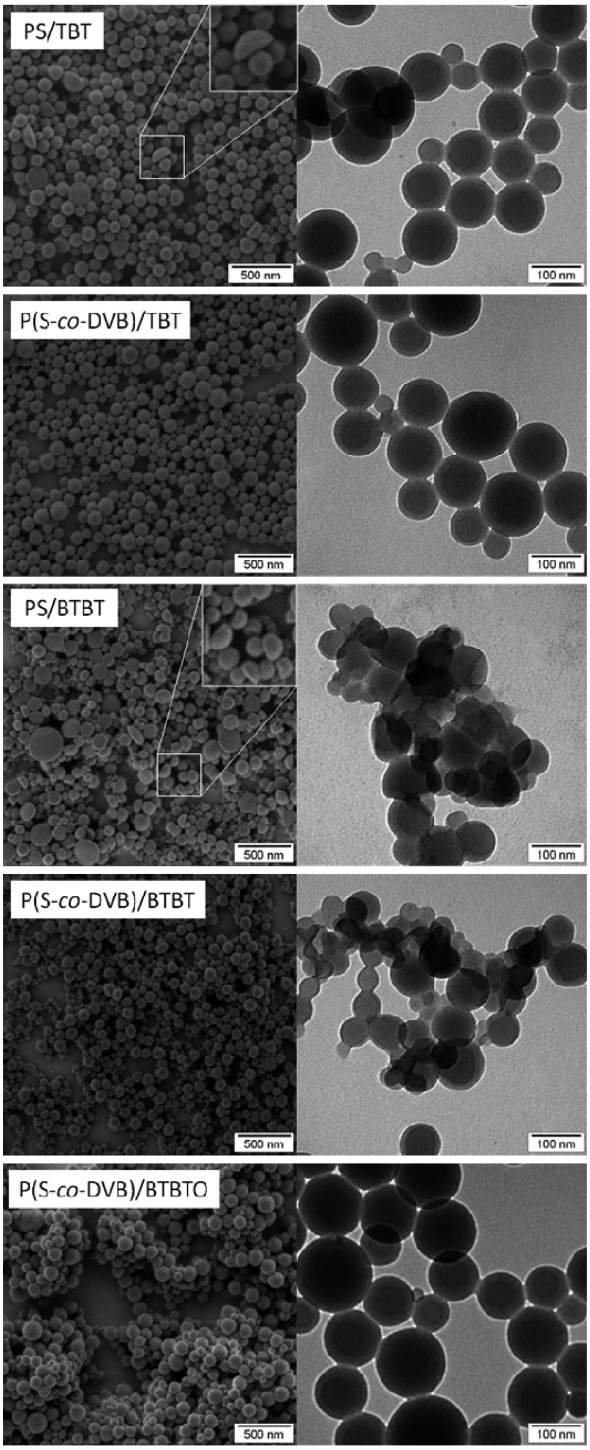

Figure 2. SEM (left) and TEM (right) micrographs of the organotin−polymer nanoparticles.

DVB)/BTBTO, respectively. These lower values compared to TBT- and BTBT-containing particles are explained by the large amount of coagulum and the high contents of BTBTO found in it. Quantitative ^{119}Sn-NMR spectroscopy revealed that the BTBTO represented 42.6 wt % of the coagulum.

The amount of metal is particularly high, especially taking into account that the hybrid nanoparticles are dispersed in water. It is expected that a further optimization of the system could lead to dispersions with even higher content of metal.

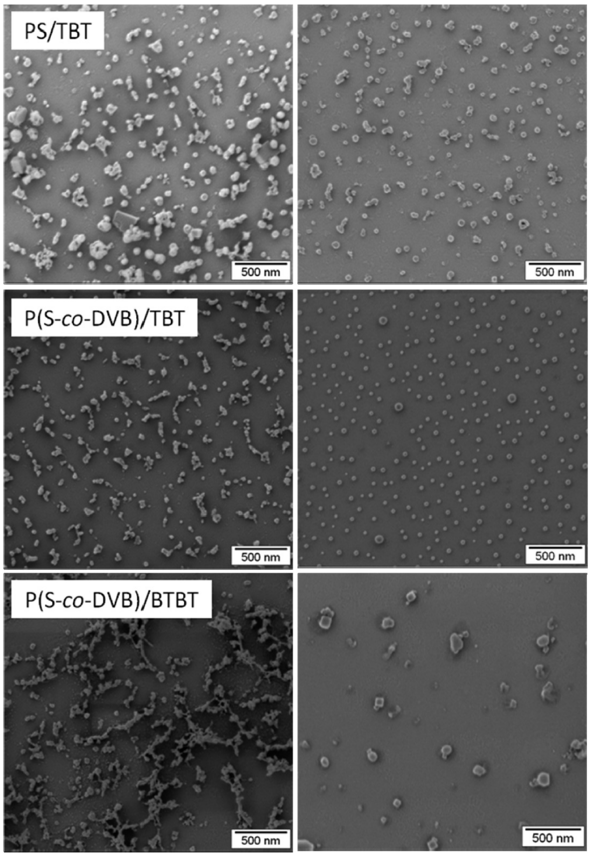

Figure 3. SEM micrographs of selected samples after treatment with oxygen plasma, casted from dilutions 1:200 (left) and 1:1000 (right) of the initial dispersion.

4. Removal of the Sacrificial Template and Formation of SnO_2 Coatings. The removal of the sacrificial polymer template and the oxidation and decomposition of the organotin compounds to form SnO_2 coatings can be achieved by two different methods: the calcinations of the samples under an oxidative atmosphere or the etching by the use of oxygen plasma. Thermogravimetric analysis (TGA) under air of freeze-dried dispersions containing TBT, described below in more detailed, showed that the temperature of decomposition of the polymer is in the same range as the boiling point of TBT, which implies that part of the TBT will evaporate before being oxidized. Therefore, for this case, the use of oxidative plasma should be more efficient, as it has been shown in the past for platinum-containing polymer nanoparticles.[34]

Figure 3 presents SEM micrographs of samples prepared with TBT and BTBT at two different dilutions of the dispersion (1:200 and 1:1000 in water). The casting of the less diluted samples led to the formation of aggregates, although the morphology of the single nanoparticles are still recognizable (Figure 3, left). In some cases, it was possible to etch single hybrid particle by consequently diluting the dispersion before casting on the substrate (Figure 3, right). The sizes of tin oxide nanoparticles observed by microscopy were matching the theoretical diameter (20−35 nm) of SnO_2 nanoparticles, D_{SnO_2}, calculated by assuming a spherical shape and that the composition of the coagulum is

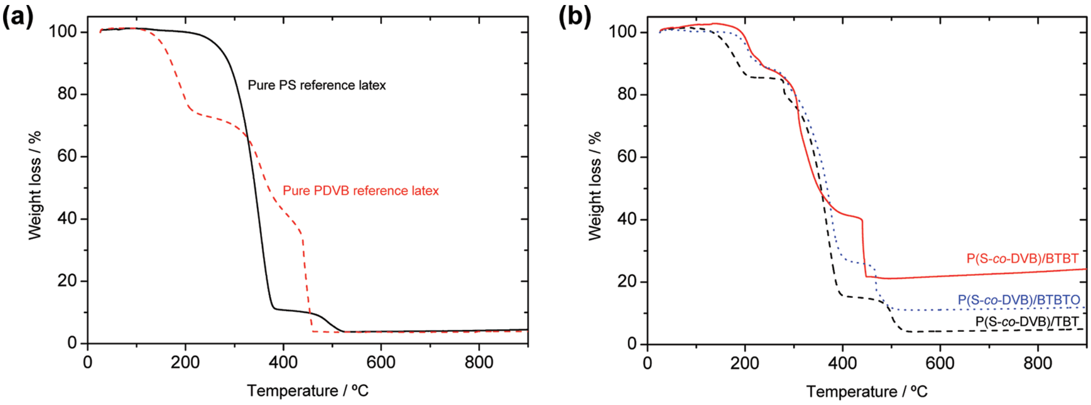

Figure 4. Thermogravimetric analysis (TGA) curves of freezed-dried samples: (a) reference polystyrene (PS) and polydivinylbenzene (PDVB) latexes; (b) cross-linked samples prepared with TBT, BTBT, and BTBTO.

the same as the composition of the dispersed phase according to

$$D_{\mathrm{SnO_2}} = D_{\mathrm{droplet}} \sqrt[3]{\frac{M_{\mathrm{SnO_2}}}{\rho_{\mathrm{SnO2}} M_{\mathrm{OT}}} \frac{m_{\mathrm{OT}}}{\frac{m_{\mathrm{OT}}}{\rho_{\mathrm{OT}}} + \frac{m_{\mathrm{P}}}{\rho_{\mathrm{P}}}}}$$

where D_{droplet} is the diameter of the droplet; ρ_{OT}, ρ_{P}, and $\rho_{\mathrm{SnO_2}}$ are the densities of the organotin compound (1.06 and 1.15 $\mathrm{g \cdot cm^{-3}}$ at 25 °C for TBT and BTBT), the polymer (1.04 $\mathrm{g \cdot cm^{-3}}$ at 25 °C for polystyrene), and cassiterite (7.15 $\mathrm{g \cdot cm^{-3}}$ at 25 °C); M_i is the molar mass of the species; and m_i is the mass of the species in the sample. The average sizes of the nanoparticles were found to range between 24 nm for sample 6 and 44 nm for sample 2 (Figure S3, Supporting Information).

The inorganic nanoparticles from noncross-linked particles (cf. Figure 3, PS/TBT) present some aggregates even in the low concentration regime, which is caused by an easier coalescence during heating in comparison to the more rigid cross-linked particles, (cf. Figure 3, P(S-*co*-DVB)/TBT and P(S-*co*-DVB)/BTBT).

Although plasma etching is excellently suited for lower concentrations, the method was not as efficient when higher concentrations (i.e., thicker films of the inorganic oxide) are required, because the polymer could not be completely removed. The calcination is clearly a more convenient strategy for obtaining thicker films, although it may have efficiency limitations with organotin compounds with a boiling point close to the thermal decomposition of the polymer, as mentioned above.

Prior to pyrolysis of the samples, the thermal decomposition of the hybrid samples was studied by TGA under an air atmosphere. After calcination, the remaining residue should be essentially composed of SnO_2 (and minor rests of carbon due to the polymer degradation). Subsequently, from the percentages of the remaining residue, we can estimate the fraction of the initially introduced organotin that converts to SnO_2 after calcination. The last column of Table 2 contains the results of this estimation. By observing the values, there are two especially remarkable aspects: first, the higher efficiency of the conversion of the noncross-linked TBT-containing sample to SnO_2 (45.0%), when compared with the cross-linked one (only 5.3%); and second, the almost complete conversion (96.0%) for the P(S-*co*-DVB)/BTBT sample. The latter is not surprising if we take into account the high boiling point of BTBT and the efficient encapsulation of the organotin in cross-linked capsules. For understanding the first observation, it is helpful to have a look to the thermal decomposition of reference PS and PDVB latexes, depicted in Figure 4a. The PS latex starts decomposing at about 250 °C, whereas the PDVB latex does it at about 140 °C. PDVB may decompose simultaneously to the evaporation of TBT, degrading the cross-linked P(S-*co*-DVB) shell and facilitating the evaporation of the encapsulated precursor, which results in a very low conversion to SnO_2. On the contrary, the efficiency will be higher with pure PS particles, even if they are not cross-linked, because they start to degrade at a higher temperature. This explanation is confirmed by the fact that 26.0 wt % of TBT could be found in the dispersed phase by ^{119}Sn NMR spectroscopy before the calcination (Table 2). To illustrate the differences between the different organotin precursors, Figure 4b contains the TGA traces of the cross-linked samples prepared with TBT, BTBT, and BTBTO.

The success of the calcination strategy could be demonstrated by calcinating at 500 °C (temperature at which the polymer has been completely removed and only SnO_2 remains, according to TGA data) samples prepared with high and low concentrations of the hybrid dispersions. EDX spectra indicated that the coatings are slightly contaminated with carbon originating from the calcination of the polymer (Figure S4, Supporting Information). Figure 5 shows the micrographs of tin oxide coatings formed after calcinations of samples with the different precursors. The casting of the as-prepared dispersions lead to thicker oxide films (Figure 5, left) and high dilutions resulted in the formation of inorganic nanoparticles from single hybrid precursor particles (Figure 5, right). The thickness of the prepared coatings was estimated with a profilometer and could be varied between ca. 100 nm and up to 500 nm, depending on the concentration of the casted dispersion. The sizes of nanoparticles produced by plasma etching and by calcination are similar.

X-ray diffraction patterns of the calcinated samples, shown in Figure 6, confirmed that the formed coatings were crystalline. The reflections can be clearly identified with those of tetragonal SnO_2 (cassiterite, JCPDS card. No. 41−1445). However, in the coatings prepared with dispersions containing BTBT, the thermodynamically stable tetragonal phase coexists with an orthorhombic SnO_2 phase, normally formed under high-pressure conditions. The appearance of the orthorhombic phase in SnO_2 films prepared under oxygen deficiency conditions has been previously reported,[46,47] and may be related with the formation of a litharge phase of SnO that transform to the orthorhombic form and not

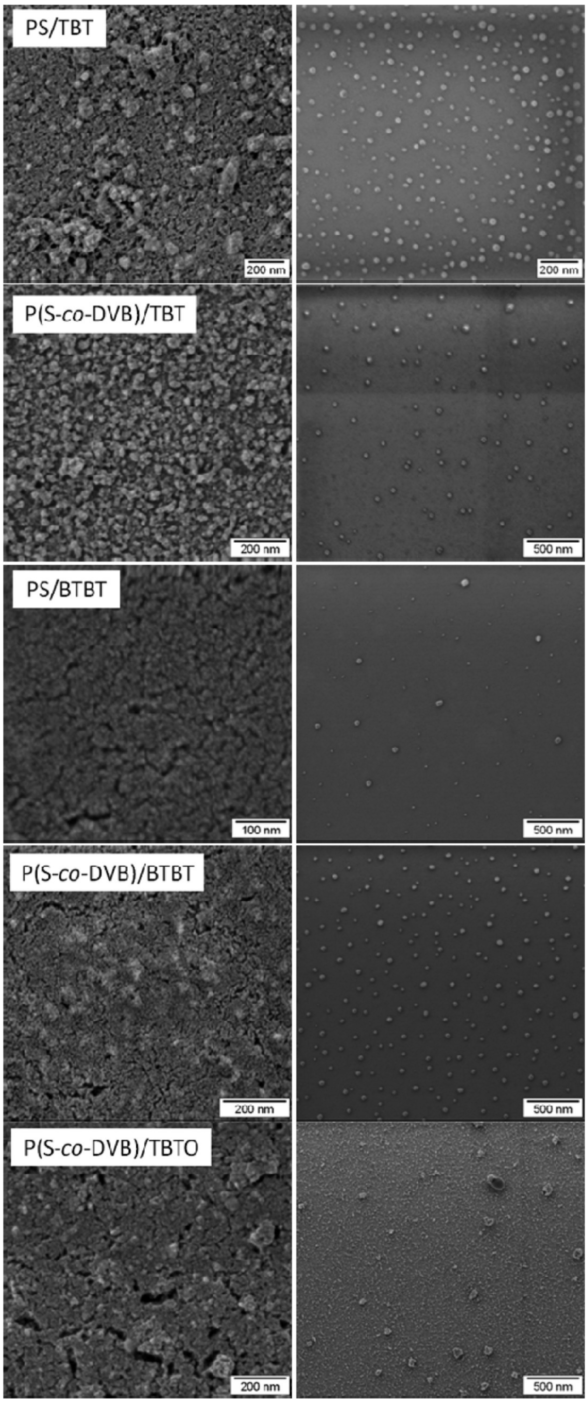

Figure 5. SEM micrographs of the samples after calcinations at 500 °C. Dispersions were casted as prepared (left) and at a dilution 1:30 (right).

to the stable cassiterite phase. The coexistence of the tetragonal and the orthorhombic phases only occurred in the BTBT samples, which can be explained as follows. As each molecule of BTBT contains two atoms of tin, the oxygen required for oxidation to SnO_2 is double than for TBT, so that an SnO intermediate phase could be formed if the oxygen is not sufficient during the calcination process. In BTBTO, the two Sn atoms are linked with an oxygen and the oxygen required for oxidation is equivalent to TBT. The size of the crystalline domains was estimated to range from 5 to 17 nm by using the Scherrer equation for the (110) reflections of cassiterite in the XRD patterns.

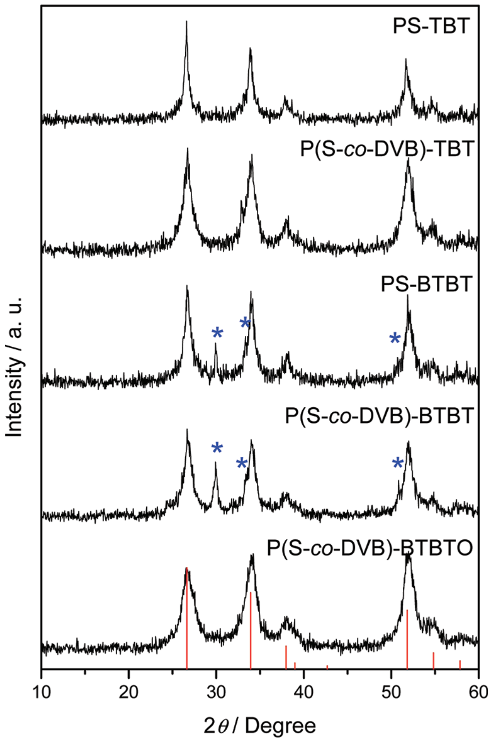

Figure 6. X-ray diffraction patterns of the samples prepared by casting the dispersions on silicon wafers and subsequent calcination at 500 °C. Te drop lines indicate the position and relative intensity of cassiterite (JCPDS card No. 41-1445). The peaks marked with an asterisk (*) are attributed to the presence of orthorhombic SnO_2 (JCPDS card No. 85-0423).

CONCLUSIONS

Miniemulsion polymerization has been shown to be a suitable technique for encapsulating liquid organotin precursors that can be converted to tin(IV) oxide either by etching with oxygen plasma or by calcinations under an oxidative atmosphere. From the different liquid organotin compounds screened, tetra-*n*-butyltin (TBT) and bis(tributyltin) (BTBT) form the most stable dispersions. TBT and BTBT can be successfully encapsulated in amounts as high as more than 30 wt % in polystyrene or poly(styrene-*co*-divinylbenzene) nanoparticles. This new approach is particularly interesting because the tin precursors are dispersed and processed in water. The resulting aqueous organotin/polymer dispersions can be easily coated and the thickness of the oxide coating obtained after etching can be simply adjusted by dilution of the initial dispersion. Estimations by thermogravimetric analysis demonstrated the efficiency of the method: for particles prepared with BTBT and poly(styrene-*co*-divinylbenzene) almost the whole initially introduced organotin (96%) could be transformed to SnO_2. X-ray diffraction confirmed the crystallinity of the prepared coating. The prepared coating were confirmed to be crystalline by X-ray diffraction and mainly identified as tetragonal SnO_2 (cassiterite), although a coexistence of this phase with orthorhombic SnO_2 was found in samples prepared with BTBT. The method can be, in principle, applied to other hydrophobic organometallic liquids for the preparation of metal oxides coatings.

ASSOCIATED CONTENT

Ⓢ Supporting Information. Description of miniemulsions with di-*n*-butyltin dilaurate and bis(2-ethyl hexanoate) tin(II) as tin oxide precursors, ^{119}Sn NMR spectroscopy of the organotin−polymer nanoparticles, determination of the particle size distribution of tin oxide nanoparticles from SEM measurements, and EDX measurements on calcinated organotin−polymer hybrid nanoparticles. This material is available free of charge via the Internet at http://pubs.acs.org.

AUTHOR INFORMATION

Corresponding Author

*E-mail: munoz@mpip-mainz.mpg.de, crespy@mpip-mainz.mpg.de.

Present Addresses

[‡]Also at Dipartimento di Scienze Chimiche, Università di Padova, Via Marzolo 1, 35131 Padua, Italy.

Author Contributions

[†]These two authors contributed equally to this work.

ACKNOWLEDGMENT

We thank Gunnar Glaser and Dr. Ingo Lieberwirth for their suggestions and assistance with the electron microscopy and EDX analysis, Sandra Seywald for the GPC measurements, and Michael Bach for the XRD measurements. P.D. thanks the Ph.D. School in Molecular Sciences of the University of Padua for financial support.

REFERENCES

(1) Evershed, R. P.; Berstan, R.; Grew, F.; Copley, M. S.; Charmant, A. J. H.; Barham, E.; Mottram, H. R.; Brown, G. *Nature* **2004**, *432*, 35–36.

(2) Greenwood, N. N.; Earnshaw, A. *Chemistry of the Elements*, 2nd ed.; Butterworth-Heinemann: Oxford, 1997.

(3) Batzill, M.; Diebold, U. *Prog. Surf. Sci.* **2005**, *79*, 47–154.

(4) Holleman, A. F.; Wiberg, E. *Lehrbuch der Anorganischen Chemie*, 102 ed.; De Gruyter: Berlin, 2007.

(5) Budd, S. M. *Thin Solid Films* **1981**, *77*, 13–20.

(6) Diebold, U.; Batzill, M. *Prog. Surf. Sci.* **2005**, *79*, 47–154.

(7) Ihokura, K.; Watson, J. *The Stannic Oxide Gas Sensor: Principles and Applications*; CRC Press: FL, 1994.

(8) Barsan, N.; Schweizer-Berberich, M.; Gopel, W. *Fresenius J. Anal. Chem.* **1999**, *365*, 287–304.

(9) Nayral, C.; Viala, E.; Fau, P.; Senocq, F.; Jumas, J. C.; Maisonnat, A.; Chaudret, B. *Chem.—Eur. J.* **2000**, *6*, 4082–4090.

(10) Gopel, W.; Schierbaum, K. D. *Sensors Actuat. B—Chem.* **1995**, *26*, 1–12.

(11) Law, M.; Kind, H.; Messer, B.; Kim, F.; Yang, P. D. *Angew. Chem., Int. Ed.* **2002**, *41*, 2405–2408.

(12) Kolmakov, A.; Zhang, X. Y.; Cheng, G. S.; Moskovits, M. *Adv. Mater.* **2003**, *15*, 997.

(13) Lee, K. S.; Park, I. S.; Cho, Y. H.; Jung, D. S.; Jung, N.; Park, H. Y.; Sung, Y. E. *J. Catal.* **2008**, *258*, 143–152.

(14) Sekizawa, K.; Widjaja, H.; Maeda, S.; Ozawa, Y.; Eguchi, K. *Appl. Catal., A* **2000**, *200*, 211–217.

(15) Yamaguchi, N.; Kamiuchi, N.; Muroyama, H.; Matsui, T.; Eguchi, K. *Catal. Today* **2011**, *164*, 169–175.

(16) Niederberger, M.; Pinna, N. *Metal Oxide Nanoparticles in Organic Solvents*; Springer: Dordrecht, 2009.

(17) Juttukonda, V.; Paddock, R. L.; Raymond, J. E.; Denomme, D.; Richardson, A. E.; Slusher, L. E.; Fahlman, B. D. *J. Am. Chem. Soc.* **2006**, *128*, 420–421.

(18) Deng, Z. T.; Peng, B.; Chen, D.; Tang, F. Q.; Muscat, A. J. *Langmuir* **2008**, *24*, 11089–11095.

(19) Ba, J. H.; Polleux, J.; Antonietti, M.; Niederberger, M. *Adv. Mater.* **2005**, *17*, 2509–+.

(20) Liu, Y.; Koep, E.; Liu, M. L. *Chem. Mater.* **2005**, *17*, 3997–4000.

(21) Rosental, A.; Tarre, A.; Gerst, A.; Uustare, T.; Sammelselg, V. *Sens. Actuator B—Chem.* **2001**, *77*, 297–300.

(22) Sun, S. H.; Meng, G. W.; Zhang, G. X.; Masse, J. P.; Zhang, L. *Chem.—Eur. J.* **2007**, *13*, 9087–9092.

(23) Hu, J. Q.; Bando, Y.; Liu, Q. L.; Golberg, D. *Adv. Funct. Mater.* **2003**, *13*, 493–496.

(24) Ristoscu, C.; Cultrera, L.; Dima, A.; Perrone, A.; Cutting, R.; Du, H. L.; Busiakiewicz, A.; Klusek, Z.; Datta, P. K.; Rose, S. R. *Appl. Surf. Sci.* **2005**, *247*, 95–100.

(25) Toupance, T.; Elhamzaoui, H.; Jousseaume, B.; Riague, H.; Saadeddin, I.; Campet, G.; Brotz, J. *Chem. Mater.* **2006**, *18*, 6364–6372.

(26) Molloy, K. C. *J. Chem. Res.* **2008**, *10*, 549–554.

(27) Tamai, T.; Ichinose, N. *Macromolecules* **2000**, *33*, 2505–2508.

(28) Tamai, T.; Ichinose, N.; Agari, Y. *Macromol. Rapid Commun.* **1999**, *20*, 179–181.

(29) Elhamzaoui, H.; Jousseaume, B.; Riague, H.; Toupance, T.; Dieudonne, P.; Zakri, C.; Maugey, M.; Allouchi, H. *J. Am. Chem. Soc.* **2004**, *126*, 8130–8131.

(30) Renard, L.; Elhamzaoui, H.; Jousseaume, B.; Toupance, T.; Laurent, G.; Ribot, F.; Saadoui, H.; Brotz, J.; Fuess, H.; Riedel, R.; Gurlo, A. *Chem. Commun.* **2011**, *47*, 1464–1466.

(31) Crespy, D.; Landfester, K. *Beilstein J. Org. Chem.* **2010**, *6*, 1132–1148.

(32) Erdem, B.; Sudol, E. D.; Dimonie, V. L.; El-Aasser, M. S. *J. Polym. Sci., Polym. Chem.* **2000**, *38*, 4431–4440.

(33) Joumaa, N.; Lansalot, M.; Theretz, A.; Elaissari, A. *Langmuir* **2006**, *22*, 1810–1816.

(34) Manzke, A.; Pfahler, C.; Dubbers, O.; Plettl, A.; Ziemann, P.; Crespy, D.; Schreiber, E.; Ziener, U.; Landfester, K. *Adv. Mater.* **2007**, *19*, 1337–1341.

(35) Molberg, M.; Crespy, D.; Rupper, P.; Nuesch, F.; Manson, J. A. E.; Lowe, C.; Opris, D. M. *Adv. Funct. Mater.* **2010**, *20*, 3280–3291.

(36) Crespy, D.; Stark, M.; Hoffmann-Richter, C.; Ziener, U.; Landfester, K. *Macromolecules* **2007**, *40*, 3122–3135.

(37) Crespy, D.; Landfester, K. *Macromol. Chem. Phys.* **2007**, *208*, 457–466.

(38) Crespy, D.; Landfester, K. *Polymer* **2009**, *50*, 1616–1620.

(39) Cao, Z. H.; Wang, Z.; Herrmann, C.; Ziener, U.; Landfester, K. *Langmuir* **2010**, *26*, 7054–7061.

(40) Crespy, D.; Landfester, K.; Schubert, U. S.; Schiller, A. *Chem. Commun.* **2010**, *46*, 6651–6662.

(41) Schreiber, E.; Ziener, U.; Manzke, A.; Plettl, A.; Ziemann, P.; Landfester, K. *Chem. Mater.* **2009**, *21*, 1750–1760.

(42) Yokoyama, T.; Kinjo, N.; Mukai, J. *J. Appl. Polym. Sci.* **1984**, *29*, 1951–1958.

(43) Davies, A. G. *Organotin Chemistry*; VCH: Weinheim, 1997.

(44) Buschhaus, H. U.; Neumann, W. P. *Angew. Chem.-Int. Ed. Engl.* **1978**, *17*, 59–59.

(45) Omae, I. *Organotin Chemistry*; Elsevier Science Publishers: Amsterdam, 1989.

(46) Shek, C. H.; Lai, J. K. L.; Lin, G. M.; Zheng, Y. F.; Liu, W. H. *J. Phys. Chem. Solids* **1997**, *58*, 13–17.

(47) Lamelas, F. J.; Reid, S. A. *Phys. Rev. B* **1999**, *60*, 9347–9351.

Journal of
Materials Chemistry

Dynamic Article Links

Cite this: *J. Mater. Chem.*, 2012, **22**, 5622

www.rsc.org/materials

PAPER

Sol–gel processes at the droplet interface: hydrous zirconia and hafnia nanocapsules by interfacial inorganic polycondensation†

Myriam Hajir,‡ Paolo Dolcet,‡§ Viktor Fischer, Julian Holzinger, Katharina Landfester and Rafael Muñoz-Espí*

Received 20th October 2011, Accepted 9th January 2012
DOI: 10.1039/c2jm15353j

We report a simple method to prepare nanocapsules of hydrous zirconia and hafnia by interfacial precipitation in water-in-oil miniemulsions. We show that the sol–gel precipitation of transition metal hydroxides, exemplified for the cases of zirconium and hafnium, can be driven to the droplet interface by addition of an organic base. The prompt addition of triethylamine generates hydroxide ions at the interface, which initiate a polycondensation of the metal hydroxo species. Electron and X-ray diffractions indicate that the resulting materials are amorphous, but can be transformed to monoclinic ZrO_2 or HfO_2 upon thermolytic treatment. Mixed oxides of Hf and Zr with different compositions ($Hf_xZr_{1-x}O_2$) can also be formed by using the desired ratios of precursors. Furthermore, the ability of the hollow particles to encapsulate efficiently hydrophilic materials without leakage has been proven with the example of a water-soluble dye (fluorescein isothiocyanate).

Introduction

The formation of inorganic matter at the liquid–liquid interface is a key issue for the preparation of hollow nanostructures and, thus, for the design of mesoporous materials, commonly used in membranes and catalysis. The increasing significance of inorganic micro- and nanocapsules arises, however, not only from their interest for generating porous structures, but also from the new possibilities that these materials offer in the confinement of chemical reactions ("nanoreactors") and in the controlled release of encapsulated substances.[1–3] Although polymeric capsules are widely applied for these purposes,[4,5] inorganic hollow particles have typically better thermal and mechanical properties, which may be advantageous in many cases.

The methods to produce inorganic capsules can be roughly classified into three groups: (i) template-free methods; (ii) hard-template routes, using a sacrificial core; and (iii) soft-template routes, mostly involving emulsion and phase separation procedures.[6,7] Although template-free methods should be the most convenient, the number of successful works in the nanoscale is still quite limited.[8–11] In hard-template methods, a sacrificial particle—very often a polymer—is coated by physical or chemical deposition with the desired material or a precursor of this material. The core is removed afterwards thermally or chemically (*e.g.*, by dissolution with the proper solvent). The hard templating has been widely investigated and applied in the last decade for various systems.[7,12,13] In a different fashion, soft-template routes allow the direct generation of capsules without any sacrificial material.[14–20]

The most common material prepared by soft templating is, by far, SiO_2. The wet chemistry of silicates is well understood and sol–gel processes have been effectively driven to the droplet interface in emulsion/phase separation procedures to generate silica micro- and nanocapsules.[21–23] In this work, however, we focus on the interfacial precipitation of transition metal compounds, which is more complex and, in contrast to silica, not well established yet.

Especially interesting are the achievements in microemulsion systems by Feldmann and coworkers, who have been able to prepare hollow nanospheres of different oxides and hydroxides, including γ-AlO(OH), $La(OH)_3$, SnO_2, and TiO_2.[14–16,24] Soft-template methods have also been used to synthesize Cu_2O and Cu_2S hollow particles.[17,25]

Following the results obtained for silica, it would be desirable to use sol–gel chemistry to prepare oxide hollow particles. Among the transition metal oxides that can be formed through sol–gel syntheses, those of the group 4 (*i.e.*, TiO_2, ZrO_2, and HfO_2) are more remarkable. Thanks to their unique physicochemical properties, zirconia (ZrO_2) and hafnia (HfO_2) are used in very different applications. The high toughness and the low thermal expansion, combined with the high thermal and chemical stabilities, make ZrO_2 and HfO_2 especially useful in ceramics[26–28] and

---

Max Planck Institute for Polymer Research, Ackermannweg 10, 55128 Mainz, Germany. E-mail: munoz@mpip-mainz.mpg.de

† Electronic supplementary information (ESI) available: Electron micrographs showing the evolution of the particle formation, the influence of the dropping rate of the organic base, and the influence of the solubility in water of the base; XRD patterns of a sample before and after washing; EDX spectra before and after calcination; and reference absorption and emission spectra of the albumin–FITC conjugate. See DOI: 10.1039/c2jm15353j

‡ These authors contributed equally to the work.

§ Also at: Dipartimento di Scienze Chimiche, Università di Padova, Via Marzolo 1, 35131 Padua, Italy.

This journal is © The Royal Society of Chemistry 2012

catalytic supports.[29] Due to their amphoteric properties, these oxides have also been used as catalyst themselves.[30–32]

Herein, we present how the sol–gel precipitation of transition metal hydroxides, exemplified by the cases of zirconium and hafnium, can be driven to the interface of droplets in water-in-oil (w/o) miniemulsions. We also show that mixed oxides can be easily formed. This work reports for the first time, to the best of our knowledge, a simple soft-template method to produce hollow particles of hydrous zirconia and hafnia in the nanometric scale, and it represents one of the very few successful attempts achieved up to date in this direction for any metal oxide or hydroxide.

Experimental section

Chemicals

Zirconium oxychloride octahydrate (Fluka, ≥99%), hafnium oxychloride octahydrate (Alfa Aesar, 98+%), toluene (Sigma-Aldrich, ≥99.7%), triethylamine (Et_3N, Fluka, ≥99.5%), methylamine (Sigma-Aldrich, 40 wt% in water), tributylamine (Bu_3N, Sigma-Aldrich, ≥99.0%), the commercial polyisobutylene succinimide pentamine OS85737 (sometimes referred to as "Lubrizol U", Lubrizol France, Rouen), and albumin–fluorescein isothiocyanate conjugate (~10 mol fluorescein isothiocyanate per mol albumin, Sigma-Aldrich) were used as received without any further purification.

Preparation of zirconium and hafnium hydroxide hollow particles

A 1 wt% stock solution of the surfactant, used as a continuous phase, was prepared by dissolving the polyisobutylene succinimide pentamine surfactant (800 mg) in toluene (80 g). The metal salt, $ZrOCl_2 \cdot 8H_2O$ (644 mg, 2 mmol) or $HfOCl_2 \cdot 8H_2O$ (819 mg, 2 mmol), was dissolved in deionized water (1.5 g) and mixed with the continuous phase (8 g). The mixture was pre-emulsified under continuous stirring for 1 h and then ultrasonicated for 2 min (Branson Sonifier W-450D, ½″ tip, 90% amplitude) while cooling in an ice-water bath. To conduct the precipitation of the metal hydroxide, a mixture of triethylamine (304 mg, 3 mmol) with continuous phase (500 mg of the surfactant solution in toluene) was promptly added with a syringe to the emulsion within one minute under constant stirring (1000 rpm).

Mixed Zr/Hf samples were prepared analogously by mixing and dissolving in water (1.5 g) the appropriate amounts of the zirconium and hafnium salts (2 mmol in total).

To compare the effect of organic bases with different solubilities in water, experiments with methylamine and tributylamine were carried out in an analogous way to those with triethylamine.

To eliminate the triethylammonium chloride formed as a byproduct, a part of the emulsion resulting after addition of the triethylamine was mixed with acetone and centrifuged three times (14 000 rpm, Eppendorf 5417C). Alternatively, the product was first separated by centrifugation and then washed with acetone and deionized water.

Investigation of the encapsulation ability

Three samples were prepared as follows:

Sample **A** (blank sample): this sample contained simply the continuous phase (1 wt% of the surfactant in toluene).

Sample **B** (reference sample before addition of Et_3N): $HfOCl_2 \cdot 8H_2O$ (644 mg, 2 mmol) was added to 1.5 g of an aqueous solution of albumin–fluorescein isothiocyanate conjugate (2 mg mL^{-1}). The resulting solution was mixed with the continuous phase (8 g). The pre-emulsification and emulsification by ultrasonication were carried out as indicated above.

Sample **C** (sample with capsules): triethylamine (304 mg mixed with 500 mg of the continuous phase) was promptly added to a dispersion prepared in the same way as sample **B**.

After preparation, samples **B** and **C** were stirred at 1000 rpm for 4 h. A defined volume (450 μL) of the three samples was mixed with an equivalent volume of deionized water and placed in Eppendorf vials. The three vials were centrifuged for 20 min at 15 000 rpm. Afterwards, the samples were homogenized with a vortex mixer and centrifuged a second time for the same period at the same speed. Portions of the aqueous phase of samples **B** and **C** were carefully extracted with a syringe to analyze the absorption and emission spectra.

Calcination of the samples

Dry washed samples were calcinated in an oven (Nabertherm Controller P330 LT 5/13) according to the following program: (1) room temperature to 600 °C at a heating rate of 5 °C min^{-1} and (2) plateau at 600 °C for 1 h. For SEM measurements, a dilution of the as-prepared emulsion was cast on a silicon wafer and then calcinated.

Characterization methods

Scanning electron microscopy (SEM) was conducted in a field-emission microscope (LEO EM1530 Gemini), operated up to 1.5 kV. Energy-dispersive X-ray spectroscopy (EDX) analysis was carried out in a Hitachi SU8000 SEM microscope equipped with a Bruker AXS spectrometer. Transmission electron microscopy (TEM) was carried out in a Zeiss EM912 microscope operated at 120 kV.

Particle sizes were determined from dilutions of the resulting dispersions by dynamic light scattering measurements at 90° with a Submicron Particle Sizer NICOMP 380. Fourier transform infrared (FTIR) spectra were registered in a Perkin Elmer Spectrum BX spectrometer.

X-Ray diffraction (XRD) patterns were recorded by using a Philips PW 1820 diffractometer with $Cu_{K\alpha}$ radiation ($\lambda = 1.5418$ Å, 40 kV, 30 mA). Crystallite sizes were estimated by using the Scherrer equation,[33] assuming that the peak broadening results only from the size of coherently scattering domains.

Absorption and photoluminescence (PL) emission spectra of the samples containing albumin–fluorescein isothiocyanate conjugate were registered in a Tecan Infinite M100 plate reader, using a quartz plate (Hellma Analytics). PL emission spectra were registered in top-reading mode with an excitation wavelength of 410 nm (bandwidth = 5 nm).

Results and discussion

The main aim of this work was to create an easily applicable method to produce hollow spheres of metal oxides and hydroxides in the nanometric scale. For this aim, we applied a soft-template approach by utilizing the miniemulsion technique. The shell formation was induced by adding an organic base that starts the polycondensation sol–gel reaction at the interface. As described in the following, triethylamine (Et_3N), which is soluble in the continuous phase but possesses as well a limited solubility in the disperse phase, was found to be the most convenient organic base.

SEM and TEM micrographs of the samples resulting after Et_3N addition, shown in Fig. 1, demonstrated the formation of a capsular morphology. The average diameter of the hollow particles, determined by dynamic light scattering measurements, had a value of about 330 nm (±40%) for the samples prepared both with $ZrOCl_2$ and $HfOCl_2$. The formation of the capsules started shortly after addition of the amine and seems to be completed after less than 4 hours (see the evolution of formation of the capsules with time in Fig. S1, ESI†).

Mechanism of formation of the hollow particles

In aqueous media, $ZrOCl_2 \cdot 8H_2O$ and $HfOCl_2 \cdot 8H_2O$ are known to form stable tetramers of structure $[M_4(OH)_8(H_2O)_{16}]^{8+}8Cl^- \cdot 12H_2O$ (M = Zr, Hf). The metal ions are interconnected through pairs of OH^- ions forming a ring; each metal ion is octacoordinated with $4OH^-$ and $4H_2O$ ligands. By addition of bases like ammonia, the tetrameric structure of the complex ions is maintained, and the precipitated $M(OH)_4 \cdot nH_2O$ presents actually the form $[M_4(OH)_8(OH)_8(H_2O)_8]$.[34] These species convert by condensation to $MO(OH)_2 \cdot nH_2O$, sometimes written as $MO_2 \cdot nH_2O$ and referred to as hydrous zirconia or hafnia, which yields MO_2 after dehydration by thermal treatment.

In our case, we expect the formation of these cluster species in the presence of Et_3N and their condensation at the interface to form hollow particles. We propose that the capsule formation takes place through the following steps, schematically depicted in Fig. 2:

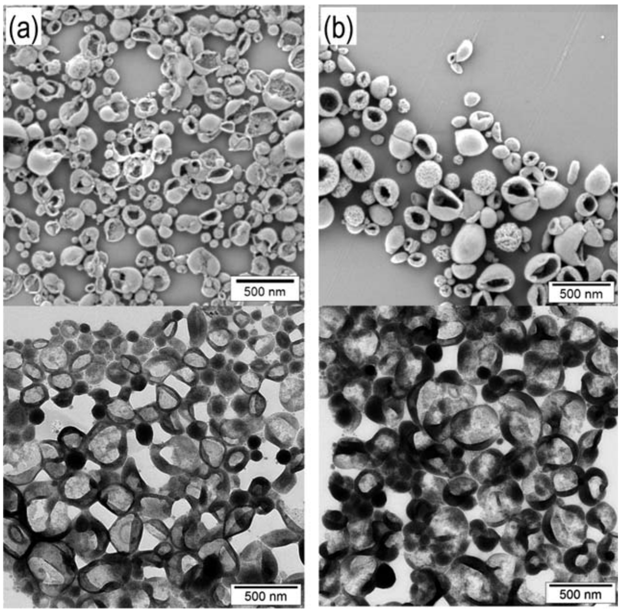

Fig. 1 SEM and TEM micrographs of (a) zirconium and (b) hafnium hydroxide hollow particles prepared with a metal-to-triethylamine molar ratio of 1 : 1.5.

(i) After addition of triethylamine, hydroxide ions are formed at the interface and within the droplets (Et_3N is partially soluble in water at room temperature) according to

$$Et_3N + H_2O \rightleftarrows Et_3NH^+OH^- \quad (1)$$

(ii) The oxychloride precursor is hydrolyzed to the metal hydroxide, which tends to form the above indicated clusters, generating triethylammonium chloride ($Et_3NH^+Cl^-$) as a byproduct. Formally, in a very simplified way and without taking into account the cluster formation, this could be written as:

$$2Et_3NH^+OH^- + MOCl_2 \rightleftarrows MO(OH)_2 + 2Et_3NH^+Cl^- \quad (2)$$

(iii) The presence of OH^- ions catalyzes the polycondensation of metal hydroxo species at the interface.

Under rapid addition of triethylamine, the concentration of OH^- is especially high at the interface, which explains the observed hollow morphology. We analyzed the influence of the speed of Et_3N addition. It was observed that a very slow addition leads to the formation of mainly solid particles instead of capsules (ESI, Fig. S2†). The results are consistent with a mechanism controlled by the diffusion of the amine from toluene to water.

Bourret and Lennox[18] reported recently a method to prepare $Cu(OH)_2$ hollow particles involving the formation of Cu(II)–methylamine complexes at the droplet interface in w/o emulsions. The size scale in their case was much larger (several micrometres) than ours. In contrast to methylamine and copper, triethylamine is not likely to form complexes with the stable Zr(IV) and Hf(IV) hydroxo complexes, but the capsule formation should rather take place through a mechanism mainly controlled by diffusion of the partially water-soluble Et_3N. Nevertheless, surface-active species between triethylammonium ions and metal hydroxide species, which would tend to move to the interface, may also be formed, analogously to similar species proposed for zirconium under addition of ammonia.[35] As a comparison, we carried out experiments substituting Et_3N with the primary amine methylamine and the tertiary tributylamine (Bu_3N), highly and very poorly soluble in water, respectively. The higher solubility in

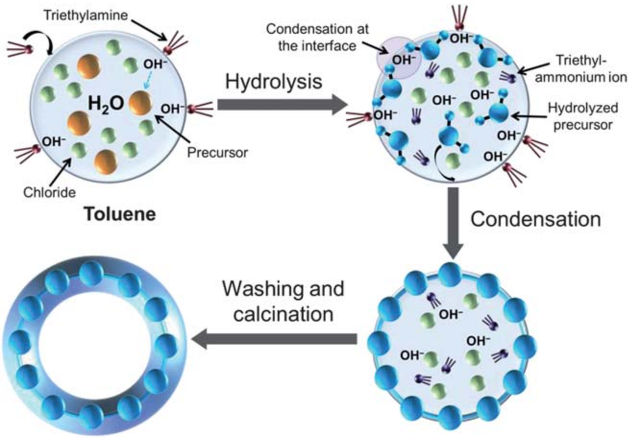

Fig. 2 Scheme of the formation of ZrO_2 and HfO_2 capsules by interfacial precipitation in the presence of triethylamine.

This journal is © The Royal Society of Chemistry 2012

water explains easily that the samples prepared with methylamine showed no capsules, but only solid particles (ESI, Fig. S3†). In the case of Bu_3N, mainly solid particles were also formed, with only sporadic occurrence of capsules (ESI, Fig. S4†). This observation can be explained by the lower basicity and more significant steric hindrance of Bu_3N in comparison to Et_3N. The slower generation of OH^- seems to favor the formation of solid particles. According to our results, the basicity and solubility in water of triethylamine are optimum for the formation of the zirconia and hafnia capsules.

Chemical and structural characterization

The presence of crystalline triethylammonium chloride, resulting from the precursor hydrolysis, was confirmed in the X-ray diffraction (XRD) patterns of the as-prepared samples (ESI, Fig. S5†). The removal of this byproduct, after washing with acetone and water, could be proven by FTIR spectroscopy. As a representative example, Fig. 3 presents the FTIR spectra of an as-prepared hafnium hydroxide sample and the same sample after washing with acetone, together with the spectrum of commercial triethylamine hydrochloride. The spectrum of the as-prepared sample indicates clearly the presence of triethylamine hydrochloride. After washing, this byproduct is mostly removed and the metal hydroxide signals are enhanced. Analogous results were obtained for the zirconium-containing samples.

In the spectrum of the washed sample in Fig. 3 (black curve), the broad peaks at 477 and 618 cm^{-1} are assigned to Hf–O modes.[36] The vibration signal at 1036 cm^{-1} originates from Hf–OH bonds and the sharp doublet at 1618 and 1637 cm^{-1} corresponds to bending modes of water coordinated to tetravalent cations, as it is also found in the tetramer structure of hafnium/zirconium hydrochloride octahydrates.[37] The broad band centered at 3414 cm^{-1} is attributed to the stretching mode of absorbed water.

Electron diffraction indicated that the resulting metal hydroxide materials forming the capsules were amorphous, as seen in Fig. 4. XRD patterns of the washed samples, presented in Fig. 5a and c, confirmed the same results.

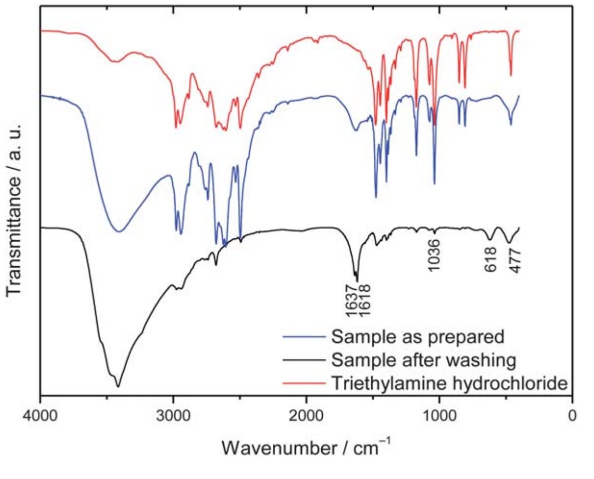

Fig. 3 FTIR spectra of a hafnium-containing sample as-prepared and after washing with acetone and water, compared with the spectrum of pure triethylamine hydrochloride.

Under thermolytic treatment at 600 °C, the amorphous capsules were transformed to monoclinic ZrO_2 and HfO_2 (Fig. 5b and d). Crystallite sizes—or, more properly speaking, sizes of the coherently scattering domains—of 24 and 20 nm were estimated for ZrO_2 and HfO_2, respectively, by using the Scherrer equation for the two most intense XRD reflections, ($\bar{1}11$) and (111). These crystallite sizes seem to correspond approximately to the thickness of the nanocapsules estimated by TEM.

Elemental analysis by EDX showed the presence of carbon and chlorine in the samples, which is ascribable to residual $Et_3NH^+Cl^-$ (ESI, Fig. S6†). Chloride ions can also become incorporated into the inorganic polymer network during the condensation process. These impurity inclusions may be helpful in forming mesoporous structures during their decomposition upon calcination.[38] After calcination, no chlorine could be detected and the carbon content was considerably reduced (ESI, Fig. S7†). Residual carbon in the calcinated sample can be attributed to an oxygen deficient combustion.

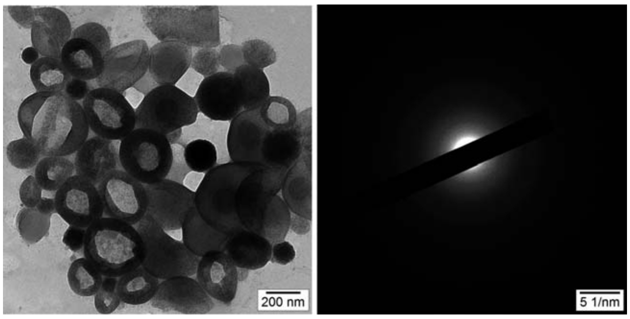

Fig. 4 TEM micrograph of a selected area of a hafnium-containing sample and corresponding electron diffraction, which indicates the amorphicity of the formed hollow particles.

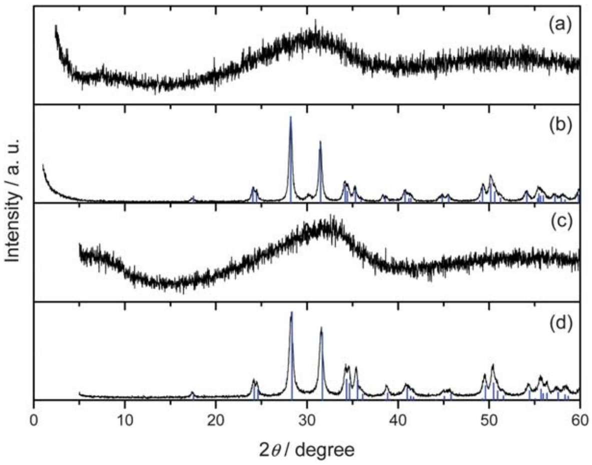

Fig. 5 XRD patterns of a Zr(IV)-containing sample (*a*: after washing, *b*: after calcination at 600 °C) and a Hf(IV)-containing sample (*c*: after washing, *d*: after calcination at 600 °C). Vertical lines indicate the positions and relative intensities of reflections of monoclinic ZrO_2 (b) and HfO_2 (d) (JCPDS cards no. 37-1484 and 34-0104, respectively).

Investigation of the encapsulation ability of the formed hollow particles

Electron microscopy had confirmed the formation of hollow particles. However, the amorphous capsules tend to collapse or break during the drying process, and it was difficult to estimate from electron micrographs whether or not the shell formation was complete. It was, thus, important to evaluate the ability of the formed hollow particles to encapsulate hydrophilic materials without leaking. For this purpose, we carried out encapsulation experiments of a substance containing a hydrophilic dye: an albumin–fluorescein isothiocyanate (FITC) conjugate. This protein–dye conjugate was chosen as a model due to its large molecular size, so that the leaking through the possibly porous shell could be minimized.

For the experiments, two miniemulsions containing $HfOCl_2 \cdot 8H_2O$ and the hydrophilic dye in the disperse phase were prepared (*cf.* Experimental section). To one of the samples, labeled as sample **C**, Et_3N was added as in the conventional experiments. The other one (sample **B**), without addition of the organic base, was taken as a reference. After stirring both samples for 4 h, aliquots of the miniemulsions were mixed with equivalent volumes of deionized water and homogenized by shaking. A third control sample (sample **A**), simply containing the continuous phase (*i.e.*, a solution of the polyisobutylene succinimide pentamine surfactant in toluene) and water, was also prepared.

After a first centrifugation, the three samples were homogenized again and centrifuged for a second time. The formed solid capsules and the aqueous and organic phases could be separated in this way. A photograph of the resulting phase separation in the samples is presented in Fig. 6. It was expected that, if the dye was efficiently encapsulated, its leak would not be significant. Otherwise, if the shells were not fully formed, the dye would be transferred to the water phase. Indeed, the hafnium hydroxide capsules formed in sample **C** had a yellow color and were collected at the bottom of the vial (Fig. 6, **C**-3). The aqueous (**C**-2) and the organic (**C**-1) phases were colorless, which indicates the absence of a significant amount of FITC. In contrast, the aqueous phase of sample **B**, in which the capsules had not been formed, had a recognizable yellow color (**B**-3). In this case the surfactant had formed a layer (**B**-2) between the organic and the aqueous phases. This could also be observed in the blank sample (**A**-2), but not in sample **C**. It can be, therefore, assumed that in sample **C** the surfactant was mostly incorporated in the shell of the formed capsules.

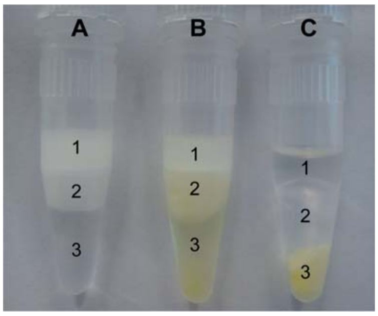

Fig. 6 Photograph of the phase separation obtained after centrifugation during the encapsulation experiments. Samples **A** (blank sample containing the continuous phase and water) and **B** (miniemulsion before addition of Et_3N): (1) organic phase, (2) surfactant, and (3) aqueous phase. Sample **C** (miniemulsion after addition of Et_3N): (1) organic phase, (2) colorless aqueous phase, and (3) hafnium hydroxide capsules containing the hydrophilic dye.

For a more precise evaluation, we recorded the absorption and photoluminescence (PL) emission spectra of the aqueous phases of samples **B** (Fig. 6, **B**-3) and **C** (Fig. 6, **C**-2), shown in Fig. 7. Sample **B** shows an absorption peak with a maximum at 444 nm and a very broad emission band with a maximum at 518 nm (excitation wavelength of 420 nm), ascribable to FITC.

As indicated before, triethylamine hydrochloride is formed during the formation of the hollow particles, which changes the pH and can influence the emission and absorption spectra of FITC. Therefore, we analyzed the change in the absorption and emission of FITC in the presence of $Et_3NH^+Cl^-$, according to the stoichiometry of formation given by eqn (2). The results (ESI, Fig. S8†) indicated that the intensity of the emission of FITC at an excitation wavelength of 420 nm is quenched by more than 50% the presence of $Et_3NH^+Cl^-$, but the emission band remains clearly observable. The intensity of the absorption band is much less affected and diminishes by less than 20%. In our case, both absorption and emission spectra of sample **C** in Fig. 7 showed that the bands were almost vanished. This result cannot be explained by a minor change of the pH and it confirms that the dye had been encapsulated in the hafnium hydroxide hollow particles without leaking to the aqueous phase.

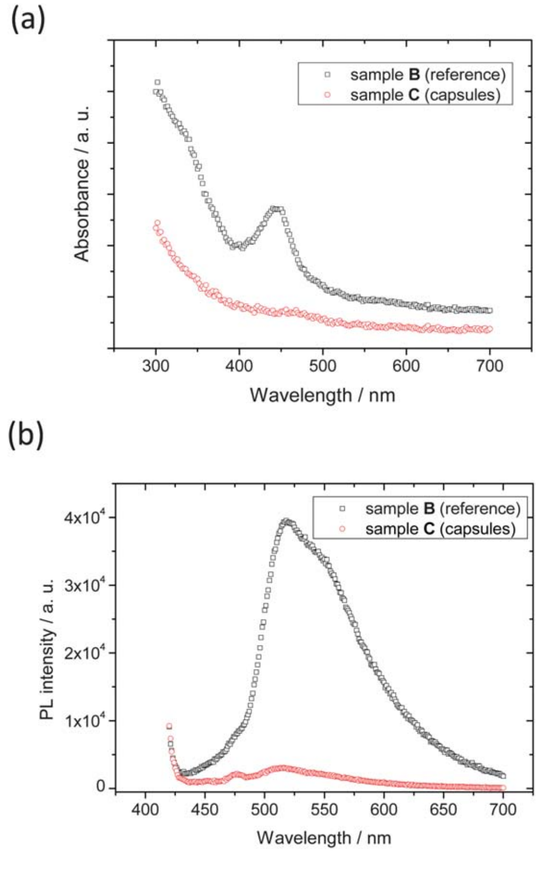

Fig. 7 (a) Absorption and (b) PL emission ($\lambda_{exc} = 420$ nm) spectra of the aqueous phase of samples **B** (reference sample) and **C** (hafnium hydroxide capsules).

This journal is © The Royal Society of Chemistry 2012

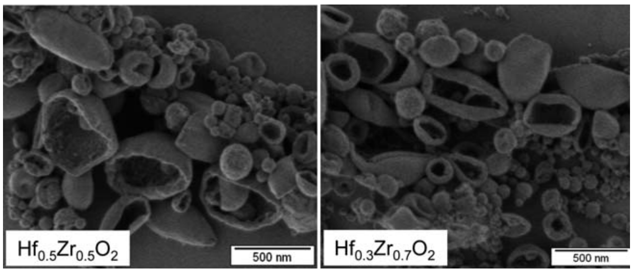

Fig. 8 SEM micrographs of $Hf_xZr_{1-x}O_2$ mixed oxides obtained after calcining at 600 °C samples prepared from mixed precursor (Hf : Zr atomic ratios of 1 : 1 and 3 : 7).

Formation of Hf/Zr mixed oxides

Due to the lanthanide contraction, zirconium and hafnium have almost identical ionic radii and the chemistry of both elements is very similar, with only small differences in solubility and volatility of some compounds.[39] However, with respect to ZrO_2, HfO_2 has a lower linear expansion coefficient, which can be of advantage in high temperature applications.[28] The catalytic activity of both metals presents also differences.[40] Thus, the properties of mixed oxides of defined compositions ($Hf_xZr_{1-x}O_2$) have been studied by different groups.[31,41,42] As the crystal structure of the oxides is essentially the same, the synthesis of mixed $Hf_xZr_{1-x}O_2$ oxides is simple. By mixing the proper molar amounts of the $ZrOCl_2$ and $HfOCl_2$ precursors, we prepared mixed hydroxide capsules with different Hf : Zr ratios that transformed into the oxides after calcination. SEM micrographs of two representative samples, with compositions $Hf_{0.5}Zr_{0.5}O_2$ and $Hf_{0.3}Zr_{0.7}O_2$, are shown in Fig. 8. The composition was checked by EDX analysis and the atomic ratio remained approximately the same, within the limits of error, as in the precursor mixtures. The larger size of the formed capsules might be explained by a different solubility of the formed species in comparison to the pure samples.

Conclusions

We have shown that the sol–gel precipitation of zirconium and hafnium hydroxides can be driven to the droplet interface by adding triethylamine to water-in-oil miniemulsions containing metal salts. In comparison to other amines, triethylamine is best suited to generate a higher concentration of OH^- at the interface, which hydrolyzes the precursor to form metal hydroxo complexes. These species generate an inorganic polymeric network by polycondensation. The formed hydroxide materials (hydrous zirconia and hafnia, $MO(OH)_2\cdot nH_2O$) are amorphous, as proven by electron and X-ray diffraction, and can be converted to the crystalline oxide (monoclinic ZrO_2 and HfO_2) by thermal treatment. Triethylamine hydrochloride is formed as a byproduct during the process, but can be removed by washing with acetone and water and by thermolysis.

The ability of our hollow particles to encapsulate hydrophilic substances could be demonstrated with a protein–dye conjugate (albumin–FITC). Spectroscopic investigations showed that the dye is encapsulated in the particles, with no significant leak, which is also a proof of the completeness of the shell formation.

The easy processability of our dispersions can offer a very convenient method for the preparation of mesoporous coatings. The preparation method is versatile and can also be used to prepare mixed metal oxides, such as $Hf_xZr_{1-x}O_2$, by adjusting the composition of the precursors contained in the disperse phase.

Acknowledgements

The authors thank Michael Steiert for the XRD measurements and Gunnar Glaßer for the assistance with the EDX analysis. Dr Umaporn Paiphansiri is acknowledged for the helpful discussions on the encapsulation experiments. P.D. thanks the PhD School in Molecular Sciences of the University of Padua for financial support.

Notes and references

1 K. An and T. Hyeon, *Nano Today*, 2009, **4**, 359–373.
2 X. W. Lou, L. A. Archer and Z. C. Yang, *Adv. Mater.*, 2008, **20**, 3987–4019.
3 S. H. Tang, X. Q. Huang, X. L. Chen and N. F. Zheng, *Adv. Funct. Mater.*, 2010, **20**, 2442–2447.
4 D. Crespy, M. Stark, C. Hoffmann-Richter, U. Ziener and K. Landfester, *Macromolecules*, 2007, **40**, 3122–3135.
5 K. Landfester and C. K. Weiss, *Adv. Polym. Sci.*, 2010, **229**, 1–49.
6 F. Caruso, *Top. Curr. Chem.*, 2003, **227**, 145–168.
7 J. Liu, F. Liu, K. Gao, J. S. Wu and D. F. Xue, *J. Mater. Chem.*, 2009, **19**, 6073–6084.
8 W. Cheng, K. B. Tang, Z. P. Liu, J. Sheng and Y. X. Qi, *Chem. Commun.*, 2009, 7185–7187.
9 L. J. Mao, C. Y. Liu and J. Li, *J. Mater. Chem.*, 2008, **18**, 1640–1643.
10 L. P. Zhu, H. M. Xiao, W. D. Zhang, G. Yang and S. Y. Fu, *Cryst. Growth Des.*, 2008, **8**, 957–963.
11 X. X. Yu, J. G. Yu, B. Cheng and B. B. Huang, *Chem.–Eur. J.*, 2009, **15**, 6731–6739.
12 Y. J. Wang, A. D. Price and F. Caruso, *J. Mater. Chem.*, 2009, **19**, 6451–6464.
13 J.-U. Park, H. J. Lee, W. Cho, C. Jo and M. Oh, *Adv. Mater.*, 2011, **23**, 3161–3164.
14 D. H. M. Buchold and C. Feldmann, *Nano Lett.*, 2007, **7**, 3489–3492.
15 F. Gyger, M. Hubner, C. Feldmann, N. Barsan and U. Weimar, *Chem. Mater.*, 2010, **22**, 4821–4827.
16 P. Leidinger, R. Popescu, D. Gerthsen and C. Feldmann, *Small*, 2010, **6**, 1886–1891.
17 H. L. Xu and W. Z. Wang, *Angew. Chem., Int. Ed.*, 2007, **46**, 1489–1492.
18 G. R. Bourret and R. B. Lennox, *J. Am. Chem. Soc.*, 2010, **132**, 6657–6659.
19 X. L. Yu, C. B. Cao, H. S. Zhu, Q. S. Li, C. L. Liu and Q. H. Gong, *Adv. Funct. Mater.*, 2007, **17**, 1397–1401.
20 W. Lu, M. Chen and L. M. Wu, *J. Colloid Interface Sci.*, 2008, **324**, 220–224.
21 Y. S. Lin, S. H. Wu, C. T. Tseng, Y. Hung, C. Chang and C. Y. Mou, *Chem. Commun.*, 2009, 3542–3544.
22 A. Guerrero-Martínez, J. Pérez-Juste and L. M. Liz-Marzán, *Adv. Mater.*, 2010, **22**, 1182–1195.
23 B. Peng, M. Chen, S. X. Zhou, L. M. Wu and X. H. Ma, *J. Colloid Interface Sci.*, 2008, **321**, 67–73.
24 C. Zurmuhl, R. Popescu, D. Gerthsen and C. Feldmann, *Solid State Sci.*, 2011, **13**, 1505–1509.
25 P. Leidinger, R. Popescu, D. Gerthsen, H. Lunsdorf and C. Feldmann, *Nanoscale*, 2011, **3**, 2544–2551.
26 C. Piconi and G. Maccauro, *Biomaterials*, 1999, **20**, 1–25.
27 J. Wang, H. P. Li and R. Stevens, *J. Mater. Sci.*, 1992, **27**, 5397–5430.
28 L. del Campo, D. De Sousa Meneses, A. Blin, B. Rousseau, E. Véron, M. Balat-Pichelin and P. Echegut, *J. Am. Ceram. Soc.*, 2011, **94**, 1859–1864.
29 T. Yamaguchi, *Catal. Today*, 1994, **20**, 199–218.

30 S. A. Steiner, T. F. Baumann, B. C. Bayer, R. Blume, M. A. Worsley, W. J. MoberlyChan, E. L. Shaw, R. Schlögl, A. J. Hart, S. Hofmann and B. L. Wardle, *J. Am. Chem. Soc.*, 2009, **131**, 12144–12154.
31 G. Jacobs, M. Milling, Y. Ji, P. Patterson, D. Sparks and B. Davis, *Catal. Lett.*, 2009, **127**, 248–259.
32 I. Salem, *Catal. Rev.: Sci. Eng.*, 2003, **45**, 205–296.
33 H. P. Klug and L. E. Alexander, *X-Ray Diffraction Procedures for Polycrystalline and Amorphous Materials*, John Wiley, New York, 1974.
34 A. F. Holleman and E. Wiberg, *Lehrbuch der Anorganischen Chemie*, De Gruyter, Berlin, 2007, (English translation of the 101st ed. available from Academic Press, 2001).
35 A. Mondal and S. Ram, *Chem. Phys. Lett.*, 2003, **382**, 297–306.
36 D. A. Powers and H. B. Gray, *Inorg. Chem.*, 1973, **12**, 2721–2726.
37 E. Barraud, S. Bégin-Coli, G. Le Caër, F. Villieras and O. Barres, *J. Solid State Chem.*, 2006, **179**, 1842–1851.
38 S. Ram and A. Mondal, *Phys. Status Solidi A*, 2004, **201**, 696–707.
39 N. N. Greenwood and A. Earnshaw, *Chemistry of the Elements*, Butterworth-Heinemann, Oxford, 1997.
40 S. Simpson and B. H. Davis, *J. Phys. Chem.*, 1987, **91**, 5664–5668.
41 R. D. Robinson, J. Tang, M. L. Steigerwald, L. E. Brus and I. P. Herman, *Phys. Rev. B: Condens. Matter Mater. Phys.*, 2005, **71**, 115408.
42 J. Tang, J. Fabbri, R. D. Robinson, Y. Zhu, I. P. Herman, M. L. Steigerwald and L. E. Brus, *Chem. Mater.*, 2004, **16**, 1336–1342.

This journal is © The Royal Society of Chemistry 2012

Nanoscale

RSC Publishing

PAPER

View Article Online
View Journal | View Issue

Cite this: *Nanoscale*, 2013, **5**, 10534

Published on 14 August 2013. Downloaded on 04/11/2013 16:07:30.

Inorganic chemistry in a nanoreactor: Au/TiO$_2$ nanocomposites by photolysis of a single-source precursor in miniemulsion†

Niels A. Heutz,*[a] Paolo Dolcet,[b] Alexander Birkner,[c] Maurizio Casarin,[b] Klaus Merz,[a] Stefano Gialanella[d] and Silvia Gross*[e]

An original synthetic route, based on the combination of a single-source precursor, UV-photodegradation and inverse w/o miniemulsion, is used to prepare Au nanoparticles (NPs) dispersed on titania. The source of the nanocomposite materials is the photolabile single-source precursor $AuCl_4(NH_4)_7[Ti_2(O_2)_2(cit)(Hcit)]_2 \cdot 12H_2O$, which is suspended in a w/o miniemulsion consisting of different surfactant/hydrocarbon/water formulations (surfactant: sodium dodecylsulfate (SDS) or Triton X-100) and subsequently irradiated with a UV lamp to promote its decomposition in the confined space of the droplets. Gold NPs that form at room temperature are found to be crystalline, while titanium dioxide occurs as an amorphous phase. Moreover, the average crystallite size of gold NPs ranges between 20 and 24 nm when using SDS and between 26 and 40 nm in the case of Triton X-100, after 4 and 8 hours of irradiation time, respectively. Scanning and transmission electron microscopies (SEM and TEM) are used to get information about the nanocomposite morphology and nanostructure, revealing that gold NPs are uniformly distributed on the titanium oxide surface. Furthermore, X-ray photoelectron spectroscopy (XPS) outcomes, besides confirming the formation of both metallic gold and titania, provide information about the high dispersion of Au NPs on the TiO$_2$ surface. In fact, the Au : Ti atomic ratio is found to be 0.45–1.5 (1 : 2–1.5 : 1), which is higher than the value determined by starting from the precursor stoichiometry (0.25). Catalytic testing in the oxidation of 2-propanol shows that decomposition of the precursor in a miniemulsion provides a nanocomposite with enhanced activity compared to the decomposition in the aqueous phase.

Received 31st July 2013
Accepted 9th August 2013

DOI: 10.1039/c3nr03977c

www.rsc.org/nanoscale

Introduction

The versatility and the wide range of possible applications in the oxidation catalysis make the nanocomposite systems M/TiO$_2$ (M = Au, Pd, Pt) the focus of growing interest.[1–7] The specific characteristics of these systems are ultimately associated with the weak interactions occurring at the metal–oxide interface,[8,9] which are a key factor to enhance the M/TiO$_2$ catalytic activity, for instance in CO and alcohol oxidation.[10–12] Au/TiO$_2$ has also been proven to be an effective catalyst for NO$_x$ reduction and the water gas shift reaction.[13,14] Furthermore, this nanocomposite has also been investigated for its outstanding photocatalytic properties[2,6,15,16] as well as for the development of photoelectrochemical solar cells.[8,17] The interest devoted to Au/TiO$_2$ systems is also motivated by their potential use in non-linear optical devices, due to the high polarizability of gold nanoparticles and the dielectric nature of the titania matrix.

We present here an original synthetic route, based on the combined use of (i) a single-source precursor, (ii) UV-photodegradation and (iii) a miniemulsion, to prepare Au nanoparticles (NPs) dispersed on TiO$_2$. Droplets formed during the miniemulsification process, which was pioneered by Landfester and co-workers,[18–25] can be used as nanoreactors which maximize the co-penetration of the two components, thus allowing us to obtain the NP nucleation and growth in a confined space. This in turn enables good control of particle size, size distribution and morphology, all of them playing a crucial role in determining the important functional properties of the resulting materials.

In this paper, we successfully explored, to the best of our knowledge for the first time, the use of water-in-oil droplets produced by a miniemulsion as nanoreactors for the *in situ* UV-photodecomposition of a tailor-made single-source precursor

---

[a] *Lehrstuhl für Anorganische Chemie I, Fakultät für Chemie und Biochemie, Ruhr-Universität Bochum, Universitätsstr. 150, D-44801 Bochum, Germany. E-mail: niels.heutz@rub.de; Tel: +49 234 3224177*

[b] *Dipartimento di Scienze Chimiche, University of Padova, INSTM, UdR Padova, Via Marzolo, 1, I-35131, Padova, Italy*

[c] *Lehrstuhl für Physikalische Chemie I, Fakultät für Chemie und Biochemie, Ruhr-Universität Bochum, Universitätsstr. 150, D-44801 Bochum, Germany*

[d] *Dipartimento di Ingegneria Industriale, University of Trento, Via Mesiano 77, 38123 Trento, Italy*

[e] *Istituto per l'Energetica e le Interfasi, IENI-CNR and Dipartimento di Scienze Chimiche, Università degli Studi di Padova, Via Marzolo, 1, I-35131, Padova, Italy. E-mail: silvia.gross@unipd.it*

† Electronic supplementary information (ESI) available: SEM and TEM images, detailed XPS peaks, thermogravimetric analysis, XRD patterns of catalysis samples and the Raman spectrum of AuTi$_4$. See DOI: 10.1039/c3nr03977c

This journal is © The Royal Society of Chemistry 2013

Published on 14 August 2013. Downloaded on 04/11/2013 16:07:30.

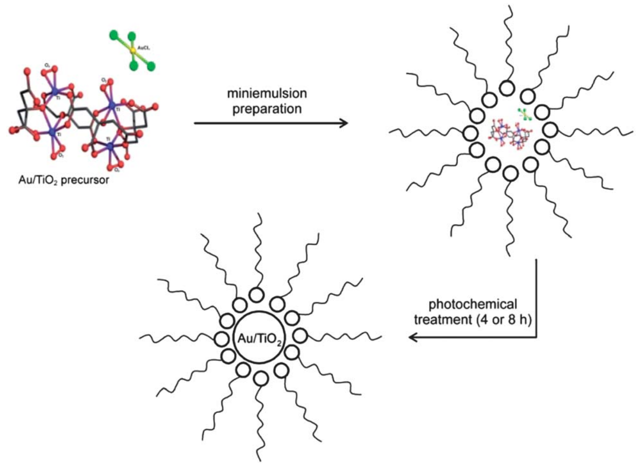

Scheme 1 Formation of Au/TiO$_2$ nanocomposite in miniemulsion by photolysis of AuCl$_4$(NH$_4$)$_7$[Ti$_2$(O$_2$)$_2$(cit)(Hcit)]$_2$·12H$_2$O.

containing both gold and titanium to give the Au/TiO$_2$ nanocomposite. The synthesis strategy is depicted in Scheme 1. The cluster AuCl$_4$(NH$_4$)$_7$[Ti$_2$(O$_2$)$_2$(Hcit)(cit)]$_2$·12H$_2$O (hereafter AuTi$_4$), prepared as described elsewhere,[6] is well known for its easy photolysis under UV irradiation. AuTi$_4$ has a well-defined structure, characterized by the coordination of titanium atoms by citric acid and peroxide groups, which favour the reduction of Au(III) to metallic gold[26] and the formation of TiO$_2$ modifications,[27,28] respectively. The addition of an aqueous AuTi$_4$ precursor solution to different surfactants (sodium dodecylsulfate (SDS) or Triton X-100)/hydrocarbon suspensions and subsequent ultrasonication resulted in a homogeneous yellow-coloured water-in-oil miniemulsion. Once the single-source precursor was embedded into the inverse micelles, the decomposition of the photolabile precursor was triggered by UV irradiation of the suspension to achieve the formation of the Au/TiO$_2$ nanocomposite directly in the nanocompartments, as sketched in Scheme 1.

Results and discussion

Experiments were carried out by changing the experimental parameters (irradiation time, chemical nature of the surfactant and dispersing phase), as summarized in Table 1, to relate their variation to the final features of the obtained nanocomposites. According to the different irradiation times and surfactants used for the preparation of the Au/TiO$_2$ nanocomposites, they are labelled as shown in Table 1.

Table 1 Sample labelling and experimental parameters used

Sample	Irradiation time [h]	Surfactant	Miniemulsion
SDS-4	4	SDS	SDS/pentanol/heptane
SDS-8	8	SDS	SDS/pentanol/heptane
T100-4	4	Triton X-100	Triton X-100/pentanol/cyclohexane
T100-8	8	Triton X-100	Triton X-100/pentanol/cyclohexane

Preparation of Au/TiO$_2$-nanocomposites in miniemulsions

Preparation in miniemulsions using the non-ionic surfactant Triton X-100. To investigate the effect of the surfactant, affecting droplet stability, as well as their size and morphology, experiments on the formation of Au/TiO$_2$ nanocomposites from miniemulsions were first performed by using a non-ionic surfactant, Triton X-100 (see Experimental section). The obtained samples were characterized by means of X-ray diffraction (XRD), transmission electron microscopy (TEM), scanning electron microscopy (SEM), X-ray photoelectron spectroscopy (XPS), and energy dispersive X-ray spectroscopy (EDXS). The results of the XRD investigations on the T100-4 and T100-8 nanocomposites, after 4 and 8 hours of irradiation time, are shown in Fig. 1. The diffraction patterns reveal the presence of fcc crystalline gold [JCPDS 4-784], whereas, although no feature ascribable to crystalline polymorphs of titania (either rutile, anatase, or brookite) was observed in the XRD patterns, the presence of titania was evidenced by XPS and EDXS analyses described in the following sections. The single crystallite sizes of the gold NPs in the nanocomposites, as evaluated from the Scherrer equation, were determined to be 26 nm after 4 hours and 40 nm after 8 hours of irradiation time, respectively. In agreement with TEM measurements (*vide infra*), this shows that increasing the irradiation time induces a growth of the metallic gold nanoparticles. In this regard, TEM micrographs (see Fig. 2) display two features representative of the microstructure of both T100-4 and T100-8: a fine dispersion of a few nanometer sized gold particles, suspended on the titania matrix, and coarser gold particles, still in the nanometric range.

Incidentally, this distribution is evidenced also by the SEM images, recorded by using the back-scattered electrons, in order to enhance the Au NP signal and allow a better size and distribution determination (see Section 1 in the ESI†). The described microstructural and crystallographic evidence is in agreement also with the SAED pattern in which gold spots and rings, although extremely weak, are visible in association with the amorphous halo. The surface composition of the nanocomposite was analyzed by XPS, providing details on both atomic percentages and chemical state of the present species. The survey spectrum (Fig. 3, top) of the powder shows peaks referring to the elements Au, Ti, O, C, and N. Details of the

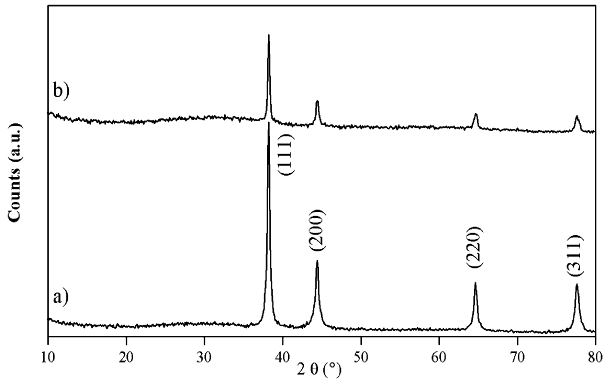

Fig. 1 XRD patterns of Au/TiO$_2$ nanocomposites: (a) T100-4 and (b) T100-8.

Published on 14 August 2013. Downloaded on 04/11/2013 16:07:30.

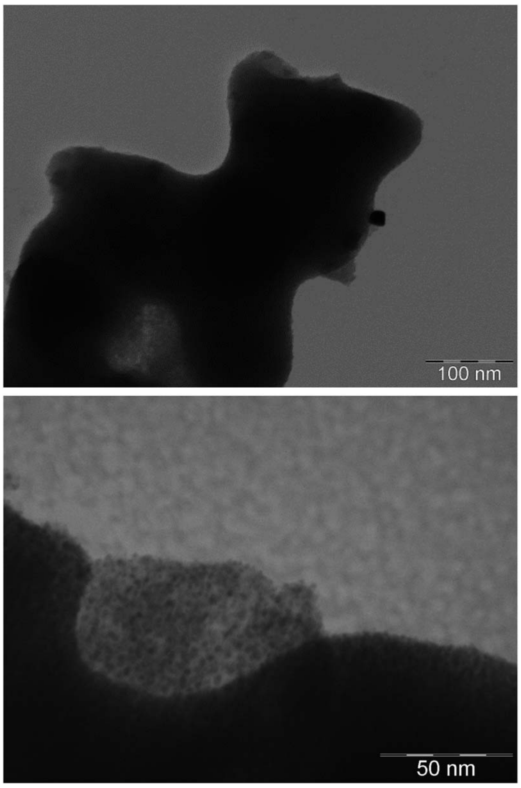

Fig. 2 TEM micrographs of the Au/TiO$_2$ nanocomposites: (top) T100-4 and (bottom) T100-8.

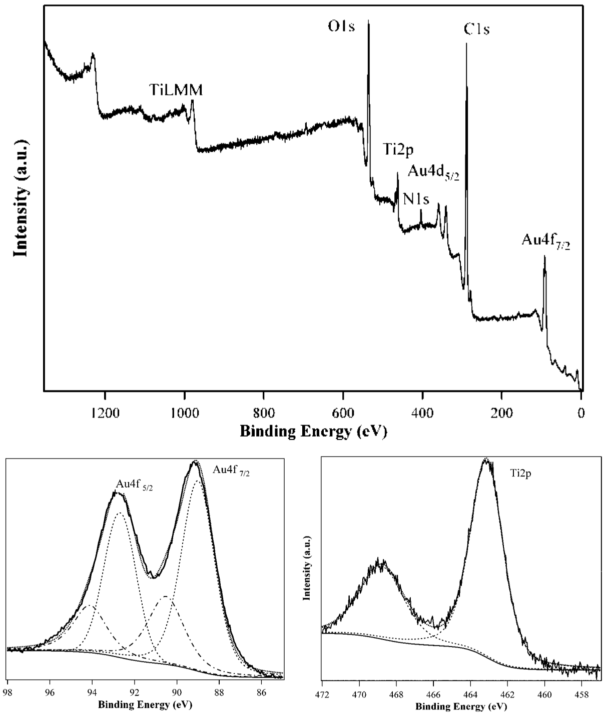

Fig. 3 XPS spectra of T100-4 (survey, Au4f, and Ti2p region).

Table 2 Elemental atomic percentages and binding energy values as determined by XPS

	BE (eV)			Atomic composition[c] (%)			
Sample	BE[a] O1s	BE[a] Ti2p	BE[b] Au4f	Ti	O	Au	C
SDS-4	529.8	459.2	84.2	2.0	21.0	3.0	74.0
	531.7	460.8	87.1				
SDS-8	529.2	461.1	84.7	2.5	21.0	2.5	74.0
	531.0	466.6	86.9				
T100-4	531.4	460.2	84.7	2.4	19.6	2.0	76.0
		465.8	85.4				
T100-8	530.2	458.6	83.9	9.4	40.0	4.2	46.4
		464.3	85.3				

[a] Values corrected for charging effects, using 284.6 eV as the carbon standard. [b] Values corrected for charging effects, using cross referencing with 458.8 eV as the titania standard. [c] Surface atomic composition determined from XPS data.

atomic percentages and Binding Energy (BE) values of the different species are summarized in Table 2 and detailed spectra can be found in the ESI (see the ESI – Section 2†). Au4f, Ti2p, and O1s are related to the Au/TiO$_2$ nanocomposite, while C1s and N1s peaks indicate residues of the surfactant and precursor. As far as the chemical nature of the different species is concerned, the deconvolution of the Au4f region (Fig. 3, bottom left) shows that two different species of Au are present in the T100-4 nanocomposite. While the BE values of the doublet at 84.7 eV and 88.3 eV are in good agreement with elemental gold,[2,5,29–32] two smaller peaks are observed at energies of 85.4 eV and 89.1 eV, thus revealing the presence of Au(III) species which can be reasonably ascribed to an incomplete decomposition of the precursor. However, the contribution to the Au(III) peak area is small, thus indicating that the precursor was mostly successfully decomposed. For T100-4, the Au(0) to Au(III) ratio (referring to the peak areas) is 2.8, indicating that the degree of conversion is as high as 74%. Although T100-8 was obtained after 8 h of irradiation, the nanocomposite still displays the presence of two gold species. The peaks referring to Au(III) contribute only to a little extent to the overall peak area, showing a Au(0) to Au(III) ratio of 2.3 (Table 3). The reason why, in this second case, a longer irradiation time does not promote a higher decomposition extent of the precursor is not clear, and it is currently under investigation. It can be argued that the longer irradiation time affects the growth of the NPs (*vide infra*) but not the decomposition rate and efficiency.

Preparation in miniemulsions using the ionic surfactant SDS. In order to compare the obtained results with a different

Table 3 Elemental atomic ratios and gold crystallite sizes of the Au/TiO$_2$ nanocomposites

Sample	T100-4	T100-8	SDS-4	SDS-8
Crystallite size[a] (nm)	26	40	26	25
Au/Ti ratio[b]	0.83	0.45	1.5	1
Au(0)/Au(III)[c]	2.8	2.3	2.2	7.3
Auger parameter α'	873.0 eV	872.9 eV	875.2 eV	873.9 eV

[a] Average particle size estimated from XRD data by using the Scherrer equation. [b] Calculated from atomic composition found by XPS. [c] Estimated from the deconvoluted peak areas of the Au4f regions.

Published on 14 August 2013. Downloaded on 04/11/2013 16:07:30.

miniemulsion system, Au/TiO_2 nanocomposites were prepared in a SDS-based miniemulsion. Samples were then prepared at irradiation times of 4 and 8 hours. XRD investigations on the obtained samples SDS-4 and SDS-8 show similar results to T100-4 and T100-8. As expected, also the Au/TiO_2 nanocomposites SDS-4 and SDS-8 consist of crystalline gold nanoparticles supported on amorphous titania. The diffraction pattern of SDS-4 in Fig. 4 confirms the presence of fcc crystalline gold [JCPDS 4-784], whereas no evidence for crystalline titania phases is observed in the XRD pattern. All this evidence mirrors the results pertaining to the nanocomposites obtained as described before. At variance with T100-4, a slightly smaller average crystallite size of about 20 nm was estimated for SDS-4. TEM analysis on the same sample substantially confirmed the picture conveyed by XRD. Gold particles appear as darker grains in Fig. 5, referring to sample SDS-4. Their size (about 100 nm), larger than the average crystallite size value provided by XRD data, indicates that they are composed of several coherently scattering domains that coalesced during the growing process. Further investigations show regions of the specimen where the presence of the above nanocrystalline gold grains is not obvious (Fig. 5) although the relevant EDXS data indicate that gold is present in these regions too. The higher magnification image shows that gold particles of about 3 nm are finely dispersed on the titania matrix (Fig. 5). Deeper insights into the morphology of the composite sample and the nanoparticle distribution were obtained by systematic SEM and TEM investigations on all synthesized materials (see the ESI– Sections 1 and 3†). XPS investigations on SDS-4 and SDS-8 give comparable results to those on T100-4 and T100-8. The survey spectra also show element specific peaks related to gold, oxygen, titanium, nitrogen, and carbon, which can be related to Au/TiO_2 and to residues of the precursor.

Detailed results of the surface composition, in particular atomic percentages and binding energy values of the different species, are summarized in Table 2 and detailed spectra are reported in the ESI.†

As for T100-4 and T100-8, the successful formation and the extent of precursor degradation were estimated from detailed XPS investigations on the gold species found in the samples. The Au : Ti atomic ratio on the surface of the powder sample SDS-4 is 1.5, whereas on the basis of the stoichiometry of the precursor a value of 0.25 could be expected. The enrichment of gold in the outer part of the material can likely be ascribed to the migration of gold towards the outer layers of the titania support and to the high surface sensitivity of XPS. The phenomenon of segregation of metallic nanoparticles in oxide matrices has been unanimously accepted.[5,33–36] The high amount of carbon has to be ascribed to the presence of surfactants. Actually, the deconvolution of the C1s region (see the ESI – Section 11†) revealed three components at 284.6, 285.9 and 288.4 eV. The first component is assigned to the aliphatic chains of the surfactant, the second one to –C–O–R groups, and the last one has a typical value for oxygen in carboxyl groups and can therefore be ascribed to residual citrate.

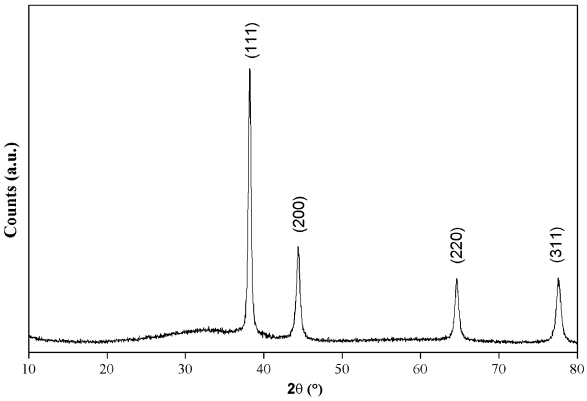

Fig. 4 XRD pattern of SDS-4.

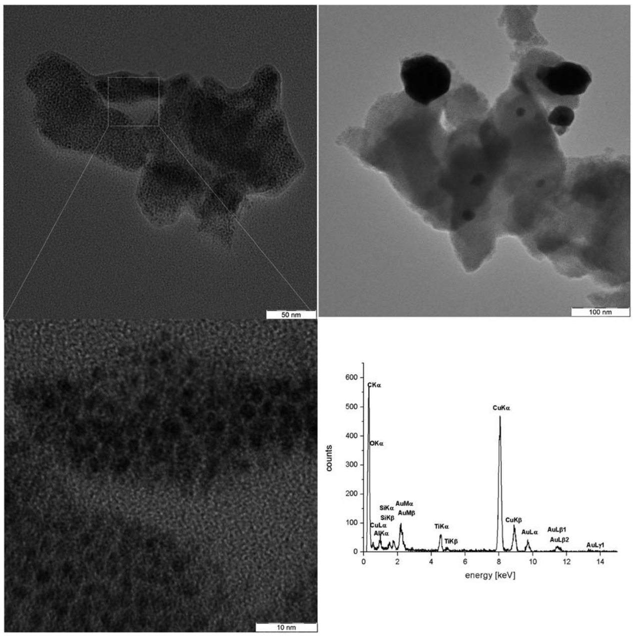

Fig. 5 TEM and EDXS of SDS-4 obtained after 4 hours.

In this regard, to evaluate the effective amount of surfactant surrounding the nanoparticles, thermogravimetric analysis was carried out, revealing a weight loss, mostly due to water, to a 12% w/w extent and to the surfactant of about 17% w/w (see the ESI – Section 17†). Also the O1s region consists of two components (see the ESI – Section 12†), one at 530.1 eV, ascribed to oxygen in the titania lattice,[2,5,37] and the latter and most intense one at 531.7 eV ascribed to the oxygen atoms of the surfactants. The presence of nitrogen has to be ultimately traced back to the presence of residual ammonium groups in the single-source precursor, whereas sulphur of the sulphate group in the surfactant could not be detected. Particularly interesting is the analysis of Ti2p and Au4f regions, shown in Fig. 6. The Ti2$p_{3/2}$ feature of the Ti2p doublet is characterized by two components, the most intense one at 459.2 eV, typical of titanium dioxide,[2,37–39] whereas the latter one, at 460.8 eV, can be ascribed to the chemical environment of titanium in the precursor, thus suggesting an incomplete decomposition. This hypothesis is further strengthened also by the Au4f region deconvolution, showing two Au4$f_{7/2}$ components at 84.2 eV and 87.1 eV.

Published on 14 August 2013. Downloaded on 04/11/2013 16:07:30.

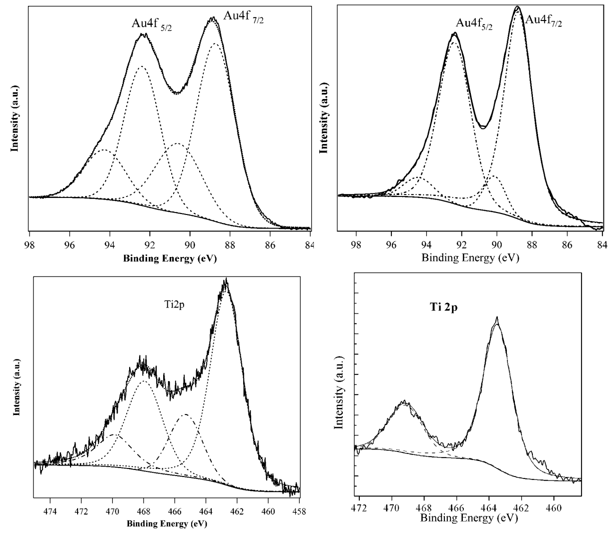

Fig. 6 XPS spectra of the Au4f (top) and Ti2p (bottom) regions of SDS-4 (left) and SDS-8 (right).

The peak at 84.2 eV corresponds to metallic gold,[2,29,30] whose presence was already evidenced by XRD analysis; the latter, at a higher energy peak (87.1 eV), was assigned to Au(III), in agreement with the above-mentioned incomplete precursor decomposition. However, it has to be pointed out that, as in the previous case, the component associated with the residual precursor has a much lower intensity than that ascribed to metallic gold on titania. As shown in Table 3, the peak area ratio of metallic gold with respect to the residual precursor line is 2.2 : 1.0, thus evidencing that the chosen route to obtain the desired compound was slightly less effective than that implying the non-ionic surfactant based droplets. In addition to the Ti2p region, the TiLMM region was also acquired to estimate the Auger parameter α' of Ti, to unambiguously determine its chemical state. The TiO_2 Auger parameter reported in the literature is 872.9 eV.[40] Detailed investigations on the interaction between TiO_2 and metals have been reported by Mejias *et al.*[41] Experimental values were, for T100 samples, in accordance with literature data. Nevertheless a α' value of 875.2 eV was calculated for SDS-4, *i.e.*, the sample with the highest Au/Ti ratio (1.5, as determined by XPS surface analysis). This finding is in very good agreement with published results,[41] which show that higher α' values are observed at a high M : TiO_2 ratio.

On the basis of XPS findings, pointing out the presence of undecomposed precursor, the irradiation time was doubled from 4 to 8 hours to trigger the complete decomposition of the Au–Ti precursor to the desired nanocomposite. The Au4f region still presents two contributions, as for SDS-4 (see Fig. 6); intense signals at 84.7 eV and 87.3 eV are in good agreement with Au4f signals of elemental gold, while the signals of lower intensity at 86.9 eV and 90.6 eV can be ascribed to the presence of Au(III) species. Compared to the Au4f region of SDS-4, though, a strong decrease of the peak intensity related to Au(III) is observed after 8 hours of irradiation in the case of SDS-8, evidencing therefore an increased precursor decomposition.

The ratio of metallic gold to residual Au(III) increased from 2.2 to 7.3, which clearly indicates an increased degradation of the precursor to form Au/TiO_2. This finding confirms the successful improvement of the precursor decomposition in the miniemulsion system by using the SDS-based miniemulsion. Compared to SDS-4 the deconvolution of the Ti2p region shows just one component. Signals at 461.1 and 466.6 eV refer to titanium dioxide. This is in agreement with our finding for O1s, where the signal at 529.2 eV can be ascribed to titanium dioxide, while the signal at 531.0 eV has to be assigned to the oxygen of the surfactant. Furthermore, in analogy with SDS-4, a higher value of the Auger parameter α' (873.9 eV) was determined for SDS-8, which is thus characterized by a gold surface enrichment; this assumption is basically confirmed also by SEM investigations (see the ESI – Section 1†). Also XRD investigations on SDS-8 revealed similar results to those on SDS-4. The diffraction pattern confirms the presence of fcc crystalline gold and no reflections ascribable to crystalline titania. The average size of the gold crystallites, estimated by using the Scherrer equation, is approximately 25 nm. In contrast to the use of a non-ionic surfactant, the miniemulsion system based on SDS seems to be more suitable to obtain smaller gold nanocrystallites or at least to limit their growth upon prolonged irradiation time.

Coherently with these indications, even TEM observations revealed a similar microstructure to that observed in sample SDS-4, as concerns in particular the coexistence of very fine and coarser gold particles. This is clearly shown by the TEM micrographs and relevant SAED patterns (see the ESI – Section 3†).

The diffraction spots, coming from the coarser particles, and the faint rings, overlapped with the amorphous halo from the titania matrix and carbon supporting film, can be both indexed to the fcc structure of metallic gold. Taken together, all these data demonstrate that the SDS-based miniemulsions are more efficient in triggering the decomposition of the precursor to yield finely dispersed gold nanoparticles on a titania matrix.

Catalytic testing – oxidation of 2-propanol

In order to investigate the influence of miniemulsions as nanoreactors on the formation of Au/TiO_2 from $AuTi_4$, the catalytic activity of the miniemulsion-prepared samples was compared to that prepared by the original route based on the decomposition of the single-source precursor in water.[6] Therefore the most promising sample SDS-8 was tested in the gaseous and liquid phase oxidation of 2-propanol as a model reaction.

Compared to the standard route, described in ref. 6 and based on the photodecomposition of $AuTi_4$ in a simple aqueous suspension, the application of miniemulsions for achieving the formation of the nanocomposite seems to be beneficial for the preparation of catalytically active Au/TiO_2. In both tests, oxidation in the gaseous phase and liquid phase, the material from the miniemulsion shows almost twice the activity (see Table 4). In the gaseous phase, an almost complete conversion and a high selectivity of 80% are observed for the sample prepared in the miniemulsion.

This journal is © The Royal Society of Chemistry 2013

Published on 14 August 2013. Downloaded on 04/11/2013 16:07:30.

Table 4 Results from catalytic testing (for details see the Experimental section)

	Gaseous phase oxidation		Liquid phase oxidation
Synthetic route	Conversion	Selectivity	TOF[c] [mol $mg_{(Cat)}^{-1}$ h^{-1}]
Miniemulsion[a]	98%	80%	0.012
Solution[b]	53%	50%	0.006

[a] SDS used as a surfactant, 8 h of irradiation time. [b] Preparation as described in ref. 6. [c] Calculated for a reaction time of 2.5 hours.

In contrast, the sample prepared in water shows only 53% conversion and lower selectivity. Also the turnover frequencies (TOFs), estimated by oxidation in the liquid phase, show twice the activity for the sample from the miniemulsion. This indicates that the miniemulsion as reaction medium influences the formation and properties of Au/TiO_2 and thereby enhances the catalytic activity.

XRD investigations (see the ESI – Section 18†) on both samples show that the gold crystallite sizes prepared in a miniemulsion and aqueous phase are 29 nm and 39 nm respectively. One explanation for this finding is that gold particles easily form agglomerates[42] in the aqueous phase and therefore tend to coalesce to bigger particles under the elevated temperature employed during the pre-treatment before the catalytic testing (see the Experimental section for further details). This indicates that preparation in a miniemulsion induces the enhanced stability of the gold particles, inhibiting at the same time particle growth during thermal treatment. Furthermore, the uniform distribution of gold nanoparticles on the titania matrix could also positively affect the catalytic activity. Thereby a more active nanocomposite is obtained compared to the original preparation method in water. These results underline the advantageous properties of miniemulsions as nanoreactors for the preparation of inorganic composite materials with unusual morphologies, controlled size and enhanced functional properties.

Conclusions

In summary, we obtained nanocrystalline gold dispersed on titania by using an original route based on photolysis of a single-source precursor in a confined space. The source of the nanocomposite materials is the photolabile single-source precursor $AuCl_4(NH_4)_7[Ti_2(O_2)_2(cit)(Hcit)]_2 \cdot 12H_2O$, which was emulsified in a w/o miniemulsion consisting of sodium dodecylsulfate/heptane/water in one case and Triton X-100/cyclohexane/water in another case, and subsequently irradiated with a UV lamp to promote its decomposition into the confined space of the droplets. Gold NPs formed at room temperature were found to be crystalline, while titanium dioxide, whose presence was confirmed by XPS and EDXS measurements, occurred in an amorphous phase. Moreover, the gold crystallite average size (evaluated using the Scherrer equation on the XRD diffractograms) was about 20 nm, increasing to 40 nm upon prolonged irradiation time in the case of T100 samples, whereas in the case of SDS ones, the average size was practically unchanged upon increased irradiation. The back-scattered SEM and TEM microscopies used to get information about the nanocomposite morphology revealed that gold NPs are uniformly distributed on the oxide surface. Furthermore, XPS outcomes, besides confirming the formation of both metallic gold and titania, also provided information about the wide dispersion of Au NPs on the TiO_2 surface. In fact, the Au : Ti ratio (1.5) was much higher than the stoichiometric one (0.25).

The thorough investigations carried out outlined that the properties of the final system (gold particle sizes and distribution) are strongly dependent on the choice of miniemulsion system and irradiation time. The miniemulsion system based on the non-ionic surfactant Triton X-100 is less favourable to form small gold particles at long irradiation time, which instead favours their growth. In contrast, SDS-based miniemulsion systems favour the formation of small sized gold particles of maximum 25 nm at any irradiation time. In both cases gold particles are finely dispersed on the supporting titania matrix, as confirmed by TEM and SEM. Our results from XPS clearly show that a high degradation of precursor material up to 88% can be induced by variation of the irradiation time.

In addition, the SDS-8 materials obtained were tested as catalysts for the oxidation of 2-propanol, showing increased catalytic activity, compared to the Au/TiO_2 reference obtained by UV decomposition of the precursor in aqueous solution.

In conclusion, it was shown that using a combined miniemulsion/single-source precursor approach, the formation of Au/TiO_2 nanocomposites with crystalline Au NPs on amorphous TiO_2 could be afforded, and that the obtained nanocomposite has also appreciable catalytic activity in model oxidation reactions.

Experimental

Materials

All chemicals were used without further purification. Sodium dodecylsulfate (SDS, $NaC_{12}H_{25}SO_4$), Triton X-100, (octylphenylether, ($C_{14}H_{22}O(C_2H_4O)_n$, $n = 9–10$)), ethanol (C_2H_5OH), 1-pentanol ($C_5H_{11}OH$), and *n*-heptane (C_7H_{16}) were purchased from Aldrich (Milan, Italy). All chemicals were used without further purification.

Synthesis of the single-source precursor $AuCl_4(NH_4)_7[Ti_4(O_2)_4(Hcit)_2(cit)_2] \cdot 12H_2O$

The precursor $AuCl_4(NH_4)_7[Ti4(O_2)_4(Hcit)_2(cit)_2] \cdot 12H_2O$ was synthesized as reported elsewhere.[6] See Fig. SI-19 in the ESI† for the Raman spectrum, confirming the presence of the Ti-peroxide group.

Preparation of Au/TiO_2 nanocomposites in a miniemulsion with ionic surfactant SDS

In a typical synthesis, 160 mg (9.2×10^{-5} mol) of the precursor were dispersed in water (10 ml), and this aqueous suspension was then added under mechanical stirring to a surfactant–solvent mixture (5.0 g SDS, 10.0 g pentanol and 25.0 g heptane;

Published on 14 August 2013. Downloaded on 04/11/2013 16:07:30.

1/2/5 w/w ratio). The resulting emulsion was then sonicated for 3 minutes (using a Sartorius Stedim Labsonic P sonifier), with an acoustic power of 322 W cm^{-2}, to generate a miniemulsion, and subsequently irradiated with a UV lamp (125 W) for 4 and 8 hours. After this treatment, the suspension turned from bright yellow to dark purple. The solid obtained was recovered by centrifugation (7000 rpm for 5 minutes) and washed with ethanol and water.

Preparation of Au/TiO_2 nanocomposites in a miniemulsion with non-ionic surfactant Triton X-100

In a typical synthesis, 152 mg (8.7×10^{-5} mol) of the precursor were dispersed in water (4 ml), and this aqueous suspension was then added under mechanical stirring to a surfactant–solvent mixture (6 g Triton X-100, 1.62 g pentanol and 46.8 g cyclohexane; 3/1/23 w/w ratio). The resulting emulsion was then sonicated for 3 minutes, with an acoustic power of 322 W cm^{-2}, to generate a miniemulsion, and subsequently irradiated with a UV lamp for 4 and 8 hours. After this treatment, the suspension turned from bright yellow to dark purple. The solid obtained was recovered by centrifugation (7000 rpm for 5 minutes) and washed with ethanol and water.

Catalytic testing

Prior to catalytic testing the samples were calcined for two hours at 600 °C. Therefore 250 mg of the Au/TiO_2 powder were dispersed in a quartz crucible and placed in a tube furnace at an airflow of 20 ml min^{-1}, and heated at 5 K min^{-1}. Gaseous phase oxidation of 2-propanol was performed in a vertical, fixed bed reactor filled with 75 mg of the sample on glass wool. Oxidation experiments were carried out for 3 h at 140 °C (413 K) with a 2-propanol/oxygen ratio of 1 : 2 mol mol^{-1}, at a total gas flow of 18 ml min^{-1}. 2-Propanol was therefore provided by a saturated nitrogen flow. Condensable reaction products were collected in a cold trap (243 K), and CO and CO_2 were analyzed with a gas detector. Liquid phase oxidation of 2-propanol (5% aq. solution) was performed in a commercial high pressure reactor BR-40 from Berghof, equipped with a thermal sensor connected to an automatic heating control, liquid sample extraction valve, gas feeding, inert inlets (TFPE) and a stirring bar. The experiments were conducted at an initial pressure of 7 atm, in synthetic air, 750 rpm stirring velocity, and 5 K min^{-1} heat ramp, up to 120 °C (393 K), holding the temperature for 2.5 h. Afterwards the heating was removed and the reactor was cooled to room temperature without further stirring. All liquid samples were analyzed by GC, using an Agilent 7820A equipped with DB-5 (30 m, 0.32 diameter, 1 μm film) and DB-WAX (30 m, 0.32 diameter, 0.5 μm film) columns.

Characterization

XPS was carried out with a Perkin-Elmer Φ 5600ci instrument using standard Al-K_α radiation (1486.6 eV) operating at 350 W. The working pressure was $<5 \times 10^{-8}$ Pa. The calibration was based on the binding energy (BE) of the $Au4f_{7/2}$ line at 83.9 eV with respect to the Fermi level. The standard deviation for the BE values was 0.15 eV. The reported BEs were corrected for the BE charging effects, assigning the BE value of 284.6 eV to the C1s line of carbon. Survey scans were obtained in the 0–1350 eV range (pass energy 187.5 eV, 1.0 eV per step, 25 ms per step). Detailed scans (58.7 eV pass energy, 0.1 eV per step, 50–150 ms per step) were recorded for the O1s, C1s, Au4f, Au4d, Ti2p, TiLMM, N1s and Na1s regions. The atomic composition, after a Shirley-type background subtraction,[43] was evaluated using sensitivity factors supplied by Perkin-Elmer.[37] Charge effects were partially compensated using a charge neutralizer (flood gun). Peak assignment was carried out according to literature data.[37] The thermogravimetric analyses (TGA) were performed in air on a LabSys Setarm SDT 2960 instrument in the temperature range 20–800 °C using a heating rate of 10 °C min^{-1}. The XRD data were collected with a Bruker D8 Advance Diffractometer equipped with a Göbel mirror. The angular accuracy was 0.001° and the angular resolution was better than 0.01°. The average crystallite sizes were calculated by means of the Scherrer formula from the most intense peaks of each spectrum. Further wide angle X-ray diffraction patterns were recorded using a Philips X'Pert PRO diffractometer operating in the θ–2θ geometry, equipped with a graphite monochromator on the diffracted beam (CuK_α radiation). For transmission electron microscopy (TEM) analyses two different instrumentations were used. Higher resolution images were acquired using a Hitachi H-8100 electron microscope (accelerating voltage of up to 200 kV, LaB_6 filament). For general images and selected area electron diffraction (SAED) patterns, a Philips CM12 microscope, operating at a maximum voltage of 120 kV, was used. Both microscopes were equipped with an energy dispersive X-ray spectroscopy (EDXS) apparatus, used to measure qualitatively the composition of the observed sample regions. SAED patterns were indexed with the software package Process Diffraction.[44] Sample preparation was quite straightforward, as it required spreading a drop of a sonicated alcohol suspension of the powder samples on a carbon coated copper TEM grid. The microstructure of the Au/TiO_2 nanocomposites (precipitates obtained before heating the suspensions at 80 °C were also investigated) was analyzed using scanning electron microscopy (SEM). Measurements were performed using a field emission SEM, Zeiss SUPRA 35VP, that, as TEMs, was equipped with an EDXS system (Oxford INCA).

Acknowledgements

Dr Chiara Maccato (Dipartimento di Scienze Chimiche, Università di Padova) is gratefully acknowledged for SEM measurements and helpful discussion.

Notes and references

1 M. Valden, X. Lai and D. W. Goodman, *Science*, 1998, **281**, 1647.

2 J. Zhao, S. Sallard, B. M. Smarsly, S. Gross, M. Bertino, C. Boissiere, H. Chen and J. Shi, *J. Mater. Chem.*, 2010, **20**, 2831.

3 X. Wang, D. R. G. Mitchell, K. Prince, A. J. Atanacio and R. A. Caruso, *Chem. Mater.*, 2008, **20**, 3917.

This journal is © The Royal Society of Chemistry 2013

Published on 14 August 2013. Downloaded on 04/11/2013 16:07:30.

4 H. Li, Z. Bian, J. Zhu, Y. Huo, H. Li and Y. Lu, *J. Am. Chem. Soc.*, 2007, **129**, 4538.
5 L. Armelao, D. Barreca, G. Bottaro, A. Gasparotto, E. Tondello, M. Ferroni and S. Polizzi, *Chem. Mater.*, 2004, **16**, 3331.
6 M. Rohe, E. Loeffler, M. Muhler, A. Birkner, C. Woell and K. Merz, *Dalton Trans.*, 2008, 6106.
7 J. S. Ratliff, S. A. Tenney, X. Hu, S. F. Conner, S. Ma and D. A. Chen, *Langmuir*, 2009, **25**, 216.
8 N. Chandrasekharan and P. V. Kamat, *J. Phys. Chem. B*, 2000, **104**, 10851.
9 A. Vittadini and A. Selloni, *J. Chem. Phys.*, 2002, **117**, 353.
10 C. H. Tseng, T. C. K. Yang, H. E. Wu and H. C. Chiang, *J. Hazard. Mater.*, 2009, **166**, 686.
11 N. Zheng and G. D. Stucky, *Chem. Commun.*, 2007, 3862.
12 J. D. Grunwaldt and A. Baiker, *J. Phys. Chem. B*, 1999, **103**, 1002.
13 A. Karpenko, Y. Denkwitz, V. Plzak, J. Cai, R. Leppelt, B. Schumacher and R. J. Behm, *Catal. Lett.*, 2007, **116**, 105.
14 J. Leerat, S. Osuwan and E. Gulari, *Catal. Lett.*, 2011, **141**(1), 62.
15 S. Zhao, G. Ramakrishnan, D. Su, R. Rieger, A. Koller and A. Orlov, *Appl. Catal., B*, 2011, **104**, 239.
16 A. Orlov, D. A. Jefferson, N. Macleod and M. Lambert, *Catal. Lett.*, 2004, **92**, 41.
17 Y. Takahashi and T. Tatsuma, *Appl. Phys. Lett.*, 2011, **99**, 182110.
18 M. Antonietti, *Colloid Chemistry II*, Springer, Berlin/Heidelberg, 2003.
19 K. Landfester, *Adv. Mater.*, 2001, **13**, 765.
20 K. Landfester, *Annu. Rev. Mater. Res.*, 2006, **36**, 231.
21 M. Antonietti and K. Landfester, *Prog. Polym. Sci.*, 2002, **27**, 689.
22 K. Landfester and M. Antonietti, in *Colloids and Colloid Assemblies*, Wiley-VCH, Weinheim, Germany, 2004, ch. 6, p. 175.
23 R. Rossmanith, C. K. Weiss, J. Geserick, N. Hüsing, U. Hoermann, U. Kaiser and K. Landfester, *Chem. Mater.*, 2008, **20**, 5768.
24 R. Schiller, C. K. Weiss, J. Geserick, N. Hüsing and K. Landfester, *Chem. Mater.*, 2009, **21**, 5088.
25 R. Muñoz-Espi, K. C. Weiss and K. Landfester, *Curr. Opin. Colloid Interface Sci.*, 2012, **17**, 212–224.
26 T. N. Vorobyova, O. N. Vrublevskaya and A. V. Vengura, *Surf. Coat. Technol.*, 2005, **200**, 2481.
27 K. Tomita, V. Petrykin, M. Kobayashi, M. Shiro, M. Yoshimura and M. Kakihana, *Angew. Chem.*, 2006, **118**, 2438–2441; *Angew. Chem., Int. Ed.*, 2006, **45**, 2378–2381.
28 Y. F. Deng, Z. H. Zhou, H. L. Wan and K. R. Tsai, *Inorg. Chem. Commun.*, 2004, **7**, 169.
29 M. P. Seah, G. C. Smith and M. T. Anthony, *Surf. Interface Anal.*, 1990, **15**, 293.
30 M. T. Anthony and M. P. Seah, *Surf. Interface Anal.*, 1984, **6**, 95.
31 G. Johansson, J. Hedman, A. Berndtsson, M. Klasson and R. Nilsson, *J. Electron Spectrosc. Relat. Phenom.*, 1973, **2**, 295.
32 W. McLean, C. A. Colmenares, R. L. Smith and G. Somorjai, *J. Phys. Chem.*, 1983, **87**, 788.
33 J. Yu, J. Xiong, B. Cheng and S. Liu, *Appl. Catal., B*, 2005, **60**, 211.
34 H. E. Chao, Y. U. Yun, H. U. Xingfang and A. Larbot, *J. Eur. Ceram. Soc.*, 2003, **23**, 1457.
35 C. He, Y. Yu, X. Hu and A. Larbot, *Appl. Surf. Sci.*, 2002, **200**, 239.
36 L. Armelao, D. Barreca, G. Bottaro, A. Gasparotto, S. Gross, C. Maragno and E. Tondello, *Coord. Chem. Rev.*, 2006, **250**, 1294.
37 W. F. Stickle, J. F. Moulder, P. E. Sobol and K. D. Bomben, *Handbook of X-ray Photoelectron Spectroscopy*, Perkin-Elmer, Eden Prairie, MN, 1992.
38 S. O. Saied, J. L. Sullivan, T. Choudhury and C. G. Pearce, *Vacuum*, 1988, **38**, 917.
39 W. E. Slinkard and P. D. DeGroot, *J. Catal.*, 1981, **68**, 423.
40 G. M. Ingo, S. Dirè and F. Babonneau, *Appl. Surf. Sci.*, 1993, **70–71**, 230.
41 J. A. Mejias, V. M. Jimenez, G. Lassaletta, A. Fernandez, J. P. Espinos and A. R. Gonzalez-Elipe, *J. Phys. Chem.*, 1996, **100**, 16255.
42 A. Fernandez, A. Caballero, A. R. Gonzalez-Elipe, J. M. Herrmann, H. Dexpert and F. Villain, *J. Phys. Chem.*, 1995, **99**, 3303.
43 D. A. Shirley, *Phys. Rev. B: Solid State*, 1972, **5**, 4709.
44 L. Labar Janos, *Ultramicroscopy*, 2005, **103**, 237.

Chapter 5.

Experimental details

This Chapter is referred to the systems which are not reported as full paper and presents the corresponding Experimental details.

5.1. Synthesis

5.1.1. *Chemicals*

All miniemulsions were prepared by using a 3:1 weight ratio of Brij® 52 and Igepal® CO-630 surfactants. Brij® 52 is a polyethylene glycol hexadecyl ether, characterized by a HLB value of 5; Igepal® CO-630 is a branched polyoxyethylene (9) nonylphenylether, with a HLB value of 13 (see Fig. 5.1). The final surfactants mixture was prepared to achieve a final HLB value of 7, well suited for stabilizing inverse miniemulsions.

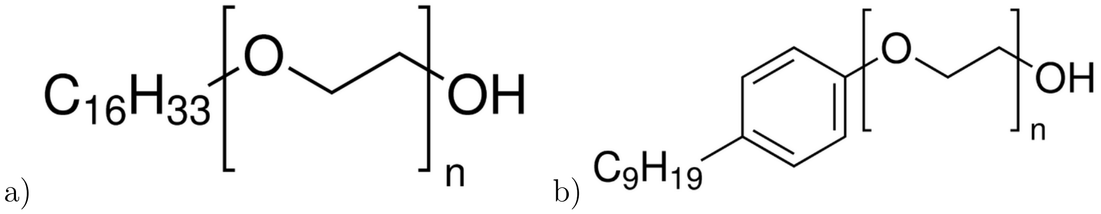

Figure 5.1.: Molecular structures for a) Brij® 52 (n=2) and b) Igepal® CO-630

All miniemulsions were homogenized bu using a Sartorious Stedim LabsonicP homogenizer, mounting a 3 mm titanium tip and operating at amplitude of 70%, corresponding to an acoustic power of 322 W/cm^2. During sonication, the miniemulsions were kept in a ice bath, in order to avoid overheating.

Chemical	**Molar mass (g/mol)**	**CAS Number**	**Supplier**
Brij® 52	330	9004-95-9	Sigma-Aldrich
C_6H_{12}	84.16	110-82-7	Sigma-Aldrich
$Ca(NO_3)_2 \bullet 4H_2O$	236.15	13477-34-4	Sigma-Aldrich
CH_3COSH	76.12	507-09-5	Sigma-Aldrich
CH_3CSNH_2	75.13	62-55-5	J.T Baker Chemicals
$Cu(NO_3)_2 \bullet 2.5H_2O$	232.59	19004-19-4	Alfa Aesar
$CuCl_2 \bullet 2H_2O$	170.48	10125-13-0	Sigma-Aldrich
$Eu(NO_3)_3 \bullet 5H_2O$	428.06	63026-01-7	Sigma-Aldrich
$Gd(NO_3)_3 \bullet 6H_2O$	451.36	19598-90-4	Sigma-Aldrich
$HSCH_2COONH_4$ 60% in H_2O	109.15	5421-46-5	Sigma-Aldrich
Igepal® CO-630	617	68412-54-4	Sigma-Aldrich
$Mn(CH_3COO)_2 \bullet 4H_2O$	245.09	6156-78-1	Sigma-Aldrich
$MnCl_2 \bullet 4H_2O$	197.91	13446-34-9	Sigma-Aldrich
$Na_2S \bullet 9H_2O$	240.18	1313-84-4	Sigma-Aldrich
NaF	41.99	7681-49-4	Sigma-Aldrich
NaOH	40.00	1310-73-2	BDH Prolabo
NH_2CSNH_2	76.12	62-56-6	Sigma-Aldrich
$Sm(CH_3COO)_3 \bullet xH_2O$	327.49	100587-91-5	Strem Chemicals
$Tb(NO_3)_3 \bullet 5H_2O$	435.02	57584-27-7	Sigma-Aldrich
$Zn(NO_3)_2 \bullet 6H_2O$	297.49	10196-18-6	Sigma-Aldrich

Table 5.1.: Used chemicals

5.1.2. *Synthesis of ZnS nanostructures*

In a typical synthesis, two identical mixtures, A and B, were prepared by dispersing 100 mg of Igepal® CO-630 (0.16 mmol) and 300 mg of Brij® 52 (0.9 mmol) in 8.0 g of cyclohexane. Subsequently, 2 ml of an aqueous 1 M $Zn(NO_3)_2 \bullet 6H_2O$ precursor solution ($2.0 \bullet 10^{-3}$ mol) were added to mixture A and stirred, yielding emulsion A', while 2 ml of Na_2S 2 M ($4.0 \bullet 10^{-3}$ mol) were added to mixture B, to generate, after mechanical stirring, emulsion B'. In the case of the doped systems, 0.04 mmol of a dopant metal salt (either $CuCl_2 \bullet 2H_2O$, $Mn(CH_3COO)_2 \bullet 4H_2O$, $Sm(CH_3COO)_3 \bullet xH_2O$, $Gd(NO_3)_3 \bullet 6H_2O$ or $Tb(NO_3)_3 \bullet 5H_2O$) were added to the Zn containing solution, to achieve a final Zn:M molar ratio of 50:1. Both emulsions were then separately sonicated for 3 minutes. The resulting miniemulsions A ' and B' were mixed together and sonicated again, with unchanged time and amplitude. The mixture was allowed to stand for one night. The precipitate that formed was separated by centrifugation (10 krpm for 10 minutes) and washed deionized water. The procedure of centrifugation and washing was repeated five times.

5.1.3. *Synthesis of CuS nanostructures*

In a typical synthesis, two identical mixtures, A and B, were prepared by dispersing 100 mg of Igepal® CO-630 (0.16 mmol) and 300 mg of Brij® 52 (0.9 mmol) in 8.0 g of cyclohexane. Subsequently, 2 ml of an aqueous 1 M Cu^{II} precursor solution ($2.0 \bullet 10^{-3}$ mol, either $Cu(NO_3)_2 \bullet 2.5H_2O$ or $CuCl_2 \bullet 2H_2O$) were added to mixture A and stirred, yielding emulsion A', while 2 ml of aqueous solution of the appropriate sulfur source (either 0.5, 1 or 2 M depending on the molar ratio) were added to mixture B, to generate, after mechanical stirring, emulsion B'. In the case of the doped systems, 0.04 mmol of a dopant metal salt (either $MnCl_2 \bullet 4H_2O$, $Eu(NO_3)_3 \bullet 5H_2O$, $Sm(CH_3COO)_3 \bullet xH_2O$, $Gd(NO_3)_3 \bullet 6H_2O$ or $Tb(NO_3)_3 \bullet 5H_2O$) were added to the Cu containing solution, to achieve a final Cu:M molar ratio of 50:1. Both emulsions were then separately sonicated for 3 minutes. The resulting miniemulsions A ' and B' were mixed together and sonicated again, with unchanged time and amplitude. The mixture was allowed to stand for one night. The precipitate that formed was separated by centrifugation (10 krpm for 10 minutes) and washed deionized water. The procedure of centrifugation and washing was repeated five times.

5.1.4. *Synthesis of CaF_2 nanostructures*

In a typical synthesis, two identical mixtures, A and B, were prepared by dispersing 100 mg of Igepal® CO-630 (0.16 mmol) and 300 mg of Brij® 52 (0.9 mmol) in 8.0 g of cyclohexane. Subsequently, 2 ml of an aqueous 0.5 M $Ca(NO_3)_2 \bullet 4H_2O$ precursor solution ($1.0 \bullet 10^{-3}$ mol) were added to mixture A and stirred, yielding emulsion A', while 2 ml of aqueous solution of 1 M NaF ($2.0 \bullet 10^{-3}$ mol) were added to mixture B, to generate, after mechanical stirring, emulsion B'. In the case of the doped systems, 0.04 mmol of a dopant metal salt (either $Sm(CH_3COO)_3 \bullet xH_2O$, $Gd(NO_3)_3 \bullet 6H_2O$ or $Tb(NO_3)_3 \bullet 5H_2O$) were added to the Ca containing solution, to achieve a final Ca:M molar ratio of 50:1. Both emulsions were then separately sonicated for 3 minutes. The resulting miniemulsions A ' and B' were mixed together and sonicated again, with unchanged time and amplitude. The mixture was allowed to stand for one night. The precipitate that formed was separated by centrifugation (10 krpm for 10 minutes) and washed deionized water. The procedure of centrifugation and washing was repeated five times.

5.2. Characterization

5.2.1. *Dynamic Light Scattering*

DLS analyses on the as-prepared suspensions were carried out using a Malvern Zetasizer Nano S (Dipartimento di Scienze Chimiche, Università di Padova, mounting a He-Ne laser, λ=633 nm), at a temperature of 20 °C, using cyclohexane as solvent reference.

5.2.2. *UV-Vis and Reflectance Spectroscopy*

Absorbance spectra were recorded using a Varian UV-CARY 5E (Dipartimento di Scienze Chimiche, Università di Padova, Italy), in the spectral range 280 – 800 nm. For reflectance measurements, the instrument was equipped with an integrating sphere coated with polytetrafluoroethylene (PTFE). The geometry used allowed to exclude the specular component of the reflected light. The spectra were collected within a range from 300 to 2000 nm, with a spectral resolution of 1 nm.

5.2.3. *Transmission Electron Microscopy*

TEM analysis was carried out using a Philips CM12 microscope (Università di Trento, Italy) operating at 120 keV and equipped with an EDXS, which allows localized chemical analyses. For each sample, both images and Selected Area Electron Diffraction (SAED) patterns were collected as well as EDXS chemical analyses to investigate morphology and dimensions of the obtained nanostructures, their crystalline nature and local chemical composition.

5.2.4. *Scanning Electron Microscopy*

The morphology of the synthesized samples was analysed by using SEM. Measurements were performed using a Field Emission (FE-SEM) Zeiss SUPRA 40VP (Dipartimento di Scienze Chimiche, Università di Padova, Italy), with a primary beam acceleration voltage of 5 kV and a conventional secondary electron detector for the SEM investigations.

5.2.5. *X-ray Diffraction*

The XRD data were collected with a Bruker D8 Advance Diffractometer (Dipartimento di Scienze Chimiche, Università di Padova, Italy), equipped with a Göbel mirror by using the CuK_α radiation. The angular accuracy was 0.001° and the angular resolution was better than 0.01°. Selected experimental data were analyzed using the Material Analysis Using Diffraction (MAUD) software package [152, 153], an original software used to work out quantitative crystallographic and microstructural information using a Rietveld code.

5.2.6. *X-ray Photoelectron Spectroscopy*

The powders were investigated by XPS with a Perkin-Elmer Φ 5600ci instrument (Dipartimento di Scienze Chimiche, Università di Padova, Italy), using standard Al K_α radiation (1486.6 eV) operating at 350 W. The working pressure was $< 5 \bullet 10^{-8}$ Pa $\sim 10^{-11}$ torr. The calibration was based on the binding energy (BE) of the $Au4f_{7/2}$ line at 83.9 eV with respect to the Fermi level. The standard deviation for the BE values was 0.15 eV. The reported BEs were corrected for charging effects, assigning the BE value of 284.6 eV to the C1s line of carbon [92, 134]. Survey scans were obtained in the 0 - 1350 eV range (pass energy 187.5 eV, 1.0 eV/step, 25 ms/step). Detailed scans (29.35 eV pass energy, 0.1 eV/step, 50-150 ms/step) were recorded for the O1s, C1s, and the other regions of interest in the different analyzed samples. The atomic composition, after a Shirley-background subtraction [161] was evaluated using sensitivity factors supplied by Perkin-Elmer [92]. Charge effects were partially compensated by using a charge neutralizer (flood gun). Peak assignment was carried out according to literature data.

5.2.7. *X-ray Absorption Spectroscopy*

Samples preparation: For metal K- or L_3-edges, samples were finely ground into an homogeneous powder with cellulose as dispersant and pressed into pellets. For S K-edge measurements, samples were finely ground, dispersed in ethanol and filtered on a previously prepared cellulose filter.

Metals K- or L_3-edges: Metal K- or L_3-edges spectra were recorded at the 2.9 T bending magnet SuperXAS beamline at Swiss Light Source (SLS), under standard ring conditions (2.4 GeV, 400 mA). For energy selection, a Si(111) double-crystal monochromator was used. Spectra were collected in the fully tuned configuration of the monochromator. Data were collected in transmission mode using an ionization chamber placed downstream of the sample or, for dopants edges, in fluorescence mode, using a 13-element Ge solid state detector. Internal energy calibration was accomplished by simultaneous measurement of the absorption of an appropriate metallic foil placed between two ionization chambers situated after the sample.

Mn K-edge spectra were collected at the bending magnet XAFS beamline at Elettra, under standard ring conditions (2.0 GeV, 300 mA). For energy selection, a Si(111) double-crystal monochromator was used. Spectra were collected in the fully tuned configuration of the monochromator. Data were collected in transmission mode using an ionization chamber placed downstream of the sample. Internal energy calibration was accomplished by simultaneous measurement of the absorption of a Mn foil placed between two ionization chambers situated after the sample.

S K-edge: S K-edge spectra were collected at the bending magnet XAFS beamline at Elettra, under standard ring conditions (2.0 GeV, 300 mA). For energy selection a Si(111) double-crystal monochromator was used. Spectra were collected in the partially detuned configuration of the monochromator, in order to provide harmonics rejection. Data were collected in transmission mode using an ionization chamber placed downstream of the sample.

Data reduction and analysis: Data reduction and analysis was performed using the Demeter package [162]; in particular, background removal was performed by the Autobk routine of the Athena software, which was also used for data alignment and calibration. The extracted EXAFS function were fitting exploiting the software Artemis.

5.2.8. *Inductively Coupled Plasma – Mass Spectrometry*

Chemicals and materials: All reagents were of analytical grade and were used as purchased: HNO_3 (CAS Number 7697-37-2) 70%, ≥99.999% (Sigma Aldrich), $HClO_4$ 70% RP Normapur (Prolabo, France). Zn (100mg/l) was present in the multi-element standard Solution CPAchem Calibration Standard (MS19EB.10.2N.L1). Gd, Sm and Tb (all 1 mg/l) were present in the ICP-MS Calibration Standard (MS98B2.1.2N.L1). All solutions were prepared in MilliQ ultrapure water obtained with a Millipore Plus System (Milan, Italy, resistivity 18.2 $M\Omega\ cm^{-1}$). The ICP-MS was tuned daily using a 1 µg/l tuning solution containing ^{140}Ce, ^{7}Li, ^{205}Tl and ^{89}Y (Agilent Technologies, UK). A 100 µg/l solution of ^{45}Sc and ^{115}In (Aristar®, BDH, UK) prepared in 2% (v/v) nitric acid was used as an internal standard through addition to the sample solution via a T-junction.

Solution setup: Multielement standard solutions were prepared in 2% v/v HNO_3. The calibration solutions were prepared by gravimetric serial dilution from multi-element standard solutions, at six different concentrations (min. 10 ppb–max. 1000 ppb). Calibration plots were obtained with an internal standard. All regressions were linear with a determination coefficient larger than 0.9999. To check for instrumental drift, one of the multi-element standards was analysed every 10 samples. Blank samples of ultrapure water and reagents were also prepared using the same procedures as for the samples. All blank levels obtained were subtracted appropriately.

NPs digestion: NPs doped samples (50 mg) were placed in a 25 ml digestion vials and added with 3 ml of 70% HNO_3 and 3 ml 60% $HClO_4$. Vials were heated on a hot plate at 200 ± 10 °C for 150 min. A PTFE cap was used to minimize sample loss from the vial. Vials were then cooled and the obtained solutions were diluted with 2% v/v HNO_3. All the elements were measured by using inductively coupled plasma coupled to mass spectrometer Agilent Technologies 7700x ICP-MS system (Agilent Technologies International Japan, Ltd., Tokyo, Japan,), equipped with an octupole collision cell. The instruments were optimized daily to achieve optimum sensitivity and stability according to manufacturer recommendations. All parameters were checked daily using an in-house optimization program.

5.2.9. *Micro-Raman Spectroscopy*

Micro-Raman experiments were performed with a with a Thermo Scientific DXR Raman microscope (Dipartimento di Scienze Chimiche, Università di Padova, Italy), operating in the range 100-6000 cm^{-1}, with a solid state laser of wavelength of 780 nm and a 10x objective.

5.2.10. *FT-IR and Attenuated Total Reflectance-Infrared Spectroscopy*

FT-IR analysis: FT-IR experiments were performed with a NEXUS 870 FT-IR (NICOLET) (Dipartimento di Scienze Chimiche, Università di Padova, Italy), operating in the transmission range 4000-400 cm^{-1}, collecting 32 scans with a spectral resolution of 4 cm^{-1}. The measurements were recorded by dispersing the powders in anhydrous KBr.

ATR: ATR spectra were collected with a NEXUS 870 FT-IR (NICOLET), equipped with an ATR accessory, operating in the range 4000-500 cm^{-1}, collecting 32 scans with a spectral resolution of 4 cm^{-1}.

5.2.11. *Thermogravimetric analysis – Differential Scanning Calorimetry*

The TGA-DSC analyses were performed in air or in N_2 atmosphere (see main text for details) on a LabSys Setarm SDT 2960 instrument (Dipartimento di Scienze

Chimiche, Università di Padova, Italy), in the temperature range 20-800° C using a heating rate of 10° C/min.

5.2.12. *Photoluminescence*

Photoluminescence measurements were performed at the University of Verona using a tunable dye laser pumped by a Nd:YAG laser as the excitation source. The emission signal was analyzed by a half-meter monochromator (HR460, Jobin Yvon) equipped with a 150 lines/mm grating and detected with a CCD detector (Spectrum One, Jobin Yvon) or with a photomultiplier. The spectral resolution of the emission spectrum is about 0.4 nm. The emission decay curves were recorded upon pulsed laser excitation and detected with a GaAs photomultiplier (Hamamatsu) and a 500 MHz digital oscilloscope (WaveRunner, LeCroy).

5.2.13. *Viability and cytotoxicity tests*

Cell culture: Human ovarian carcinoma cells ES2 were cultured in T75 flasks until confluence in RPMI-1860 (Euroclone, Italy) supplemented with 10% inactivated fetal bovine serum, 2 mM L-Glutamine and penicillin-streptomycin (Invitrogen, US). Then, cells were trypsinized and seeded in 48-well plates at a density of $2 \bullet 10^4$ cells/cm^2 in 1 ml of medium. 24 hours after seeding, cells started to be cultured in full medium with doped $Ca(OH)_2$ or $Mg(OH)_2$ nanoparticles. Two concentrations were chosen to evaluate the influence of each NP on cell behavior: 100 µg/ml (high concentration) and 30 µg/ml (low concentration). As a negative control for the following tests, a group of samples were kept in NP-free medium. Before use, nanoparticles were incubated in ethanol 70% (Roth, Germany) overnight at 4°C. Subsequently, after a centrifugation for 5 minutes at 3000 rpm, NP were resuspended in sterile distilled water and centrifuged again three times to completely remove the ethanol. After the last centrifugation, NP were dispersed in full media at the appropriate concentrations.

AlamarBlue assay: Cell viability was evaluated after 2, 24 and 48 hours of incubation in medium with nanoparticles. To this purpose, AlamarBlue assay (Invitrogen, US) was performed according to manufacturer's instructions. Briefly, culture medium (with or without NP) was removed from samples and substituted with 1 ml of full medium with 10% v/v of AlamarBlue solution. Cells were incubated at 37°C for 3 hours and subsequently, 100 µl of the supernatant were transferred in a black 96-well plate. The amount of AlamarBlue reduced by viable cells was assessed measuring the corresponding fluorescence signal (excitation wavelength: 565 nm; emission wavelength: 595 nm) with a microplate reader (Tecan Infinite M200 Pro). 10% v/v AlamarBlue solution was also incubated as a control and its fluorescence was subtracted from those of samples.

Lactate dehydrogenase assay: Cytotoxicity of $Ca(OH)_2$ and $Mg(OH)_2$ nanoparticles at high and low concentration was evaluated after 24 hours of incubation. A lactate dehydrogenase-based (LDH) assay was used (in vitro toxicology assay kit, Sigma-Aldrich, US) following the provided instructions. In short, LDH enzymes are released by cells into the external environment when the cellular membrane is damaged. Therefore, the activity of LDH in the culture medium is a measure of cell necrosis and/or apoptosis and can be evaluated by means of a colorimetric reaction involving the reduction of NAD and the subsequent conversion of a tetrazolium salt into a colored compound. The amount of this product after the enzymatic reaction in the sample culture media was assessed measuring the absorbance of the supernatant at 490 nm, using the absorbance at 690 nm as a reference to normalize the measurements.

Chapter 6.

Conclusions and perspectives

The aim of this work was to investigate the use of the soft-templating colloidal route of inverse miniemulsions for the controlled synthesis of inorganic nanostructures. This route has proven to be very versatile, easily affording, through different chemical processes, the formation of a wide variety of products, ranging from pure and doped binary (ZnO, ZnS, CuS, SnO_2) and ternary (Mg- and Ca- hydroxides) compounds to more complex systems (e.g., nanocomposites), with different chemical processes involved. In addition, a series of hybrid organic/inorganic materials was also prepared, in this case by means of direct miniemulsions.

For all the investigated systems, this colloidal route proved to be highly reproducible, allowing a good control of the stoichiometry of the systems, both for pure systems and for doped ones. As far as this latter case is concerned, the matrix-to-dopant molar ratios showed excellent agreement between nominal and experimental ratio. Furthermore, it is worth noting as the chosen methodology indeed influenced the size and the morphology of the obtained products. Additionally, the collected evidences showed that the confining imposed by the miniemulsions droplets has a strong influence on the crystallization process. This influence is not limited to the aforementioned anisotropic growths, but it extends to the formation of pure nanocrystalline materials at room temperature. Similar syntheses, carried out in the same experimental conditions (e.g., nature of precursors, molarity, molar ratio, aging time) but in bulk solutions rather than in a colloidal system, did not yield the crystallization of a pure phase, instead a co-presence of different phases was pointed out.

This thesis focused on two class of functional inorganic materials, which i) may be exploited as contrast agents in optical bioimaging, or ii) might find use in catalysis.

As far as the former are concerned, the aim of the work was to obtain luminescent materials by selectively doping biocompatible matrices, and correlate measured functional properties with structural and morphological characteristics. In most cases this was successfully achieved, and the methodology chosen proved to be effective in embedding the dopants. Doped ZnO (Sec. 3.4), Mg and Ca hydroxides (Sec. 3.5), and CaF_2 (Sec. 3.8) all displayed interesting luminescent properties and, for the first two cases, preliminary cytotoxicity and cell viability assays were performed, showing promising results in terms of biocompatibility. Furthermore, for zinc oxide and hydroxides nanostructures the choice of surfactant proved to be essential in promoting the formation of crystalline materials (e.g., see the case of Span® 80 in Sec. 3.5).

As far as the sulfides are concerned, even though the dopants embedding was confirmed, no luminescence ascribable to these species was revealed. The exact nature of this quenching is still under investigation. A preliminary and tentative explanation could be the role played by the adsorbed surfactants or, especially in the case of CuS, to an highly adsorbing matrix. This quenched luminescence and the formation of oxidic superficial layers are challenges that will need a further improvement in the synthetic procedure.

Moving to the second class of materials, those for catalysis, results herein reported clearly demonstrate the wide versatility of miniemulsions: the involved systems are very different, characterized by distinct chemistries (i.e, polymerization, sol-gel interfacial reaction and photodecomposition); nevertheless, all of them were successfully controlled, also in terms of morphologies (e.g., Sec. 4.2 & Sec. 4.3). In addition, the nanocomposite Au/TiO_2 showed once again the importance of the confinement effect, since its catalytic activity and selectivity resulted as twice the one of the same systems prepared as a bulk.

Another interesting point, evidencing the importance of the surfactant choice, was the different stability achieved by varying surfactants. Different surface-active agents were used, both cationic (SDS) and non-ionic (PVP, Triton® X-100, Igepal® CO-630, Brij® 52). Surprisingly, emulsion stability was also achieved when using SDS, despite its high HLB value. On the other hand, high amounts of surfactant were needed to ensure stability. Better results were obtained, as expected, by using non-ionic surfactants, in particular the Igepal® CO-630 - Brij® 52 mix. When using pure Triton® X-100 (or Igepal® CO-630), the corresponding miniemulsion were characterized by a smaller average hydrodynamic diameter (35-40 nm) than when using the surfactants mix (140-180 nm), but the amount of surfactant and solvent used also were greater in the former case. The surfactants also played a significant role in determining the morphology of the obtained nanostructures. For example, Triton® X-100 was found to induce the formation of ZnO platelets, whereas in the presence of PVP, spherical particles formed. In the case of the surfactants mixture, on the other hand, the nanostructures morphology was mostly dictated by their chemistry (e.g., CuS platelets).

Overall, these systems represented a challenge in terms of their characterization, often showing apparently contrasting results. In this regard, only a synergy of different analytical techniques allowed a complete description of the systems, not only in terms of chemico-physical, structural and morphological properties, but also when the interplay between these features and the functional properties is tackled.

The evidences so far collected disclose an interesting perspective for future developments, in particular a more detailed investigation of the non-classical crystallization paths observed in the confined space.

In addition, a way to further improve crystallinity and an effective insertion of doping ions in the host lattice might be the coupling of the miniemulsion route with microwave irradiation, thus combining control of size and morphology with structural one. In fact, microwaves induce very fast, efficient and homogeneous heat deposition, affecting the nucleation and growth of single crystalline domains [163, 164].

Appendix A.

Characterization Methods

A.1. Dynamic Light Scattering

DLS is a technique that is used to determine the average hydrodynamic size and its distribution profile for particles or polymers in suspension. The investigated suspension is irradiated with a laser beam and the presence of particles in suspension gives rise to scattering phenomena. The suspended particles, on the other hand, undergo Brownian motion and therefore the distances between the scatterer centers is constantly changing, thus also affecting the constructive and destructive interference of the scattered waves. The practical effect is that the scattered intensity experiences a time-dependent fluctuation, with faster fluctuation with decreasing particle size.

DLS instruments record these intensity fluctuations and generate an auto-correlation curve *g(t)* in the form:

$$g(t) = \frac{\langle I(t)I(t+\tau)\rangle}{\langle I(t)\rangle^2} \tag{A.1}$$

where I is the scattered intensity and τ is the delay time. This curve is then modeled with an exponentially decay function, whose exponential includes the particles diffusion coefficient D. This is directly connected to the average hydrodynamic diameter d_H through the Stokes-Einstein [165] equation:

$$d_H = \frac{k_B T}{3\pi\eta D} \tag{A.2}$$

where η is the viscosity of the solvent, k_B is Boltzmann's constant and T is the absolute temperature.

In this PhD thesis, DLS was used to determine the average size of the droplets forming the exploited miniemulsions.

A.2. UV-Vis and Reflectance Spectroscopies

Uv-Vis and Reflectance spectroscopies involve the study of the electronic transition occurring in the specimen when it is irradiated with radiation in the UV-Vis range (typically intended as the 250 nm-800 nm range). Whereas standard UV-Vis is performed in transmission mode and thus requires the specimen to be in solution, reflectance spectroscopy is useful for solid sample. In the case of Reflectance measurement, a photometric sphere normally called “integrating sphere” is connected to the instrument. The purpose of this sphere is to integrate the diffusely reflected light both from the sample and the standard (the sphere is internally coated with either MgO or $BaSO_4$, both white materials that can work as standard) [166]. The diffuse reflectance R_{sample} is defined as

$$R_{sample} = \frac{R_{tot}}{R_{standard}}$$

where R_{tot} is the total diffuse reflectance measurement collected whereas R_{standard} is the component only due to the standard. This definition is formally similar to the definition of transmittance in normal absorption mode.

In this PhD thesis these spectroscopies where exploited in order to investigate the band gap of the synthesized semiconductors and their modification due to the presence of the doping ions.

A.3. Transmission Electron Microscopy

A Transmission Electron Microscope allows the direct imaging of objects with a resolution in the nanometers range. The sample is irradiate by an electron beam, generated by a thermoionic or field emission gun and focused on the sample by electromagnetic lenses. When the electron beam hits the sample, it undergoes scattering and, if the specimen is properly prepared (i.e., very thin), the electron beam will go through the sample (the transmitted wave can be considered as a forward elastically-scattered wave). The transmitted beam is then focused on the recording system, usually a charge coupled device (CCD). The electron image which forms is the interference result of the beams scattered at different angles and patterns collected by the detector are then converted mathematically into images. The ultimate resolution of the images is influenced by aberrations introduced by the lenses.

In addition to direct images, selected area electron diffraction (SAED) patterns can be recorded, also allowing to obtain crystallographic information from the imaged regions.

In this PhD thesis, TEM microscopy was used to investigate the morphology of the obtained powders and, through the coupled use of SAED, to further confirm the crystallographic data obtained by XRD.

A.4. Scanning Electron Microscopy

Similarly to TEM, Scanning Electron Microscopy is also used for the direct imaging of objects, with resolution in the nanometer range (depending on the recording modality used). In a SEM, an electron beam scans the specimen and several different signal can be collected, following the different kinds of interaction of the electron beam with the sample. The most commonly signal used corresponds to the secondary electrons, generated by photoionization of the sample surface. This modality enables a topographical analysis of the specimen. Alternatively, backscattered electrons can be collected, corresponding to primary electrons which undergo elastic scattering when impinging on the sample. Since the backscattering intensity is strongly related to the atomic number Z of the atom interacting with the electron, this recording mode can give information about the distribution of elements in an inhomogeneous sample. A more precise determination of the specimen composition and elements distribution can be achieved by collecting the X-ray fluorescence signal which follows the photoionization process. This is the basis of the Energy Dispersive X-ray spectroscopy (EDXS).

In this PhD thesis, SEM microscopy was used to determine the morphology of the obtained nanostructures and, in the case of the Au/TiO_2 nanocomposite, to map the distribution of the components through the acquisition of the backscattered signal.

A.5. X-ray Diffraction

X-ray diffraction is a technique to determine the crystal structure of a specimen through the detection and interpretation of the interference pattern created by X-rays diffracted by a periodic lattice.

When a specimen is irradiated by an X-ray beam, its electronic density will interfere with the incoming beam and, being the wavelength comparable in size with the interatomic distances, it will diffract it (elastic scattering). If the specimen is crystalline and therefore the electronic density is periodical, the diffracted beams will interfere following a precise pattern. This phenomenon is described by Bragg's law, depicted schematically in Fig. A.1

$$n\lambda = 2d\sin\theta \tag{A.3}$$

where n (n=1,2,3....) is the order of diffraction, λ is the source wavelength (typically Cu K_α, with λ=1.5406 Å), d is the distance between crystal planes and θ is the incident angle (with respect to the surface).

Whenever the conditions expressed by Eq. A.3 are satisfied, constructive interference occur and a reflection signal will be detected. A typical diffractrogram presents a

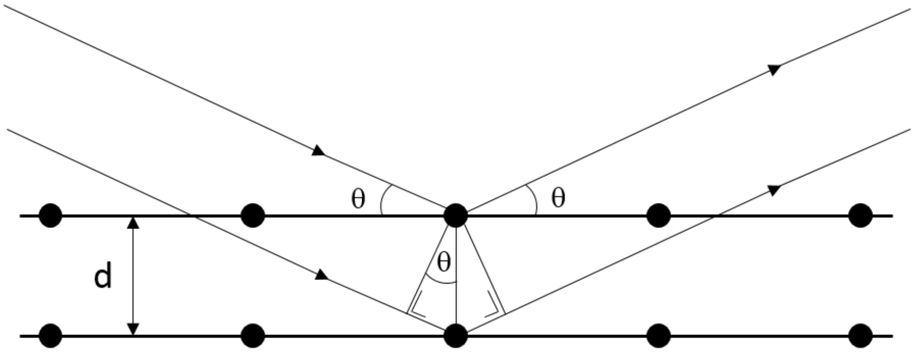

Figure A.1.: Schematic representation of Bragg's law

series of Bragg's peak in order of increasing 2θ values. The choice of 2θ is due to the fact that, in the most common experimental setup (Bragg-Brentano geometry), both X-ray source and detector move simultaneously of an angle θ each. The position of the reflections are related by Bragg's law to the interplanar spacings in the crystal and the relative intensities of the reflections are connected to the nature (in terms of Z) of the atoms which generate that signal and to the crystallographic direction is detected. In addition, if various phases are present, reflections intensities are indicative of the amount of each phase present. Small shifts in the Bragg's peaks positions can be traced back to distortions and strains in the crystalline lattice, whereas the investigation of the peak shape can give information about the crystallite size.

Regarding this last point, a rough estimate of the average crystallite size d_{av} can be given from the width of the reflections by applying the Scherrer formula [129]:

$$d_{av} = \frac{K\lambda}{\beta cos\theta} \tag{A.4}$$

where K is an adimensional constant related to the crystal cell shape (e.g., for a cubic crystal cell, K is equal to 0.94) and β is the reflection's broadening, usually expressed as FWHM (in radians). The Scherrer formula is easy to apply, but due to some rather crude underlying approximations, its accuracy is limited. A more detailed investigation of the diffraction pattern can be achieved through a full pattern refinement method, in particular the Rietveld refinement method [167–169]. It uses a least square approach to refine a theoretical line profile in order to achieve the best match with the experimental pattern. Through this approach it is possible not only to estimate more accurately the average crystallite size d_{av}, but also to evaluate lattice stresses, strains and preferred orientations.

A.6. X-ray Absorption Fine Structure Spectroscopy

X-ray radiation is an electromagnetic wave characterized by energy in the 500 eV to 50 keV range, corresponding to wavelengths of about 25 to 0.25 Å [170]. Within this high energy range, X-rays interact with all matter, through the photoelectric effect, firstly fully understood by Einstein [171]. During an X-ray photoelectric event, a photon is destroyed (e.g. through absorption) by a tightly bound inner shell electron (from 1s or 2p state) of an atom and the excess energy is transferred to the electron, which is then ejected as photoelectron. This is satisfied only if the incoming photon possesses energy greater (or equal) to that of the binding energy of the electron. If this condition is not satisfied, the bound electron will remain unperturbed. .

As introduced above, when an X-ray beam travels through matter it will experience intensity attenuation, mostly due to absorption phenomena (scattering phenomena also occur, but the cross sections for these are much lower). The intensity I of an X-ray beam passing through a sample of thickness t is related to the incoming intensity by Beer's law: $I = I_0 e^{-\mu(E)t}$, where $\mu(E)$ is the absorption coefficient, and I and I_0 are the intensities of the transmitted and incoming beams respectively. This absorption coefficient depends on the sample density ρ, the atomic number Z, atomic mass A, and the X-ray energy E as

$$\mu(E) \approx \frac{\rho Z^4}{AE^3} \tag{A.5}$$

This is generally a smooth function, but when the energy E corresponds to the binding energy of a core-level electron there is a sharp increase in the absorption, and an absorption edge arises. XAFS, more specifically, is the modulation of $\mu(E)$ as a function of energy near and just above these edges. Since each element has core-level electrons with well-defined binding energies and the incoming beam energy can be chosen accordingly, XAFS is an element-specific spectroscopy [170].

After an X-ray photon is absorbed, the atom is left in an excited state, since a photoelectron is ejected and a core-hole is formed. This excited state has a lifetime in the range 10^{-15}-10^{-17} s (depending on Z), and it can decay through two mechanisms. The first is X-ray fluorescence, in which a higher-energy electron fills the core hole, releasing the excess energy (element-specific) as X-ray photons. The second possible process is the Auger effect, a two-electron process in which an electron from a higher-energy level fills the hole and the excess energy is used to eject a second electron into the continuum. These decay mechanisms coexist, but the harder the incoming X-ray, the more the fluorescence is likely to occur (for E>2keV X-ray fluorescence dominate). They take place contextually with the absorption, but the latter is not affected by them. Furthermore, since they involve hole annihilation (which is proportional to the absorption of photons), they can also be used for determining $\mu(E)$ when absorption mode does not yield the desired results (i.e. highly diluted samples), with fluorescence usually preferred over Auger effect.

During a XAFS experiment, the modulation of μ with energy E is measured either in transmission as

$$\mu(E) = ln\left(\frac{I_0}{I}\right) \tag{A.6}$$

or in X-ray fluorescence (or Auger emission) as

$$\mu(E) \propto \frac{I_f}{I_0} \tag{A.7}$$

where I_f is the fluorescence intensity.

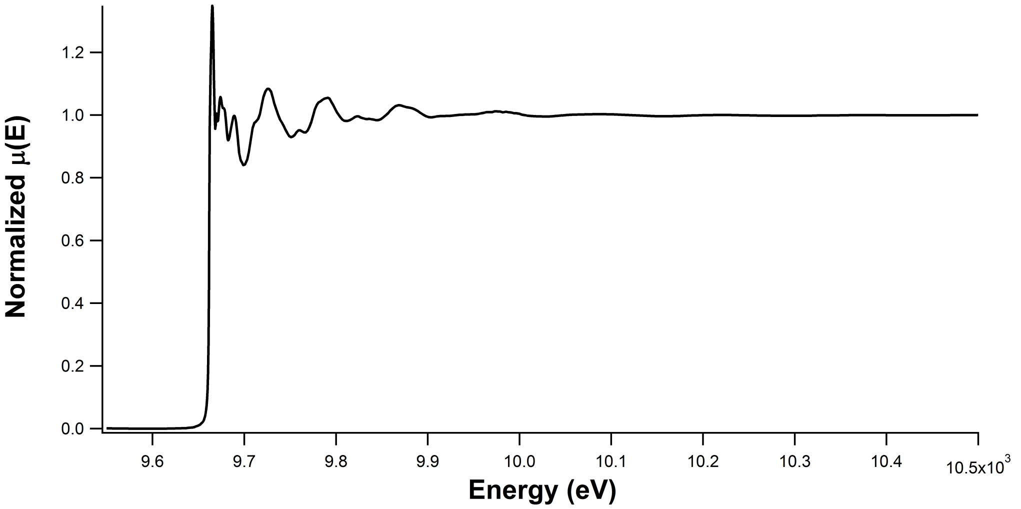

Figure A.2.: Normalized $\mu(E)$ for ZnS at Zn K-edge

In Fig. A.2, the typical XAFS spectrum for the Zn K-edge of ZnS is shown. As it can be seen, there is a sharp edge centered at about 9.66 keV, followed by a series of oscillations. Generally a XAFS spectrum is divided in two regions: the first portion encompassing the near-edge area, within 40-50 eV from the edge, called X-ray Absorption Near Edge Structure (XANES); the second develops up to hundreds of eV from the edge and collects all the modulations, which are collectively called Extended X-ray Absorption Fine Structure (EXAFS). These two regions can in first approximation be described by the same basic physical principle, but they provide different information, with the EXAFS part which is currently easier to interpret in a quantitative way then the XANES portion.

The oscillations found in the EXAFS spectrum are generated by the interference effect involving scattering of the outgoing photoelectron from the neighboring atoms. The probability of an absorption event depends on both the initial and final state of the electron (*vide infra*). The initial state is the core level corresponding to the edge investigated (K, L_1, L_2, L_3, ...), whereas the final state is represented by the outgoing photoelectron (immersed in the potential of all the neighboring atoms), which is usually described as a spherical wave. The outgoing spherical wave will have wavelength $\lambda = 2\pi/k$, where

$$k = \sqrt{\frac{2m}{\hbar^2}(E - E_0)} \tag{A.8}$$

E is the incident photon energy and E_0 is the threshold energy for the investigated edge. For an isolated atom (i.e. monatomic gas), the $\mu(E)$ will have a smooth decay. In the presence of neighboring atoms, the outgoing photoelectron wave will be backscattered by these, producing an incoming wave that will interfere (either constructively or destructively) with the outgoing wave. This interference will generate the sinusoidal oscillatory behavior constituting the EXAFS portion. The amplitude and frequency of the undulatory modulation of $\mu(E)$ depends on type and number of the neighboring atoms and their distance from the absorber. The oscillations are described by the EXAFS fine-structure function $\chi(E)$, defined as

$$\chi(E) = \frac{\mu(E) - \mu_0(E)}{\mu_0(E)} \tag{A.9}$$

Where $\mu_0(E)$ is the smooth background absorption. In order to relate more easily the structure function $\chi(E)$ with the structural parameters, it is necessary to convert the X-ray energy to the modulus of the wave vector k, leading to the EXAFS function $\chi(k)$. In the k space, the EXAFS equation can be modeled as

$$\chi(k) = \sum_j N_j F_j(k) S_i(k) e^{-2\sigma_j^2 k^2} e^{-2r_j/\lambda_j(k)} \frac{sin\left(2kr_j + \phi_{ij}(k)\right)}{kr_j^2} \tag{A.10}$$

Here $F_j(k)$ is the backscattering amplitude from each of the N_j neighboring atoms of the jth kind, characterized by a Debye-Waller factor σ_j (to take into account both thermal and static disorder), at a distance r_j from the scatterer. $S_i(k)$ is the amplitude reduction factor due to many-body inelastic effects (e.g shake-up/off processes). The term $e^{-2r_j/\lambda_j(k)}$ describes the inelastic losses due to the scattering processes the photoelectron experiences, being $\lambda_j(k)$ the electron mean free path; $\phi_{ij}(k)$ is the total phase shift experience by the photoelectron [172]. This EXAFS equation, even though complicated, is quite powerful since, by knowing the scattering amplitude $F_j(k)$ and the phase shift $\phi_{ij}(k)$ it is possible to determine N_j, r_j and σ_j, thus precisely unraveling the local structure around the scatterer, since the backscattering factors depend on the Z of the atomic species, giving atomic specificity.

In more detail, the absorption process is an event involving a transition between two quantum states, and therefore the absorption coefficient $\mu(E)$ can be describe by Fermi's Golden rule as

$$\mu(E) \propto \left|\left\langle f \middle| \hat{V} \middle| i \right\rangle\right|^2 \tag{A.11}$$

Where $|i\rangle$ is the initial state (X-ray photon and core electron, no photoelectron), $\langle f|$ is the final state (core hole and photoelectron, no X-ray photon) and $\hat{V}$ is the interaction potential, causing the transition. The core electron is tightly bound to the absorbing atom, therefore the initial state is not affected by the presence of neighboring atoms. On the other hand, the final state is perturbed since the photoelectron will be scattered by those atoms; it can therefore be expanded as a sum of an isolated unperturbed atom $\langle f_0|$ contribution and a perturbation $\langle f_{scat}|$. Within this approximation, it can be derived that $\mu(E) \propto \langle f_{scat}| \hat{V} |i\rangle$. For a tightly bound core electron, $|i\rangle$ can be approximated as an atomic wavefunction, localized at the position of the absorber, and the interaction potential gives rise to a term proportional to e^{ikr}; the perturbation $\langle f_{scat}|$ can be represented as the wavefunction of the scattered photoelectron, $\psi_{scat}(r)$. Combining these terms, the EXAFS is described by the expression:

$$\chi(E) \propto \int dr\delta(r)e^{ikr}\psi_{scat}(r) = \psi_{scat}(0) \tag{A.12}$$

This indicates that the EXAFS function $\chi(E)$ is proportional to the amplitude of the photoelectron scattered in a volume restricted to the center of the absorbing atom. The outgoing spherical wave described by the wave vector k, at the position r_j where a scattering atom is located, is proportional to

$$\psi_{out}(r_j) \propto \frac{sin(kr_j)}{r_j} \tag{A.13}$$

The presence of the jth neighboring atom will produce a scattered wave with amplitude of the incoming wave, but scaled by $F_j(k)$, the backscattering amplitude characteristic of the jth atom, and with a phase shift $\pi/2$:

$$\psi_{scat}(r_j) \propto \frac{sin(kr_j)}{r_j}F_j(k)\frac{sin(kr + {}^{\pi}\!/_{2})}{r} \tag{A.14}$$

Keeping in mind that only the region around the center of the absorbing atom is of interest, the above expression is reduced to:

$$\psi_{scat}(r_j) \propto F_j(k)\frac{sin(kr_j)}{r_j}\frac{sin(kr_j + {}^{\pi}\!/_{2})}{r_j} = F_j(k)\frac{sin(2kr_j)}{2r_j^2} \tag{A.15}$$

This is valid for an electron moving in a constant potential, but the photoelectron travels in a varying potential, which cause a phase shift $\phi_{ij}(k)$:

$$\psi_{scat}(r_j) \propto F_j(k)\frac{sin(2kr_j + \phi_{ij}(k))}{2r_j^2} \tag{A.16}$$

For the considerations discussed above, the same proportionality also holds for the EXAFS signal $\chi(k)$:

$$\chi(k) \propto F_j(k)\frac{sin(2kr_j + \phi_{ij}(k))}{2r_j^2} \tag{A.17}$$

Furthermore, the terms $F_j(k)$ and $\phi_{ij}(k)$ are dependent on the Z of the neighboring atom, therefore they make EXAFS sensitive to the atomic species [172]. In condensed phases, many atoms surround the absorbing atom; the overall EXAFS is obtained by summing up the N_j different backscattered waves, introducing additional terms. For example, in ordered structures, the distance r_j has to be treated as an average of all possible absorber-j atom pairs, since thermal and static disorder in the bond distances will give a range of different possible distances; this range is accounted for by the mean square displacement σ_j^2 (usually termed Debye-Waller factor). Furthermore, in addition to elastic scattering events, inelastic events can also take place; the scattered wave, moreover, has to travel back to the absorber before the excited state decays (core-hole is filled). Both the inelastic scattering and the finite core-hole lifetime are taken into account by the electron mean free path $\lambda_j(k)$ (typically in the 5 to 30 Å range, showing a universal dependence on k). EXAFS spectroscopy, therefore, gives information on the type (through amplitude $F_j(k)$) and number (N_j) of neighboring atoms, and their distance (r_j) from the absorber. The values of the backscattering amplitudes $F_j(k)$ and the phase shifts $\phi_{ij}(k)$ are transferable between different systems and can be calculated within the muffin tin approximation. In order to extract the EXAFS function from the collected data (data reduction), several preliminary steps are needed [173]:

- The measured intensities are converted to a $\mu(E)$ curve ($\mu(E) = ln(I_0/I)$)
- Data are corrected from spurious contributions by subtracting a pre-edge background
- The atomic background $\mu_0(E)$ is removed and data are normalized
- The EXAFS function $\chi(E)$ is isolated and converted to $\chi(k)$
- The EXAFS $\chi(k)$ is k^{n}-weighted (with n=1,2 or 3) and Fourier-transformed into the R space, giving a pseudo radial distribution function

For the EXAFS analysis, only the region above the absorption edge is of interest. The first step to isolate the desired information is to remove the contribution of instrumental background, lower-energy edges and elastic and Compton scattering to the absorption coefficient below the edge. The pre-edge region is modeled by using different possible functions (linear, polynomial, Victoreen-spline [174, 175]), the fitted function extrapolated beyond the edge and subtracted from the experimental $\mu(E)$, obtaining the true “elemental” absorption coefficient $\mu_t(E)$. The second step, the atomic background removal, is crucial for extracting good quality data, since choosing a wrong function might lead to removal of the EXAFS itself. The atomic function $\mu_0(E)$ is generally not known, but is usually assumed that the smooth part of “elemental” $\mu_t(E)$ can approximate it. One commonly used method for determining the $\mu_0(E)$ function is to fit $\mu_t(E)$ with polynomial or B-splines using a least squares procedures [172]. These splines are divided into sections of polynomials of some order which are connected to each other at knots, where the value and first derivative of the two joining polynomials match. This guarantees a high flexibility of the overall function, and enables the removal of low frequency components without affecting the high frequency EXAFS oscillations. The background-removed curve must be then normalized with respect to $\mu_0(E)$.

The next step is the conversion from photon energy E to photoelectron wave vector k through the relation:

$$k = \sqrt{\frac{2m}{\hbar^2}(E - E_0^{exp})} \tag{A.18}$$

E_0^{exp} is usually determined as the maximum of the first derivative of the absorption curve, but the exact choice is not essential during the data reduction process since its value will be refined during the final analysis. The $\chi(k)$ is usually multiplied by some power of k (k^n with n usually 1-3), in order to counterbalance the attenuation of the EXAFS amplitude with increasing *k*, due to the functional form of the backscattering amplitude *F_j(k)* and the $1/k$ dependence in the EXAFS equation. [1]

The obtained EXAFS function $\chi(k)$ can be interpreted by fitting it with theoretical models, but usually a final step is taken, even if not strictly necessary. By Fourier-transforming $\chi(k)$ into the r space a pseudo radial function is obtained, which can be fitted to unravel the structural parameters or serve as a simple approximated physical picture of the local structure around the absorbed. The transformation is completed according to

$$\tilde{\chi}(r') = \frac{1}{\sqrt{2\pi}} \int_{k_{min}}^{k_{max}} k^n \chi(k) e^{i2kr'} dk \tag{A.19}$$

This yields a complex function, consisting in an imaginary sine and real cosine part. The most illustrative representation is the modulus of the Fourier transform

$$|FT\left[\chi(k)\right]| = Mod\left[\tilde{\chi}(r')\right] = \sqrt{Re^2\left[\tilde{\chi}(r')\right] + Im^2\left[\tilde{\chi}(r')\right]} \tag{A.20}$$

which can be interpreted as a pseudo radial function, as mentioned above. The peaks appearing in $\tilde{\chi}(r')$ (and $Mod\left[\tilde{\chi}(r')\right]$) are shifted from the true distance r by $\alpha = r - r'$, which is usually in the range of 0.2-0.5 Å and depends on the atomic species involved, the chosen E_0^{exp} and the weighting scheme.

a) b) c) d) Figure 2 Data reduction steps: a) raw data; b) identification of pre-edge (red line) and post-edge (blue) backgrounds; c) identification of $\mu_0(E)$ (red line); d) normalized data

Along with the EXAFS region, also the XANES one can provide useful information. Albeit the lack of a simple analytical description of this region (even a complete physical understanding of the underlying phenomena is still missing), XANES holds a lot of chemical information, mainly regarding the oxidation state of the absorber and the coordination environment. For example, for K shell (1s state) absorption the

---

[1] Different weighting schemes have been suggested [176] for backscatterers with Z>57 (n=1), 36<Z<57 (n=2) and Z<36 (n=3), but no strict rule is usually applied.

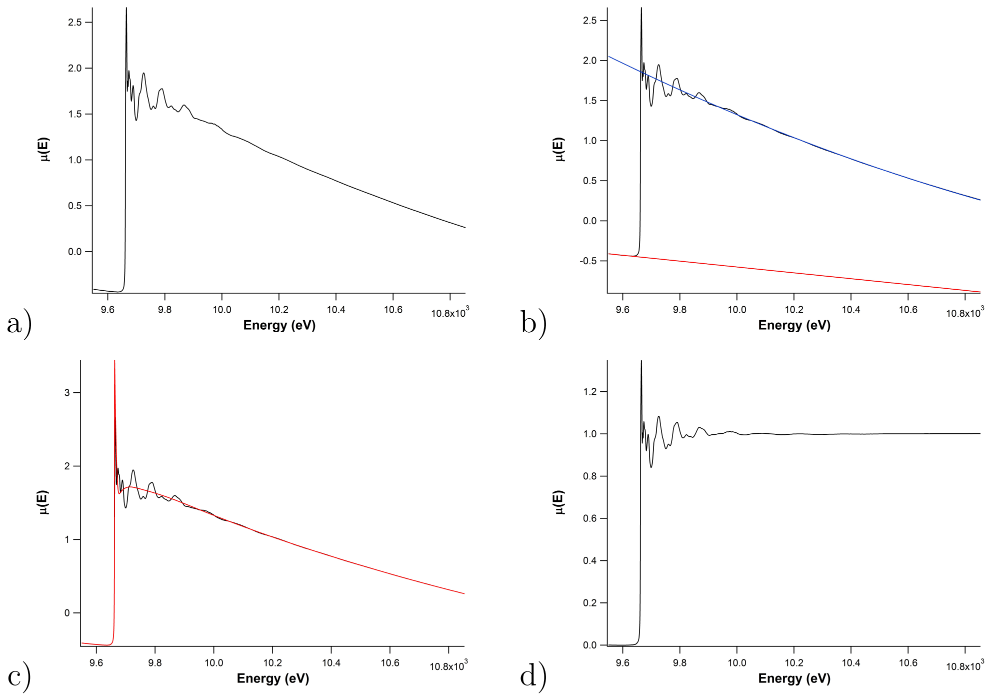

Figure A.3.: Data reduction steps: a) raw data; b) identification of pre-edge (red line) and post-edge (blue) backgrounds; c) identification of $\mu_0(E)$ (red line); d) normalized data

photoelectron must end up in a p state ($\Delta l = \pm 1$) and if there are no such available states, no 1s absorption will occur even is the photon energy is adequate. This is particularly evident for transitions to bound states. Transition metals compounds, for example, present a filled 3p band and the 2p levels of the ligands (e.g. oxygen) are usually too high in energy to overlap efficiently with the 1s state, therefore no absorption should occur. On the other hand, the metals have 3d states near the Fermi level which are only partially filled and which can hybridize with the ligands 2p levels, giving rise to pre-edge features. The XANES region is really sensitive to the degree of this hybridization, especially in correlation with the coordination geometry, since tetrahedral geometry favors the hybridization with respect to octahedral one (in a $\mathrm{T_d}$ field p orbitals have t_2 symmetry and d ones t_2 and e; in a $\mathrm{O_h}$ field p orbitals have t_{1u} symmetry while d t_{2g} and e_g). XANES can also be used to determine or confirm the oxidation state of the absorber, since in most cases there is a noticeable edge shift towards higher energy with increasing oxidation state (within similar ligand systems). With appropriate model samples, also different oxidation state ratios can be determined.

A.7. X-ray Photoelectron Spectroscopy

X-ray Photoelectron Spectroscopy, also known as Electron Spectroscopy for Chemical Analysis (ESCA) is a technique apt to the investigation of the chemical nature of the surface of a sample. It is based on the irradiation a sample with soft X-rays (1.2-1.5 keV) and the measurement of the kinetic energy of electrons [134] subsequently emitted by photoelectric effect [171]. The photoionization process can be summarized as

$$A + h\nu \rightarrow A^{+} + e^{-} \tag{A.21}$$

where A is a generic atom and $h\nu$ is the X-ray radiation of frequency ν. The energy conservation principle implies that

$$E(A) + h\nu = E(A^{+}) + E(e^{-}) \tag{A.22}$$

where the energy of the electron $E(e^{-})$ is in the form of kinetic energy $KE = E(e^{-})$. Eq. A.22 can be rearranged as

$$KE = h\nu - \Big[E(A^{+}) - E(A)\Big] = h\nu - BE \tag{A.23}$$

The term in bracket, representing the difference in energy between the ionized atom and the same atom in the ground state, corresponds to the binding energy (BE) of the emitted photoelectron.

In solids, the binding energy is usually referred to the solid's Fermi level, and therefore the corresponding work function φ_s must be added to Eq. A.23 :

$$KE = h\nu - BE - \varphi_s$$

It follow that, for the photoelectric process to occur, the X-ray energy $h\nu$ must be greater than the sum of the electron binding energy and the work function. Most commonly, Mg K_α($h\nu$=1253.6 eV) or Al K_α($h\nu$=1486.6 eV) X-ray sources are used, and the measured KE will vary depending on the source used. On the other hand, is common practice to discuss experimental values in terms of BE rather than KE, in order to avoid confusion if different sources are used.

The binding energy is the key to the chemical specificity of XPS for different chemical species, since each element and, for a given element, each different transition are characterized by typical values of BE, specific to the internal energy levels involved, and according to the chemical environment and oxidation state. The presence of a peak at a given energy is therefore diagnostic of a certain element on the surface of the analyzed sample, whilst the area of the peak is correlated to the atomic concentration of the element in the sampled area. In addition, the binding energy values (and correspondingly the peak shape and broadness) are also influenced by the oxidation state of the atom and its chemical surrounding, giving a detailed information on each element present in the atom. XPS is hence a qualitative and semiquantitative analysis technique, capable of detecting nearly all elements (hydrogen and helium are exceptions due to their low cross-sections with respect to X-rays).

The inner hole formed during the photoionization process might relax either in a radiative way (through the emission of X-ray photons, process known as X-ray fluorescence) or in a non-radiative way, through the emission of secondary electrons. This latter phenomenon is known as the “Auger emission” and Auger electrons possess an energy which is independent from the source used and is also element-specific (see Fig. A.4).

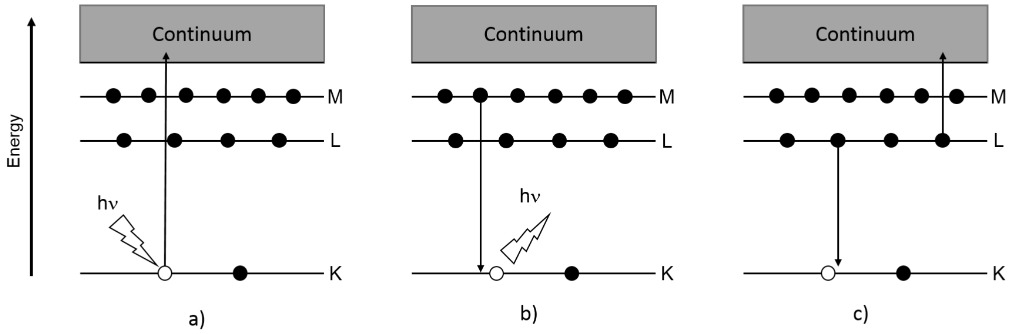

Figure A.4.: XPS phenomena: a) photoexcitation; b) X-ray fluorescence; c) Auger emission

The soft X-rays employed in this technique have a penetration depth of 1-10 µm but the information collected is limited to a much narrower range corresponding to few atomic layers, about 10-50 Å. This is due to the fact that only the photoelectrons coming from the outermost layers will be able to escape from the surface without undergoing any collision with other particles, whereas the electrons originating from the deeper layers will be decelerated by the interaction with the nuclei, and the corresponding information collected forms a background known as “Bremsstrahlung” (a German word meaning “braking radiation”).

Due to the photoelectric effect and Auger processes, the sample surfaces (in particular for insulating samples) might acquire a charge, leading to a slight shift of the peaks towards higher BE values (few eV). In order to counterbalance this phenomenon, the surface might be irradiated with a low energy electron beam, through a device called “neutralizer” or “flood gun”. Additionally, it is common practice to calculate the surface charging by using a reference and shift the experimental data accordingly. The most common reference is the C1s peak relative to adventitious surface carbon, which is found at BE=284.6 eV.

A typical instrument layout consists of an X-ray source, an analysis chamber constantly, an ion gun, an electron gun (i.e. neutralizer), an electron analyzer, connected to an electron detector and counter and a computer for data acquisition, storage and elaboration. The analysis chamber must be kept under ultrahigh vacuum (UHV) conditions in order to be able to collect the emitted electron beam and to limit the contamination of the sample surface.

A.8. Inductively Coupled Plasma - Mass Spectrometry

Inductively Coupled Plasma - Mass Spectrometry is an analytical technique used for accurate elemental determinations. An ICP-MS spectrometer combines a plasma torch, which ionizes the atoms constituting the investigated sample, with a mass spectrometer, which separates and detects the ions through its quadrupole filter. The plasma discharge generates positively charged ions, therefore highly electronegative elements (i.e., halogens) are difficult to analyze. For the determination of lanthanide ions in particular, it is preferable to ICP-Atomic Emission Spectroscopy, due to superior detection capabilities of mass spectrometers and higher speed.

In this PhD thesis, ICP-MS was used to determine the matrix-to-dopant atomic ratios of doped samples.

A.9. MicroRaman and Fourier Transformed Infrared Spectroscopies

Raman and FT-IR are analytical techniques sensitive to the vibrational modes of the analyzed specimens, with characteristic frequencies in the 50-4000 cm^{-1} range. Whereas FT-IR is an absorption spectroscopy, Raman is based upon the inelastic scattering of the electromagnetic radiation. For IR, the only active modes are those where molecular dipole changes, whereas in Raman spectroscopy only modes inducing a change in molecular polarisability are active [177]. These spectroscopic techniques are therefore considered complementary, as usually the modes not detectable to one analysis will be detectable to the other [166].

In Raman spectroscopy, due to the low intensity of scattered light compared to the incident beam, monochromatic lasers are the preferred choice as sources, in order to boost the collected signal and obtain better spectra. In microRaman configuration, the Raman spectrometer is coupled with a microscope, allowing systematic measurements to be carried out on different points of the sample, thus affording information on possible compositional gradient and allowing mapping of the sample composition to be performed.

A.10. Thermogravimetric Analysis and Differential Scanning Calorimetry

A thermogravimetric analysis investigates the change in mass of a sample upon heating and is used to study thermal stability and corresponding decomposition phenomena, oxidation, desorption and vaporization phenomena. Through data analysis, it is also possible to identify the reaction type which occurs in correspondence with each mass variation. In case of reactions occurring simultaneously, by deriving the thermogram curve ($\partial \mathrm{m}/\partial \mathrm{T}$), which isolates the temperatures where mass loss is fastest, it is possible to separate these overlapping curves. Measurements can be carried out both in air and in controlled atmosphere (e.g., nitrogen, argon, etc.), the latter in order to avoid oxidation processes and investigate pyrolysis events.

Differential Scanning Calorimetry (DSC) is an analytical method in which the energy input needed to maintain the sample at the same temperature as an inert reference material is recorded during a programmed change of temperature [178]. The temperature difference ΔT between the sample and the reference material should be null until a thermal event occurs. When this change is endothermic, the sample temperature lags behind the reference one, while when an exothermic event occurs, it leads the reference temperature. As soon as a thermal event takes place in the sample, a temperature difference ΔT is recorded as a net voltage in a thermocouple and consequently the power supplied to the sample is changed in order to reequilibrate the temperature. The resulting thermogram, showing the applied heat flow ($\partial \mathrm{H}/\partial \mathrm{T}$) versus temperature, will display a peak corresponding to every detected transition. The nature of each transition can be deduced from baseline changes (in the case of a glass transition) or from the peak type. Different setups however might show an exothermic reaction as a positive or negative peak, thus requiring graphs to specify whether they are exothermic-down or -up.

The presence of two thermocouples in the TGA apparatus enables the contextual collection of the corresponding DSC thermogram ($\partial \mathrm{H}/\partial \mathrm{T}$ versus T). Calibration is carried out for temperature, weight and DSC signal; for the first, standard metal samples having known melting points, such as zinc ($\mathrm{T_m}$ = 419.60°C) and indium ($\mathrm{T_m}$ = 156.53°C) are used; for weight measurements carried out in set conditions (empty and with known mass weights); lastly, DSC signal is measured with empty sample holders and with sapphire standards references.

A.11. Photoluminescence Spectroscopy

Photoluminescence spectroscopy analyzes the electronic structure of material, by investigating the phenomenon of light absorption and re-emission from a sample. It is one of the leading technique to investigate the band-gap of semiconductors, and a typical experiment usually consist in two parts. In the first part of the experiment, known as photoluminescence excitation (PLE), the specimen is irradiated while tuning the laser energy (detecting the signal at a fixed wavelength), and when the excitation laser matches an optical transition of the sample, the acquired signal increases. The collected spectrum is thus analogous to the absorption spectrum. Conversely, in the second part, which is more precisely the recording of the photoluminescence itself, the sample is irradiated with a specific wavelength, usually corresponding to the maximum of the PLE spectrum, and the emitted photons are collected. The PL spectrum thus represents the radiative recombination of the core-hole pairs and its modification due to the presence of localized defects or impurity levels, also due to the presence of doping ions.

A.12. Lactate Dehydrogenase Cytotoxicity Assay

Lactate Dehydrogenase enzymes can be used to assay to measure cytotoxicity since these enzymes are released by cells into the external environment when the cellular membrane is damaged. The activity of LDH in the culture medium is a measure of cell necrosis and/or apoptosis and can be evaluated by means of a colorimetric reaction involving the reduction of NAD in the presence of lactate and the subsequent conversion of a tetrazolium salt into a colored compound. The amount of this product after the enzymatic reaction, assessed by measuring its absorbance, is therefore directly correlate to damages induced by an external agent (e.g., nanoparticles).

A.13. Resazurin Cell Viability Assay

The Resazurin cell viability assay is a simple and fast way to determine the viability of mammalian cells by colorimetry. Metabolically active cells are able to reduce the non-fluorescent dye resazurin, present in the kits used for such assays, to its fluorescent form resofurin. The measured fluorescence intensity is proportional to the number of viable cells, and can also be correlated to their proliferation rate. Cell viability can be negatively influenced by the presence of an external agent, and consequently the fluorescence intensity decreases.

Bibliography

[1] A. D.McNaught and A.Wilkinson. *IUPAC. Compendium of Chemical Terminology, 2nd ed. (the "Gold Book").* Wiley Blackwell, Hoboken, New Jersey, 2nd edition.

[2] D. H.Everett. Manual of Symbols and Terminology for Physicochemical Quantities and Units, Appendix II: Definitions, Terminology and Symbols in Colloid and Surface Chemistry. *Pure Appl. Chem.*, 31:577, 1972.

[3] G.Schmid. *Nanoparticles: From Theory to Application.* Wiley-VC, Weinheim, 2004.

[4] K.Drexler, C.Peterson, and G.Pergamit. *Unbounding the future: the nanotechnology revolution.* Morrow, New York, 1991.

[5] B.Bhushan, editor. *Springer Handbook of Nanotechnology.* EngineeringPro collection. Springer, Heidelberg, 2nd edition, 2010.

[6] E.Matijevic. Uniform inorganic colloid dispersions. achievements and challenges. *Langmuir*, 10(1):8–16, 1994.

[7] R.Muñoz Espí, C. K.Weiss, and K.Landfester. Inorganic nanoparticles prepared in miniemulsion. *Curr. Opin. Colloid Interface Sci.*, 17(4):212–224, 2012.

[8] K.Landfester and M.Antonietti. Miniemulsions for the convenient synthesis of organic and inorganic nanoparticles and "single molecule" applications in materials chemistry. *Colloids and Colloid Assemblies*, 2004.

[9] R.Muñoz Espí, Y.Mastai, S.Gross, and K.Landfester. Colloidal systems for crystallization processes from liquid phase. *CrystEngComm*, 15(12):2175–2191, 2013.

[10] N.Bechthold, F.Tiarks, M.Willert, K.Landfester, and M.Antonietti. Miniemulsion polymerization: Applications and new materials. *Macromol. Symp.*, 151:549–555, 2000.

[11] K.Landfester, M.Willert, and M.Antonietti. Preparation of Polymer Particles in Nonaqueous Direct and Inverse Miniemulsions. *Macromolecules*, 33(7):2370–2376, 2000.

[12] M.Antonietti and K.Landfester. Polyreactions in miniemulsions. *Prog. Polym. Sci.*, 27(4):689–757, 2002.

[13] P.Sharma, S.Brown, G.Walter, S.Santra, and B.Moudgil. Nanoparticles for bioimaging. *Adv. Colloid Interface Sci.*, 123–126(0):471–485, 2006.

[14] M. Y.Berezin and S.Achilefu. Fluorescence Lifetime Measurements and Biological Imaging. *Chem. Rev.*, 110:2641, 2010.

[15] U.Schubert and N.Hüsing. *Synthesis of Inorganic Materials.* Wiley-VCH, Weinheim, 2005.

[16] C.Ostwald. *Grundriss der Kolloidchemie.* Number v. 1 in Grundriss der Kolloidchemie. T. Steinkopff, 1919.

[17] C.Ostwald. *Die Welt der vernachlässigten Dimensionen: eine Einführung in die moderene Kolloidchemie mit besonderer Berucksichtigung ihrer Anwendungen.* Theodor Steinkopf, 1922.

[18] I.Freestone, N.Meeks, M.Sax, and C.Higgitt. The Lycurgus Cup - A Roman nanotechnology. *Gold Bulletin*, 40(4):270–277, 2007.

[19] M.-P.Pileni. Water in oil colloidal droplets used as microreactors. *Adv. Colloid Interface Sci.*, 46(0):139–163, 1993.

[20] M. P.Pileni. Nanosized Particles Made in Colloidal Assemblies. *Langmuir*, 13(13):3266–3276, 1997.

[21] M.-P.Pileni. The role of soft colloidal templates in controlling the size and shape of inorganic nanocrystals. *Nat. Mater.*, 2(3):145–150, 2003.

[22] M.Boutonnet, S.Lögdberg, and E. E.Svensson. Recent developments in the application of nanoparticles prepared from w/o microemulsions in heterogeneous catalysis. *Curr. Opin. Colloid Interface Sci.*, 13(4):270–286, 2008.

[23] M.Sanchez-Dominguez, K.Pemartin, and M.Boutonnet. Preparation of inorganic nanoparticles in oil-in-water microemulsions: A soft and versatile approach. *Curr. Opin. Colloid Interface Sci.*, 17(5):297–305, 2012.

[24] I.Capek. Preparation of metal nanoparticles in water-in-oil (w/o) microemulsions. *Adv. Colloid Interface Sci.*, 110(1-2):49–74, 2004.

[25] J.Eastoe, M. J.Hollamby, and L.Hudson. Recent advances in nanoparticle synthesis with reversed micelles. *Adv. Colloid Interface Sci.*, 128-130(0):5–15, 2006.

[26] T.Cosgrove. *Colloid Science: Principles, Methods and Applications.* John Wiley & Sons, Chichester, West Sussex, 2nd edition, 2010.

[27] B.Derjaguin and L.Landau. Theory of the stability of strongly charged lyophobic sols and of the adhesion of strongly charged particles in solutions of electrolytes. *Acta Physico Chemica URSS*, 14:633, 1941.

[28] E.Verwey, J.Overbeek, and J.Overbeek. *Theory of the Stability of Lyophobic Colloids.* Elsevier, Amsterdam, 1948.

[29] P. J.Flory. Thermodynamics of high polymer solutions. *J. Chem. Phys.*, 9(8):660–660, 1941.

[30] M. L.Huggins. Solutions of long chain compounds. *J. Chem. Phys.*, 9(5):440–440, 1941.

[31] S.Asakura and F.Oosawa. On interaction between two bodies immersed in a solution of macromolecules. *J. Chem. Phys.*, 22(7):1255–1256, 1954.

[32] S.Asakura and F.Oosawa. Interaction between particles suspended in solutions of macromolecules. *J. Polymer Sci.*, 33(126):183–192, 1958.

[33] K.Landfester. Miniemulsions for Nanoparticle Synthesis. In *Colloid Chemistry II*, pages 75–123. Springer Berlin / Heidelberg, 2003.

[34] J. T.Davies. A quantitative kinetic theory of emulsion type, I. Physical chemistry of the emulsifying agent. *Gas-Liquid and Liquid-Liquid Interface Proceedings of the 2nd International Congress of Surface Activity*, pages 426–438, 1957.

[35] J. W.Goodwin. *Emulsions and Microemulsions*, pages 177–194. Colloids and Interfaces with Surfactants and Polymers - An Introduction. John Wiley & Sons, New York, 2004.

[36] H.Schlaad, H.Kukula, J.Rudloff, and I.Below. Synthesis of α,ω-Heterobifunctional Poly(ethylene glycol)s by Metal-Free Anionic Ring-Opening Polymerization. *Macromolecules*, 34(13):4302–4304, 2001.

[37] Z.Cao and U.Ziener. Synthesis of nanostructured materials in inverse miniemulsions and their applications. *Nanoscale*, 5(21):10093–10107, 2013.

[38] J. N.Israelachvili, D. J.Mitchell, and B. W.Ninham. Theory of self-assembly of hydrocarbon amphiphiles into micelles and bilayers. *J.Chem.Soc. Faraday Trans.2*, 72(0):1525–1568, 1976.

[39] C.Stubenrauch, T.Wielpütz, T.Sottmann, C.Roychowdhury, and F. J.DiSalvo. Microemulsions as templates for the synthesis of metallic nanoparticles. *Colloid Surface A*, 317(1-3):328–338, 2008.

[40] M.Sanchez-Dominguez, M.Boutonnet, and C.Solans. A novel approach to metal and metal oxide nanoparticle synthesis: the oil-in-water microemulsion reaction method. *J. Nanopart. Res.*, 11(7):1823–1829, 2009.

[41] J. A.Lopez Perez, M. A.Lopez Quintela, J.Mira, J.Rivas, and S. W.Charles. Advances in the preparation of magnetic nanoparticles by the microemulsion method. *J. Phys. Chem. B*, 101(41):8045–8047, 1997.

[42] D.Dodoo-Arhin, M.Leoni, P.Scardi, E.Garnier, and A.Mittiga. Synthesis, characterisation and stability of Cu_2O nanoparticles produced via reverse micelles microemulsion. *Mater. Chem. Phys.*, 122(2-3):602–608, 2010.

[43] A. K.Ganguli, T.Ahmad, S.Vaidya, and J.Ahmed. Microemulsion route to the synthesis of nanoparticles. *Pure Appl. Chem.*, 80(11):2451, 2008.

[44] C.Li, Y.Yin, H.Hou, N.Fan, F.Yuan, Y.Shi, and Q.Meng. Preparation and characterization of $Cu(OH)_2$ and CuO nanowires by the coupling route of microemulsion with homogenous precipitation. *Solid State Commun.*, 150(13-14):585–589, 2010.

[45] X.Li, G.He, G.Xiao, H.Liu, and M.Wang. Synthesis and morphology control of ZnO nanostructures in microemulsions. *J. Colloid Interface Sci.*, 333(2):465–73, 2009.

[46] D.Feldman and A.Barbalata. *Synthetic Polymers: Technology, Properties, Applications*. Springer, 1996.

[47] K. S.Suslick. *Ultrasound: Its Chemical, Physical, and Biological Effects*. Wiley-VCH, Weinheim, 1988.

[48] T. J.Mason. *Sonochemistry*. Oxford University Press, Oxford, 1999.

[49] K.Landfester, N.Bechthold, F.Tiarks, and M.Antonietti. Formulation and stability mechanisms of polymerizable miniemulsions. *Macromolecules*, 32(16):5222–5228, 1999.

[50] K.Landfester. Synthesis of colloidal particles in miniemulsions. *Annu. Rev. Mater. Res.*, 36(1):231–279, 2006.

[51] K.Landfester. The Generation of Nanoparticles in Miniemulsions. *Adv. Mater.*, 13(10):765–768, 2001.

[52] M.Willert, R.Rothe, K.Landfester, and M.Antonietti. Synthesis of Inorganic and Metallic Nanoparticles by Miniemulsification of Molten Salts and Metals. *Chem. Mater.*, 13(12):4681–4685, 2001.

[53] R.Schiller, C. K.Weiss, J.Geserick, N.Hüsing, and K.Landfester. Synthesis of mesoporous silica particles and capsules by miniemulsion technique. *Chem. Mater.*, 21(21):5088–5098, 2009.

[54] R.Rossmanith, C. K.Weiss, J.Geserick, N.Hüsing, U.Hörmann, U.Kaiser, and K.Landfester. Porous anatase nanoparticles with high specific surface area prepared by miniemulsion technique. *Chem. Mater.*, 20(18):5768–5780, 2008.

[55] R.Schiller, C. K.Weiss, and K.Landfester. Phase stability and photocatalytic activity of Zr-doped anatase synthesized in miniemulsion. *Nanotechnology*, 21(40):405603, 2010.

[56] A. M.Collins, C.Spickermann, and S.Mann. Synthesis of titania hollow microspheres using non-aqueous emulsions. *J. Mater. Chem.*, 13(5):1112–1114, 2003.

[57] A.Taden, M.Antonietti, A.Heilig, and K.Landfester. Inorganic Films from Three Different Phosphors via a Liquid Coating Route from Inverse Miniemulsions. *Chem. Vap. Deposition*, 16(24):5081, 2004.

[58] R.Muñoz Espí, Y.Qi, I.Lieberwirth, C. M.Gomez, and G.Wegner. Surface-functionalized latex particles as controlling agents for the mineralization of zinc oxide in aqueous medium. *Chem. - Eur. J.*, 12(1):118–129, 2006.

[59] Z.Cao, Z.Wang, C.Herrmann, U.Ziener, and K.Landfester. Narrowly Size-Distributed Cobalt Salt Containing Poly(2-hydroxyethyl methacrylate) Particles by Inverse Miniemulsion. *Langmuir*, 26(10):7054–7061, 2010.

[60] E.Schreiber, U.Ziener, A.Manzke, A.Plettl, P.Ziemann, and K.Landfester. Preparation of narrowly size distributed metal-containing polymer latexes by miniemulsion and other emulsion techniques: Applications for nanolithography. *Chem. Mater.*, 21(8):1750–1760, 2009.

[61] A.Manzke, A.Plettl, U.Wiedwald, L.Han, P.Ziemann, E.Schreiber, U.Ziener, N.Vogel, C. K.Weiss, K.Landfester, K.Fauth, J.Biskupek, and U.Kaiser. Formation of Highly Ordered Alloy Nanoparticles Based on Precursor-Filled Latex Spheres. *Chem. Mater.*, 24(6):1048–1054, 2012.

[62] R.Weissleder and U.Mahmood. Molecular imaging. *Radiology*, 219(2):316–333, 2001.

[63] R.Weissleder and V.Ntziachristos. Shedding light onto live molecular targets. *Nat. Med.*, 9(1):123–128, 2003.

[64] G. G.Stokes. On the change of refrangibility of light. *Philos. Trans. Roy. Soc. London*, 142:463–562, 1852.

[65] E.Hutter and D.Maysinger. Gold nanoparticles and quantum dots for bioimaging. *Microsc. Res. Tech.*, 74(7):592–604, 2011.

[66] H.Kobayashi, M.Ogawa, R.Alford, P. L.Choyke, and Y.Urano. New Strategies for Fluorescent Probe Design in Medical Diagnostic Imaging. *Chem. Rev.*, 110(5):2620–2640, 2010.

[67] M.Roskamp, A. K.Schaper, J. H.Wendorff, and S.Schlecht. Colloidal CdS/SiO_2 Nanocomposite Particles from Charged Colloids of CdS and Silica. *Eur. J. Inorg. Chem.*, 2007(17):2496–2499, 2007.

[68] E.Boisselier and D.Astruc. Gold nanoparticles in nanomedicine: preparations, imaging, diagnostics, therapies and toxicity. *Chem. Soc. Rev.*, 38(6):1759–1782, 2009.

[69] M.-C.Daniel and D.Astruc. Gold Nanoparticles: Assembly, Supramolecular Chemistry, Quantum-Size-Related Properties, and Applications toward Biology, Catalysis, and Nanotechnology. *Chem. Rev.*, 104(1):293–346, 2004.

[70] A.Llevot and D.Astruc. Applications of vectorized gold nanoparticles to the diagnosis and therapy of cancer. *Chem. Soc. Rev.*, 41(1):242–257, 2012.

[71] L.Pasquato, P.Pengo, and P.Scrimin. Functional gold nanoparticles for recognition and catalysis. *J. Mater. Chem.*, 14(24):3481–3487, 2004.

[72] P. K.Jain, X.Huang, I.El-Sayed, and M.El-Sayed. Noble Metals on the Nanoscale: Optical and Photothermal Properties and Some Applications in Imaging, Sensing, Biology, and Medicine. *Acc. Chem. Res.*, 41(12):1578–1586, 2008.

[73] P. K.Jain, K. S.Lee, I.El-Sayed, and M.El-Sayed. Calculated Absorption and Scattering Properties of Gold Nanoparticles of Different Size, Shape, and Composition: Applications in Biological Imaging and Biomedicine. *J. Phys. Chem. B*, 110(14):7238–7248, 2006.

[74] I. L.Medintz, H. T.Uyeda, E. R.Goldman, and H.Mattoussi. Quantum dot bioconjugates for imaging, labelling and sensing. *Nat. Mater.*, 4(6):435–446, 2005.

[75] F.Vetrone, R.Naccache, la Fuente Juarranz de, F.Sanz-Rodriguez, A.Blazquez-Castro, E. M.Rodriguez, D.Jaque, J. G.Sole, and J. A.Capobianco. Intracellular imaging of HeLa cells by non-functionalized $NaYF_4 : Er^{3+}$, Yb^{3+} upconverting nanoparticles. *Nanoscale*, 2(4):495–498, 2010.

[76] S. V.Eliseeva, B.Song, C. D. B.Vandevyver, A.-S.Chauvin, J. B.Wacker, and J.-C. G.Bunzli. Increasing the efficiency of lanthanide luminescent bioprobes: bioconjugated silica nanoparticles as markers for cancerous cells. *New J. Chem.*, 34:2915–2921, 2010.

[77] N.Erathodiyil and J. Y.Ying. Functionalization of Inorganic Nanoparticles for Bioimaging Applications. *Acc. Chem. Res.*, 44(10):925–935, 2011.

[78] L.Yin and Y.Bando. Semiconductor morphology: Optimizing properties by tuning morphology. *Nat. Mater.*, 4(12):883–884, 2005.

[79] H.Hu and W.Zhang. Synthesis and properties of transition metals and rare-earth metals doped ZnS nanoparticles. *Opt. Mater.*, 28(5):536–550, 2006.

[80] Z.Deng, L.Tong, M.Flores, S.Lin, J.-X.Cheng, H.Yan, and Y.Liu. High-Quality Manganese-Doped Zinc Sulfide Quantum Rods with Tunable Dual-Color and Multiphoton Emissions. *J. Am. Chem. Soc.*, 133(14):5389–5396, 2011.

[81] Z.Yu, X.Ma, B.Yu, Y.Pan, and Z.Liu. Synthesis and characterization of ZnS:Mn/ZnS core/shell nanoparticles for tumor targeting and imaging in vivo. *J. Biomater. Appl.*, 28(2):232–240, 2013.

[82] H.Li, M.Li, W. Y.Shih, P. I.Lelkes, and W. H.Shih. Cytotoxicity tests of water soluble ZnS and CdS quantum dots. *J. Nanosci. Nanotechnol.*, 11(4):3543–3551, 2011.

[83] J.Cao, J.Yang, Y.Zhang, L.Yang, Y.Wang, M.Wei, Y.Liu, M.Gao, X.Liu, and Z.Xie. Optimized doping concentration of manganese in zinc sulfide nanoparticles for yellow-orange light emission. *J. Alloys Compd.*, 486(1-2):890–894, 2009.

[84] R. N.Bhargava, D.Gallagher, X.Hong, and A.Nurmikko. Optical properties of manganese-doped nanocrystals of ZnS. *Phys. Rev. Lett.*, 72(3):416–419, 1994.

[85] S. J.Xu, S. J.Chua, B.Liu, L. M.Gan, C. H.Chew, and G. Q.Xu. Luminescence characteristics of impurities-activated ZnS nanocrystals prepared in microemulsion with hydrothermal treatment. *Appl. Phys. Lett.*, 73(4):478–480, 1998.

[86] D.Rosenthal and T. I.Taylor. A study of the mechanism and intermediates in the precipitation of cations with thioacetamide. *J. Am. Chem. Soc.*, 82(16):4169–4174, 1960.

[87] R.Shannon. Revised effective ionic radii and systematic studies of interatomic distances in halides and chalcogenides. *Acta Crystallogr. A*, 32(5):751–767, 1976.

[88] E. D.la Rosa, L. A.Diaz-Torres, P.Salas, and R. A.Rodríguez. Visible light emission under UV and IR excitation of rare earth doped ZrO_2 nanophosphor. *Opt. Mater.*, 27(7):1320–1325, 2005.

[89] K.Manzoor, S. R.Vadera, N.Kumar, and T. R. N.Kutty. Synthesis and photoluminescent properties of ZnS nanocrystals doped with copper and halogen. *Mater. Chem. Phys.*, 82(3):718–725, 2003.

[90] K.Sooklal, B. S.Cullum, S. M.Angel, and C. J.Murphy. Photophysical Properties of ZnS Nanoclusters with Spatially Localized Mn^{2+}. *J. Phys. Chem.*, 100(11):4551–4555, 1996.

[91] A. A.Bol, R.van Beek, and A.Meijerink. On the Incorporation of Trivalent Rare Earth Ions in II-VI Semiconductor Nanocrystals. *Chem. Mater.*, 14(3):1121–1126, 2002.

[92] J. F.Moulder, W. F.Stickle, P. E.Sobol, and K. D.Bomben. *Handbook of X-Ray Photoelectron Spectroscopy.* Physical Electronics Inc., Eden Praire, 1992.

[93] A. V.Naumkin, A.Kraut-Vass, S. W.Gaarenstroom, and C. J.Powell. NIST X-ray Photoelectron Spectroscopy Database.

[94] A.Kotronarou, G.Mills, and M. R.Hoffmann. Oxidation of hydrogen sulfide in aqueous solution by ultrasonic irradiation. *Environ. Sci. Technol.*, 26(12):2420–2428, 1992.

[95] D.Li, G.Bancroft, M.Kasrai, M.Fleet, B.Yang, X.Feng, K.Tan, and M.Peng. Sulfur K- and L-edge X-ray absorption spectroscopy of sphalerite, chalcopyrite and stannite. *Phys. Chem. Miner.*, 20(7):489–499, 1994.

[96] A. A.Bol, J.Ferwerda, J. A.Bergwerff, and A.Meijerink. Luminescence of nanocrystalline ZnS:Cu^{2+}. *J. Lumin.*, 99(4):325–334, 2002.

[97] P.Kumar, R.Nagarajan, and R.Sarangi. Quantitative X-ray absorption and emission spectroscopies: electronic structure elucidation of Cu_2S and CuS. *J. Mater. Chem. C*, 1(13):2448–2454, 2013.

[98] Y.Soo, Z.Ming, S.Huang, Y.Kao, R.Bhargava, and D.Gallagher. Local structures around Mn luminescent centers in Mn-doped nanocrystals of ZnS. *Phys. Rev. B*, 50(11):7602–7607, 1994.

[99] E.Wiberg, A. F.Holleman, and N.Wiberg. *Lehrbuch Der Anorganischen Chemie*. Walter de Gruyter, Berlin, 101st edition, 1995.

[100] P. W.Loeffen, R. F.Pettifer, S.Müllender, M. A.van Veenendaal, J.Röhler, and D. S.Sivia. Deconvolution of lifetime broadening at rare-earth L_{III} edges compared to resonant inelastic x-ray scattering measurements. *Phys. Rev. B*, 54(21):14877–14880, 1996.

[101] T.Moeller, D. F.Martin, L. C.Thompson, R.Ferrus, G. R.Feistel, and W. J.Randall. The Coordination Chemistry of Yttrium and the Rare Earth Metal Ions. *Chem. Rev.*, 65(1):1–50, 1965.

[102] R. D.Yang, S.Tripathy, F. E. H.Tay, L. M.Gan, and S. J.Chua. Photoluminescence and micro-Raman scattering in Mn-doped ZnS nanocrystalline semiconductors. *J. Vac. Sci. Technol. B*, 21(3):984, 2003.

[103] K.Nakamoto. Applications in Inorganic Chemistry. In *Infrared and Raman Spectra of Inorganic and Coordination Compounds*, pages 149–354. John Wiley & Sons, Inc.

[104] D.Schultze, U.Steinike, J.Kussin, and U.Kretzschmar. Thermal Oxidation of ZnS Modifications Sphalerite and Wurtzite. *Cryst. Res. Technol.*, 30(4):553–558, 1995.

[105] F.Di Benedetto, M.Borgheresi, A.Caneschi, G.Chastanet, C.Cipriani, D.Gatteschi, G.Pratesi, M.Romanelli, and R.Sessoli. First evidence of natural superconductivity: covellite. *Eur. J. Mineral.*, 18(3):283–287, 2006.

[106] H. T.Evans and J. A.Konnert. Crystal structure refinement of covellite. *Am. Mineral.*, 61(9-10):996–1000, 1976.

[107] C.-H.Lai, K.-W.Huang, J.-H.Cheng, C.-Y.Lee, B.-J.Hwang, and L.-J.Chen. Direct growth of high-rate capability and high capacity copper sulfide nanowire array cathodes for lithium-ion batteries. *J. Mater. Chem.*, 20:6638–6645, 2010.

[108] M.Kristl, N.Hojnik, S.Gyergyek, and M.Drofenik. Sonochemical preparation of copper sulfides with different phases in aqueous solutions. *Mater. Res. Bull.*, 48(3):1184–1188, 2013.

[109] Y.-H.Tseng, Y.He, S.Lakshmanan, C.Yang, W.Chen, and L.Que. Optical and thermal response of single-walled carbon nanotube-copper sulfide nanoparticle hybrid nanomaterials. *Nanotechnology*, 23(45):455708, 2012.

[110] A. K.Dutta, S.Das, S.Samanta, P. K.Samanta, B.Adhikary, and P.Biswas. CuS nanoparticles as a mimic peroxidase for colorimetric estimation of human blood glucose level. *Talanta*, 107(0):361–367, 2013.

[111] S.Goel, F.Chen, and W.Cai. Synthesis and biomedical applications of copper sulfide nanoparticles: From sensors to theranostics. *Small*, pages n/a–n/a, 2013.

[112] G.Ku, M.Zhou, S.Song, Q.Huang, J.Hazle, and C.Li. Copper Sulfide Nanoparticles As a New Class of Photoacoustic Contrast Agent for Deep Tissue Imaging at 1064 nm. *ACS Nano*, 6(8):7489–7496, 2012.

[113] Y.Li, W.Lu, Q.Huang, C.Li, and W.Chen. Copper sulfide nanoparticles for photothermal ablation of tumor cells. *Nanomedicine*, 5(8):1161–1171, 2010.

[114] Q.Lu, F.Gao, and D.Zhao. One-step synthesis and assembly of copper sulfide nanoparticles to nanowires, nanotubes, and nanovesicles by a simple organic amine-assisted hydrothermal process. *Nano Lett.*, 2(7):725–728, 2002.

[115] A.Ghezelbash and B. A.Korgel. Nickel sulfide and copper sulfide nanocrystal synthesis and polymorphism. *Langmuir*, 21(21):9451–9456, 2005.

[116] Y.Ni, H.Liu, F.Wang, G.Yin, J.Hong, X.Ma, and Z.Xu. Self-assembly of CuS nanoparticles to solid, hollow, spherical and tubular structures in a simple aqueous-phase reaction. *Appl. Phys. A: Mater.*, 79(8):2007–2011, 2004.

[117] T.Thongtem, A.Phuruangrat, and S.Thongtem. Characterization of copper sulfide nanostructured spheres and nanotubes synthesized by microwave-assisted solvothermal method. *Mater. Lett.*, 64(2):136–139, 2010.

[118] H.Xu, W.Wang, and W.Zhu. Sonochemical synthesis of crystalline CuS nanoplates via an in situ template route . *Mater. Lett.*, 60(17–18):2203–2206, 2006.

[119] L.Armelao, D.Camozzo, S.Gross, and E.Tondello. Synthesis of copper sulphide nanoparticles in carboxylic acids as solvent. *J. Nanosci. Nanotechnol.*, 6(2):401–408, 2006.

[120] H.Zhu, J.Wang, and D.Wu. Fast Synthesis, Formation Mechanism, and Control of Shell Thickness of CuS Hollow Spheres. *Inorg. Chem.*, 48(15):7099–7104, 2009.

[121] A.Dutta and S. K.Dolui. Preparation of colloidal dispersion of CuS nanoparticles stabilized by SDS. *Mater. Chem. Phys.*, 112(2):448–452, 12/1 2008.

[122] J. N.Solanki, R.Sengupta, and Z.Murthy. Synthesis of copper sulphide and copper nanoparticles with microemulsion method. *Solid State Sci.*, 12(9):1560–1566, 2010.

[123] L.Gao, E.Wang, S.Lian, Z.Kang, Y.Lan, and D.Wu. Microemulsion-directed synthesis of different CuS nanocrystals. *Solid State Commun.*, 130(5):309–312, 2004.

[124] X.Zhang, G.Wang, A.Gu, Y.Wei, and B.Fang. Cus nanotubes for ultrasensitive nonenzymatic glucose sensors. *Chem.Commun.*, (45):5945–5947, 2008.

[125] X.Dong, D.Potter, and C.Erkey. Synthesis of CuS Nanoparticles in Water-in-Carbon Dioxide Microemulsions. *Ind. Eng. Chem. Res.*, 41(18):4489–4493, 2002.

[126] G.Morgese. Nanostrutture inorganiche funzionali via miniemulsione: sintesi, caratterizzazione e funzionalizzazione. Master's thesis, 2013.

[127] A. E.Lewis. Review of metal sulphide precipitation. *Hydrometallurgy*, 104(2):222–234, 2010.

[128] D. R.Lide. *CRC Handbook of Chemistry and Physics.* CRC, Boca Raton, Florida, 85th edition, 2004.

[129] P.Scherrer. Bestimmung der Größe und der inneren Struktur von Kolloidteilchen mittels Röntgenstrahlen. *Nachrichten von der Gesellschaft der Wissenschaften zu Göttingen, Mathematisch-Physikalische Klasse*, 2:98–100, 1918.

[130] H. P.Klug and L. E.Alexander. *X-ray diffraction procedures for polycrystalline and amorphous materials.* John Wiley & Sons, New York, 1974.

[131] X.-P.Shen, H.Zhao, H.-Q.Shu, H.Zhou, and A.-H.Yuan. Self-assembly of cus nanoflakes into flower-like microspheres: Synthesis and characterization. *J. Phys. Chem. Solids*, 70(2):422–427, 2009.

[132] W.Du, X.Qian, X.Ma, Q.Gong, H.Cao, and J.Yin. Shape-Controlled Synthesis and Self-Assembly of Hexagonal Covellite (CuS) Nanoplatelets. *Chem. - Eur. J.*, 13(11):3241–3247, 2007.

[133] R.Pattrick, J.Mosselmans, J.Charnock, K.England, G.Helz, C.Garner, and D.Vaughan. The structure of amorphous copper sulfide precipitates: An X-ray absorption study. *Geochim. Cosmochim. Acta*, 61(10):2023–2036, 1997.

[134] D.Briggs and M. P.Seah. *Practical Surface Analysis: Auger and X-ray photoelectron spectroscopy*, volume 2nd of *Practical Surface Analysis.* Wiley, New York, 1990.

[135] C. D.Wagner. Auger parameter in electron spectroscopy for the identification of chemical species. *Anal. Chem.*, 47(7):1201–1203, 1975.

[136] D.Li, G.Bancroft, M.Kasrai, M.Fleet, X.Feng, B.Yang, and K.Tan. S K- and L-edge XANES and electronic structure of some copper sulfide minerals. *Phys. Chem. Miner.*, 21(5):317–324, 1994.

[137] F.Zhang and S. S.Wong. Controlled synthesis of semiconducting metal sulfide nanowires. *Chem. Mater.*, 21(19):4541–4554, 2009.

[138] P.Kumar, M.Gusain, and R.Nagarajan. Synthesis of $Cu_{1.8}S$ and CuS from Copper-Thiourea Containing Precursors; Anionic (Cl^-, $NO_3{}^-$, $SO_4{}^{2-}$) Influence on the Product Stoichiometry. *Inorg. Chem.*, 50(7):3065–3070, 2011.

[139] X.Jiang, Y.Xie, J.Lu, W.He, L.Zhu, and Y.Qian. Preparation and phase transformation of nanocrystalline copper sulfides (Cu_9S_8, Cu_7S_4 and CuS) at low temperature. *J. Mater. Chem.*, 10(9):2193–2196, 2000.

[140] X. L.Yu, C. B.Cao, H. S.Zhu, Q. S.Li, C. L.Liu, and Q. H.Gong. Nanometer-sized copper sulfide hollow spheres with strong optical-limiting properties. *Adv. Funct. Mater.*, 17(8):1397–1401, 2007.

[141] I. D.Shah and S. E.Khalafalla. Thermal decomposition of CuS to $Cu_{1.8}S$. *Metall. Trans.*, 2(2):605–606, 1971.

[142] J. G.Dunn. The oxidation of sulphide minerals. *Thermochim. Acta*, 300(1–2):127–139, 1997.

[143] A.Bensalah, M.Mortier, G.Patriarche, P.Gredin, and D.Vivien. Synthesis and optical characterizations of undoped and rare-earth-doped CaF_2 nanoparticles. *J. Solid State Chem.*, 179(8):2636–2644, 2006.

[144] M.Pedroni, F.Piccinelli, T.Passuello, M.Giarola, G.Mariotto, S.Polizzi, M.Bettinelli, and A.Speghini. Lanthanide doped upconverting colloidal CaF_2 nanoparticles prepared by a single-step hydrothermal method: toward efficient materials with near infrared-to-near infrared upconversion emission. *Nanoscale*, 3:1456–1460, 2011.

[145] G.Zhi, J.Song, B.Mei, and W.Zhou. Synthesis and characterization of Er^{3+} doped CaF_2 nanoparticles. *J. Alloys Compd.*, 509(37):9133–9137, 2011.

[146] W.Zheng, S.Zhou, Z.Chen, P.Hu, Y.Liu, D.Tu, H.Zhu, R.Li, M.Huang, and X.Chen. Sub-10nm Lanthanide-Doped CaF_2 Nanoprobes for Time-Resolved Luminescent Biodetection. *Angew. Chem., Int. Ed.*, 52(26):6671–6676, 2013.

[147] B. C.Hong and K.Kawano. Syntheses of CaF_2:Eu nanoparticles and the modified reducing TCRA treatment to divalent Eu ion. *Opt. Mater.*, 30(6):952–956, 2008.

[148] X.Sun and Y.Li. Size-controllable luminescent single crystal CaF_2 nanocubes. *Chem. Commun.*, 9(14):1768–1769, 2003.

[149] C.Pandurangappa, B. N.Lakshminarasappa, and B. M.Nagabhushana. Synthesis and characterization of CaF_2 nanocrystals. *J. Alloys Compd.*, 489(2):592–595, 2010.

[150] C.Feldmann, M.Roming, and K.Trampert. Polyol-Mediated Synthesis of Nanoscale CaF_2 and CaF_2:Ce,Tb. *Small*, 2(11):1248–1250, 2006.

[151] Z.Quan, D.Yang, P.Yang, X.Zhang, H.Lian, X.Liu, and J.Lin. Uniform colloidal alkaline earth metal fluoride nanocrystals: Nonhydrolytic synthesis and luminescence properties. *Inorg. Chem.*, 47(20):9509–9517, 2008.

[152] I.Lonardelli, H. R.Wenk, L.Lutterotti, and M.Goodwin. Texture analysis from synchrotron diffraction images with the Rietveld method: dinosaur tendon and salmon scale. *J. Synchrotron Radiat.*, 12(3):354–360, 2005.

[153] L.Lutterotti, S.Matthies, H. R.Wenk, A. S.Schultz, and J.Richardson J.W. Combined texture and structure analysis of deformed limestone from time-of-flight neutron diffraction spectra. *J. Appl. Phys.*, 81(2):594–600, 1997.

[154] D. H.Templeton and C. H.Dauben. Lattice Parameters of Some Rare Earth Compounds and a Set of Crystal Radii. *J. Am. Chem. Soc.*, 76(20):5237–5239, 1954.

[155] P.Samuel, H.Ishizawa, Y.Ezura, K. I.Ueda, and S. M.Babu. Spectroscopic analysis of Eu doped transparent CaF_2 ceramics at different concentration. *Opt. Mater.*, 33(5):735–737, 2011.

[156] D. C.Krupka and D. M.Mahoney. Electroluminescence and Photoluminescence of Thin Films of ZnS Doped with Rare-Earth Metals. *J. Appl. Phys.*, 43(5):2314–2320, 1972.

[157] S. V.Eliseeva and J. C. G.Bünzli. Lanthanide luminescence for functional materials and bio-sciences. *Chem. Soc. Rev.*, 39:189, 2010.

[158] P.Hänninen and H.Härmä. *Lanthanide Luminescence: Photophysical, Analytical and Biological Aspects*. Springer Series on Fluorescence, Methods and Applications. Springer, Heidelberg, 2011.

[159] O.Deutschmann, H.Knözinger, K.Kochloefl, and T.Turek. *Heterogeneous Catalysis and Solid Catalysts*. Wiley-VCH, Weinheim, 2000.

[160] N.Nabih, R.Schiller, I.Lieberwirth, E.Kockrick, R.Frind, S.Kaskel, C. K.Weiss, and K.Landfester. Mesoporous CeO_2 nanoparticles synthesized by an inverse miniemulsion technique and their catalytic properties in methane oxidation. *Nanotechnology*, 22(13):135606, 2011.

[161] D. A.Shirley. High-resolution x-ray photoemission spectrum of the valence bands of gold. *Phys. Rev. B*, 5:4709–4714, 1972.

[162] B.Ravel and M.Newville. *ATHENA*, *ARTEMIS*, *HEPHAESTUS*: data analysis for X-ray absorption spectroscopy using *IFEFFIT*. *J. Synchrotron Radiat.*, 12(4):537–541, 2005.

[163] S.Horikoshi and N.Serpone. *Microwaves in Nanoparticle Synthesis: Fundamentals and Applications*. Wiley-VCH, Weinheim, 2013.

[164] S.Mascotto, O.Tsetsgee, K.Muller, C.Maccato, B.Smarsly, D.Brandhuber, E.Tondello, and S.Gross. Effect of microwave assisted and conventional thermal heating on the evolution of nanostructured inorganic-organic hybrid materials to binary ZrO_2-SiO_2 oxides. *J. Mater. Chem.*, 17:4387–4399, 2007.

[165] A.Einstein. Über die von der molekularkinetischen Theorie der Wärme geforderte Bewegung von in ruhenden Flüssigkeiten suspendierten Teilchen. *Annalen der Physik*, 322(8):549–560, 1905.

[166] H.Perkampus. *Encyclopedia of Spectroscopy*. Wiley-VCH, Weinheim, 1995.

[167] H. M.Rietveld. Line profiles of neutron powder-diffraction peaks for structure refinement. *Acta Crystallogr.*, 22(1):151–152, 1967.

[168] H. M.Rietveld. A profile refinement method for nuclear and magnetic structures. *J. Appl. Crystallogr.*, 2(2):65–71, 1969.

[169] A.Le Bail, I.Madsen, L. M. D.Cranswick, J. K.Cockcroft, P.Norby, A. D.Zuev, A.Fitch, J.Rodriguez-Carvajal, C.Giacovazzo, R. B.Von Dreele, P.Scardi, N. C.Popa, R.Allmann, L. A.Solovyov, B.Hinrichsen, U.Schwarz, A.Altomare, A.Moliterni, R.Caliandro, R.Rizzi, N. V. Y.Scarlett, and M.Jansen. *Powder Diffraction*. The Royal Society of Chemistry, Cambridge, 2008.

[170] M.Newville. Fundamentals of XAFS. *Consortium for Advanced Radiation Sources, University of Chicago (USA)[http://xafs. org]*, 2004.

[171] A.Einstein. Über einen die Erzeugung und Verwandlung des Lichtes betreffenden heuristischen Gesichtspunkt. *Annalen der Physik*, 322(6):132–148, 1905.

[172] B. K.Teo. *Exafs: Basic Principles and Data Analysis*. Springer-Verlag, Heidelberg, 1986.

[173] M.Bauer and H.Bertagnolli. X-ray Absorption Spectroscopy - The Method and Its Applications. *Bunsen Magazin*, 6:216, 2007.

[174] J. A.Victoreen. Probable X-Ray Mass Absorption Coefficients for Wavelengths Shorter Than the K Critical Absorption Wavelength. *J. Appl. Phys.*, 14(2):95–102, 1943.

[175] J. A.Victoreen. The Absorption of Incident Quanta by Atoms as Defined by the Mass Photoelectric Absorption Coefficient and the Mass Scattering Coefficient. *J. Appl. Phys.*, 19(9):855–860, 1948.

[176] B.-K.Teo and P. A.Lee. Ab initio calculations of amplitude and phase functions for extended x-ray absorption fine structure spectroscopy. *J. Am. Chem. Soc.*, 101(11):2815–2832, 1979.

[177] R.McCreery. *Raman Spectroscopy for Chemical Analysis*. Chemical Analysis: A Series of Monographs on Analytical Chemistry and Its Applications. John Wiley & Sons, New York, 2005.

[178] E.Kaufmann. *Characterization of Materials, 2 Volume Set*. Characterization of Materials. Wiley & Sons, Hoboken, New Jersey, 2003.

Acknowledgments

First of all, I am deeply grateful to my supervisor, Prof. Maurizio Casarin for giving me the opportunity to undertake this Ph.D. and for all the precious advices. My special thanks go to Dr. Silvia Gross, for teaching me a lot, for always supporting and encouraging me, and having so much trust in me. My words are not enough to express all my gratitude.

Scuola di Dottorato in Scienze Molecolari (Dip. Scienze Chimiche, Università degli Studi di Padova) is thanked for the financial support.

My most sincere thanks also go to Prof. Katharina Landfester (Max Planck Institut für Polymerforschung, Mainz) for letting me join her work group for the first months of my Ph.D. and to Dr. Rafael Muñoz-Espí, who tutored me during my staying there, for all the precious discussions and advices. Also, my thanks go to all members in the Landfester work group for the friendship they extended to me.

Grateful thanks also go to all the people who actively contributed to this work. In particular, Prof. Stefano Gialanella (University of Trento) is acknowledged for TEM data collection and discussion, Prof. Adolfo Speghini (University of Verona) is thanked for PL measurements and interpretation. Prof. Antonella Motta (University of Trento) is gratefully thanked for the cytotoxicity tests, and also for allowing me to witness one of these tests. I would also like to extend my gratitude to Dr. Chiara Maurizio, from the Department of Physics (University of Padova), for the help in interpreting the EXAFS data, and to Dr. Daniel Forrer, for his patience in teaching me the basis of DFT calculations.

I would also like to acknowledge all the people in the University of Padova which helped me by carrying out some analyses on my samples. In particular, Prof. Paolo Pastore and Dr. Denis Badocco, who performed ICP-MS measurements, and Dr. Roberta Saini, who carried out TGA-DSC measurements. Prof. Fabrizio Mancin is also acknowledged for allowing me to use the DLS instrument.

I am also very obliged to the Società Italiana di Luce di Sincrotrone (SILS) for financial support to attend the "XII Synchrotron Radiation School" and to the CALIPSO program of the European Union, for granting me support for many beamtimes. At this regard, I would also like to acknowledge the beamline scientists who helped me during the XAS measurements, in particular Giuliana Aquilanti and Luca Olivi (Elettra), Maarten Nachtegaal (SLS) and Emiliano Fonda (Soleil).

Finally, I must thank all the people in my work group, starting with Francesca, Erika and Giulia, which gave a great contribution in this work, and continuing with

Marilisa, Stefano, Gabriele, Niels, Antonio and Francesco. Each one of you helped to make the life in the lab and outside it easier and more fun.